Design of Mixed Ionic-Electronic Polymeric Conductors for Organic Electrochemical Transistors

Maximilian Moser

Linacre College

Department of Chemistry

University of Oxford

June 2021

A thesis submitted in partial fulfilment of the requirements for the degree of Doctor of Philosophy in Chemistry

To my parents and family, for their love, time, and inspiration over the past 25 years.

I Declaration of Originality

The work presented in this thesis was conducted between October 2017 and June 2021 at Imperial College London and the University of Oxford. All the work is my own unless otherwise stated and has not been submitted for any other degree at this or any other university.

Maximilian Moser

June 2021

II Copyright Declaration

III Abstract

Organic electrochemical transistors (OECTs) are electronic devices that have gained significant attention for many biomedical applications, including as electrophysiological recording elements, cell activity monitors, and biomolecule sensors. Compared to conventional transistors, one distinguishing feature of OECTs is the requirement of the employed channel material to conduct both ionic and electronic charge carriers. Currently, poly(3,4-ethylenedioxythiophene):poly(styrenesulfonate) (**PEDOT:PSS**), has established itself as OECT benchmark channel material, predominantly due to its widespread commercial availability. **PEDOT:PSS**-based OECTs, however, display several disadvantages, such as moderate steady-state performances and **PEDOT:PSS**' limited chemical tunability preventing the formulation of structure-property relationships to guide future material design. Based on these limitations, this thesis focuses on the development of ethylene glycol (EG) functionalised conjugated polymers capable of conducting both ionic and electronic charge carriers to advance OECT performance, while concomitantly also establishing molecular design guidelines for the development of future channel materials.

In **Chapter 2** a series of four polythiophenes with pendant EG side-chain lengths ranging between two and six EG repeat units is synthesised and characterised. Specifically, **p(g3T2-T)**, the polymer employing triethylene glycol side-chains is shown to incur the highest OECT performance, with both EG side-chain length shortening and lengthening proving to be detrimental towards OECT performance.

Chapter 3 builds on the results of Chapter 2 and explores how variation in the relative distribution of the EG side-chains in polythiophenes impacts their swelling and therefore their OECT performance and stability. While intermediate degrees of polymer swelling boost device performance, minimising the polymers' swelling improves device stability.

The importance of maximising OECT device performance and stability are highlighted by employing one of the newly developed polymers as the channel material in a SARS-CoV-2 OECT biosensor, incurring better sensing performances compared to the **PEDOT:PSS** benchmark.

Chapter 4 investigates the use of the diketopyrrolopyrrole (DPP) unit to improve the p-type performance of donor-acceptor copolymers in OECTs, whose performance has lagged far behind their all-donor counterparts. In particular, control over both the overall and relative energy levels in these polymers is demonstrated to be of utmost importance to tune their performance and stability in devices.

IV Acknowledgements

First, I would like to dearly thank my supervisor Prof. Iain McCulloch for giving me the opportunity to join his research group and for his fantastic support throughout the years. Thank you, Iain, for having been the best supervisor one could wish for both in and out of the lab, and for providing me with the correct balance of guidance and independence to develop as a scientist and as a person. Thank you also for your belief in me even before starting my DPhil and for assisting me in securing a Schrödinger Scholarship, which has provided me with the financial support to conduct my research throughout the years. I will be forever grateful to you for guiding me through both successful and unsuccessful times.

Andy and Nicola, thank you too for having acted as sources of inspiration, learning, and feedback since the very early days. You have played key roles throughout my DPhil and I will never forget what you have done for me. Thank you also for the wonderful friendship that we have built outside of the academic context.

I am also thankful to all past and present members of the McCulloch research group, including: Adam, Alex, Petruţa, Sophie, Helen, Flo, James, Karl, Maryam, Cameron, Mark, Catherine, Ben, Maxime, Matt, Andreea, Sarah, Zeinab, Shao, and Ada, for transferring their knowledge and skills to me. Thank you also for rendering each day in the laboratory a pleasure and for making the weekdays feel as good as the weekends. Similarly, I am also grateful to the McCulloch group members at King Abdullah University of Science and Technology, including Alexandra, Balaji, Craig, Hu, Jan, Rajendar, Rawad, Weimin, and Weijuan. Thank you also to the students in the Heeney group and in particular to Martina, Simon, Tom, Notina, Simeng, Adam, Charlotte, Qiao, Xiantao, Pete, Florian, Filip, Fei, and Shengyu for ensuring a great work atmosphere throughout the years.

I would also like to thank Prof. Sahika Inal for her generosity and for having hosted me on several occasions in her laboratory at King Abdullah University of Science and Technology in Saudi Arabia. Thank you for making me feel like being part of your research group and for the wonderful collaboration that we have developed over the years. Tania, Achilleas, David, Jokubas, Shofarul, Anil, Keying, Amer, Abdulelah, Prem, and Victor, a big thank you also to you for supporting me throughout, my thesis output would not be the same without your help. Thank you also to all other collaborators across the world for your feedback and assistance, it has been an honour and privilege to work alongside you.

I also want to thank my friends and in particular Philipp, Chris, and Mario for rendering every moment outside of university unforgettable. Philipp, thank you very much for your encouragement and support since starting our undergraduate degree together; I truly believe that neither of us would be where we are today had we not met each other. Chris, thank you for making me realise that life outside of university is equally as important as life at university and making the most of both is key to live a happy life. Mario, thank you for teaching me that showing and acknowledging your weaknesses is fundamental to overcome them. Chelsie, thank you for your unconditional support in everything I do and for making me live my best life, you truly are a blessing.

Last but certainly not least, thank you to my outstanding parents for having given me everything I could have wished for during the past 25 years. Your love and support have been irreplaceable and your dedication and commitment towards your own goals have been the biggest source of inspiration to me. Thank you, grandma, for having been here throughout, for your love, generosity, and for coming to visit me numerous times. Thank you also to my grandparents who I lost throughout this journey, your impact in the earlier days has made a lasting impact on me and I will always carry your memories with me.

V Publications

1) A. Marks, N. Gasparini, I. McCulloch, and **M. Moser**, A Review on Organic Electrochemical Transistor Biosensors, Manuscript in preparation.
2) L. Q. Flagg, **M. Moser**, I. McCulloch, and L. Richter, *In situ* GIWAXS Studies Describing the Swelling Behaviour of Ethylene Glycol Functionalised Conjugated Polymers, Manuscript in preparation.
3) B. D. Paulsen, **M. Moser** (co-first author), D. Meli, R. Wu, I. McCulloch, and J. Rivnay, Chalcogen Atom Substiution in Ethylene Glycol Functionalised Conjugated Polymers for Organic Electrochemical Transistor Applications, Manuscript in preparation.
4) A. Marks, X. Chen, R. B. Rashid, X. Ji, B. D. Paulsen, **M. Moser**, S. Griggs, J. Rivnay, and I. McCulloch, High Performing Glycolated Mixed Conduction Acceptor-acceptor Fused Ladder-type Polymers for n-type OECTs, Manuscript in preparation.
5) T. C. H. Castillo, **M. Moser**, C. Cendra, P. Nayak, A. Salleo, I. McCulloch, and S. Inal, Effect of Solvent Additives and Molecular Dopants on the Performance of a p-type Organic Electrochemical Transistor, Manuscript in preparation.
6) J. Kosco, S. Gonzalez-Carrero, C. T. Howells, W. Zhang, **M. Moser**, R. Sheelamanthula, B. Willner, T. C. Hidalgo, H. Faber, B. Purushothaman, M. Sachs, H. Cha, T. Anthopoulos, S. Inal, J. R. Durrant, and I. McCulloch, Oligoethylene Glycol Sidechains Increase Charge Generation in Organic Semiconductor Nanoparticles for Enhanced Photocatalytic Hydrogen Evolution, Submitted to *Adv. Mater.*
7) S. T. M. Tan, T. Quill, **M. Moser**, X. Chen, A. Salleo, and A. Giovannitti, Recyclable Aqueous-Based Polymeric Energy Storage Devices, Submitted to *ACS Energy Lett.*

8) **M. Moser**, I. B. Dimov, G. Malliaras, and I. McCulloch, Organic Semiconductors for Neural Applications, Submitted to *Chem. Rev*.

9) F. Torricelli, D. Z. Adrahtas, Z. Bao, M. Berggren, F. Biscarini, A. Bonfiglio, C. A. Bortolotti, D. Frisbie, E. Macchia, G. G. Malliaras, I. McCulloch, **M. Moser**, T.-Q. Nguyen, R. M. Owens, A. Salleo, A. Spanu, and L. Torsi, Electrolyte-gated Transistors for Enhanced Performance Bioelectronics, Submitted to *Nat. Rev. Methods Primers*.

10) **M. Moser**, Y. Wang, T. C. Hidalgo, J. Surgailis, F. Moruzzi, S. Griggs, A. Marks, N. Gasparini, A. Wadsworth, S. Inal, I. McCulloch, and W. Yue, Propylene and Butylene Glycol: New Alternatives to Ethylene Glycol in Conjugated Polymers for Bioelectronic Applications, Submitted to *Mater. Horiz.*

11) J. F. Ponder Jr., H. Chen, A. M. T. Luci, S. Moro, M. Turano, A. L. Hobson, G. S. Collier, L. M. A. Perdigão, **M. Moser**, W. Zhang, G. Costantini, J. R. Reynolds, and I. McCulloch, Low Defect, High Molecular Weight Indacenodithiophene (IDT) Polymers via C-H Activation: Evaluation of a Simpler and Greener Approach to Organic Electronic Materials, Submitted to *ACS Mater. Lett.*

12) S. T. M. Tan, S. Keene, A. Giovannitti, A. Melianas, **M. Moser**, I. McCulloch, and A. Salleo, Operation Mechanism of Organic Electrochemical Transistors as Redox Chemical Transducers, Submitted to *J. Mater. Chem. C*

13) R. K. Hallani, B. D. Paulsen, A. J. Petty II, R. Sheelamanthula, **M. Moser**, K. J. Thorley, W. Sohn, R. B. Rashid, A. Savva, S. Moro, J. P. Parker, O. Drury, M. Alsufyani, M. Neophytou, J. Kosco, S. Inal, G. Costantini, J. Rivnay, and I. McCulloch, Regiochemistry-driven Organic Electrochemical Transistor Performance Enhancement in Ethylene Glycol Functionalized Polythiophenes, *J. Am. Chem. Soc.* **2021**, DOI: 10.1021/jacs.1c03516.

14) K. Guo, S. Wustoni, A. Koklu, E. Diaz-Galicia, **M. Moser**, A. Hama, A. A. Alqahtani, A. N. Ahmad, F. S. Alhamlan, M. Shuaib, A. Pain, I. McCulloch, S. T. Arold, R. Grünberg, and S. Inal, Rapid Single-molecule Detection of COVID-19 and MERS Antigens via Nanobody-functionalized Organic Electrochemical Transistors, *Nat. Biomed. Eng.* **2021**, DOI: 10.1038/s41551-021-00734-9.

15) T. Zhang, **M. Moser**, A. D. Scaccabarozzi, H. Bristow, P. Jacoutot, A. Wadsworth, T. D. Anthopoulos, I. McCulloch, and N. Gasparini, Ternary Organic Photodetectors Based On Pseudo-Binaries Nonfullerene-based Acceptors, *J. Phys. Mater.* **2021**, *4*, 045001.

16) **M. Moser**, J. Gladisch, S. Ghosh, T. C. Hidalgo, J. F. Ponder Jr., R. Sheelamanthula, Q. Thiburce, N. Gasparini, A. Wadsworth, A. Salleo, S. Inal, M. Berggren, I. Zozoulenko, E. Stavrinidou, and I. McCulloch, Controlling Electrochemically Induced Volume Changes in Conjugated Polymers by Chemical Design: from Theory to Devices, *Adv. Funct. Mater.* **2021**, *31*, 2100723.

17) **M. Moser**, A. Wadsworth, N. Gasparini, and I. McCulloch, Challenges to the Success of Commercial Organic Photovoltaics Products, *Adv. Energy Mater.* **2021**, *11*, 2100056.

18) A. Koklu, S. Wustoni, V. E. Musteata, D. Ohayon, **M. Moser**, I. McCulloch, S. Nunes, and S. Inal, Microfluidic Integrated Organic Electrochemical Transistor with a Nanoporous Membrane for Amyloid-β Detection, *ACS Nano* **2021**, *15*, 8130.

19) S. T. M. Tan, A. Giovannitti, A. Melianas, **M. Moser**, B. L. Cotts, D. Singh, I. McCulloch, and A. Salleo, High-Gain Chemically Gated Organic Electrochemical Transistor¸ *Adv. Funct. Mater.* **2021**, *31*, 2010868.

20) **M. Moser**, A. Savva, K. Thorley, B. D. Paulsen, T. C. Hidalgo, D. Ohayon, H. Chen, A. Giovannitti, A. Marks, N. Gasparini, A. Wadsworth, J. Rivnay, S. Inal, and I.

McCulloch, Polaron Delocalization in Donor-Acceptor Polymers and its Impact on Organic Electrochemical Transistor Performance, *Angew. Chem. Int. Ed.* **2021**, *60*, 7777.

21) H. Chen, **M. Moser** (co-first author), S. Wang, C. Jellett, K. Thorley, G. T. Harrison, X. Jiao, M. Xiao, B. Purushothaman, M. A. Alsufyani, H. Bristow, S. De Wolf, A. Wadsworth, C. R. McNeill, H. Sirringhaus, S. Fabiano, and I. McCulloch, Acene Ring Size Optimization in Fused Lactam Polymers Enabling High n-Type Organic Thermoelectric Performance, *J. Am. Chem. Soc.* **2021**, *143*, 260.

22) H. Bristow, P. Jacoutot, A. D. Scaccabarozzi, M. Babics, **M. Moser**, A. Wadsworth, T. D. Anthopoulos, A. Bakulin, I. McCulloch, and N. Gasparini, Nonfullerene-Based Organic Photodetectors for Ultrahigh Sensitivity Visible Light Detection, *ACS Appl. Mater. Interfaces* **2020**, *12*, 48836.

23) **M. Moser**, T. C. Hidalgo, J. Surgailis, J. Gladisch, S. Ghosh, R. Sheelamanthula, Q. Thiburce, A. Giovannitti, A. Salleo, N. Gasparini, A. Wadsworth, I. Zozoulenko, M. Berggren, E. Stavrinidou, S. Inal, and I. McCulloch, Side Chain Redistribution as a Strategy to Boost Organic Electrochemical Transistor Performance and Stability, *Adv. Mater.* **2020**, *32*, 2002748.

24) K. E. Watts, B. Neelamraju, **M. Moser**, I. McCulloch, E. L. Ratcliff, and J. E. Pemberton, Thermally Induced Formation of HF4TCNQ^{-} in F4TCNQ-Doped Regioregular P3HT, *J. Phys. Chem. Lett.* **2020**, *11*, 6586.

25) **M. Moser**, L. R. Savagian, A. Savva, M. Matta, J. F. Ponder Jr., T. C. Hidalgo, D. Ohayon, R. Hallani, M. Reisjalali, A. Troisi, A. Wadsworth, J. R. Reynolds, S. Inal, and I. McCulloch, Ethylene Glycol-Based Side Chain Length Engineering in Polythiophenes and its Impact on Organic Electrochemical Transistor Performance, *Chem. Mater.* **2020**, *32*, 6618.

26) A. F. Paterson, A. Savva, S. Wustoni, L. Tsetseris, B. D. Paulsen, H. Faber, A. H. Emwas, X. Chen, G. Nikiforidis, T. C. Hidalgo, **M. Moser**, I. P. Maria, J. Rivnay, I. McCulloch, T. D. Anthopoulos, and S. Inal, Water Stable Molecular n-doping Produces Organic Electrochemical Transistors with High Transconductance and Record Stability, *Nat. Commun.* **2020**, *11*, 3004.

27) X. Wu, A. Surendran, **M. Moser**, S. Chen, B. T. Muhammad, I. P. Maria, I. McCulloch, and W. L. Leong, Universal Spray-Deposition Process for Scalable, High-Performance, and Stable Organic Electrochemical Transistors, *ACS Appl. Mater. Interfaces* **2020**, *12*, 20757.

28) A. Giovannitti, R. Rashid, Q. Thiburce, B. D. Paulsen, C. Cendra, K. Thorley, D. Moia, J. Mefford, D. Hanifi, W. Du, **M. Moser**, A. Salleo, J. Nelson, I. McCulloch, and J. Rivnay, Energetic Control of Redox-Active Polymers toward Safe Organic Bioelectronic Materials, *Adv. Mater.* **2020**, *32*, 1908047.

29) J. Gladisch, E. Stavrinidou, S. Ghosh, A. Giovannitti, **M. Moser**, I. Zozoulenko, I. McCulloch, and M. Berggren, Reversible Electronic Solid–Gel Switching of a Conjugated Polymer, *Sci. Adv.* **2020**, *7*, 1901144.

30) A. Wadsworth, H. Chen, K. J. Thorley, C. Cendra, M. Nikolka, H. Bristow, **M. Moser**, A. Salleo, and I. McCulloch, Modification of Indacenodithiophene-based Polymers and its Impact on Charge Carrier Mobility in Organic Thin-film Transistors, *J. Am. Chem. Soc.* **2020**, *142*, 652.

31) R. K. Hallani, **M. Moser**, H. Bristow, M. V. C. Jenart, H. Faber, M. Neophytou, E. Yarali, A. F. Paterson, T. D. Anthopoulos, and I. McCulloch, Low-temperature Cross-linking Benzocyclobutene Based Polymer Dielectric for Organic Thin Film Transistors on Plastic Substrates, *J. Org. Chem.* **2020**, *85*, 277.

32) **M. Moser**, J. F. Ponder Jr., A. Wadsworth, A. Giovannitti, and I. McCulloch,

Materials in Organic Electrochemical Transistors for Bioelectronic Applications: Past, Present, and Future, *Adv. Funct. Mater.* **2019**, *29*, 1807033.

33) **M. Moser**, K. J. Thorley, F. Moruzzi, J. F. Ponder Jr., I. P. Maria, A. Giovannitti, S. Inal, and I. McCulloch, Highly Selective Chromoionophores for Ratiometric Na^+ Sensing Based on an Oligoethyleneglycol Bridged Bithiophene Detection Unit, *J. Mater. Chem. C* **2019**, *7*, 5359.

34) A. Wadsworth, **M. Moser**, A. Marks, M. Little, N. Gasparini, C. J. Brabec, D. Baran, and I. McCulloch, Critical Review of the Molecular Design Progress in Non-fullerene Electron Acceptors Towards Commercially Viable Organic Solar Cells, *Chem. Soc. Rev.* **2019**, *48*, 1596.

35) N. Gasparini, A. Wadsworth, **M. Moser**, D. Baran, I. McCulloch, and C. J. Brabec, The Physics of Small Molecule Acceptors for Efficient and Stable Bulk Heterojunction Solar Cells, *Adv. Energy Mater.* **2018**, *8*, 1703298.

36) A. Wadsworth, R. S. Ashraf, M. Abdelsamie, S. Pont, M. Little, **M. Moser**, Z. Hamid, M. Neophytou, W. Zhang, J. R. Durrant, D. Baran, and I. McCulloch, Highly Efficient and Reproducible Nonfullerene Solar Cells from Hydrocarbon Solvents, *ACS Energy Lett.* **2017**, *2*, 1494.

VI List of Abbreviations

°	Degree
Å	Angstrom
AFM	Atomic force microscopy
atm	Standard atmosphere
BPy	2,2′-Bipyridine
br.	Broad
C	Double layer capacitance
*C**	Volumetric capacitance
C=C	Carbon-carbon double bond
calcd	Calculated
C–C	Carbon-carbon single bond
d	Channel thickness
D	Dissipation
Đ	Dispersity
Da	Dalton
D-A	Donor-acceptor
d_{e2e}	End-to-end distance
DFT	Density functional theory
DHAP	Direct heteroarylation polymerisation
DMF	*N,N'*-Dimethylformamide
DMSO	Dimethyl sulfoxide
DNA	Deoxyribonucleic acid
DPP	Diketopyrrolopyrrole

EDL	Electrical double layer
E_{Fc/Fc^+}	Half-wave potential of the ferrocene/ferrocenium couple
EG	Ethylene glycol
E_g	Bandgap
$E_{g,opt}$	Optical gap
EGOFET	Electrolyte gated organic field-effect transistor
EIS	Electrochemical impedance spectroscopy
$E_{ox,aq}$	Onset of oxidation in aqueous media
$E_{ox,org}$	Onset of oxidation in organic media
eQCM-D	Electrochemical quartz crystal microbalance with dissipation
equiv.	Equivalents
EtOAc	Ethyl acetate
eV	Electron-volt
f	Oscillation frequency
f_0	Fundamental frequency
FET	Field-effect transistor
FMO	Frontier molecular orbital
FWHM	Full width at half maximum
GIWAXS	Grazing incidence wide-angle X-ray scattering
g_m	Transconductance
GPC	Gel permeation chromatography
HOMO	Highest occupied molecular orbital
HRMS	High-resolution mass spectrometry
Hz	Hertz
ICT	Intramolecular charge transfer

$I_{D,lin}$	Drain current in the linear regime
$I_{D,sat}$	Drain current in the saturation regime
$I_D/I_{D,0}$	Percentage retention of the initial drain current
IID	Isoindigo
I_{max}	Maximum current
IP	Ionisation potential
ITO	Indium tin oxide
IUPAC	International Union of Pure and Applied Chemistry
J	Coupling constant
k	Kilo
K	Kelvin
K_2CO_3	Potassium carbonate
L	Channel length
L_c	Coherence length
LOD	Limit of detection
LUMO	Lowest unoccupied molecular orbital
m/z	Mass to charge
MD	Molecular dynamics
Me_3SnCl	Trimethyltin chloride
MeOT2	3,3'-Dimethoxy-2,2'-bithiophene
M_n	Number average molecular weight
mol%	Mol percentage
NBS	*N*-Bromosuccinimide
n	Overtone number
n-BuLi	*n*-Butyllithium

NDI	Naphthalene tetracarboxylic diimide
$Ni(COD)_2$	Bis(1,5-cyclooctadiene)nickel(0)
NMR	Nuclear magnetic resonance
OECT	Organic electrochemical transistor
OFET	Organic field-effect transistor
OLED	Organic light-emitting diode
OMIEC	Organic mixed ionic-electronic conductor
On/off	On/off ratio
OPV	Organic photovoltaics
ORR	Oxygen reduction reaction
OTE	Organic thermoelectric
P(*o*-OMePh)$_3$	Tris(*o*-methoxyphenyl)phosphine
P3HT	Poly(3-hexylthiophene)
PBS	Phosphate buffered saline
Pd_2dba_3	Tris(dibenzylideneacetone)dipalladium(0)
PE	Petroleum ether
PEDOT	Poly(3,4-ethylenedioxythiophene)
ppm	Parts per million
PSS	Polystyrenesulfonate
PTSA	*p*-Toluenesulfonic acid
q_{xy}	In-plane direction
q_z	Out-of-plane direction
R_f	Retention factor
R_p	Parallel resistance
R_s	Series resistance

RT	Room temperature
RT-PCR	Reverse transcription polymerase chain reaction
SAM	Self-assembled monolayer
SARS-CoV-2	Severe acute respiratory syndrome coronavirus 2
SCLC	Space-charge-limited current
S_N	Nucleophilic substitution
T2	2,2'-Bithiophene
TBA PF_6	Tetrabutylammonium hexafluorophosphate
TCE	1,1,2,2-Tetrachloroethane
TFT	Tetrafluorophenylene
THF	Tetrahydrofuran
TLC	Thin-layer chromatography
TsCl	Tosyl chloride
TT	Thieno[3,2-*b*]thiophene
UV-Vis	Ultraviolet-visible
v/v	Volume by volume
V_D	Drain voltage
V_G	Gate voltage
V_S	Source voltage
V_{Th}	Threshold voltage
v_q	Shear wave velocity in quartz
W	Channel width
wt	Weight
δ	Chemical shift
ε	Elasticity

η	Viscosity
$\lambda_{max.film}$	Maximum absorption wavelength in thin film
$\lambda_{max.soln}$	Maximum absorption wavelength in solution
μ	Electronic charge carrier mobility
μ_{lin}	Electronic charge carrier mobility in the linear regime
μ_{sat}	Electronic charge carrier mobility in the saturation regime
ρ_q	Density of quartz
σ	Electrical conductivity

VII List of Figures, Schemes, and Tables

Chapter 1

Figure 1.15	Operating mechanism of a p-type organic field-effect transistor with a top gate, bottom contact architecture and the various applied source (V_S), gate (V_G), and drain voltages (V_D) highlighted.
Figure 1.16	Typical a) output and b) transfer curves recorded for an OFET with highlights showing important transistors parameters that can be extracted from these plots.
Figure 1.17	a) Schematic of a p-type EGOFET highlighting the formation of electrical double layers at both the gate-electrolyte and electrolyte-semiconductor interface. b) Comparison of poly(3-hexylthiophene)'s (**P3HT**) transfer characteristics when employing a conventional OFET architecture including a SiO_2 dielectric (dashed line, top x-axis) and an EGOFET architecture making use of a polyethylene oxide/lithium perchlorate electrolyte (solid line, bottom x-axis).
Figure 1.18	Operating principle of a p-type a) depletion and b) accumulation mode organic electrochemical transistor, highlighting the formation of EDLs across the bulk of the organic semiconductor channel.
Figure 1.19	Different classes of OECT channel materials, including a) conjugated polymer composites (*e.g.* **PEDOT:PSS**), b) conjugated polyelectrolytes (*e.g.* **PTHS**), and c) EG functionalised conjugated polymers (*e.g.* **p(g3T2)**). Conceptual sketches highlight the defining characteristics of each OMIEC class. Broad ribbons correspond to polymer backbones, while narrow ribbons to pendant side-chains. Blue and red colours denote material sections responsible for electronic and ionic charge carrier transport, respectively.

Chapter 2

Figure 2.5	Normalised thin film UV-Vis absorption spectra recorded for the **p(g*x*T2-T)** series while applying a dedoping potential of -0.2 V.
Figure 2.6	Optical absorption profiles of a) **p(g2T2-T)**, b) **p(g3T2-T)**, c) **p(g4T2-T)**, and d) **p(g6T2-T)** in a 0.1 M aqueous NaCl supporting electrolyte upon the application of external applied potentials (between -0.2 V and +0.8 V, in increments of 0.1 V).
Figure 2.7	Colour of **p(g3T2-T)** polymer films in a) their fully dedoped state at -0.2 V (blue) and b) in their doped stated at +0.8 V (colourless).
Figure 2.8	Grazing incidence wide-angle X-ray scattering patterns recorded for as-cast films of **p(g3T2-T)**, **p(g4T2-T)**, and **p(g6T2-T)**.
Figure 2.9	a) MD snapshot highlighting a section of **p(g3T2-T)**'s simulation box and the π-π stacking interaction between two **p(g3T2-T)** oligomers. b) Histogram of the end-to-end distances (d_{e2e}) calculated for **p(g3T2-T)** and **p(g4T2-T)**. c) Radial distribution functions obtained for **p(g3T2-T)** and **p(g4T2-T)**. d) Calculated fraction of π-π stacking thiophene rings in **p(g3T2-T)** and **p(g4T2-T)**.
Figure 2.10	OECT steady-state performance recorded for the **p(g*x*T2-T)** polymer series employing an aqueous 0.1 M NaCl solution as the supporting electrolyte. OECT output curves recorded for a) **p(g2T2-T)**, b) **p(g3T2-T)**, and c) **p(g4T2-T)**. Transfer curves plotted on a d) linear and e) logarithmic current scale. f) Recorded transconductance curves.
Table 2.2	Summary of the polymers' steady-state OECT performance.

Chapter 3

Figure 3.1	Chemical structures of high-performance OECT channel materials employing the g3T2 unit in their conjugated polymer backbone (highlighted in red) and their respective μC^* measured in devices.
Figure 3.2	Chemical structures of the developed polymers.
Scheme 3.1	Acid-catalysed transetherification reaction of 3-methoxythiophene into the various 3-alkoxythiophenes.
Scheme 3.2	Synthesis of the 3,3'-bisalkoxy-2,2'-bithiophene intermediates through a) a one-step or b) two-step C–C bond forming reaction.
Scheme 3.3	Synthesis of the brominated and stannylated monomers.
Scheme 3.4	Synthesis of the polymers **p(g3T2)**, **p(g2T2-g4T2)**, **p(g1T2-g5T2)**, and **p(g0T2-g6T2)**.
Figure 3.3	Cyclic voltammograms recorded for **p(g3T2)**, **p(g2T2-g4T2)**, **p(g1T2-g5T2)**, and **p(g0T2-g6T2)** employing a) a 0.1 M TBA PF_6 in acetonitrile solution and b) a 0.1 M NaCl in distilled water solution as the supporting electrolyte.
Table 3.1	Summary of the polymers' optoelectronic properties.
Figure 3.4	Repeated CV addressing of the polymers in 0.1 M aqueous NaCl solutions.
Figure 3.5	**Figure 3.5.** Normalised UV-Vis absorption spectra of **p(g3T2)**, **p(g2T2-g4T2)**, **p(g1T2-g5T2)**, and **p(g0T2-g6T2)** in a) dilute chloroform solutions and b) thin film while applying a negative dedoping bias of -0.5 V.

Figure 3.6	Spectroelectrochemistry of a) **p(g3T2)**, b) **p(g2T2-g4T2)**, c) **p(g1T2-g5T2)**, and d) **p(g0T2-g6T2)** employing a 0.1 M TBA PF_6 in acetonitrile solution. Spectroelectrochemistry of e) **p(g3T2)**, f) **p(g2T2-g4T2)**, g) **p(g1T2-g5T2)**, and h) **p(g0T2-g6T2)** employing a 0.1 M NaCl in distilled water solution as the supporting electrolyte.
Figure 3.7	Visual representation of the volume changes occurring for a p-type OMIEC during electrolyte exposure and electrochemical doping. a) OMIEC on a conductive substrate in air. b) Passive swelling of the OMIEC upon electrolyte exposure due to the transport of hydrated ions and water molecules into the OMIEC. c) Active swelling of the OMIEC including counterion migration into the OMIEC in response to hole injection from the conductive substrate.
Table 3.2	Summary of the polymers' swelling properties.
Figure 3.8	eQCM-D results for a) **p(g3T2)**, b) **p(g2T2-g4T2)**, c) **p(g1T2-g5T2)**, and d) **p(g0T2-g6T2)**. Dashed trace corresponds to the polymer thickness on the gold substrate in air in the absence of any electrolyte and applied bias. Solid trace corresponds to the polymer thickness when immersed in an aqueous 0.1 M NaCl supporting electrolyte in the absence of an applied bias (white background), +0.5 V doping potential (sky blue background) and in the presence of a -0.5 V dedoping potential (amaranth background).
Figure 3.9	Number of chloride ions (*n* Cl^-, solid line) and number of water molecules (*n* H_2O, dashed line) injected into the polymers upon application of a +0.5 V doping potential in an aqueous 0.1 M NaCl solution.

Chapter 4

Figure 4.7	GIWAXS scattering patterns (left panels) and in-plane (q_r) and out-of-plane (q_z) linecuts (right panels) recorded for a,b) **p(gDPP-TT)**, c,d) **p(gDPP-T2)**, and e,f) **p(gDPP-MeOT2)**, respectively.
Figure 4.8	Optimised DFT geometries and graphical representation of the HOMO of a) **p(gDPP-TT)**, b) **p(gDPP-T2)**, and c) **p(gDPP-MeOT2)** employing a ωB97XD functional, a 6-31G* basis set, and a 0.02 isovalue.
Figure 4.9	a) Illustration highlighting the subdivision of the oligomers into shorter segments. b) DFT population analysis highlighting the contribution of the individual fragments to the oligomers' HOMO. c) DFT calculations of the charge distribution over the various polymer fragments in the polymers' polaronic form.
Figure 4.10	Representative output curves recorded for a) **p(gDPP-TT)**, b) **p(gDPP-T2)**, and c) **p(gDPP-MeOT2)**. Corresponding transfer curves plotted on a d) linear and e) logarithmic y-axis scale. f) Corresponding transconductance curves. All devices featured a channel width (W) of 100 μm and length (L) of 10 μm and were operated in a 0.1 M aqueous NaCl solution.
Table 4.2	Summary of the polymers' OECT steady-state performance.
Figure 4.11	Electrochemical impedance spectroscopy of a) **p(gDPP-TT)**, b) **p(gDPP-T2)**, and c) **p(gDPP-MeOT2)** while applying a V_G of 0 V or the one incurring the highest OECT performance.
Figure 4.12	Operational stability of a) **p(gDPP-TT)**, b) **p(gDPP-T2)**, and c) **p(gDPP-MeOT2)** upon repeated electrochemical biasing in a 0.1 M aqueous NaCl supporting electrolyte.

Chapter 5

Figure 5.1	OECT steady-state performance comparison of the polymers developed in a) **Chapter 3** and b) **Chapter 4** against relevant OECT benchmark channel materials.
Figure 5.2.	a) Proposed polymer series making use of alternative polyether side-chains to modulate the polymers' swelling tendency. b) Proposed polymer series making use of chalcogen atom substitution to improve the polymers' electronic performance.

Chapter 8

Scheme 8.1	Synthesis of hexaethylene glycol monomethyl ether.
Scheme 8.2.	Synthesis of pentaethylene glycol monomethyl ether.
Figure 8.1	Licence agreement to reproduce the content reported in I. McCulloch, R. S. Ashraf, L. Biniek, H. Bronstein, C. Combe, J. E. Donaghey, D. I. James, C. B. Nielsen, B. C. Schroeder, W. Zhang, *Acc. Chem. Res.* **2012**, *45*, 714.
Figure 8.2	Licence agreement to reproduce the content reported in M. L. Chabinyc, M. F. Toney, R. J. Kline, I. McCulloch, M. Heeney, *J. Am. Chem. Soc.* **2007**, *129*, 3226.
Figure 8.3	Licence agreement to reproduce the content reported in M. Nikolka, K. Broch, J. Armitage, D. Hanifi, P. J. Nowack, D. Venkateshvaran,

	A. Sadhanala, J. Saska, M. Mascal, S.-H. Jung, J. Lee, I. McCulloch, A. Salleo, H. Sirringhaus, *Nat. Commun*. **2019**, *10*, 2122.
Figure 8.4	Licence agreement to reproduce the content reported in E. Poverenov, M. Li, A. Bitler, M. Bendikov, *Chem. Mater.* **2010**, *22*, 4019.
Figure 8.5	Licence agreement to reproduce the content reported in J. Rivnay, S. Inal, B. A. Collins, M. Sessolo, E. Stavrinidou, X. Strakosas, C. Tassone, D. M. Delongchamp, G. G. Malliaras, *Nat. Commun.* **2016**, *7*, 11287.
Figure 8.6	Licence agreement to reproduce the content reported in M. J. Panzer, C. D. Frisbie, *Adv. Mater.* **2008**, *20*, 3177.
Figure 8.7	Licence agreement to reproduce the content reported in K. Guo, S. Wustoni, A. Koklu, E. Díaz-Galicia, M. Moser, A. Hama, A. A. Alqahtani, A. N. Ahmad, F. S. Alhamlan, M. Shuaib, A. Pain, I. McCulloch, S. T. Arold, R. Grünberg, S. Inal, *Nat. Biomed. Eng.* **2021**, DOI 10.1038/s41551-021-00734-9.

VIII Table of Contents

'The task is not to see what has never been seen before, but to think what has never been thought before about what you see every day.'

— Erwin Schrödinger

1

Introduction

Contents

1.1 Origins of Polymer Chemistry

According to the Compendium of Chemical Terminology published by the International Union of Pure and Applied Chemistry (IUPAC) a polymer is defined as 'a substance composed of macromolecules'.[1] Macromolecules, in turn, are described as 'molecules of high relative molecular mass, the structure of which essentially comprises the multiple repetition of units derived, actually or conceptually, from molecules of low relative molecular mass'.[1] It is precisely this multiple repetition of molecules of low relative molecular mass that differentiates polymers from conventional organic molecules and imparts them with their unique properties over their small molecule counterparts.

Polymers are plentiful in nature, with prominent examples of such biopolymers including cellulose, proteins, wool, and remarkably also the material that provides us with our own identity, DNA, see **Figure 1.1**. In contrast, the history of synthetically derived polymers is considerably briefer, with the earliest example of a synthetic polymer typically being credited to Leo Hendrik Baekeland, when he developed Bakelite in 1907.[2] Bakelite, a resin derived from multiple sequential condensation reactions between phenol and formaldehyde, quickly attracted attention across the entirety of the United States, where it was used as a natural electrical insulator to meet the needs of the rapidly electrifying country. Since this seminal report, significant advances in the understanding and tailoring of the physical and chemical properties of synthetic polymers have been made. The great strides made in synthetic polymer chemistry over the past century have also gained considerable appraisal from the scientific community, with the Nobel Prize in Chemistry of 1953, 1963, 1974, and 2000 all having been awarded to polymer chemists.

Contemporary examples of synthetic polymers include polystyrene, polyethylene, polyacetylene, Teflon, Kevlar, amongst many others, see **Figure 1.1**. Nowadays, scientists

are able to create polymers with virtually any desired specific property, including mechanical stiffness or elasticity; optical transparency or opacity; gas permeability or impermeability; *etc.* This versatility of polymeric materials has prompted them to be employed across all aspects of modern-day life, such as for food packaging, auto parts, furniture, circuit boards, spaceships, water desalination, and medical uses. Given this meteoric rise of polymer-based products, it is unsurprising to see that global polymer production has increased from $1.5 \cdot 10^6$ metric tons in 1950 to $368 \cdot 10^6$ metric tons in 2019, with further gains set to be added over the coming years.[3] Polymers are thus set to play a significant role in our lives also for the decades ahead.

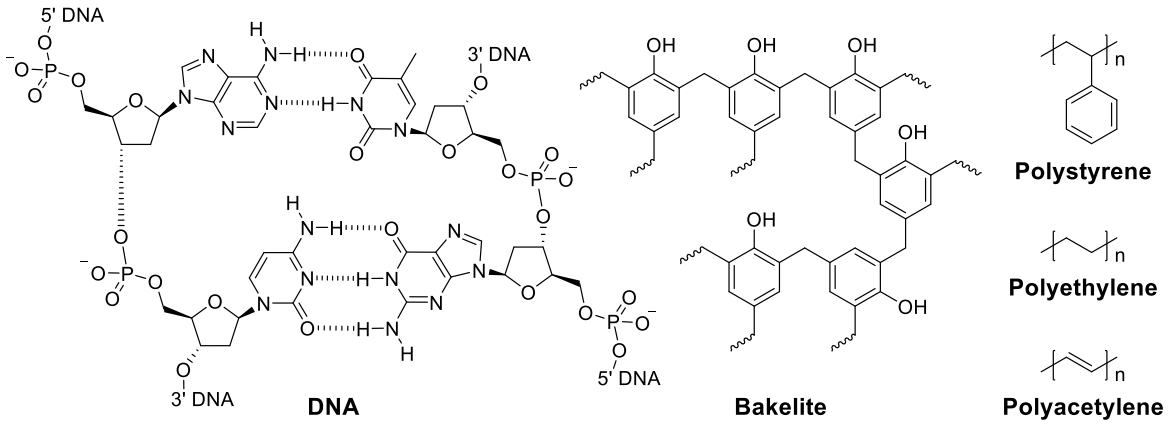

Figure 1.1. *Chemical structures of notable naturally occurring (DNA) and synthetically derived polymers (Bakelite, polystyrene, polyethylene, and polyacetylene).*

1.2 From Conventional to Conjugated Polymers

1.2.1 History of Conjugated Polymers

As exemplified by the case of Bakelite, historically speaking, synthetic polymers have mainly found applications as electrically insulating materials. In 1977, however, scientific research efforts led by Shirakawa, MacDiarmid, and Heeger demonstrated that the electrical conductivity of polyacetylene, a polymer featuring an alternating arrangement of carbon-

carbon single bonds and carbon-carbon double bonds, *i.e.* a conjugated system, could be rendered electrically conductive through a chemical oxidation reaction, therefore displaying semiconductive behaviour.[4] In comparison to their inorganic counterparts, these organic semiconductors possess several advantages including their i) ease of processing, allowing for cheap solution-based high throughput methods such as inkjet or roll-to-roll printing, ii) facile tuning of their properties by synthetic means, iii) use of earth-abundant elements, further benefiting their reduced production costs, and iv) mechanical flexibility, enabling them to conform to a wide array of shapes and geometries.[5–11]

Since the seminal discovery of conjugated polymers 44 years ago, tremendous advances have been made in the field, culminating in the commercialisation of various organic semiconductor technologies. Specific examples are organic light-emitting diodes (OLEDs), which nowadays are found in virtually every area of lighting, including in Apple's latest smartphone models (iPhone X and iPhone 12),[12] in the taillights of Audi's most recent automotive vehicles,[13] and in LG's curved and rollable TV screens;[14] or electrochromic displays, which are used as dimmable windows in Boeing's most recent wide-body aircrafts,[15] see **Figure 1.2**. Alternative modern-day applications of conjugated polymers that are yet to be translated into fully commercially viable technologies include their use as channel materials in organic field-effect transistors (OFETs),[16] photoabsorbing layers in organic photovoltaics (OPVs),[10] and legs in organic thermoelectric (OTE) generators,[17] amongst various others. Thus, despite great advances having been made in the field of conjugated polymers over the past decades, considerable research efforts are still required to raise their performance to the level of inorganic semiconductors and promote their widespread adoption.

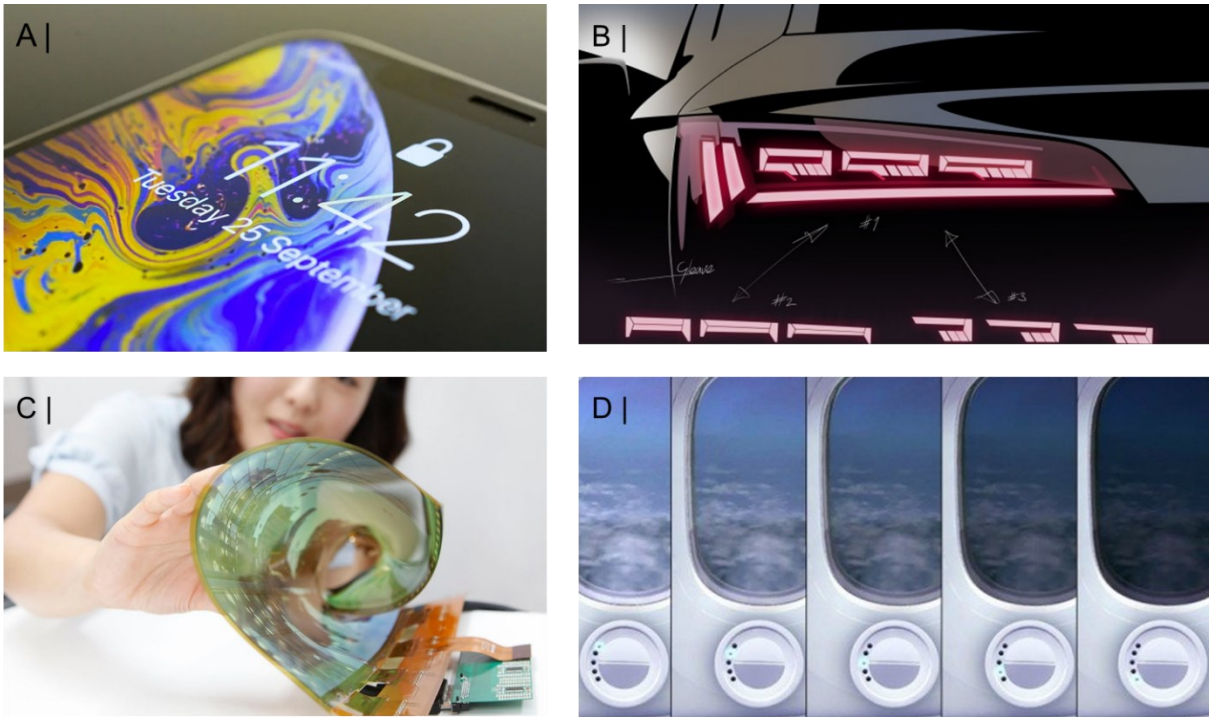

Figure 1.2. *Various commercial products employing organic semiconductor technologies, including a) Apple's most recent iPhone models,*[12] *b) Audi's latest car models,*[13] *c) LG's rollable TV screens,*[14] *and d) Boeing's new wide body aircrafts.*[15]

1.2.2 Origin of Semiconducting Nature

The origin of conjugated polymers' semiconducting nature can be explained upon consideration of their chemical and electronic structure, which in turn is described by molecular orbital theory. For simplicity purposes, the electronic structure of ethene, the smallest member of the hydrocarbon series featuring a C=C double bond, will be considered first, see **Figure 1.3**. In an ethene molecule, both carbon atoms are sp^2 hybridised. This sp^2 hybridisation arises from the orbital mixing of one 2s orbital and two 2p orbitals in one carbon atom. The three resulting sp^2 orbitals are equivalent and are used to form two C–H bonds and one C–C bond by their head-on overlap with the 1s atomic orbitals of two hydrogen atoms and one sp^2 atomic orbital of the adjacent carbon atom, respectively. Note that the overlap of all these atomic orbitals leads to the generation of orbitals that are

cylindrically symmetrical, marking these as σ orbitals. Another important aspect that must be considered is that depending on whether the constituent atomic orbitals have been combined in-phase or out-of-phase, they either yield a σ-bonding or σ-antibonding (σ*) orbital, respectively. The remaining singly occupied p_z orbitals on the two carbon atoms on the other hand overlap sideways to form one bonding π orbital and one antibonding π* orbital, whose plane between the two out-of-phase combined orbitals is known as a nodal plane. Considering the above orbital interactions and focusing only on the orbital overlap between the two adjacent carbon centres, following the Aufbau principle, the lowest energy conformation in ethene occurs by filling the bonding σ and π orbitals, while leaving the antibonding σ* and π* orbitals vacant, therefore giving rise to the double bond across the two carbon centres. In the resulting ethene molecule, the highest occupied molecular orbital is referred to as the HOMO, while the lowest unoccupied molecular orbital is referred to as the LUMO. Together these orbitals are referred to as frontier molecular orbitals (FMOs) with the energy gap between them defined as the bandgap (E_g).

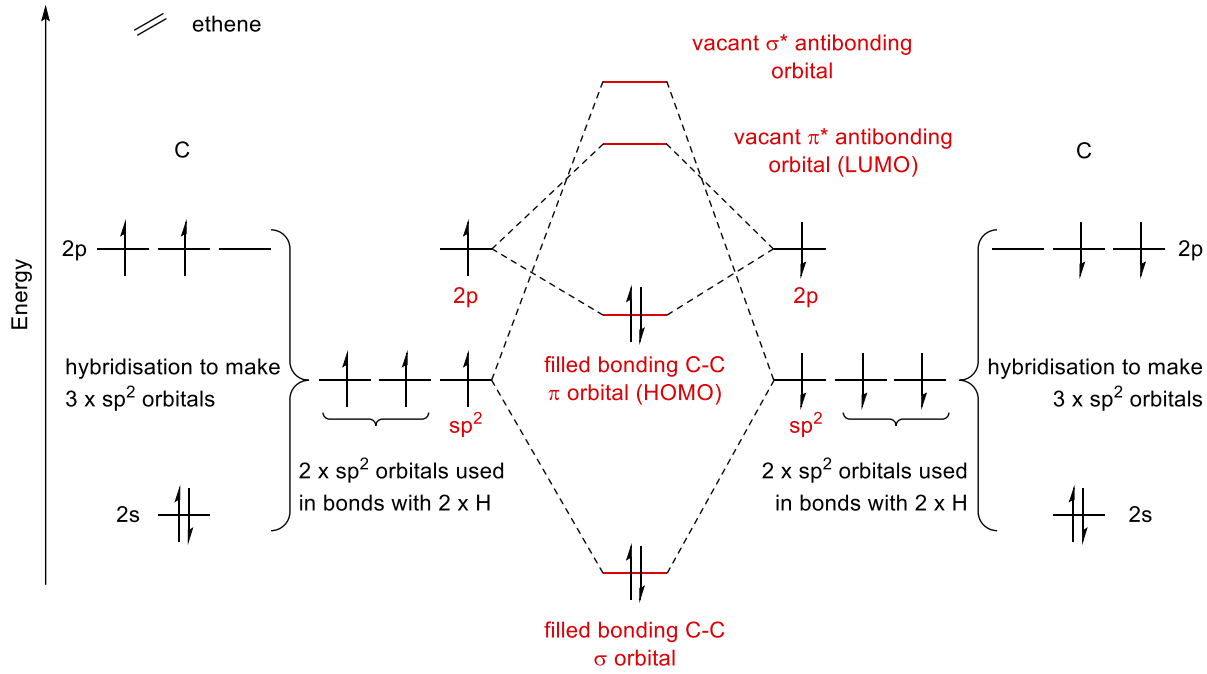

Figure 1.3. *Molecular orbital diagram of ethene disregarding the C-H σ bonds in the molecule, and solely focusing on the orbital overlap between the two carbon atoms.*

Let us now consider the case of 1,3-butadiene, which contains an alternating arrangement of C–C single and C=C double bonds, causing the two C=C bonds to be in conjugation. Conjugation arises from the interaction of π and π* orbitals on successive C=C bonds and gives rise to molecular orbitals that extend over the entirety of the molecular framework. It is precisely this interaction that provides π-electrons with pathways extending above and below the molecule's σ framework along which they can move freely. π-electrons in conjugated systems are hence referred to as being delocalised. Note that the π and π* orbitals themselves arise from the interaction of p_z atomic orbitals on adjacent carbon atoms, see **Figure 1.4**. From **Figure 1.4** it can be seen that unlike in ethene, where only two possible combinations exist for adjacent p_z orbitals to overlap, four overlap possibilities exist in 1,3-butadiene, thus giving rise to four molecular orbitals: one in which all of the p_z orbitals combine in-phase (ψ_1), two in which some of the p_z orbitals combine in-phase and some out-of-phase (ψ_2 and ψ_3), and one in which all of the p_z orbitals combine out-of-phase (ψ_4). The relative bonding or antibonding character of these orbitals and hence their relative energies can be determined by evaluation of the number of nodal planes present, with an increasing number of nodal planes leading to energetically less stable orbitals, see **Figure 1.4**.

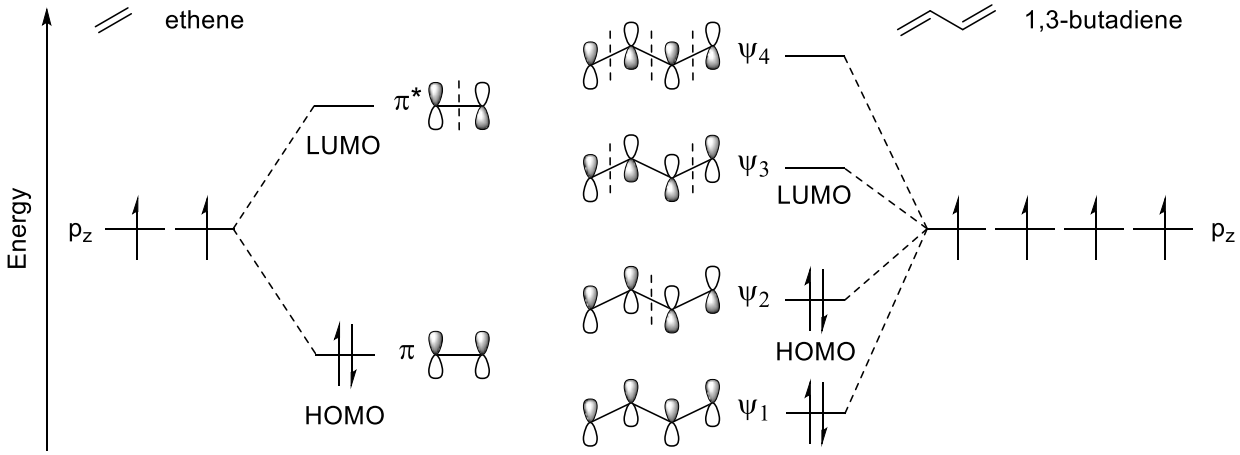

Figure 1.4. *Molecular orbital diagrams of ethene and 1,3-butadiene focusing solely on the π-electron molecular orbitals.*

Given the presence of four unpaired p_z electrons and again following the Aufbau principle, the lowest energy arrangement of these electrons involves filling of the ψ_1 and ψ_2 orbitals, while leaving ψ_3 and ψ_4 vacant. ψ_2 and ψ_3 hence mark the HOMO and LUMO of 1,3-butadiene, respectively. Notice from **Figure 1.4** the effects of conjugation on the energy levels of 1,3-butadiene relative to those of ethene. First, the HOMO of 1,3-butadiene is higher in energy than the HOMO of ethene. This is because of some degree of antibonding character present in the ψ_2 orbital. Conversely, the LUMO of 1,3-butadiene is lower in energy than the LUMO of ethene. This is due to the presence of some bonding character present in the ψ_3 orbital of 1,3-butadiene. Following the above trend, as the number of alternating C–C single bonds and C=C double bonds (*i.e.* the conjugation length) is extended, as in the case of polyacetylene, the HOMO of the resulting conjugated system becomes progressively higher in energy with the opposite effect occurring for the LUMO, see **Figure 1.5**. In parallel, the energy difference within polyacetylene's set of bonding and antibonding orbitals converges, thus leading to the formation of energy bands rather than discrete energy levels like those observed in ethene or 1,3-butadiene. While the collection of filled energy levels is referred to as the valence band, the collection of vacant energy levels is known as the conduction band. From **Figure 1.5**, it is also important to note that the trend in HOMO and LUMO energies upon increasing conjugation is not infinite, hence meaning that the bandgap for polyacetylene cannot become zero. This effect occurs due to Peierls distortion, which results due to electron-lattice interactions, ultimately breaking the perfect order of the one-dimensional lattice and giving rise to bond length alternation in polyacetylene.[18] This effect also prevents conjugated polymers from becoming electrical conductors and instead confines them to their semiconducting nature. Ultimately, the energetic values of the conjugated material's HOMO, LUMO, and bandgap are crucial as they dictate several of the polymer's properties, such as its optical and electronic ones, which

in turn are of paramount importance for any device application. Due to Peierls distortion, modulating the length of a conjugated polymer can be employed as a viable molecular engineering strategy to tune the polymer's optoelectronic characteristics, but is of rather limited use. Instead, to design high-performance conjugated polymers with optimally aligned frontier molecular orbital energy levels, alternative molecular design strategies are required.

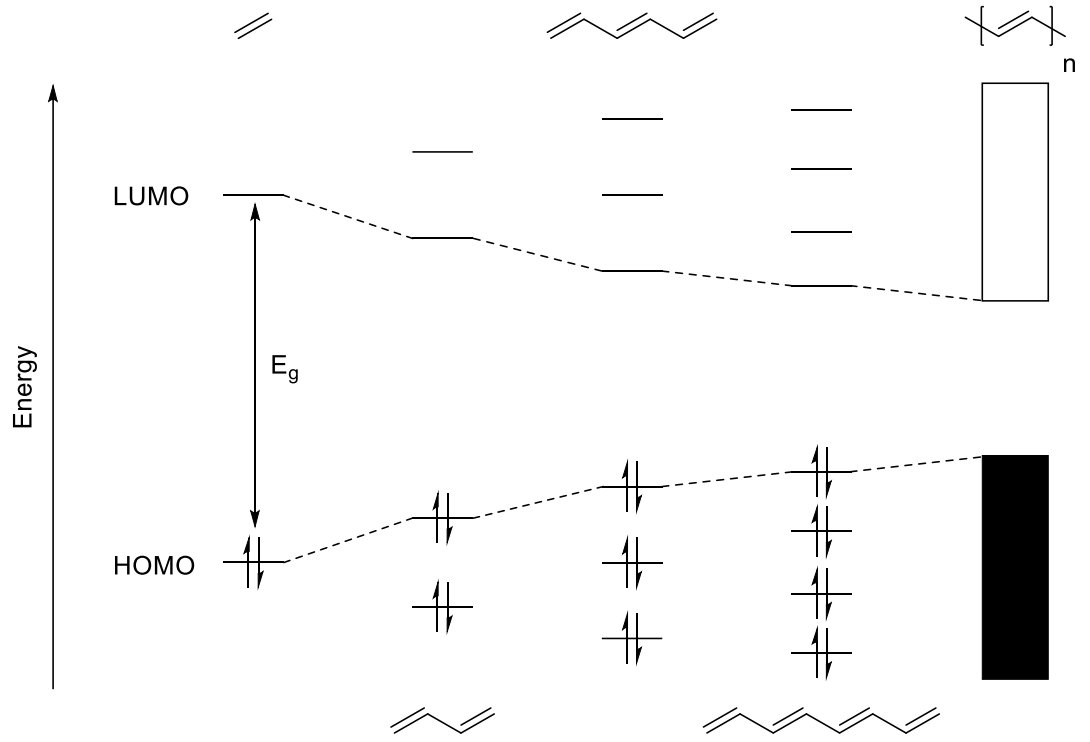

Figure 1.5. *Effect of conjugation length upon going from ethene to polyacetylene on the FMO energy levels.*

1.2.3 Molecular Design Strategies to Tune the Energy Levels of Conjugated Polymers

One straightforward option to modulate the energetics of conjugated polymers is by modulation of the employed conjugated building blocks. Popular examples include aromatic moieties such as benzene and thiophene. Both of these units can have two different resonance forms, the aromatic and quinoidal form, see **Figure 1.6**. Of the two resonance

forms, the aromatic form is energetically more stable than its quinoidal counterpart. Consequently, aromatic building blocks with greater tendencies to adopt their quinoidal resonance form tend to destabilise, *i.e.* raise the HOMO of the resulting conjugated system, while simultaneously lowering the LUMO.[19]

An additional consideration that has to be made when joining together aromatic building blocks by single σ bonds is the presence of any steric requirements that can lead to a deviation from planarity of the conjugated polymer backbone and result in so-called backbone twists. Backbone twists act as breaks in the conjugation, thereby leading to a deepening of the system's HOMO and a shallowing of its LUMO. A visual representation of backbone twists can be seen in **Figure 1.6**, which demonstrates that the coupling of two benzene rings at the 1,1'-positions results in a rather large torsional angle (35-45°) due to the presence of hydrogen atoms in all *ortho* positions of the C–C σ bond joining the two phenyl units together.[20–22] On the other hand, coupling of two thiophene rings together at the 2,2'-positions is subject to less steric requirements, leading to a significantly more planar dihedral angle (~ 25°) between the two thiophene rings.[23,24]

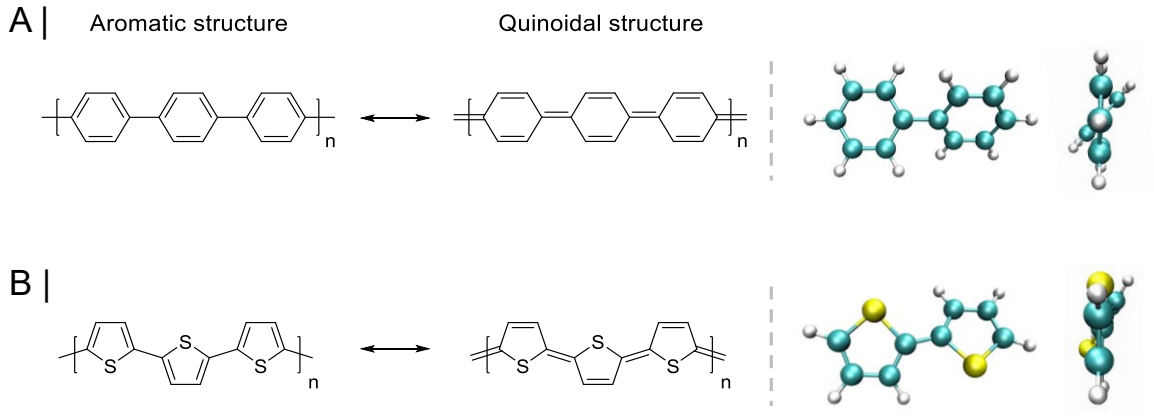

Figure 1.6. *Aromatic and quinoidal resonance structures of a) polyphenylene and b) polythiophene (left). Torsional angles between successive phenyl and thienyl rings (right). Dimer structures adapted with permission from I. McCulloch et al., Acc. Chem. Res.* ***2012****, 45, 714. Copyright (2012) American Chemical Society.[22] ACS distribution licence obtained on 27.05.2021, see* ***Appendix Section 8.2****.*

So far, only polymers comprising one single type of aromatic building block, *i.e.* homopolymers, have been considered. The use of multiple different conjugated building blocks is, however, an easy and straightforward strategy to access a virtually endless array of conjugated polymer structures, while in parallel allowing for the judicious tailoring of the polymers' resultant energy levels. In this context, one of the most commonly employed design principles is the 'donor-acceptor' approach, also typically referred to as 'push-pull' approach.[25–27] The fundamental principle of this tactic involves linking electron-rich building blocks (*i.e.* donor moieties) with electron-deficient ones (*i.e.* acceptor moieties). Although there is no exact definition of what comprises an electron-rich and an electron-deficient building block, a good benchmark for determining the relative donor or acceptor nature of a conjugated building block is by comparison of its electron density relative to benzene. Prominent examples of electron-rich units include thiophene, furan, pyrrole, selenophene, benzodithiophene, indacenodithiophene, carbazole, and cyclopentabithiophene, while naphthalene tetracarboxylic diimide, benzothiadiazole, triazine, naphthobisthiadiazole, and quinoxaline are all types of electron-deficient units, see **Figure 1.7**. Finally, certain chemical motifs, such as diketopyrrolopyrrole, isoindigo, bithiopheneimide, and thienopyrrolodione are considered both electron-donating and electron-withdrawing; a property which renders them particularly attractive for the realisation of ambipolar materials, *i.e.* those capable of transporting both positively (holes) and negatively charged (electrons) electronic carriers.

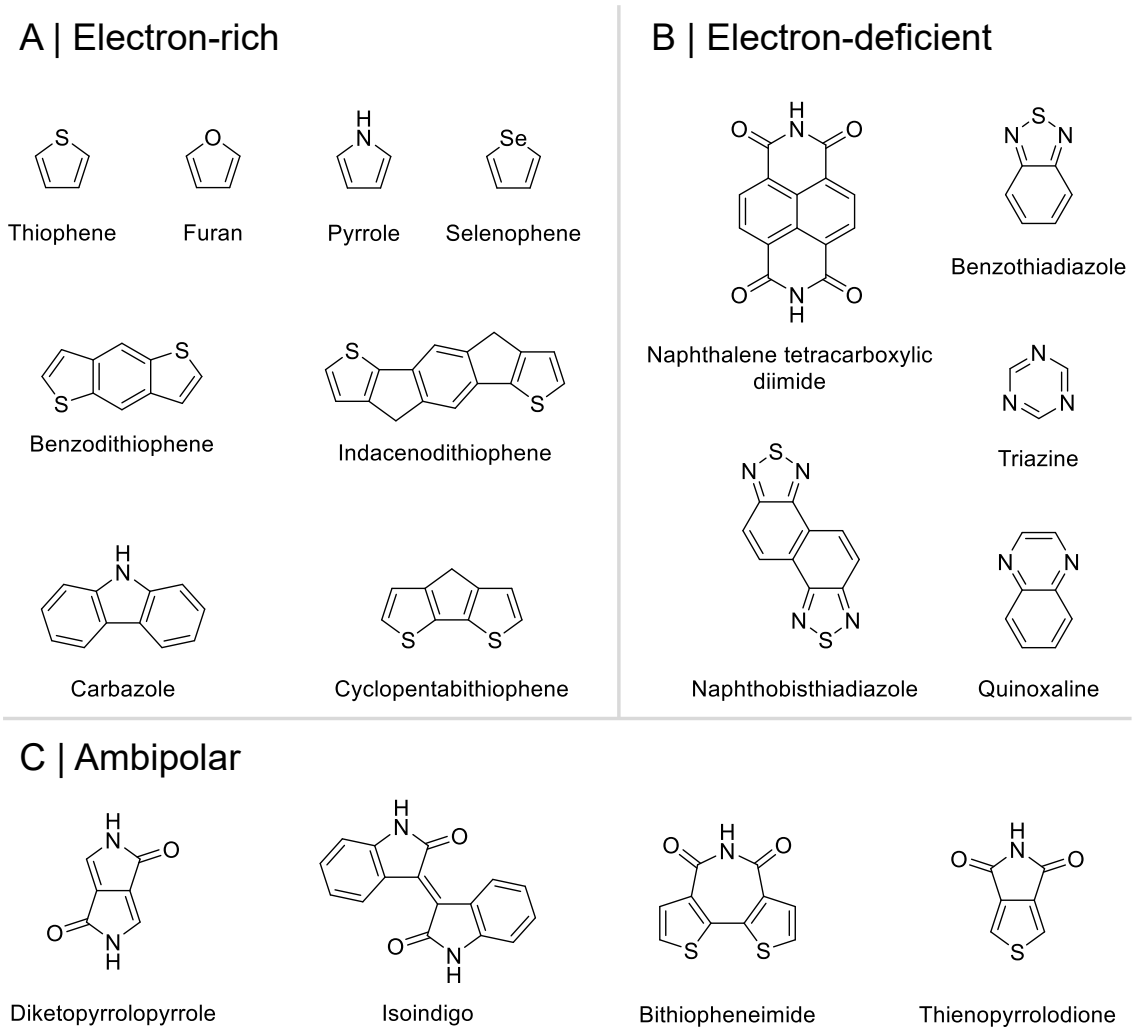

Figure 1.7. *Chemical structures of commonly employed a) electron-rich (donor), b) electron-deficient (acceptor), and c) electron-rich and electron-deficient (ambipolar) units in the synthesis of donor-acceptor copolymers.*

The impact of joining electron-rich and electron-deficient units together in an alternating fashion is the mixing of their frontier molecular orbitals, see **Figure 1.8**. Specifically, as shown in **Figure 1.8**, the HOMO of the resulting system is energetically similar to the one of the donor monomer, while the LUMO resembles the one of the acceptor monomer. A direct consequence thereof is that the HOMO of the resulting polymer tends to physically reside predominantly on the donor units and the LUMO on the acceptor units. This

subsequently allows for the HOMO and LUMO of the polymer to be tuned to a large extent independently, by manipulating the donor and acceptor monomer, respectively.

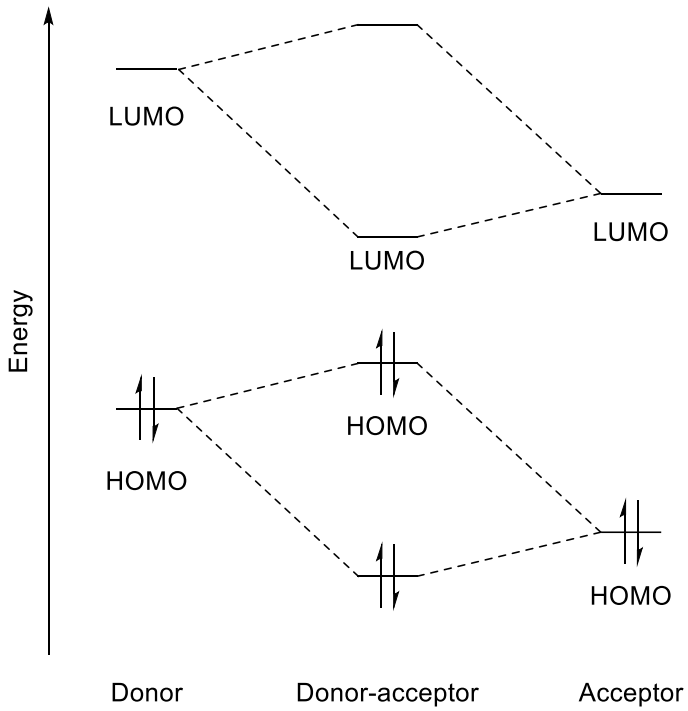

Figure 1.8. *Molecular orbital diagram highlighting the effects of mixing electron-rich donor monomers with electron-deficient acceptor monomers to incur a donor-acceptor system with the HOMO resembling that of the donor and the LUMO that of the acceptor.*

Further control of the polymers' energy levels can be attained through the use of various substituents on the conjugated polymer backbone. Akin to the conjugated building blocks themselves, substituents are often characterised according to their tendency to either donate or withdraw electron density from the conjugated system, either through inductive or resonant effects. Specific examples of commonly employed substituents in the design of conjugated polymers are given in **Figure 1.9**. Rather than just modulating the polymers' energy levels, substituents are also frequently employed to instil solubility into the conjugated polymers. This is especially the case for larger and bulkier substituents, such as

long alkyl, ethylene glycol (EG), or fluoroalkyl chains. Ensuring good polymer solubility is crucial for guaranteeing their compatibility with cheap processing techniques, for example roll-to-roll printing, inkjet printing, *etc.*, but also to ensure the realisation of high conjugation length polymers during their synthesis.

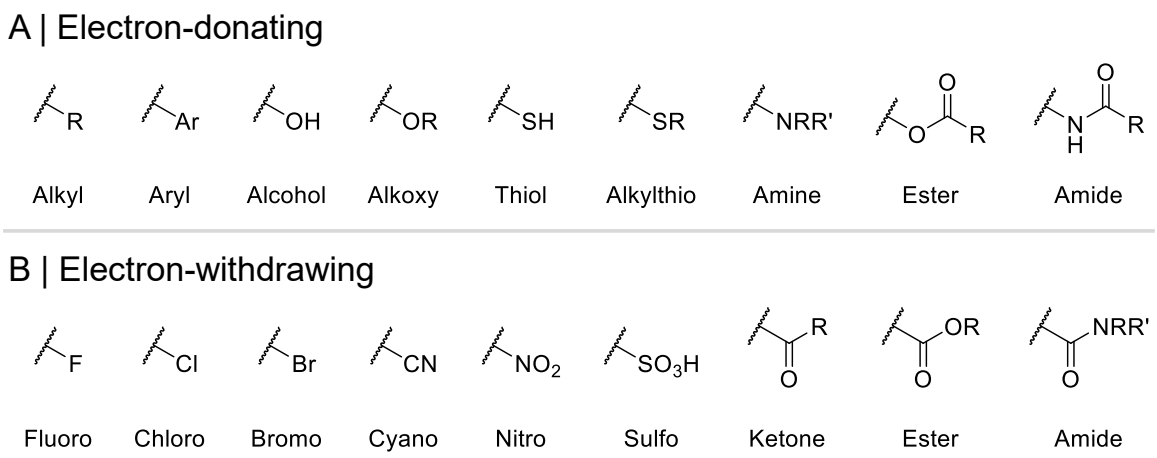

Figure 1.9. *Chemical structures of commonly employed a) electron-donating and b) electron-withdrawing substituents in the design of conjugated polymers.*

So far, we have only evaluated the impact of various molecular design strategies on the energy levels of conjugated polymers. Changes in the chemical structure of polymers, however, also have a direct impact on their morphological properties, including their organisation in thin films, which in turn is of paramount importance in terms of the semiconductor's electrical properties. In this context, conjugated polymers with a high degree of backbone planarity typically exhibit strong π-π stacking interactions between neighbouring conjugated chains, hence leading to the formation of structures with a relatively high degree of order and a strong tendency to aggregate, see **Figure 1.10**. On the other hand, the occurrence of frequent backbone twists typically results in rather weak intermolecular π-π stacking interactions, yielding predominantly disordered and amorphous materials.[28,29] There are, however, notable exceptions to this trend, such as in the case of

indacenodithiophene-*co*-benzothiadiazole (**IDT-BT**)-based polymers, which despite featuring a high degree of backbone planarity, typically do not incur high degrees of long-range intermolecular ordering in the solid state.[30,31] Side-chains also play a pivotal role in tailoring the structural properties of an organic semiconductor, whereby subtle changes in the employed side-chains can often lead to dramatic morphology changes, therefore leading to substantial gains in electrical performance, while leaving the polymer's energy levels virtually unaffected. For example, linear alkyl chain groups are known to be able to interdigitate between adjacent polymer chains, such as in **pBTTT-C14**,[32,33] leading to additional order within the material and enhancing its electrical performance. On the other hand, given their bulkier nature, branched or aryl group containing alkyl chains are known to yield the opposite effect, which can however also be exploited in the case of materials with excessive aggregation tendencies.

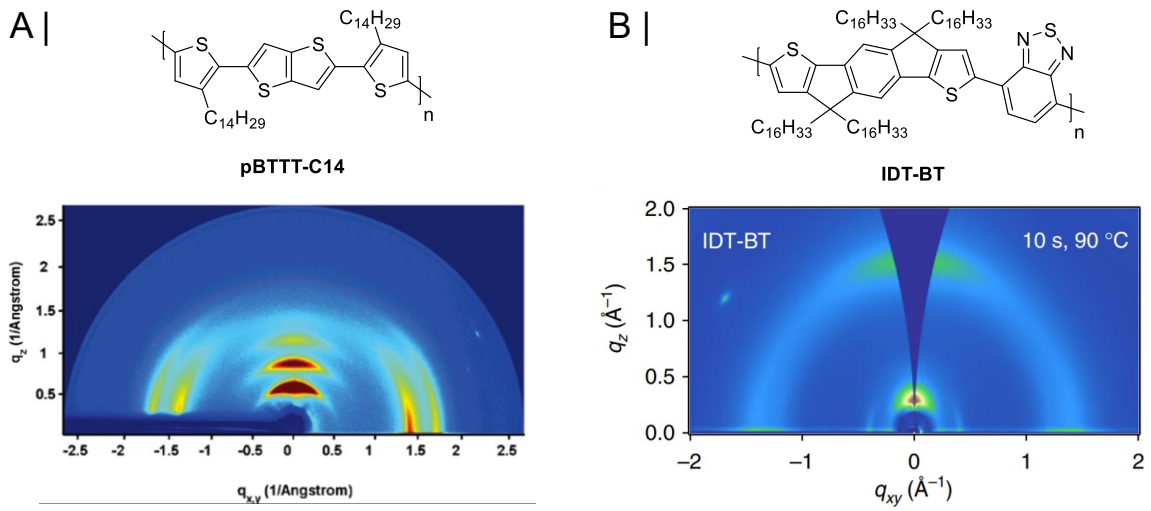

Figure 1.10. *Comparison of the morphological properties incurred by two different organic semiconducting polymers, namely a)* ***pBTTT-C14*** *and b)* ***IDT-BT****. Grazing incidence wide-angle X-ray scattering (GIWAXS) image for* ***pBTTT-C14*** *adapted with permission from M. L. Chabinyc et al., J. Am. Chem. Soc.* ***2007****, 129, 3226. Copyright (2007) American Chemical Society.[34] ACS distribution licence obtained on 27.05.2021, see* ***Appendix Section 8.2****. GIWAXS image for* ***IDT-BT*** *adapted with permission from M. Nikolka et al., Nat. Commun.* ***2019****, 10, 2122. Copyright (2019) Springer Nature.[31] Springer Nature distribution licence obtained on 27.05.2021, see* ***Appendix Section 8.2****.*

1.2.4 Doping of Conjugated Polymers

For semiconductors to be electrically conductive, unpaired charges must be present in either the HOMO or LUMO. Although thermal excitation results in a small number of free charges to exist in the pristine semiconductor, thermal excitation is typically not sufficient to incur semiconductors with high electrical conductivities. Additional free charges can be introduced into semiconductors through a process referred to as doping. Doping of conjugated polymers can be classified in various ways, most notably by distinguishing whether electrons are removed from the polymer's HOMO (p-type doping) or whether they are added to its LUMO (n-type doping), see **Figure 1.11**. In addition to this categorisation, the doping process also tends to be distinguished according to whether the doping process occurs through chemical means (chemical doping) or electrochemical means (electrochemical doping). Specifically, while chemical doping arises from the electron transfer between the semiconductor and an added chemical species, electrochemical doping occurs due to the electron transfer between a semiconductor and a metal electrode. Overall, control of the doping process is critical for numerous applications of organic semiconductors, as the doping process has a direct impact on the electronic and optical properties of the semiconductor. These concepts have been extensively described in the literature.[35–37]

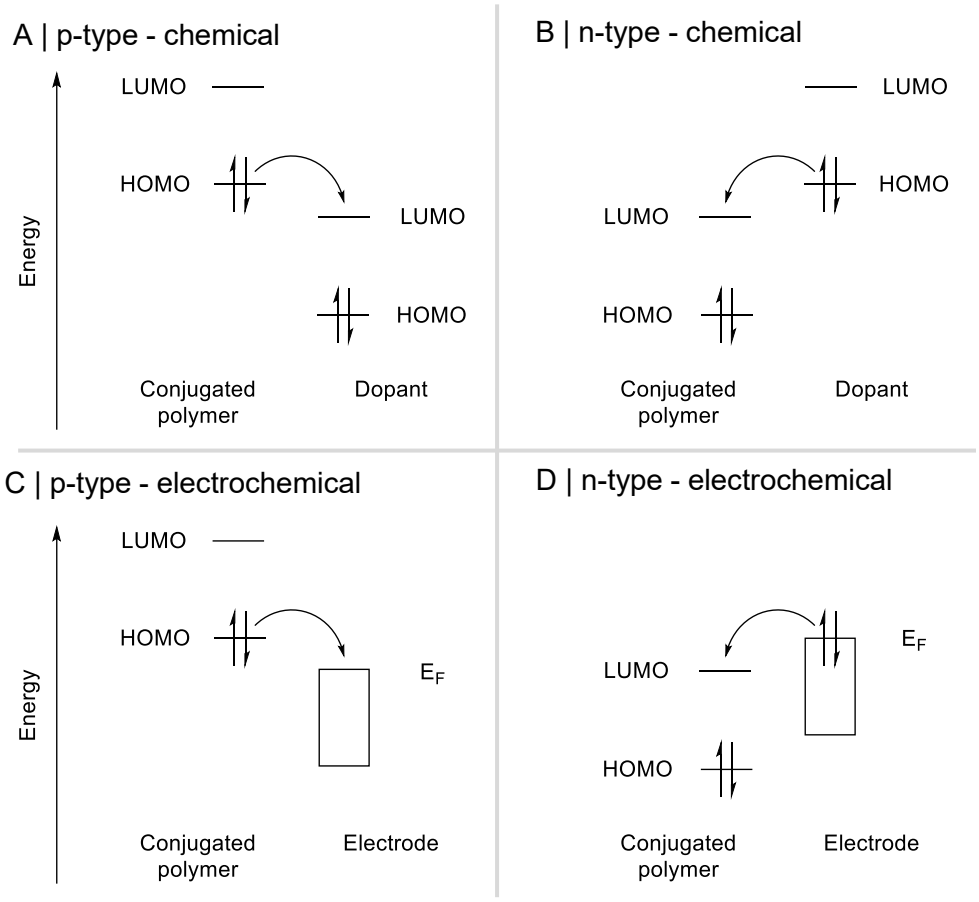

Figure 1.11. *a,b) Comparison of p- and n-type chemical doping and c,d) comparison of p- and n-type electrochemical doping.*

1.2.5 Synthesis of Conjugated Polymers

Synthetically, conjugated polymers can be accessed through two primary polymerisation methods, one based on an electrochemical approach, and one based on a chemical one. Electrochemical polymerisation typically proceeds through the electrochemical oxidation of the employed monomer, which is dissolved in an electrolyte containing solvent.[38–40] The oxidised monomer species can then further react with either another oxidised monomer or a neutral monomer species, thereby leading to the formation of oligomers and subsequently polymers, see **Figure 1.12**. Reports on reductive electropolymerisation methods also exist

in the literature, however, the scope of compatible monomers with this type of electropolymerisation is very limited.[41,42]

In the electropolymerisation approach, the properties of the final polymer can easily be tuned by changing the employed deposition method (potentiostatic, galvanostatic, pulsed, or cyclic voltammetry), applied potential, amount of passed charge, and scanning speed.[43–46] Similarly, monomer concentration, electrolyte concentration and nature, and solvent choice can also have drastic impacts on the resulting electrical and morphological properties of the polymer, see **Figure 1.12**.[43,47,48] In this context typical solvents include acetonitrile,

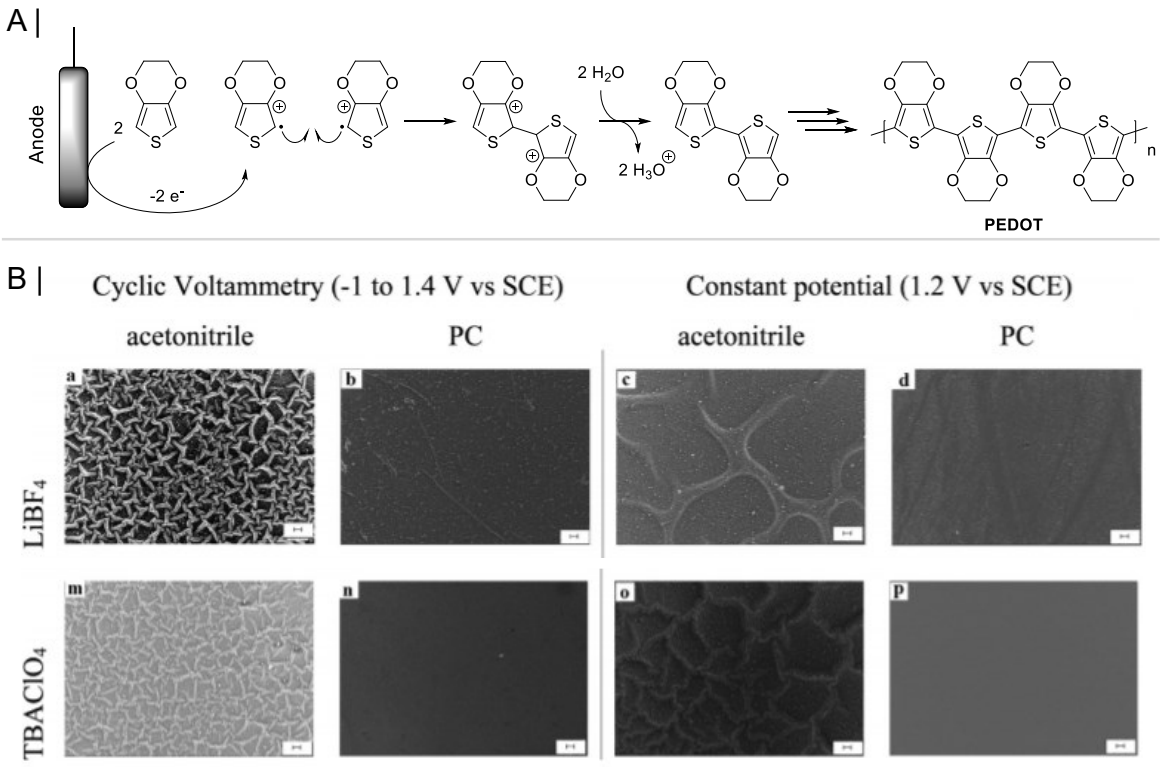

Figure 1.12. *a) Reaction mechanism of the electrochemical polymerisation of 3,4-ethylenedioxythiophene into poly(3,4-ethylenedioxythiophene) (**PEDOT**). b) Impact of varying the employed deposition method, solvent, and electrolyte on the morphological properties of **PEDOT**. Panel b adapted with permission from E. Poverenov et al., Chem. Mater. **2010**, 22, 4019. Copyright (2010) American Chemical Society.[43] ACS distribution licence obtained on 27.05.2021, see **Appendix Section 8.2**.*

propylene carbonate, and water, while common electrolytes include lithium perchlorate, tetrabutylammonium perchlorate, and tetrabutylammonium hexafluorophosphate. Despite the synthetic flexibility of the electrochemical polymerisation method, its primary drawback is the necessity for a conductive surface for the polymerisation process to occur, therefore, severely limiting substrate choice and rendering it unsuitable for large-scale polymer synthesis. Characterisation of the resulting polymer is also limited to a narrower range of analytical techniques, hence complicating the determination of structure-property relationships. Finally, this method is also typically only compatible with the synthesis of structurally rather simple homopolymers, hence severely impacting the range of polymer structures that can be investigated.

Solution-based chemical polymerisation methods thus tend to be preferred. In the early phases of conjugated polymer synthesis, chemical oxidative polymerisations were frequently employed. This involved dissolving the monomer in the presence of an oxidant in a common solvent. Variation in either of these three synthetic handles, as well as their concentration, reaction time, temperature, *etc.* could then be employed to tune the resulting material's properties.[49–52] Common oxidant species include iron (III) and persulfate salts, while alternative oxidants such as bromine and copper (II) chloride have also been employed.[53,54] The shortcomings of this method were its main suitability only towards the synthesis of homopolymers and its poor functional group selectivity, often leading to polymers with numerous defects in their conjugated backbone and consequently poor electrical performances.[55] Oxidative polymerisation methodologies have thus largely been replaced by transition-metal catalysed ones, such as the Grignard Metathesis (GRIM) method, which was first developed in 1999 and is nowadays used as the method of choice in the synthesis of highly regular poly(3-alkylthiophenes).[56,57] Several variations of palladium catalysed cross-coupling polymerisations have also been developed and have

been demonstrated to not only incur highly regular conjugated polymers, but have also been found to be compatible with a very wide range of aromatic building blocks, therefore, giving access to a broad array of polymers, including homo- and copolymers. The general mechanism of such cross-coupling polymerisations is given in **Figure 1.13**.

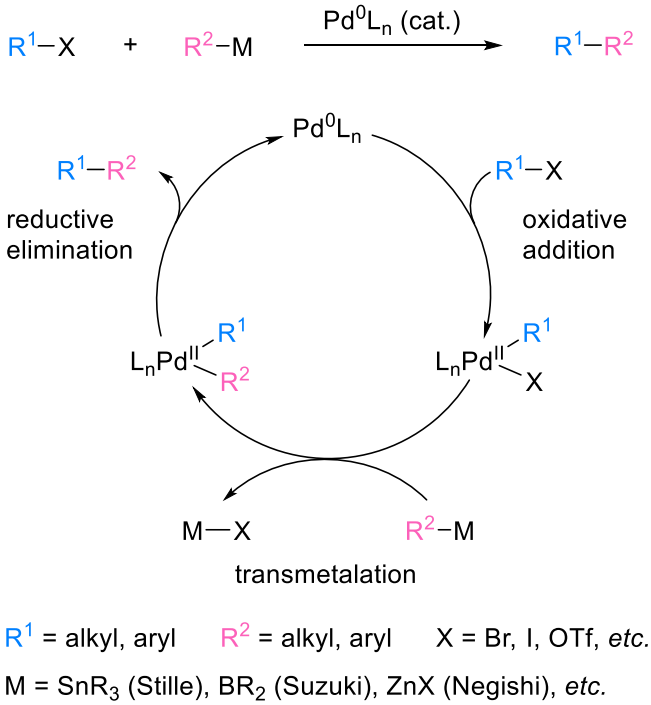

Figure 1.13. *General mechanism of a palladium catalysed cross-coupling reaction.*

Specific examples of palladium catalysed cross-coupling reactions include Stille,[58] Suzuki,[59] and Negishi chemistries,[60,61] all of which have been employed for synthesising semiconducting polymers. While all of these polymerisation techniques share many commonalities, subtle differences exist, nonetheless. Stille cross-coupling polymerisations for example make use of organostannanes as the organometallic species and typically tend to be compatible with a wide range of functional groups. Organostannanes are however known to be highly toxic, thus posing significant health and safety risks during polymer synthesis and purification and require anhydrous reaction conditions for polymerisation reactions to proceed efficiently. Moreover, the necessity to synthesise organotin

intermediates leads to increased synthetic steps and reduced atom economies. Alternative polymerisation approaches, including direct heteroarylation polymerisation (DHAP), are hence currently being developed to forego these drawbacks of Stille chemistry. Although the suitability of DHAP as a synthetic method for the realisation of high-performance conjugated polymers has been demonstrated in the literature, its applicability to a broad range of conjugated building blocks still has to be proven.[62,63] Finally, another polymerisation strategy that has recently gained significant attention is Aldol polycondensation, which not only foregoes the use of expensive palladium catalysts but also benefits from high atom economies and low toxicity with the only by-product of the reaction being water.[64–66]

1.3 Organic Mixed Ionic-Electronic Conductors, More Than Just Electrically Conductive Materials

The ability of conjugated polymers to transport electronic charge carriers has been exploited in numerous organic electronic devices, including OLEDs, OFETs, and OPVs, which have found several practical applications. A more recent endeavour of the scientific community has come from the desire to apply conjugated polymers for a range of electrochemical applications, which rely on the transport of both electronic and ionic charge carriers. Organic semiconductors that satisfy the demanding role of conducting both types of charge carriers are referred to as organic mixed ionic-electronic conductors (OMIECs) and have found numerous applications,[67] including as next-generation energy storage devices,[68] biomedical technologies such as electrophysiological recorders[69–71] or metabolite sensors,[72,73] and as actuators.[74,75] Note that as the majority of the practical aforementioned applications relies on the operation of the organic semiconductor in an aqueous medium, the

ability of a conjugated polymer to conduct ions will herein solely be defined as its ability to conduct ions in an aqueous environment.

The most well studied OMIEC to date is the conjugated polymer-polyelectrolyte composite poly(3,4-ethylenedioxythiophene):polystyrenesulfonate (**PEDOT:PSS**), which was developed in the late 80s by Bayer AG.[76–78] In this system, the conjugated **PEDOT** backbone provides a pathway for electronic charge carrier transport, while the hydrophilic nature of the **PSS** polyanion is responsible for water uptake into the material, hence giving rise to pathways for efficient ionic conduction in and out of the material. In the most fundamental terms, ionic conduction in OMIECs is therefore instilled by the introduction of hydrophilicity. The excellent suitability of **PEDOT:PSS** as an OMIEC has been demonstrated in both experimental and theoretical studies.[79] In fact, moving front experiments highlighted that the ionic mobilities of small hydrated cations (Na^+ and K^+) in **PEDOT:PSS** can be as high as their mobilities in bulk water. Increasing the ionic mobility in **PEDOT:PSS**-based systems is, however, often accompanied by a negative impact on the OMIEC's electrical charge transport abilities.[80] As either ionic or electronic transport can limit the performance of OMIECs in resulting devices, caution has to be exerted on finding the best balance of these opposing factors, see **Figure 1.14**. Further evidence highlighting the necessity for conflicting molecular design requirements come from *in situ* electrochemical microscopy, which demonstrated that ionic transport in conjugated polymers is facilitated by less ordered and looser domains, with the opposite effect typically observed for electronic charge carrier transport.[81]

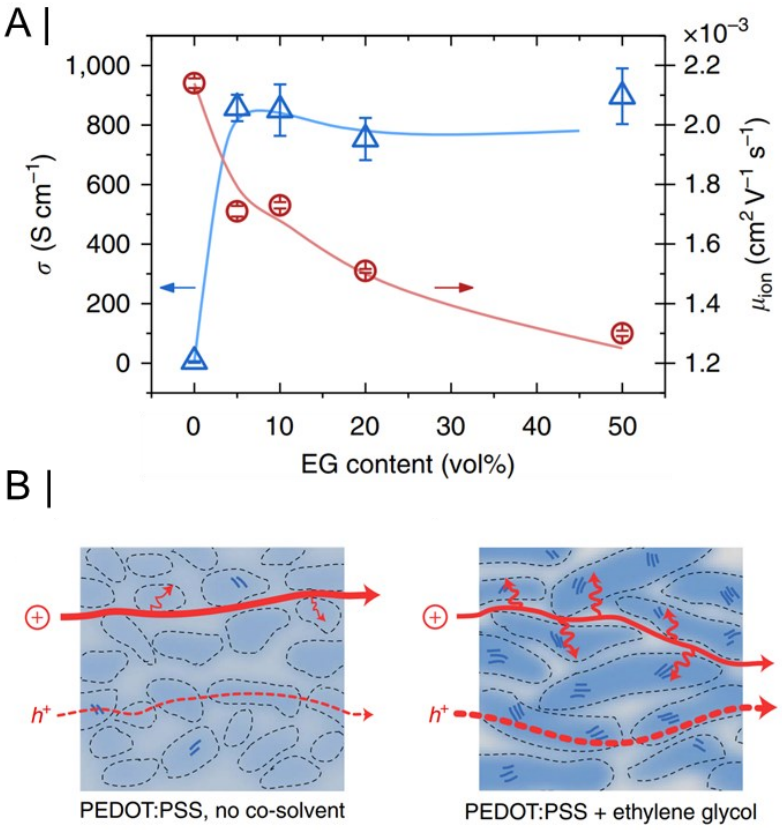

Figure 1.14. *a) Electrical conductivity (blue trace) and K^+ ion mobility (red trace) of* ***PEDOT:PSS*** *as a function of ethylene glycol formulation content. b) Schematic highlighting the impact of ethylene glycol addition on the morphology of* ***PEDOT:PSS*** *and the associated changes in ionic and electronic charge carrier transport. Width of the red arrows denotes the relative ease of electronic and ionic charge carrier transport across the material. Figure adapted with permission from J. Rivnay et al., Nat. Commun.* ***2016****, 7, 11287. Copyright (2016) Springer Nature.*[80] *Springer Nature distribution licence obtained on 27.05.2021, see* ***Appendix Section 8.2****.*

Rather than blending a conjugated polymer with a hydrophilic yet electrically insulating component to endow the resulting composite with mixed conduction properties, a more recent strategy has involved the grafting of hydrophilic side-chains directly onto the backbones of conjugated polymers.[82,83] The advantage of employing such single component systems not only lies in their less complex structure, thus facilitating structure-property investigations, but also in a greater synthetic flexibility.

1.4 Organic Electrochemical Transistors

A particular device exploiting the mixed conduction abilities of OMIECs is the organic electrochemical transistor (OECT). OECTs have received considerable recent interest due to their ability to track biological activity. Specifically, OECT have been employed as neural recording elements,[71,84] ion sensors,[85,86] biomolecule detectors,[72,87,88] cell activity monitors,[89,90] amongst many others.

OECTs were first developed in the mid-1980s and share many commonalities with the more widely known and explored OFETs.[91–93] Therefore, to understand the operating principles of OECTs it is worthwhile to consider the fundamental operation of an OFET.

1.4.1 From Organic Field-Effect to Organic Electrochemical Transistors

Transistors are electronic devices that can modulate the flow of electric current, with the concept of a transistor first introduced by Julius Edgar Lilienfeld in 1925.[94] The first examples of working field-effect transistors (FETs), however, only came decades later through extensive research efforts in the late 1940s at Bell Telephone Laboratories.[95] Despite enjoying considerable economic success and finding numerous commercial applications, one of the main drawbacks of conventional FETs included the high costs associated with sourcing and processing the employed inorganic materials, thus prompting the search for cheaper alternatives. A breakthrough came in 1986, when researchers at Mitsubishi Electric reported the first successful realisation of a FET making use of an organic active layer, marking the beginning of the era of organic field-effect transistors (OFETs).[96,97]

OFETs are three-terminal electronic devices, making use of a source, drain, and gate electrode. The channel of the material is defined by an organic semiconductor that stretches

across the source and drain electrodes and is separated from the gate electrode through a dielectric. Typical electrode materials employed for OFETs include gold, calcium, and silver, which have adequately aligned work functions to enable facile charge injection and extraction from the organic semiconductor.[98,99] On the other hand, common dielectrics include silicon dioxide, poly(methyl methacrylate), CYTOP^{TM}, and benzocyclobutene-based polymers.[100–102] In parallel to considerable electrode and dielectric material developments, the past thirty years have also witnessed the synthesis of countless organic conjugated polymers and small molecules that have been discussed in several comprehensive reviews in the literature.[103,104] Broadly speaking these typically tend to be categorised depending on their ability to either transport holes (p-type) or electrons (n-type) as electronic charge carriers. The working principle of an OFET employing a p-type organic semiconductor is shown in **Figure 1.15**. In the absence of applied gate ($V_G = 0$) and drain ($V_D = 0$) biases, the organic semiconductor is unperturbed, and no current is flowing through the device. The device is therefore in its 'OFF' state. Application of a negative potential at the gate electrode ($V_G < 0$) results in the polarisation of the dielectric and a layer of positively charged electronic carriers (holes) accumulates at the semiconductor-dielectric interface. These charge carriers can subsequently be swept across the device's channel by application of a negative potential at the drain electrode ($V_D < 0$), leading to current flow (I_D) and the device being in its 'ON' state. As long as the drain potential is less negative than the gate potential ($V_G << V_D < 0$), I_D increases linearly with decreasing V_D, following Ohm's law. Under these conditions, the transistor is said to be working in the linear regime.

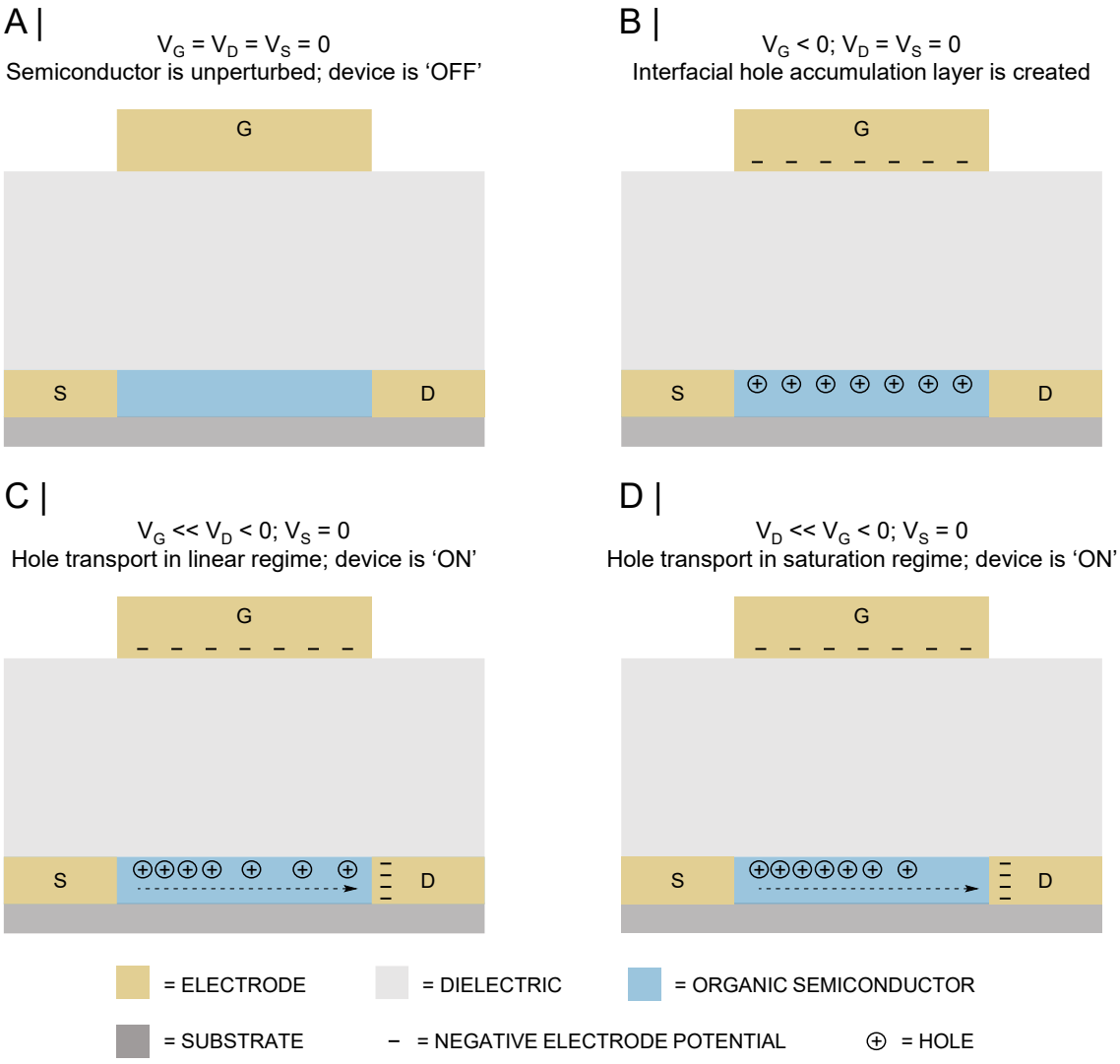

Figure 1.15. *Operating mechanism of a p-type organic field-effect transistor with a top gate, bottom contact architecture and the various applied source (V_S), gate (V_G), and drain voltages (V_D) highlighted.*

On the other hand, as the drain voltage becomes of similar magnitude compared to the gate voltage ($V_D \approx V_G$), the charge carriers near the drain electrode are depleted and the channel becomes 'pinched-off'. Further decreasing the drain voltage extends the depleted region, moving it progressively closer to the source electrode ($V_D << V_G < 0$) and the transistor operating in saturation mode. The mathematical equations describing the transistor's current flow in the linear and saturation mode are given in **Equations 1.1** and **1.2**, respectively.

$$I_{D,lin} = \frac{W}{L}\mu_{lin}C(V_G - V_{Th})V_D \qquad \textbf{Equation 1.1}$$

$$I_{D,sat} = \frac{W}{2L}\mu_{sat}C(V_G - V_{Th})^2 \qquad \textbf{Equation 1.2}$$

Where $I_{D,lin}$ is the drain current in the linear regime, W the channel width, L the channel length, μ_{lin} the electronic charge carrier mobility in the linear regime, C the capacitance, V_{Th} the threshold voltage, $I_{D,sat}$ the drain current in the saturation regime, and μ_{sat} the electronic charge carrier mobility in the saturation regime.

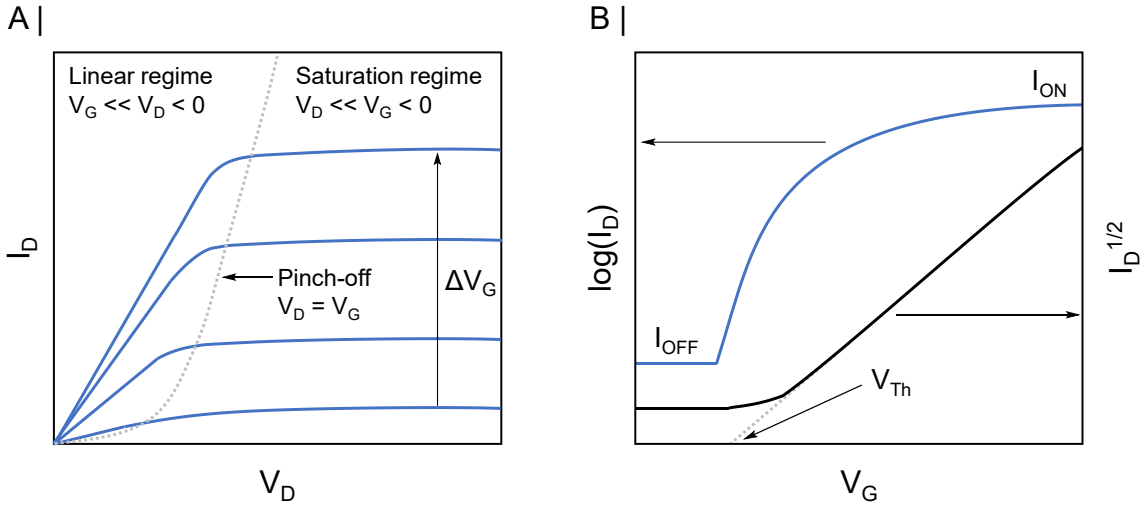

Figure 1.16. *Typical a) output and b) transfer curves recorded for an OFET with highlights showing important transistors parameters that can be extracted from these plots.*

The current-voltage properties of OFETs are typically summarised in the transistor's output and transfer plots, see **Figure 1.16**. In the output characteristics, the drain current (I_D) is recorded as a function of the applied drain voltage (V_D) at different gate voltages. On the other hand, in the transfer characteristics, I_D is measured as a function of V_G at a specific V_D. When used in combination, many of the transistor's performance parameters can be extracted from these plots, including the transistor's maximum current on/off ratios (I_{ON}/I_{OFF}) and its threshold voltage (V_{Th}). Of the various performance metrics, the

semiconductor's electronic charge carrier mobility in the linear (μ_{lin}) and saturation regime (μ_{sat}) are of particular importance. These can in turn be obtained by solving **Equations 1.3** and **1.4**, respectively, which in turn are derived from **Equations 1.1** and **1.2**.

$$\mu_{lin} = \frac{L}{WCV_D}\frac{\partial I_{D,lin}}{\partial V_G} \qquad \textbf{Equation 1.3}$$

$$\mu_{sat} = \frac{2L}{WC}\left(\frac{\sqrt{I_{D,sat}}}{\partial V_G}\right)^2 \qquad \textbf{Equation 1.4}$$

Over the past three decades, the mobility of OFETs has been drastically increased by a factor of 10^5-10^6 with numerous conjugated polymers nowadays incurring mobility values > 1 cm^2 V^{-1} s^{-1}, which are comparable to those of their inorganic counterparts.[104,105] While the development of tailor-made organic semiconductors has played a crucial role in advancing this technology, progress in device engineering and semiconductor processing has also been invaluable to close the inorganic-organic performance gap.[106,107] Despite this progress, OFETs typically still suffer from high gate voltages required to drive devices between their 'ON' and 'OFF' states, incurring high power requirements and reducing their practicality. This has prompted research into alternative dielectric materials, including electronically insulating, but ionically conducting electrolytes, which has given rise to a new class of organic transistors, namely electrolyte gated field-effect transistors (EGOFETs), see **Figure 1.17**.

In the case of an EGOFET making use of a p-type organic semiconductor, application of a negative gate bias leads to the accumulation of negative surface charges on the metal electrode, thereby attracting mobile cations in the electrolyte and resulting in the formation of an electrical double layer (EDL) at the gate-electrolyte interface. Concomitantly, negatively charged ions are repelled from the gate, leading to the creation of a negatively charged anion layer at the semiconductor-electrolyte interface and causing holes to be

injected into the semiconductor from the source contact. Like in OFETs these can then be swept across the organic semiconductor channel by application of a negative voltage at the drain electrode. The particularly attractive feature of EGOFETs compared to OFETs is the incredibly large capacitance of the generated electrical double layers,[108,109] hence inducing much larger charge carrier densities into the semiconductor channel at low applied potentials, see **Figure 1.17**. An additional benefit is also the significant boost in current, further benefiting the polymer's mobility as dictated by **Equations 1.3** and **1.4**. In the above description of EGOFET operation, the employed organic semiconductor is impermeable to ions, causing the ionic-electronic interaction to be limited to only take place

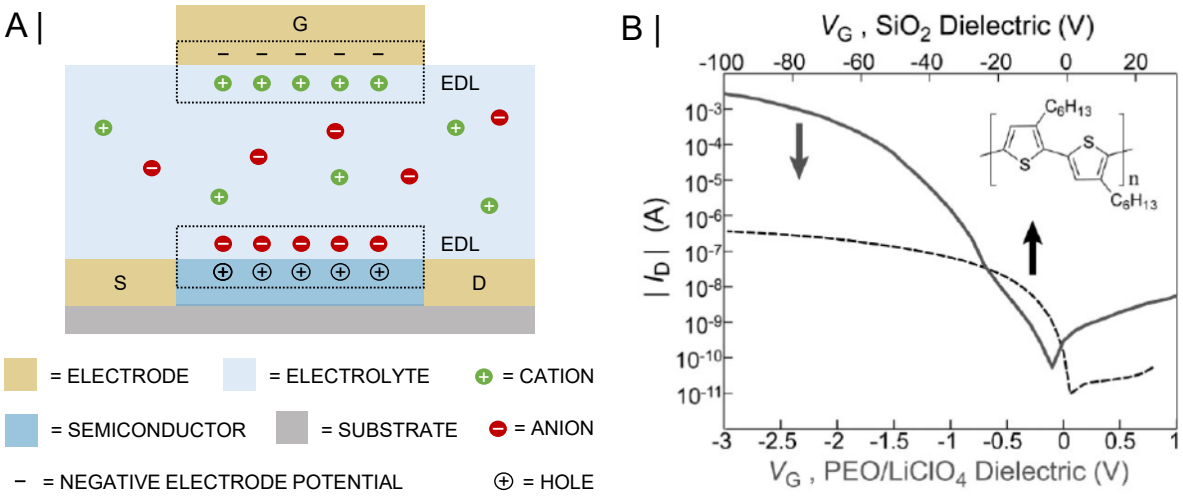

Figure 1.17. *a) Schematic of a p-type EGOFET highlighting the formation of electrical double layers at both the gate-electrolyte and electrolyte-semiconductor interface. b) Comparison of poly(3-hexylthiophene)'s (**P3HT**) transfer characteristics when employing a conventional OFET architecture including a SiO_2 dielectric (dashed line, top x-axis) and an EGOFET architecture making use of a polyethylene oxide/lithium perchlorate electrolyte (solid line, bottom x-axis). Panel b adapted with permission from M. J. Panzer et al., Adv. Mater. **2008**, 20, 3177. Copyright (2008) John Wiley and Sons.*[109] *John Wiley and Sons distribution licence obtained on 27.05.2021, see **Appendix Section 8.2**.*

at the electrolyte-semiconductor interface. A distinct mode of EGOFET operation occurs when the employed channel material, typically a conjugated polymer, is replaced by an OMIEC, which is permeable to the ions present in the electrolyte. In this scenario, EDL formation is no longer restricted to solely occur in the plane parallel to the semiconductor-electrolyte interface but instead leads to EDL formation across the whole three-dimensional volume of the channel, see **Figure 1.18**. EGOFETs operating in such mode are referred to as organic electrochemical transistors (OECTs).

As depicted in **Figure 1.18**, like OFETs and EGOFETs, OECTs also feature a three-terminal architecture with an organic semiconductor spanning across the device's channel. The categorisation of semiconductors into p-type and n-type is also analogous to the one made in OFETs and EGOFETs. In OECTs, a further distinction of semiconductors tends to be made, which depends on the doping level of the employed channel material at zero gate bias. This divides channel materials into two groups: those operating in accumulation mode (semiconductor not doped at zero gate bias) and those operating in depletion mode (semiconductor doped at zero gate bias).[82,83,110] Taking **PEDOT:PSS** as an example, the operation of OECTs can be described as follows. **PEDOT:PSS** is a p-type semiconductor given that its conjugated polymer backbone is comprised of electron-rich thiophene rings, conferring it with a shallow HOMO, *i.e.* a low ionisation potential (*IP*). **PEDOT:PSS**' *IP* is in fact so low, that the **PEDOT** conjugated polymer backbone is susceptible to spontaneous doping reactions with oxygen under ambient conditions.[111,112] Charge neutrality in **PEDOT:PSS** is ensured by the negatively charged sulfonate groups of the **PSS** polyanion compensating for the holes present on the **PEDOT** backbone.

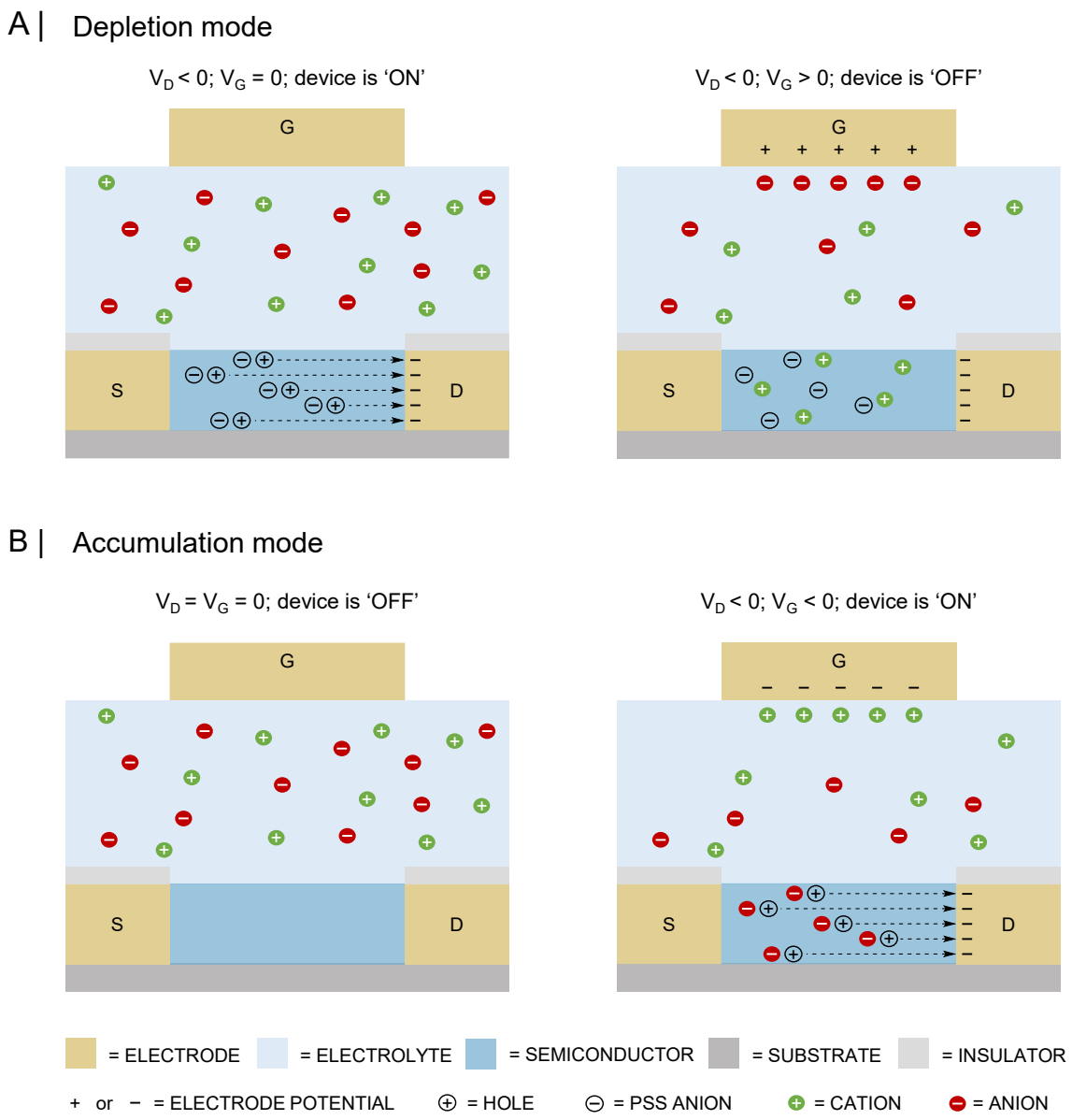

Figure 1.18. *Operating principle of a p-type a) depletion and b) accumulation mode organic electrochemical transistor, highlighting the formation of EDLs across the bulk of the organic semiconductor channel.*

PEDOT:PSS, therefore, operates in depletion mode. Application of a negative drain bias ($V_D < 0$) in the absence of an applied gate voltage ($V_G = 0$) hence results in the flow of a hole current across the channel and the device being 'ON'. The device is turned 'OFF' by applying a positive gate voltage ($V_G > 0$), causing cations to be repelled from the gate electrode and injected into the **PEDOT:PSS** channel. The injection of cations into

PEDOT:PSS leads to a charge balancing of the **PSS** anions and holes from being ejected from **PEDOT:PSS** conduction band. In contrast, accumulation mode devices rely on channel materials that are in their dedoped state at zero gate bias and are switched 'ON' upon the application of a negative gate bias ($V_G < 0$), leading to the concomitant injection of anions into the channel material. Analogous operating mechanisms hold true for n-type accumulation and depletion mode channel materials, albeit with the flow of charge carriers opposite in sign. A direct advantage arising from the bulk electrochemical doping operating mode of OECTs compared to EGOFETs includes significantly larger current amplification,[84,113] which in turn are beneficial in the context of recording low amplitude biological signals such as electrophysiological potentials. Moreover, the favourable low operating potentials that EGOFETs enjoy are retained in OECTs, thus rendering OECTs also compatible for operation within the narrow electrochemical window of water and the compatibility of these devices to being used for interfacing with biological systems.

1.4.2 OECT Performance Metrics

Historically, the main figure of merit that has been employed to describe the ability of OECTs to amplify an input signal is the transconductance, g_m, which is the first derivative of the transfer curve ($\partial I_D/\partial V_G$).[91–93] A mathematical model to describe the steady-state performance of OECTs was proposed in 2007,[114] which relies on the description of OECTs as being composed of two circuits: an electronic circuit that captures the electronic charge carrier transport across the organic semiconductor, and an ionic circuit that depicts the transport of ions in the electrolyte. By drawing analogies to charge carrier transport in conventional FETs, an equation for the transconductance can be obtained. When operating in the saturation regime, the transconductance of depletion mode devices is given by **Equation 1.5**, with the voltage terms inverted for accumulation mode devices.

$$g_m = \frac{Wd}{L}\mu C^*(V_{Th} - V_G) \qquad \textbf{Equation 1.5}$$

Where W is the channel width, d the channel thickness, L the channel length, μ the electronic charge carrier mobility, C^* the volumetric capacitance, and V_{Th} the threshold voltage.

As follows from **Equation 1.5**, g_m is hence dependent on both device geometry (W, d, and L) and material-dependent (μ and C^*) terms. A facile way to improve the device's transconductance, therefore, consists of varying the device's dimensions. Although maximising the device's transconductance by tuning its areal dimensions is conceptually a viable strategy, various biological applications of OECTs (*e.g.* electrophysiological recordings) often require miniaturisation of the device's areal footprint. Hence, the most commonly investigated means to enhance g_m is to increase the channel's thickness.[84] Device thickness increments are however accompanied by slower response times, therefore limiting the frequencies at which devices can be operated. A more convenient and interesting strategy thus relies on maximising the product μC^*, requiring the optimisation of the channel material's electronic and ionic properties through synthetic means.[115]

A further consideration arising from **Equation 1.5** is that the performance comparison of two different channel materials by means of the recorded transconductance is challenging, given the transconductance's dependence on the OECT's geometry. The product μC^* has therefore been proposed as a more appropriate figure of merit that more closely captures the device's performance inherent to the employed OMIEC.[115] Furthermore, by measuring either or both of the mobility and capacitance terms independently of another, a greater insight into the performance of the employed OMIEC can be obtained. The C^* of an OMIEC can, for example, be estimated through electrochemical impedance spectroscopy (EIS) of an OMIEC coated electrode. In this technique, the impedance of a given material is measured as a function of the applied potential's frequency. The resulting data can subsequently be fit

to a Randles circuit to obtain a fitted capacitance value which can then be normalised by the OMIEC's volume to incur its C^*.[84] The OMIEC's electronic charge carrier mobility can subsequently be estimated by dividing the recorded μC^* product by the recorded C^* value. Alternatively, constant gate current or impedance matching methods can also be used to extract the hole mobility of the employed OMIEC.[89,114]

Recently, the development of novel OMIECs has been used in conjunction with additional strategies to enhance the maximum μC^* that can be attained by the semiconductor in OECTs. Specifically, the use of molecular additives such as ethylene glycol or ionic liquids has been found to greatly boost the μC^* that can be realised.[80,116] Alternatively, engineering of the processing solvent has also proven to be highly fruitful.[117] Finally, varying both the concentration and nature of the employed electrolyte can also have a dramatic effect on the OMIEC's μC^*.[118–120] Therefore, comparison of the OECT performance of different channel materials should ideally be performed by employing the same electrolyte and concentration, or at minimum the same charge compensating counterion and concentration. In this context, 0.1 M aqueous solutions of sodium or potassium chloride are typically employed, given the dominance of potassium, sodium, and chloride ions in various biological media.[121,122]

While the steady-state performance of OECTs can in large be described through the combination of the product μC^*, μC^* does not provide any information on the device's transient response or stability. Fast transient responses are, however, of particular importance in the context of recording short-lived biological signals such as brain activity oscillations, which tend to have frequencies in the range of 0.5-200 Hz.[69,110] A common metric to capture the device's transient response is by measurement of its 'ON' and 'OFF' times, which are defined as the time taken to reach 90% of the I_D for the 'ON' state and 10% of the I_D for the 'OFF' state.[123] Device stability measurements on the other hand typically involve repeated electrochemical cycling of the device by application of square-wave gate

voltage pulses. The typically employed figure of merit to capture the device's electrochemical stability is the retention of the device's 'ON' current over a specific number of electrochemical cycles or addressing time, with high values being preferred.[124–126] During these stability measurements, care must also be taken to ensure a fair comparison across different channel materials given their different energetics and tendencies to undergo electrochemical doping. It is therefore recommended that the gate voltage used to define the 'ON' state corresponds to the one incurring the maximum device performance, *i.e.* transconductance, thus minimising stability differences due to different degrees of electrochemical doping of the OMIEC.

1.4.3 OECT Channel Materials

Broadly speaking, OMIECs utilised as OECT channel materials can be classified into three main categories, see **Figure 1.19**, namely conjugated polymer composites, conjugated polyelectrolytes, and EG functionalised conjugated polymers. The key distinguishing features across these materials classes is whether they make use of a single component responsible for both ionic and electronic charge carrier transport (conjugated polyelectrolytes and EG functionalised conjugated polymers) or whether they employ multiple components to segregate ionic from electronic charge carrier transport (conjugated polymer composites).

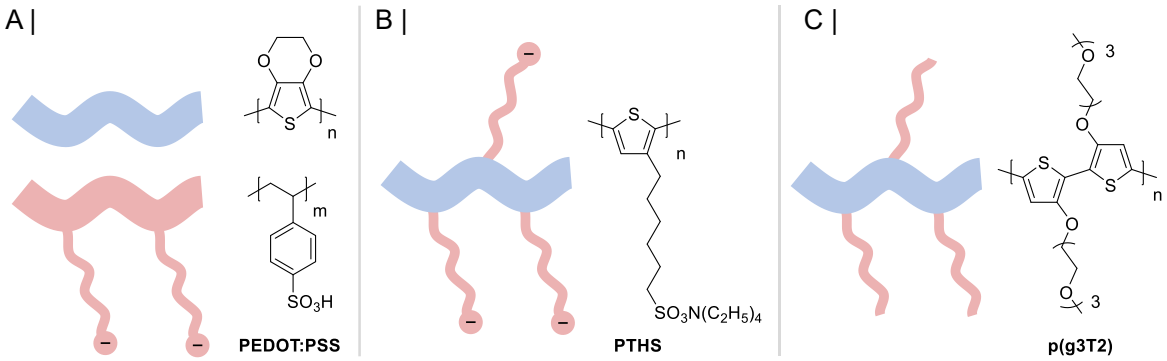

Figure 1.19. *Different classes of OECT channel materials, including a) conjugated polymer composites (e.g.* ***PEDOT:PSS****), b) conjugated polyelectrolytes (e.g.* ***PTHS****), and c) EG functionalised conjugated polymers (e.g.* ***p(g3T2)****). Conceptual sketches highlight the defining characteristics of each OMIEC class. Broad ribbons correspond to polymer backbones, while narrow ribbons to pendant side-chains. Blue and red colours denote material sections responsible for electronic and ionic charge carrier transport, respectively.*

To date, the most widely explored and well-studied OECT channel material is the commercially available conjugated polymer composite **PEDOT:PSS**, see **Figure 1.20**, which is sold as aqueous dispersions under various trade names (Clevios PH1000, Baytron P, Orgacon). Structurally, **PEDOT:PSS**' film morphology has been reported to be composed of **PEDOT**-rich domains dispersed in a **PSS**-rich matrix.[127–129] In their pristine form, films cast from these dispersions typically incur low g_m values of ~ 0.3 mS (W = 50 µm, L = 50 µm, and d = 390 nm), which also translate into low μ and C^* values of 0.2 cm^2 V^{-1} s^{-1} and 37 F cm^{-3}, respectively.[80] The addition of molecular additives, such as common organic solvents (*e.g.* ethylene glycol, DMSO, *etc.*) often referred to as secondary dopants, has however been demonstrated to be an effective method to improve **PEDOT:PSS**' OECT performance.[69,80,130,131] For example, the use of a 5 v/v% ethylene glycol (EG) formulation additive was shown to boost the transconductance of **PEDOT:PSS**-based devices to ~ 9.5 mS (W = 50 µm, L = 50 µm, and d = 208 nm), including enhanced μ and C^* values of 1.9 cm^2 V^{-1} s^{-1} and 39 F cm^{-3}, respectively.[80] Similar increments in **PEDOT:PSS**' OECT

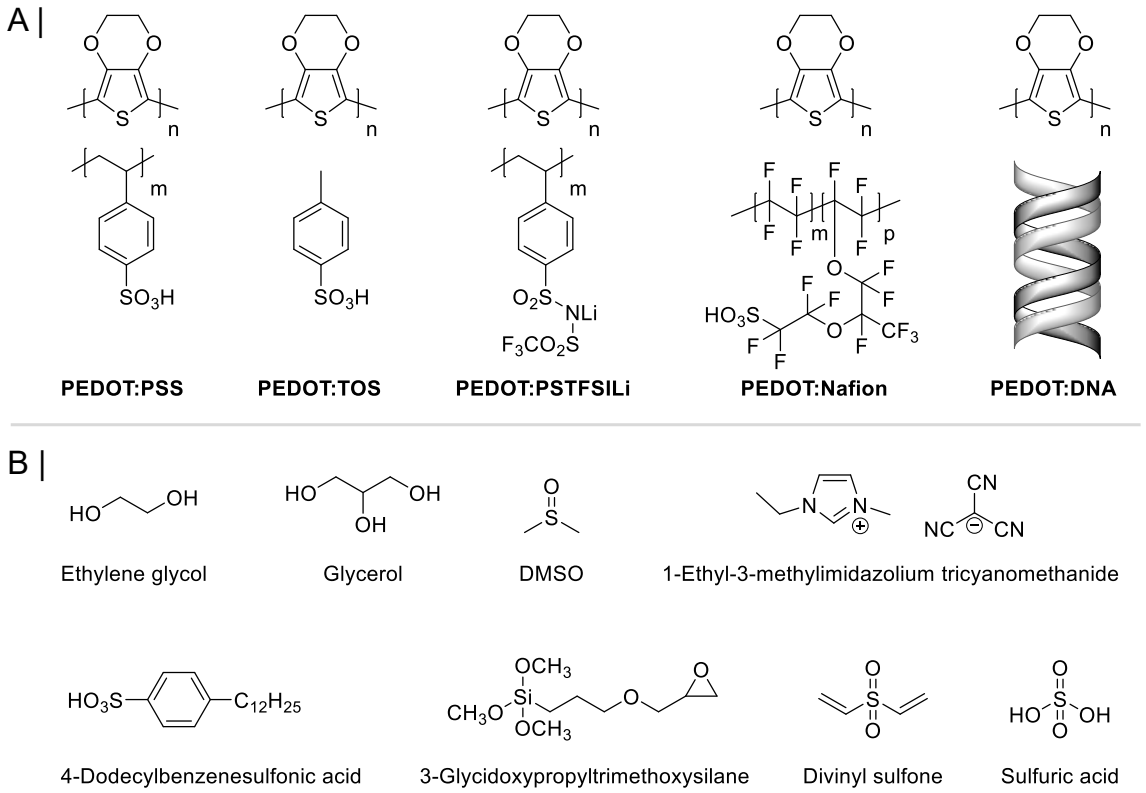

Figure 1.20. *Chemical structures of a)* ***PEDOT****-based conjugated polymer composites and b) commonly employed additives to improve the OECT steady-state performance, stability or processability of such systems.*

performance were also demonstrated by adding 1.5 wt% of the ionic liquid, 1-ethyl-3-methylimidazolium tricyanomethanide [EMIM][TCM], to a **PEDOT:PSS** solution prior to casting on devices.[116] In fact, devices making use of the aforementioned casting protocol were found to incur a peak g_m of 14.2 mS (W = 1000 μm, L = 100 μm, and d = 200 nm) and a μC^* figure of merit of 335 F cm^{-1} V^{-1} s^{-1}.[116] The performance increments brought by the use of secondary dopants are typically related to the formation of more ordered and heterogeneous microstructures, which tend to primarily aid electronic charge carrier transport. An alternative approach to modifying **PEDOT:PSS**' structural and electronic properties, was recently demonstrated and involves post-deposition treatment of as-spun **PEDOT:PSS** films with concentrated sulfuric acid.[124] This strategy has previously already been deployed to incur **PEDOT:PSS** films with excellent electrical conductivities (up to

4200 S cm^{-1}) and charge carrier mobilities (> 4 cm^2 V^{-1} s^{-1}).[132,133] When translated to OECTs, this enabled **PEDOT:PSS**-based devices to incur a maximum g_m of 19 mS (W = 80 μm, L = 20 μm, and d = 200 nm) and a μC^* value of 490 F cm^{-1} V^{-1} s^{-1}. Other additives commonly employed in **PEDOT:PSS** composites to ensure good OECT performance are the molecular surfactant 4-dodecylbenzenesulfonic acid (DBSA) and the crosslinking agent 3-glycidoxypropyltrimethoxysilane (GOPS). Unlike the aforementioned secondary dopants, the primary purpose of these molecular additives is not to boost OECT performance, but instead facilitate organic semiconductor processing or thin film stabilisation onto device substrates.[79,130,134–138]

Alternative ways to modulate the electronic performance and structural properties of **PEDOT:PSS** have been investigated, for example through substitution of the employed counterion, as in the case of **PEDOT:TOS**, **PEDOT:PSTFSILi**, **PEDOT:Nafion**, *etc.*, however, these strategies have typically resulted in lower performance OECT channel materials.[115,135,139–142] Consequently, although great strides have been made in advancing the performance of **PEDOT:PSS** in OECTs, **PEDOT:PSS**-based OECTs still display several shortcomings, including i) **PEDOT:PSS**' complex morphology, hence complicating structure-property investigations, ii) the presence of electrically insulating PSS component, limiting the C^* that can be achieved, iii) their depletion mode of operation, incurring lower on/off current ratios and higher power requirements, and iv) **PEDOT:PSS**' ability to solely transport holes as electronic charge carriers. These limitations have sparked the development of alternative channel material classes, including conjugated polyelectrolytes and EG functionalised conjugated polymers.

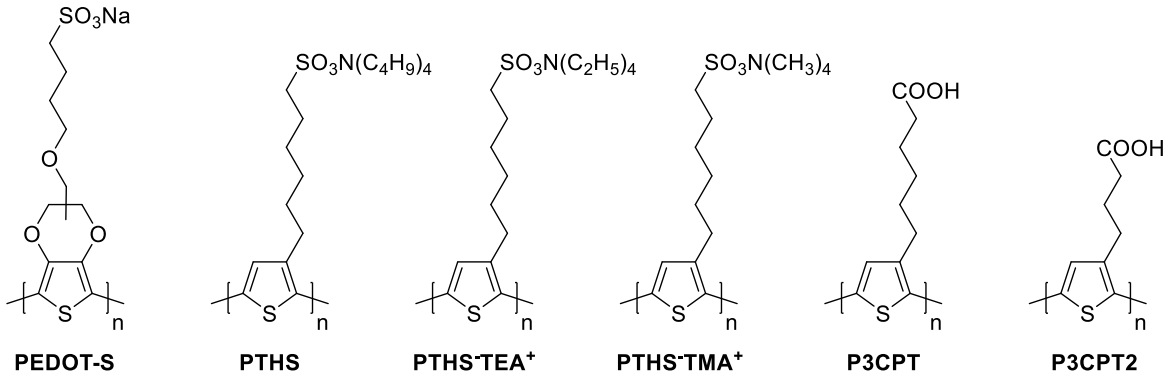

Figure 1.21. *Chemical structures of selected conjugated polyelectrolytes that have been employed as OECT channel materials.*

Conjugated polyelectrolytes are a class of OMIECs in which ionic conductivity is achieved through covalent attachment of hydrophilic charged moieties in the conjugated polyelectrolyte's side-chains. Analogous to their alkylated counterparts, grafting of these side-chains onto the conjugated backbone results in these materials being solution processable. Prominent representatives of conjugated polyelectrolytes that have been employed in OECTs are shown in **Figure 1.21**. One early example is **PEDOT-S**, which also makes use of a 3,4-ethylenedioxythiophene-based conjugated polymer backbone like the one employed in **PEDOT:PSS**.[143,144] The primary difference between the two materials stems from the charge balancing sulfonate moieties in **PEDOT-S** being covalently attached to the conjugated polymer backbone through an alkyl spacer. Given the similar energetics of both polymers, **PEDOT-S** also operates in a p-type depletion mode and was found to incur a maximum g_m of 16.2 mS (W = 39000 µm, L = 20 µm, and d = 75 nm).[123] Due to **PEDOT-S**' tendency to disperse in aqueous media, this transconductance value was however achieved by having to resort to a solid state gel electrolyte, limiting the biological applications of this OMIEC. Moreover, **PEDOT-S**-based OECTs made use of significantly wider channels compared to those employed in the aforementioned **PEDOT:PSS** studies, thus implying lower μC^* values for **PEDOT-S**-based OECTs compared to those based on **PEDOT:PSS**.

An early example of a conjugated polyelectrolyte designed specifically to operate in accumulation mode is the polythiophene, **PTHS**.[145] Analogously to **PEDOT-S**, **PTHS**' hydrophilicity was imparted by the terminal ionic sulfonate group grafted directly on its six-carbon atom containing alkyl side-chain. The dominance of the sulfonate moiety to impart hydrophilicity in conjugated polyelectrolytes is unsurprising given sulfonic acids' low pKa (around -2), leading to a reduced pH-dependent behaviour under the typical pH range (1-14) in comparison to their carboxylic acid counterparts, whose higher pKa (around 5), makes them susceptible to stronger pH-dependent electrochemical behaviour.[146] OECTs fabricated with **PTHS** were operated employing a 0.1 M aqueous sodium chloride solution as the supporting electrolyte, whereby application of increasingly negative gate biases resulted in increasing currents flowing across the channel, hence confirming the polymer's accumulation mode of behaviour. From a chemical design point of view this can be attributed to **PTHS**' side-chains not containing any strong electron-donating substituents that are in direct electronic communication with the polymer's conjugated polymer backbone, hence not rendering **PTHS** susceptible to spontaneous oxidation under ambient conditions.[111] Ultimately a peak g_m of 0.40 mS (W = 250 μm, L = 5 μm, and d = 60 nm) was recorded for **PTHS**, whereby the recorded g_m could be further improved to 2.0 mS (W = 250 μm, L = 5 μm, and d = 60 nm) through the use of EG as a secondary dopant.[145] In a follow-up study, the polymer's steady-state performance ascribed by the metric μC^* was calculated to be 5.5 F cm^{-1} V^{-1} s^{-1}.[115] Recently, several **PTHS**-derived polymers (**PTHS**$^-$**TEA**$^+$ and **PTHS**$^-$**TMA**$^+$) have been synthesised and tested for OECT applications, however, neither of the newly synthesised polymers was able to outperform the **PTHS** benchmark.[147,148] Carboxylic acid functionalised polythiophenes, including **P3CPT** and **P3CPT2**, have also gained significant attention from the OECT community, in particular given their reduced propensity to be dispersed in aqueous media, therefore foregoing the

necessity of using any stabilising cross-linkers, and their wider commercial availability. While high g_m values of 13 mS (W = 39000 µm, L = 20 µm, and d = 30 nm) and 26 mS (W = 39000 µm, L = 10 µm, and d = 165 nm) have been reported for **P3CPT** and **P3CPT2**, respectively, the corresponding OECTs typically featured very large products of Wd/L.[149,150] Direct performance comparisons against alternative channel materials are hence complicated, especially as μC^* values for carboxylic acid functionalised polythiophenes have thus far not been reported.

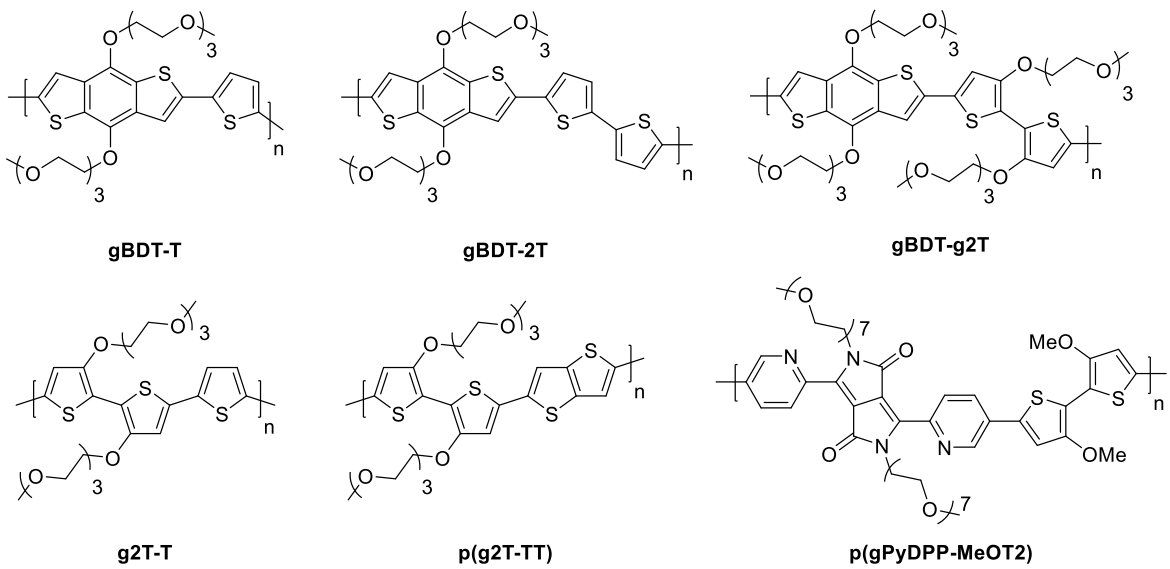

Figure 1.22. *Chemical structures of EG functionalised conjugated polymers.*

The most recently developed class of OECT channel materials are EG functionalised conjugated polymers, which were designed specifically to overcome **PEDOT:PSS**' limitations. As shown in **Figure 1.22**, the chemical structures of EG functionalised semiconducting polymers are closely related to those of conjugated polymers that have been employed for conventional organic electronic devices, such as OFETs. Consequently, this category of materials aims to exploit the vast knowledge of structure-property relationships that have been established for conjugated polymers over the past three decades. The seminal

report detailing the targeted synthesis of EG functionalised semiconducting polymers for OECT applications came in 2016,[151] when a series of thiophene- and benzodithiophene-based polymers, comprising **gBDT-T**, **gBDT-2T**, **gBDT-g2T**, and **g2T-T**, was synthesised by conventional Stille cross-coupling polymerisation. Thiophene and benzodithiophene moieties were chosen as aromatic building blocks given their electron-rich nature and tendency to incur high degrees of backbone planarity, which in turn should result in low operating voltages (necessary for stable OECT operation in the electrochemical window of water) and good electronic charge carrier transport abilities.[152–154] For each polymer, hydrophilic triethylene glycol chains were selected as pendant side-chains to impart sufficient solubility, hydrophilicity, and ion transport abilities to the polymer. Of the developed polymer series the highest performing member was found to be **g2T-T**, incurring a g_m of 7.9 mS (W = 100 µm, L = 10 µm, and d = 103 nm), which could further be improved to 21 mS (W = 100 µm, L = 10 µm, and d = 160 nm) upon increasing the device thickness and altering the polymer casting method, which compared favourably with **PEDOT:PSS**-based devices of similar dimensions.[151] These findings were verified in a follow-up study, in which the μC^* of **g2T-T** was found to be 167 F cm^{-1} V^{-1} s^{-1}.[115]

The most widely investigated EG functionalised semiconducting polymer is **p(g2T-TT)**, a close structural analogue of **g2T-T**, in which the thiophene comonomer has been substituted by a thieno[3,2-*b*]thiophene (TT) one.[155] From a molecular design point of view, the fused and more extended nature of the TT unit compared to its thiophene counterpart should lead to higher conjugated backbone rigidities, hence also increased π–π stacking interactions and higher charge carrier mobilities.[32] The successful translation of this design concept is well reflected in the grazing incidence wide-angle X-ray scattering (GIWAXS) data, revealing tighter π–π stacking distances of 3.5 Å for **p(g2T-TT)** compared to the 3.6 Å distance obtained for **g2T-T**. A direct consequence of the polymer's more favourable microstructure

was the improvement of the polymer's electronic charge carrier mobility from 0.28 $cm^2\ V^{-1}\ s^{-1}$ for **g2T-T** to ~ 1 $cm^2\ V^{-1}\ s^{-1}$ for **p(g2T-TT)**.[151,155] The superior overall performance of **p(g2T-TT)** was also reflected in the higher μC^* product that could be achieved, with **p(g2T-TT)** incurring a maximum μC^* of 261 $F\ cm^{-1}\ V^{-1}\ s^{-1}$, a record value at the time of publication.[115] One drawback of **p(g2T-TT)**-based OECTs is their limited operational stability, which is typically evaluated through pulsed electrochemical cycling measurements. As the figure of merit employed to quantify the operational stability of an OECT is the percentage retention of the initial drain current ($I_D/I_{D,0}$), this type of experiment mainly assesses the stability of the doped state of the channel material. Over a 2 h timeframe, OECTs based on **p(g2T-TT)** were able to only retain ~ 75% of their initial drain current, thus highlighting the relative instability of **p(g2T-TT)**'s doped state. The retention of high 'ON' currents and hence OECT performances is, however, imperative for many biological applications of OECTs, where signal recording can span over multiple days, weeks or even months.[156]

Additional stability evaluations on **p(g2T-TT)** were conducted recently,[112] whereby the focus of these investigations was not the polymer's doped state, but instead its dedoped one. Here, the stability of the polymer's dedoped state was assessed by examining the polymer's propensity to undergo oxygen reduction reactions (ORRs). These in turn can occur due to electron transfer reactions between the polymer's HOMO and ambient oxygen molecules, which result in the formation of hydrogen peroxide (H_2O_2).[111] Formation of H_2O_2 is, however, undesirable during device operation, as it can cause oxidative damage either to device materials or the biological system under evaluation.[157–159] Following extensive investigations, the authors concluded that the tendency of OMIECs to undergo ORR reactions is strongly linked to their *IP*. In particular, it was found that OMIECs featuring low *IP*s, such as **p(g2T-TT)** and **PEDOT:PSS** readily undergo ORR reactions when

dedoped. Conversely larger *IP* energy materials, such as the newly developed donor-acceptor copolymer **p(gPyDPP-MeOT2)**, see **Figure 1.22**, showed no signs of H_2O_2 formation during device operation. **p(gPyDPP-MeOT2)**-based OECTs, however, displayed several drawbacks, incurring a significantly lower maximum g_m of ~ 0.2 mS (W = 100 µm, L = 10 µm, and d = 120 nm) and a reduced operational stability, retaining only 84% of their $I_D/I_{D,0}$ after 25 min of continuous cycling.[112] Ultimately, these studies demonstrate that progress in both device performance and stability are still required to render OECT technologies viable candidates for industrial scale up and for practical long term biological recordings.

1.5 Thesis Aims and Objectives

The overarching goal of this thesis is the synthesis of ethylene glycol functionalised p-type polymers with mixed ionic-electronic conduction abilities and their evaluation as channel materials for organic electrochemical transistors operating in aqueous electrolytes. Through the synthesis of three polymer series, this work aims to advance the steady-state performance and operational stability of current OECT technologies, while in parallel elucidating structure-property relationships for the design of next generation channel materials. Specifically, during material development particular attention will be placed on evaluating the polymers' electrochemical, morphological, and water uptake properties.

Specific questions that will be answered across **Chapters 2-4** in this thesis are:

1. What is the impact of EG side-chain length modulation in polythiophene-based OECT channel materials and how can OECT steady-state performance be maximised through such a molecular design strategy?

2. Does the relative distribution of EG side-chains across a conjugated polymer backbone affect the electrochemical, morphological, and water uptake abilities of polythiophenes and therefore their OECT steady-state performance?
3. Do EG side-chain modifications also impact the stability of OECT channel materials and if so, how can device stability be maximised?
4. Are OECT steady-state performance and stability improvements useful towards the practical application of OECTs?
5. What aspects govern the performance and stability of donor-acceptor copolymers and how can their performance be improved to match the one of their all-donor counterparts?

'Scientific knowledge is in perpetual evolution; it finds itself changed from one day to the next.'

— Jean Piaget

2

Impact of Ethylene Glycol Side-Chain Length Engineering on the Ionic and Electronic Conduction Properties of Polythiophenes

Contents

2.1 General Information and Attributions

Monomer and polymer synthesis was supervised by Dr James F. Ponder (Imperial College London). Gel permeation chromatography (GPC) experiments were conducted by Dr Graham Collier (Georgia Institute of Technology). Polymer electrochemical measurements were conducted by Lisa Savagian (Georgia Institute of Technology). Grazing incidence wide-angle X-ray scattering (GIWAXS) measurements were performed by Lisa Savagian (Georgia Institute of Technology) at the Stanford Synchrotron Radiation Lightsource, SLAC National Accelerator Laboratory, and assisted by Dr Sandra Pittelli (Georgia Institute of Technology). Density functional theory (DFT) and molecular dynamics (MD) simulations were carried out by Micaela Matta (University of Liverpool) and Maryam Reisjalali (University of Liverpool). OECTs were fabricated by Tania Cecilia Hidalgo (King Abdullah University of Science and Technology). Polymer deposition onto OECT substrates and OECT testing were carried out in collaboration with Dr Achilleas Savva during a research visit at King Abdullah University of Science and Technology.

2.2 Introduction

Thiophene rings are one of the most commonly encountered aromatic building blocks for the synthesis of p-type conjugated polymers, with notable examples making use of such moieties including **P3HT**, **pBTTT-C14**, and **PC12TV12T**.[32,160–164] The widespread adoption of thiophene-based units in conjugated polymers can be ascribed due to their: i) electron-rich nature, leading to relatively low ionisation potentials and facilitating injection of holes into their valence band, ii) relatively high degree of planarity, resulting in good intramolecular electronic charge carrier transport, and iii) ability to form highly ordered and crystalline materials, benefiting intermolecular charge carrier transport.[164,165] Given these

favourable properties of thiophene rings, OFETs making use of thiophene-based channel materials have been found to incur good electronic charge carrier mobilities, with hole mobilities of up to 1 $cm^2\ V^{-1}\ s^{-1}$ having been reported.[163,164] The successful translation of polythiophenes' high electrical performances from OFET to OECT applications came in 2016, when a series of conjugated polymers making use of thiophene and benzodithiophene aromatic building blocks was synthesised, see **Figure 2.1**.[151] Of these newly developed materials, the polythiophene **g2T-T**, was found to incur the highest OECT performance, yielding a maximum g_m of 21 mS (W = 100 µm, L = 10 µm, and d = 160 nm), a μC^* of 167 $F\ cm^{-1}\ V^{-1}\ s^{-1}$, and a μ of 0.28 $cm^2\ V^{-1}\ s^{-1}$, thus ranking it as one of the highest performing OECT channel materials to date.[115]

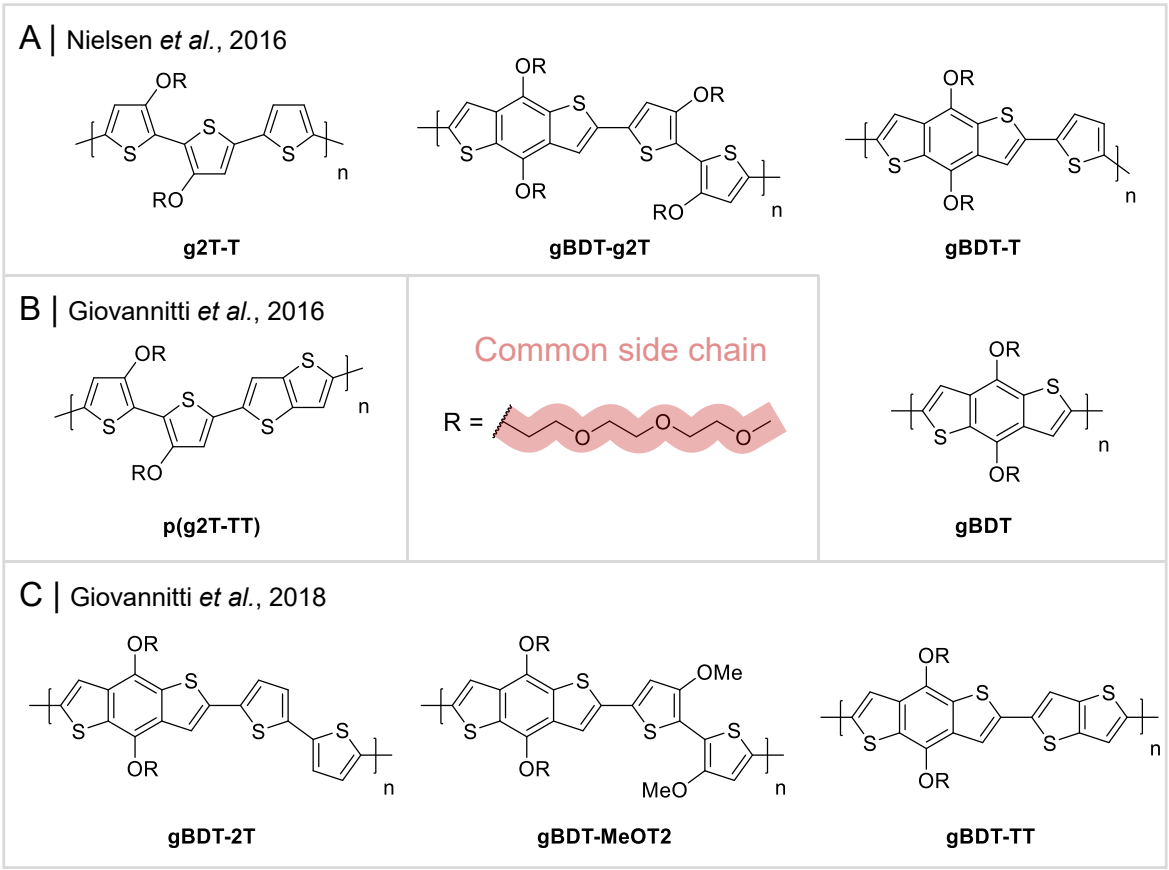

Figure 2.1. *Chemical structures of high-performance p-type EG functionalised conjugated polymers published until 2018, including those published by a) Nielsen et al.,*[151] *b) Giovannitti et al.,*[155] *and c) Giovannitti et al.*[166]

Shortly after this seminal study, two additional investigations on EG functionalised polymer structures were published, whereby the focus in these was to tune the employed aromatic building blocks to improve the polymers' OECT performance, see **Figure 2.1**.[155,166] A notable aspect of each newly developed channel material was that irrespective of the employed aromatic building blocks, all polymers made use of the same triethylene glycol side-chains, with no direct comparison against shorter or longer EG bearing derivatives being made, see **Figure 2.1**.

Side-chain engineering, has however been demonstrated on numerous occasions to be a highly effective strategy to optimise several physical properties of conjugated polymers, including their molecular packing, optical absorption, and charge carrier transport.[167,168] For example, OFET charge carrier mobilities of regioregular poly(3-alkylthiophene)s could be improved by three orders of magnitude by judicious tuning of the employed side-chain length, therefore, resulting in a more favourable thin film microstructure.[169] Similar findings were reported for OPV blends making use of poly(3-alkylthiophene)s as the donor component, with space-charge-limited current (SCLC) analyses demonstrating a 10^2 improvement in the polymers' electronic charge carrier mobilities depending on the employed side-chain length.[170] Here, the use of side-chains with an intermediate length (hexyl) afforded the highest electrical performance by striking the best balance between minimising the intermolecular hopping distance between neighbouring conjugated polymer backbones (increases with increasing alkyl side-chain length) and maximising the fraction of crystalline material present (increases with decreasing alkyl side-chain length). Similarly strong dependencies of the electrical conductivity (σ) on the length of the employed side-chain were also found for polythiophenes functionalised with ethylene glycol (EG) side-chains.[171] In this case, extending the length of the EG side-chain from one to two repeat units was found to significantly increase the solubility of the resulting polymer, therefore

also the molecular weights and conjugation lengths that can be achieved, ultimately boosting σ to values between 500-1000 S cm^{-1}. Side-chain length variation thus affects several properties of the polymers in parallel and can be a highly fruitful strategy to incur polymer derivatives with superior electrical performances.

With the above considerations in mind, this chapter focuses on investigating the effects of varying the EG side-chain length in a series of polythiophene polymers for OECT applications.[172] The conjugated polymer family is based on the previously reported **g2T-T** polymer and includes four materials herein referred to as **p(g*x*T2-T)** (where x = 2, 3, 4, or 6), see **Figure 2.2**. **g2T-T**'s conjugated polymer backbone was selected due to its ability to incur high-performance OECT channel materials.[115,151] Moreover, the lack of any large and fused rings in this conjugated polymer backbone was also envisaged to confer the polymers with sufficient solubility to investigate the effects of both EG chain length shortening and elongation, thereby providing a comprehensive picture of side-chain length engineering for this OMIEC class.

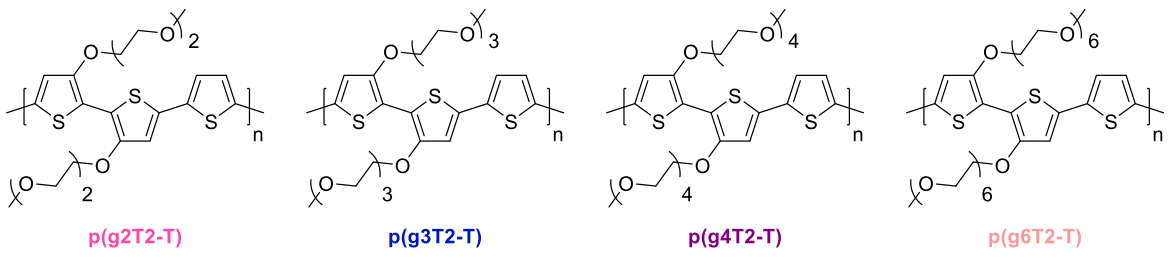

Figure 2.2. *Chemical structures of the synthesised* ***p(gxT2-T)*** *polymer series, where x = 2, 3, 4, or 6.*

2.3 Polymer Synthesis

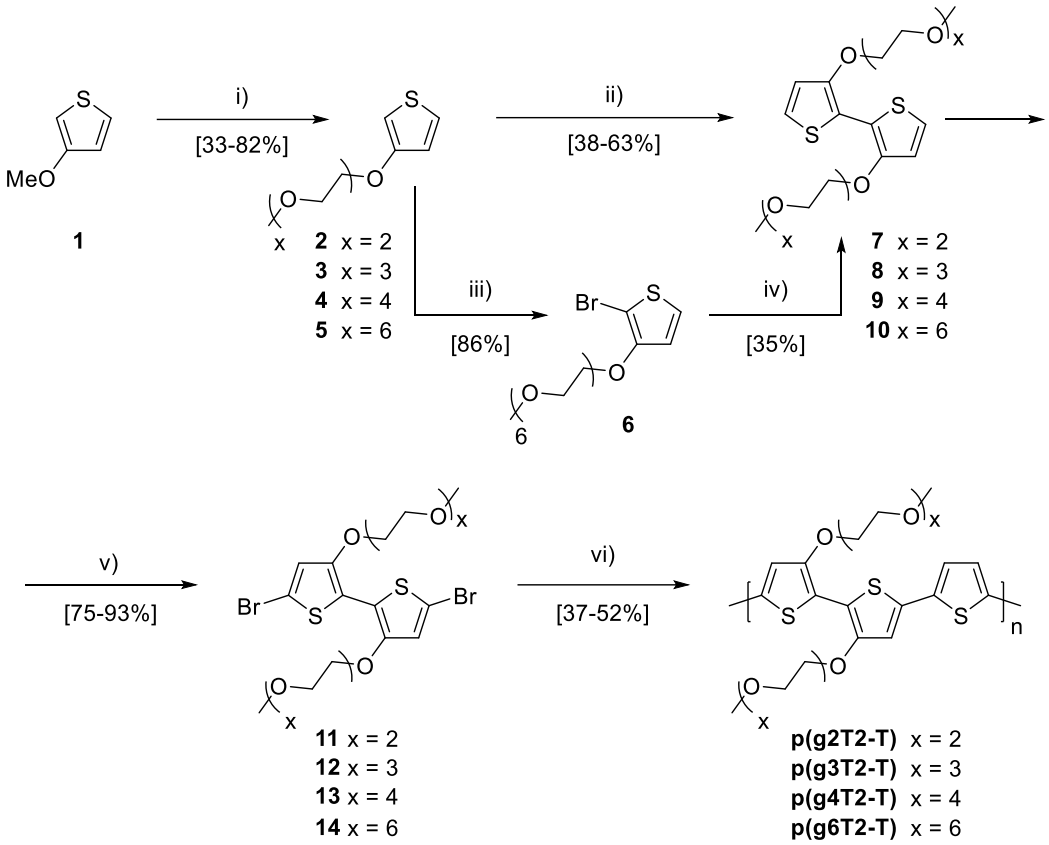

Scheme 2.1. *Synthesis of the* ***p(gxT2-T)*** *polymer series. Reagents and conditions: i) Di-, tri-, tetra-, or hexaethylene glycol monomethyl ether (2.5 equiv.), PTSA (0.1 equiv.), toluene, 110 °C; ii) n-BuLi (1.2 equiv.), $Fe(acac)_3$ (1.0 equiv.), THF, -20 °C then 65 °C; iii) NBS (1.0 equiv.), THF, -10 °C; iv) $Ni(COD)_2$ (1.5 equiv.), COD (1.0 equiv.), BPy (1.5 equiv.), DMF, toluene, 80 °C; v) NBS (2.1 equiv.), THF, -20 °C; vi) 2,5-bis(trimethylstannyl)thiophene (1.0 equiv.), Pd_2dba_3 (2 mol%), $P(o\text{-}OMePh)_3$ (8 mol%), toluene, 110 °C.*

The chemical structures of the synthesised polymer series are shown in **Figure 2.2** and their synthesis in **Scheme 2.1**. Given the commercial availability of the monomethyl ether derivatives of di-, tri-, and tetraethylene glycol, the first step towards the synthesis of **p(g2T2-T)**, **p(g3T2-T)**, and **p(g4T2-T)** involved functionalisation of the thiophene ring at the 3-position with the corresponding EG monomethyl ether chain. In the case of **p(g6T2-T)**, whose hexaethylene glycol monomethyl ether side-chain is not commercially available,

it was necessary to first synthesise the appropriate EG side-chain, see **Appendix Section 8.1.1**. In brief, this involved tosylation of diethylene glycol monomethyl ether followed by a nucleophilic substitution (S_N) reaction with tetraethylene glycol.

When using alcohol terminated side-chains, as in the case of EG-based chains, a common way for installing the side-chains on the 3-position of the thiophene ring is through an Ullmann-type reaction of 3-bromothiophene with the desired alcohol functionalised side-chain.[151,173,174] Although this type of reaction can proceed in satisfactory yields, typical drawbacks include the necessity of a relatively high catalyst loading (10-20 mol%), the requirement of segregating the generated copper-based waste from the organic waste streams, and the formation of emulsions during the reaction workup, thereby complicating the isolation of the target compound. As a result, the typically employed 3-bromothiophene starting material was replaced with 3-methoxythiophene thus allowing for the formation of intermediates **2-5** through an acid-catalysed transetherification reaction.[175–177] Compounds **2-5** were obtained in yields between 33-82% with reaction yields decreasing almost linearly upon increasing the length of the employed EG side-chain. A potential explanation for the reduced yields of the intermediates functionalised with the longer EG side-chains might be due to each EG repeat unit being able to bind to approximately 2.5 molecules of water, causing the longer EG monomethyl ether starting materials to bind to increasingly more water molecules per EG monomethyl ether molecule.[178,179] The excess water molecules bound to the EG monomethyl ether starting materials may then react analogously as to the alkoxide chains with 3-methoxythiophene, thereby leading to the increased formation of undesirable side products.

Next, bithiophenes **7-9** were synthesised through selective lithiation of the 2-position of intermediates **2-4** with *n*-BuLi at -20 °C, followed by oxidative coupling employing iron(III) acetylacetonate. Reaction yields between 38-63% were obtained and are on par with those

reported in the literature for related compounds.[151,180] Attempts at forming the hexaethylene glycol functionalised dimerised product, **10**, by the same procedure as for the shorter EG side-chain derivatives proved to be unsuccessful. It is speculated that the longer, more hydrophilic hexaethylene glycol side-chains render complete water removal from this compound more challenging, thereby interfering with the lithiation of compound **5**, which necessitates anhydrous conditions. **10** was instead obtained by bromination of the 2-position of **5** with *N*-bromosuccinimide (NBS) at -10 °C to give **6**, followed by a nickel-mediated homocoupling of **6**.[155,181] The last step of the monomers' synthesis involved bromination of the 5,5'-positions of **7-10** with NBS at -20 °C, whereby the dibromide monomers **11-14** were obtained in good yields between 74-93%. Ultimately, the **p(g*x*T2-T)** polymers were obtained by Stille cross-coupling polymerisation of the various EG functionalised bithiophene dibromide monomers **11-14** with 2,5-bis(trimethylstannyl)thiophene.

2.4 Polymer Characterisation

As anticipated, due to the significant variation in the side-chain length of the polymers, the polymers displayed markedly different solubilities. Specifically, this resulted in **p(g2T2-T)** being on the cusp of solubility in chloroform, **p(g3T2-T)** being readily soluble in chloroform, **p(g4T2-T)** dissolving in both chloroform and hot ethyl acetate, and **p(g6T2-T)** being soluble in a range of organic solvents including chloroform, ethyl acetate, acetone, and methanol.

The polymers' number average molecular weight (M_n) and dispersity ($Đ$) were measured by gel permeation chromatography (GPC) against a narrow set of polystyrene standards and employing chloroform as the eluent at 40 °C. Comparable molecular weights were obtained for the polymers (M_n = 11-28 kDa), see **Table 2.1**.

2.4.1 Electrochemical Properties

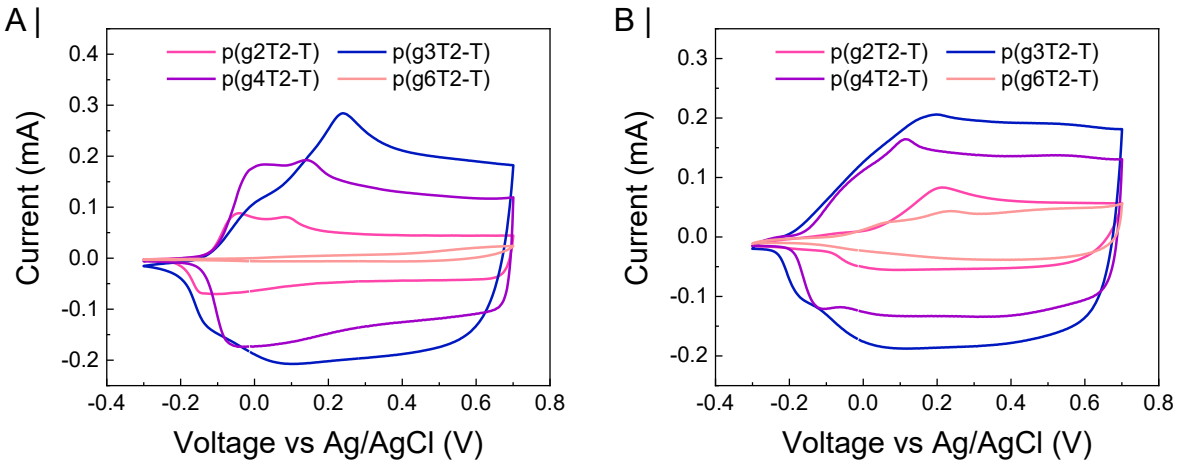

Figure 2.3. *Cyclic voltammograms recorded for the* ***p(gxT2-T)*** *polymer series employing either a) an organic (0.1 M TBA PF_6 in acetonitrile) or b) an aqueous (0.1 M NaCl in distilled water) supporting electrolyte.*

The electrochemical properties of the polymers were evaluated by cyclic voltammetry (CV), see **Figure 2.3**, employing both an organic and an aqueous supporting electrolyte, specifically a 0.1 M solution of tetrabutylammonium hexafluorophosphate in acetonitrile and a 0.1 M solution of sodium chloride in distilled water, respectively. The polymers' onsets of oxidation in organic media ($E_{ox,org}$) were found to occur around -0.07 V vs Ag/AgCl with a variation of ±0.05 V identified across the polymer series. The ionisation potentials (*IP*) of the polymers were subsequently calculated according to **Equation 2.1**.[182]

$$IP\ (eV) = \left(5.1 + E_{ox,org} - E_{Fc/Fc^+}\right) \qquad \textbf{Equation 2.1}$$

where E_{Fc/Fc^+} is the half-wave potential of the ferrocene/ferrocenium couple in a 0.1 M solution of tetrabutylammonium hexafluorophosphate in acetonitrile.

IP values for the polymers were calculated to lie between 4.54-4.64 eV, see **Table 2.1**, highlighting that EG side-chain length alteration does not strongly impact the energy levels

of the polymers. These findings were supported by the polymers' similar onset of oxidation in aqueous media ($E_{ox,aq}$), see **Figure 2.3** and **Table 2.1**, which were also found to lie within a narrow potential range between -0.19 V and -0.06 V. Given the presence of both anodic and cathodic peaks in the polymers' aqueous CV traces, it also followed that each of the four derivatives can be oxidised and reduced reversibly in water, therefore highlighting their suitability as OECT channel materials. The presence of two anodic peaks on the other hand pointed towards the successive oxidation of first the aggregated or crystalline domains of the polymers, featuring longer conjugation lengths, and subsequently their disordered or amorphous regions, which are composed of shorter conjugated polymer sections.[183,184]

Table 2.1. *Summary of the polymers' molecular weight and optoelectronic properties.*

Polymer	M_n (kDa)	$Đ$	$E_{ox,org}$ (V vs Ag/AgCl)[a]	IP (eV)	$E_{ox,aq}$ (V vs Ag/AgCl)[b]	$\lambda_{max,film}$ (nm)[c]	$E_{g,opt}$ (eV)[c,d]
p(g2T2-T)	11.4	1.3	-0.12	4.54	-0.13	614, 658	1.67
p(g3T2-T)	22.6	2.0	-0.12	4.54	-0.19	601, 652	1.69
p(g4T2-T)	28.0	2.5	-0.10	4.56	-0.16	611, 655	1.69
p(g6T2-T)	12.5	2.1	-0.02	4.64	-0.06	600, 646	1.68

[a]Recorded employing a 0.1 M solution of TBA PF_6 in acetonitrile as the supporting electrolyte. [b]Recorded employing a 0.1 M solution of NaCl in distilled water as the supporting electrolyte. [c]Determined while applying a dedoping bias of -0.2 V. [d]Calculated from the onset of absorption in thin film.

From **Figure 2.3** it also follows that in comparison to **p(g3T2-T)**, increasing or decreasing the length of the polymers' pendant side-chains decreased the maximum anodic current recorded in one CV cycle, with the maximum anodic current decreasing in the following order **p(g3T2-T)** > **p(g4T2-T)** > **p(g2T2-T)** ~ **p(g6T2-T)**. This trend was unexpected considering the polymers' electroactive mass percentages, *i.e.* the mass of the polymers'

conjugated backbone relative to the mass of the whole polymer, which were calculated to be 50%, 43%, 37%, and 29% for **p(g2T2-T)**, **p(g3T2-T)**, **p(g4T2-T)**, and **p(g6T2-T)**, respectively. **p(g2T2-T)** was however originally envisaged to incur the highest amount of charge passed across one electrochemical charging cycle given its higher electroactive mass percentage. A potential cause for **p(g2T2-T)**'s lower than anticipated ability to store electronic charges may be due to its short side-chains significantly increasing its tendency to aggregate, rendering it insoluble in virtually every processing solvent and therefore perhaps also less permeable to charge compensating counterions. Increasing the EG side-chain length by one repeat unit, as in the case of **p(g3T2-T)** on the other hand instilled sufficient ionic permeability and counterion storage capacity, thus allowing **p(g3T2-T)** to store the highest amount of charge across the polymer series. Conversely, further lengthening of the pendant EG side-chains led to a dilution of the polymers' electroactive fraction without any beneficial gains in terms of ion permeability or storage properties, hence resulting in a reduced current. Careful balancing in the employed EG side-chain length is therefore required to maximise the polymers' electrical charging abilities in the design of OMIECs for OECT applications.

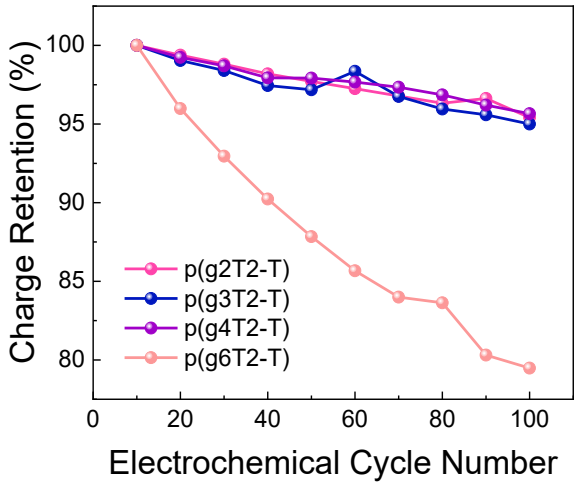

Figure 2.4. *Charge retention of the* ***p(gxT2-T)*** *polymer series as a function of electrochemical cycle number upon repeated CV addressing in a 0.1 M aqueous NaCl supporting electrolyte.*

Repeated CV scans in an aqueous electrolyte were utilised as a preliminary tool to evaluate the polymers' electrochemical stability and simulate the conditions encountered during OECT operation, see **Figure 2.4**. Throughout these measurements, each member of the **p(g*x*T2-T)** polymer series was subjected to 100 electrochemical charging/discharging cycles across a -0.5 V to +0.8 V voltage range. After 100 doping/dedoping cycles, **p(g2T2-T)**, **p(g3T2-T)**, and **p(g4T2-T)** were found to retain more than 95% of the initial charge passed, whereby the good electrochemical cycling stability of these polymers indicated their suitability as OECT channel materials. In contrast, **p(g6T2-T)** was found to incur the lowest electrochemical stability, retaining only ~ 80% of its initial passed charge. Given the similar *IP* values recorded for the polymers, **p(g6T2-T)**'s lower stability was not attributed to any energetic effect, but instead due to its longer EG side-chains. These are known to lead to increased polymer swelling and deswelling upon repeated electrochemical addressing, hence explaining the partial delamination of the polymer from the conductive substrate during successive electrochemical addressing.[185]

2.4.2 Optical Properties

The optical properties of the polymers in thin film were evaluated through UV-Vis absorption spectroscopy, see **Figure 2.5**. Given the polymers' low *IP*, the polymers had a tendency to spontaneously oxidise under ambient conditions, thus requiring the application of a negative bias to fully dedope the polymer films. Consequently, the polymers' absorption spectra given in **Figure 2.5** are those in their fully dedoped state. As demonstrated in **Figure 2.5**, the four polymers incurred similar absorption profiles in their fully discharged forms, with all polymers exhibiting two maximum absorption peaks, one centred around 600 nm and one around 650 nm. These were in turn ascribed to the polymers' 0-1 and 0-0 transitions, respectively. The polymers' optical gaps ($E_{g,opt}$) were recorded from their onset of absorption

in thin film. Similar ($E_{g,opt}$) values between 1.67-1.69 eV were found for the **p(g*x*T2-T)** polymer series, further confirming the similar optical and energetic properties of the four polymers. Although the optical signatures of the various polymers shared many commonalities, one difference between them was the relative intensity of the 0-0 and 0-1 transitions, which in turn can provide insights into the solid state ordering of the polymers.[186,187] Specifically, while the 0-0 and 0-1 transitions in **p(g2T2-T)**, **p(g3T2-T)**, and **p(g4T2-T)** were of similar intensity, the low energy 0-0 transition in **p(g6T2-T)** was considerably less well resolved and weaker in intensity, in turn suggesting a lower degree of order in the solid state of **p(g6T2-T)** relative to the other polymers.

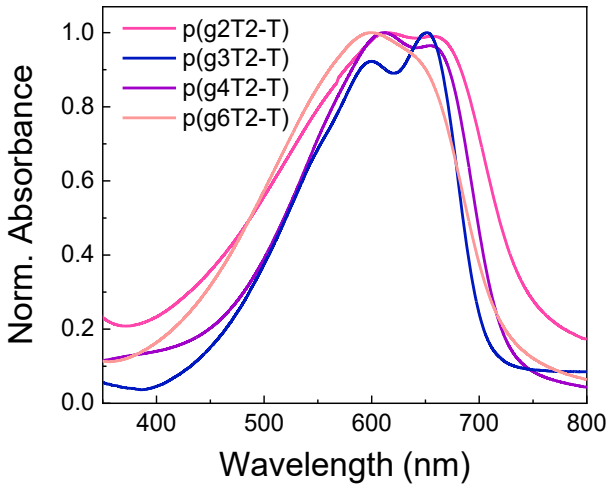

Figure 2.5. *Normalised thin film UV-Vis absorption spectra recorded for the* ***p(gxT2-T)*** *series while applying a dedoping potential of -0.2 V.*

Spectroelectrochemical measurements were conducted to investigate the doping process of the polymers in an aqueous environment. This involved the casting of polymer films onto indium tin oxide (ITO) functionalised glass substrates followed by the application of electrical biases while recording the polymers' UV-Vis absorption profiles, see **Figure 2.6**. As highlighted in **Figure 2.6**, each polymer required the application of a negative bias to fully discharge the polymer, therefore, indicating that under ambient conditions the polymer

films are partially oxidised. Following the complete dedoping of the polymer films, the applied potential was incremented from -0.2 V to +0.4 V in 0.1 V potential steps, resulting in a progressive depression of the polymers' π-π* absorption feature centred around 625 nm and the concomitant appearance of a new absorption band with a maximum absorption wavelength around 900 nm. This lower energy feature was ascribed to the formation of charged polymer species, in particular the polymers' polaron.[188,189] Further increases in the applied bias from +0.4 V to +0.8 V on the other hand led to a depression of the polymers' π-π* and polaronic absorption bands and the emergence of an even lower energy absorption feature, which in turn was attributed to the polymers' doubly charged bipolaronic state.[188,189]

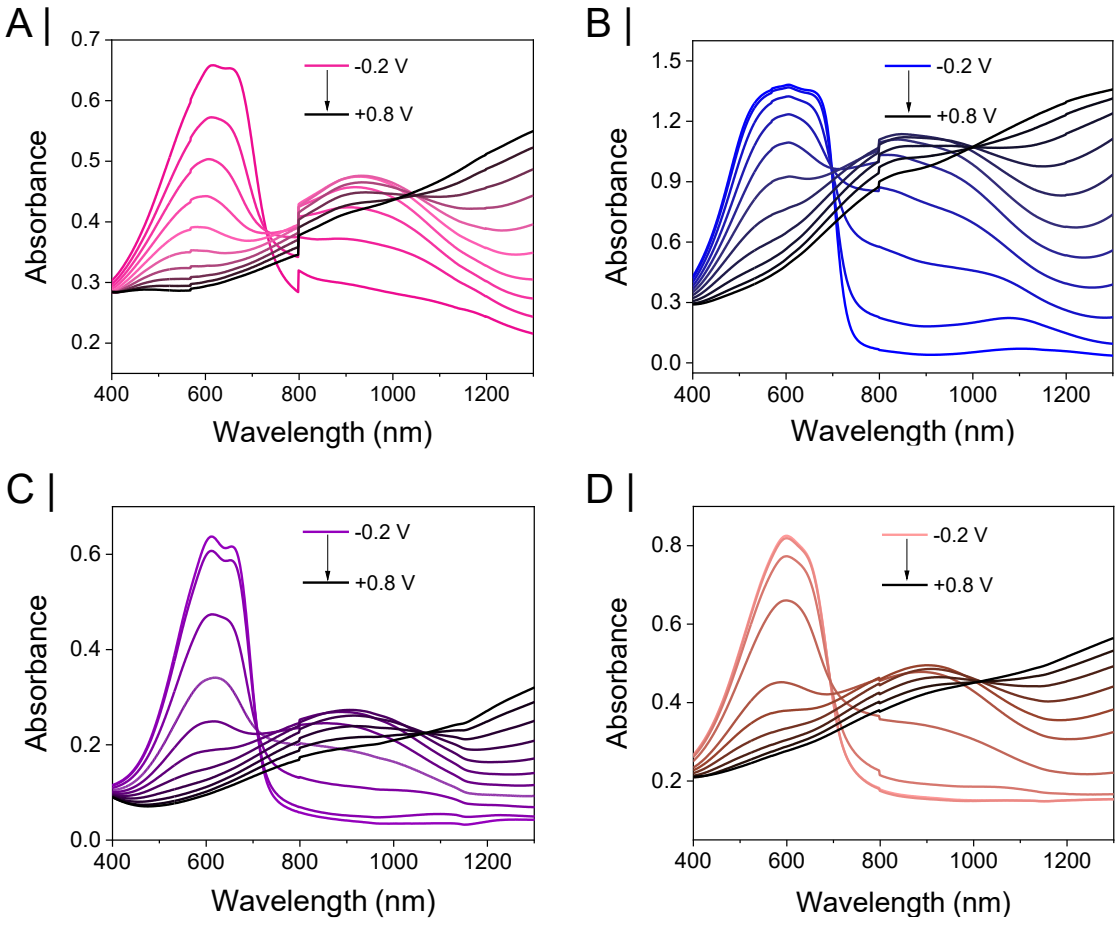

Figure 2.6. *Optical absorption profiles of a)* ***p(g2T2-T)****, b)* ***p(g3T2-T)****, c)* ***p(g4T2-T)****, and d)* ***p(g6T2-T)*** *in a 0.1 M aqueous NaCl supporting electrolyte upon the application of external applied potentials (between -0.2 V and +0.8 V, in increments of 0.1 V).*

As evidenced in **Figure 2.7**, the change in the polymers' optical absorption properties upon electrochemical doping could also be viewed clearly by the naked eye. Specifically, in the dedoped state, the polymers' π-π* absorption band around 625 nm caused polymer films to have a dark blue appearance. Conversely quenching of this absorption feature by electrochemical addressing resulted in virtually colourless polymer films, as evidenced in **Figure 2.7**.

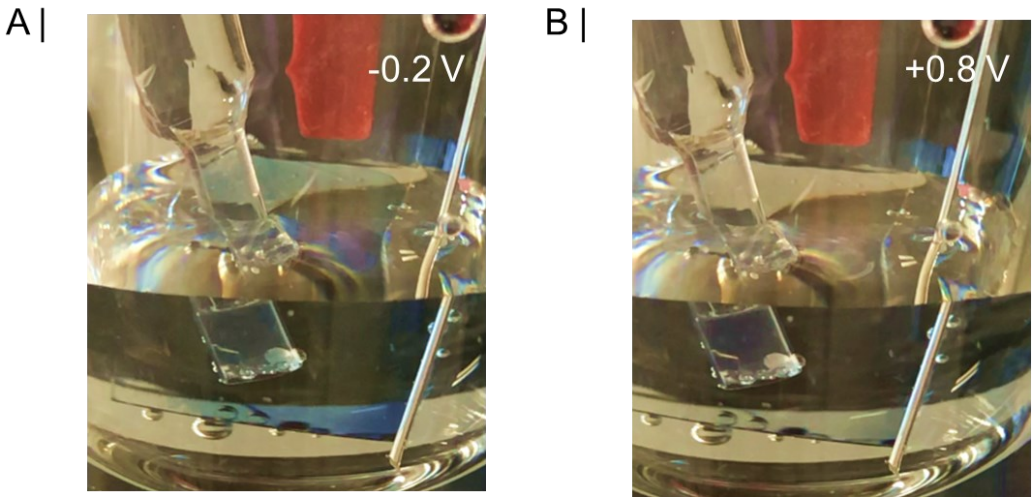

Figure 2.7*. Colour of* ***p(g3T2-T)*** *polymer films in a) their fully dedoped state at -0.2 V (blue) and b) in their doped stated at +0.8 V (colourless).*

2.4.3 Morphological Properties

The structural properties of the polymers **p(g3T2-T)**, **p(g4T2-T)**, and **p(g6T2-T)** were evaluated by grazing incidence wide-angle X-ray scattering (GIWAXS) of as-cast films, with their scattering patterns reported in **Figure 2.8**. Due to the limited solubility of **p(g2T2-T)**, homogeneous films for GIWAXS experiments could not be prepared, therefore excluding this polymer from any additional analyses. As shown in **Figure 2.8**, both **p(g3T2-T)** and **p(g4T2-T)** displayed a strong (010) scattering peak in the out-of-plane (q_z) direction arising from π-π stacking within the polymer crystallites. Similar d-spacings around 3.55 Å

were calculated for this scattering feature for both polymers and were of similar magnitude as those reported for alternative EG functionalised polythiophenes.[151,155] Notably, this peak was absent in the scattering pattern recorded for **p(g6T2-T)**, therefore indicating its reduced molecular order in the solid state and confirming the findings from thin film UV-Vis absorption spectroscopy. Whereas **p(g4T2-T)** only displayed a (010) scattering peak in the out-of-plane direction, **p(g3T2-T)** also featured one of comparable intensity in the in-plane (q_{xy}) direction. Consequently, while **p(g4T2-T)** solely assumes a face-on orientation on the substrate, **p(g3T2-T)** adopts a mixed face-on/edge-on orientation, which may be beneficial in terms of three-dimensional electronic charge carrier transport as required in OECTs. **p(g4T2-T)**'s tendency to solely orient in a face-on orientation was in turn related to its higher solubility in the processing solvent compared to **p(g3T2-T)**, a feature which was previously reported to favour the orientation of conjugated polymers in a face-on manner onto substrates.[190–192]

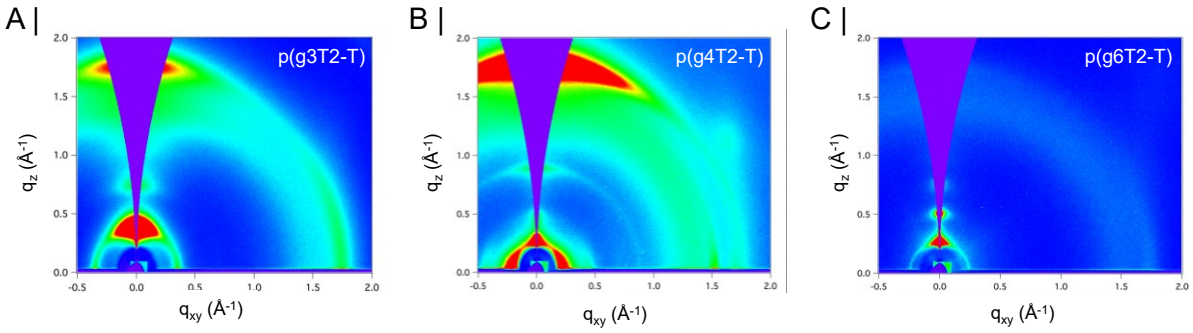

Figure 2.8. *Grazing incidence wide-angle X-ray scattering patterns recorded for as-cast films of* ***p(g3T2-T)****,* ***p(g4T2-T)****, and* ***p(g6T2-T)****.*

In conjunction with the (010) scattering peaks, all three polymers also exhibited two clear orders of lamellar scattering in the out-of-plane direction, (100) and (200), highlighting the

formation of ordered structures also in the polymers' side-chains. Lamellar d-spacings were calculated from the (100) scattering peak of the various polymers yielding values of 16.3 Å, 24.4 Å, and 23.8 Å for **p(g3T2-T)**, **p(g4T2-T)**, and **p(g6T2-T)**, respectively, whereby the values obtained for **p(g3T2-T)** were in line with those reported previously.[151] Therefore, while increasing the polymers' side-chain length from three to four EG repeat units had a substantial impact on the lamellar spacing, this was not the case upon further extending the polymers' side-chain length. This may arise from the potential interdigitation of the side-chains in **p(g6T2-T)** or alternatively due to their increased coiling.

A limitation of the above morphological analyses is that all of the polymers' GIWAXS scattering profiles were collected in the polymers' dry, as-cast forms, thus not taking into consideration the effect of any water molecules or ionic species that may be present within the polymer films under OECT operating conditions. While exposure to water and ions in the absence of an applied electrochemical bias was found to not have a significant effect on the scattering patterns of related EG functionalised polythiophenes, application of a doping bias during electrolyte exposure was found to permanently alter the polymers' lamellar and π-π stacking distances.[118,193] Care must therefore be taken when employing the above GIWAXS analyses to rationalise any device data.

2.4.4 Computational Simulations

Following the evaluation of the polymers' electrochemical and morphological properties, **p(g3T2-T)** and **p(g4T2-T)** appeared to be the most suited as OECT channel materials, given their ability to pass the highest amount of charge during one electrochemical doping-dedoping cycle and their tendency to incur more ordered microstructures. **p(g3T2-T)**'s and **p(g4T2-T)**'s structural properties were hence also assessed through molecular dynamics

(MD) simulations. As is common in the field, **p(g3T2-T)**'s and **p(g4T2-T)**'s polymeric structures were simplified to shorter chain oligomers, thereby minimising computational costs.[194,195] Specifically, this involved reducing the length of **p(g3T2-T)**'s and **p(g4T2-T)**'s conjugated polymer chain lengths to four repeat units (12 thiophene rings), a size that is sufficiently long to correctly describe the polymeric nature of the materials without paying excessive computational costs. Prior to conducting MD simulations, density functional theory (DFT) calculations were performed to optimise the oligomers' geometries, including their bond angles and bond lengths. 64 individual oligomer chains were subsequently placed in the chosen simulation box and equilibrated at 1 atm and 300 K. The MD results are shown in **Figure 2.9**.

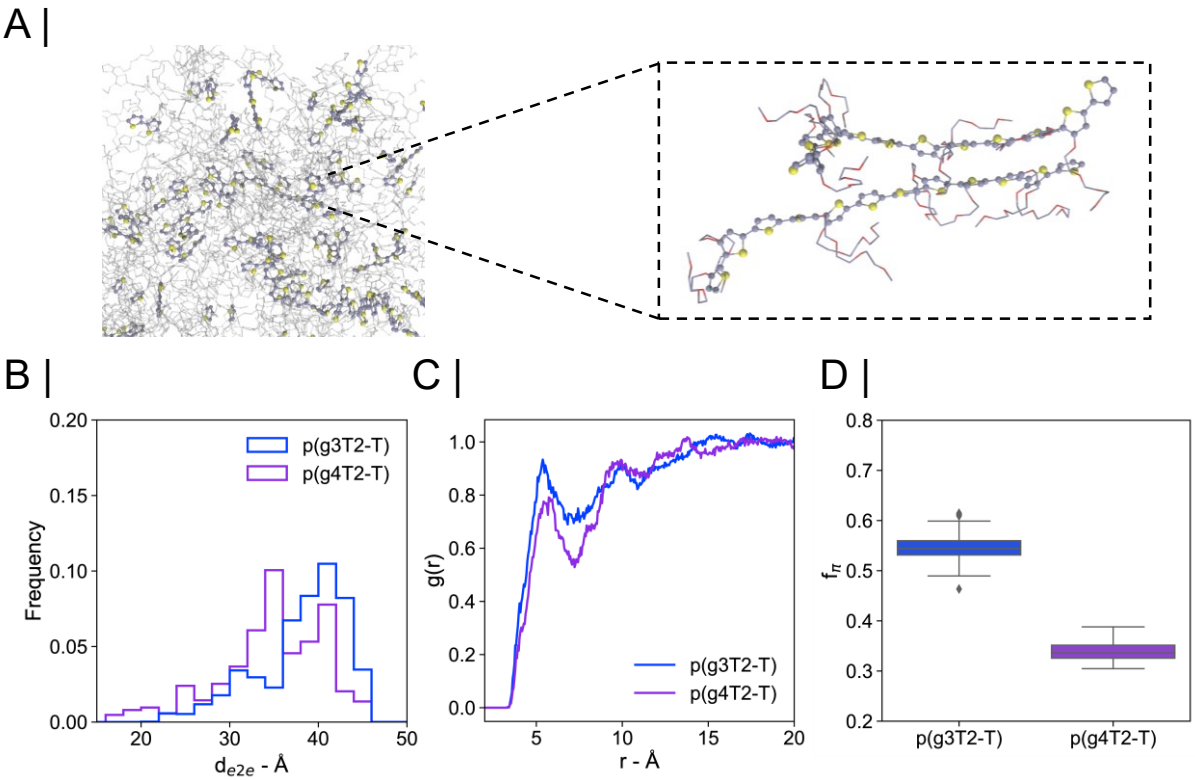

Figure 2.9. *a) MD snapshot highlighting a section of* ***p(g3T2-T)****'s simulation box and the π-π stacking interaction between two* ***p(g3T2-T)*** *oligomers. b) Histogram of the end-to-end distances (d_{e2e}) calculated for* ***p(g3T2-T)*** *and* ***p(g4T2-T)****. c) Radial distribution functions obtained for* ***p(g3T2-T)*** *and* ***p(g4T2-T)****. d) Calculated fraction of π-π stacking thiophene rings in* ***p(g3T2-T)*** *and* ***p(g4T2-T)****.*

The histograms in **Figure 2.9** depict the end-to-end distances (d_{e2e}) of the conjugated polymer backbone chain ends, which describe the stiffness and planarity of the conjugated backbones.[196] As shown in **Figure 2.9** a longer d_{e2e} was calculated for **p(g3T2-T)** compared to **p(g4T2-T)**, meaning that **p(g4T2-T)**'s conjugated polymer backbone tends to assume more coiled conformations with lower degrees of planarity. This was ascribed to side-chain lengthening leading to an increased tendency for the side-chains to interact with each other, thereby allowing the conjugated polymer backbone to overcome some of the energetic torsional penalties arising from a nonplanar conjugated system and undergo backbone twisting.[197,198] A more twisted conjugated polymer backbone should in turn also lead to reduced intermolecular backbone-backbone interactions, which is well reflected in the radial distribution function (RDF) of the thiophene rings, where the short distance peak around 5 Å is lower in intensity for **p(g4T2-T)** compared to **p(g3T2-T)**. This concept is also reaffirmed in the calculated fraction of π-π stacking thiophene rings in **p(g3T2-T)** and **p(g4T2-T)** oligomers, see **Figure 2.9**. While in **p(g3T2-T)** ~ 55% of all thiophene rings are engaged in intermolecular π-π stacking, only ~ 30% are in **p(g4T2-T)**. Therefore, increasing the EG side-chain length from three to four repeat units, specifically upon going from **p(g3T2-T)** to **p(g4T2-T)** significantly lowers the polymers' short-range order.

2.5 OECT Performance

As evidenced by the electrochemical and spectroelectrochemical measurements, the polymers' ability to be doped stably and reversibly in an aqueous electrolyte made the materials excellent candidates for organic electrochemical transistors. Consequently, OECTs with a channel length (L) of 10 µm, a width (W) of 100 µm, and thickness (d) around 50 nm were fabricated for each polymer following previous literature procedures,[151] with

details surrounding the device fabrication process outlined in Section **6.1.8**. Following device fabrication, polymer films were deposited onto the OECT substrates by spin coating from chloroform solutions. The OECT performance of the polymers was then evaluated by employing a 0.1 M aqueous NaCl solution as the supporting electrolyte and an Ag/AgCl pellet as the gate electrode. Given **p(g6T2-T)**'s significantly higher solubility compared to the remaining members of the **p(g*x*T2-T)** polymer series, delamination issues prevented the successful fabrication of stable OECTs for this polymer.

The polymers' OECT performance, including output, transfer, and transconductance curves are given in **Figure 2.10** and summarised in **Table 2.2**. From **Figure 2.10** it can be seen that all polymers operate in accumulation mode, with the devices turning 'ON' upon the application of a negative gate potential ($V_G < 0$). Specifically, V_{Th} values between -0.18 V and -0.20 V were determined for the three polymers, thus being in line with the aqueous cyclic voltammetry experiments and highlighting that EG side-chain length modification does not appear to have a strong impact on the energetics of the conjugated polymer backbone.

Transconductance values of 0.12 mS (W = 100 µm, L = 10 µm, and d = 46 nm), 3.03 mS (W = 100 µm, L = 10 µm, and d = 63 nm), and 0.88 mS (W = 100 µm, L = 10 µm, and d = 53 nm) were calculated for **p(g2T2-T)**, **p(g3T2-T)**, and **p(g4T2-T)**, respectively, suggesting **p(g3T2-T)** to incur the highest OECT steady-state performance. As the transconductance is however dependent on both a material (μC^*) and device geometry dependent term (Wd/L) a more appropriate figure of merit to compare the OECT performance of different OECT channel materials is the product μC^*.[115] μC^* values of 9 F cm^{-1} V^{-1} s^{-1}, 135 F cm^{-1} V^{-1} s^{-1}, and 54 F cm^{-1} V^{-1} s^{-1} were incurred for **p(g2T2-T)**, **p(g3T2-T)**, and **p(g4T2-T)**,

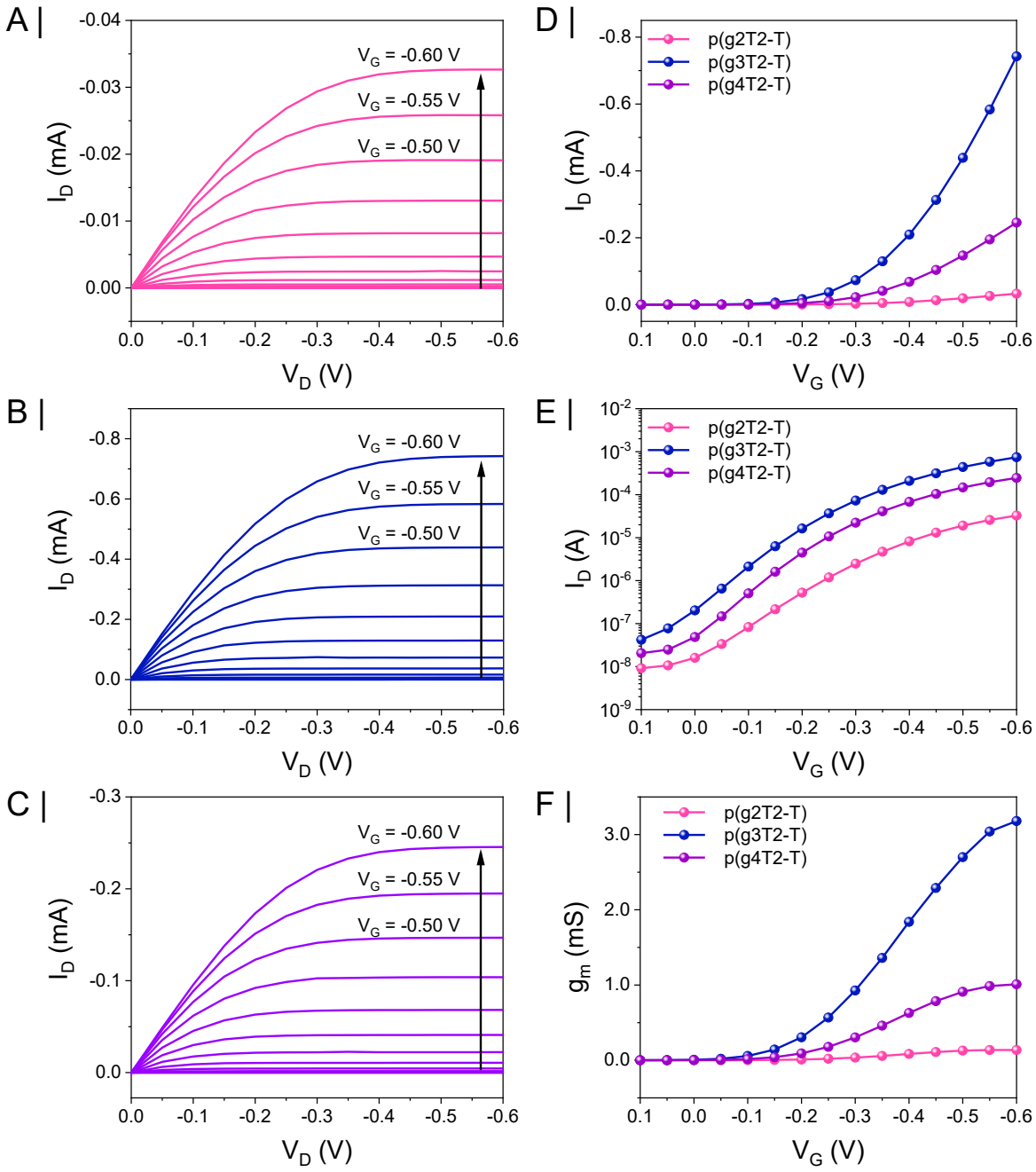

Figure 2.10. *OECT steady-state performance recorded for the* ***p(gxT2-T)*** *polymer series employing an aqueous 0.1 M NaCl solution as the supporting electrolyte. OECT output curves recorded for a)* ***p(g2T2-T)****, b)* ***p(g3T2-T)****, and c)* ***p(g4T2-T)****. Transfer curves plotted on a d) linear and e) logarithmic current scale. f) Recorded transconductance curves.*

Table 2.2. *Summary of the polymers' steady-state OECT performance.*

Polymer	*d* (nm)	V_{Th} (V)	*On/off*	g_m (mS)	μC^* (F cm^{-1} V^{-1} s^{-1})[a]	C^* (F cm^{-3})[b]	μ (cm^2 V^{-1} s^{-1})[c]
p(g2T2-T)	46	-0.20	10^4	0.12	9	8	~ 10^{-4}[†]
p(g3T2-T)	63	-0.18	10^5	3.03	135	190	0.16
p(g4T2-T)	53	-0.19	10^5	0.88	54	157	0.06

[a]Calculated from the slope of g_m as a function of $[(Wd/L)(V_{Th}-V_G)]$. [b]Values determined from electrochemical impedance spectroscopy at the gate voltage incurring the highest g_m. [c]Determined through the impedance matching method, as detailed in previous literature.[89] *[†]Mobility too low to be determined accurately.*

respectively, therefore confirming the performance trend suggested by the polymers' transconductance and reaffirming the superior OECT performance brought by the use of triethylene glycol side-chains. Note that the μC^* value of 135 F cm^{-1} V^{-1} s^{-1} reported for **p(g3T2-T)** was closely in line with the one published previously, thereby further validating the polymers' incurred performance trend.[115]

To obtain a deeper insight into the performance difference across the various polymers, electrochemical impedance spectroscopy (EIS) and impedance matching measurements were conducted on the polymers to assess the polymers' corresponding volumetric capacitance (C^*) and electronic charge carrier mobility (μ). EIS measurements were conducted by depositing OMIECs onto freshly cleaned ITO functionalised glass substrates and recording changes in their impedance magnitude and phase upon the application of an external bias. The low-frequency portion of the impedance spectrum was subsequently fit to Randles circuit, $R_s(R_p||C)$, where R_s is a series resistance, R_p a parallel resistance and C the double-layer capacitance. C^* was then obtained by dividing the calculated C value by the dimensions of the cast polymer film. From **Table 2.2** it can be seen that **p(g3T2-T)** afforded

the highest C^* value of 190 F cm^{-3}, with **p(g2T2-T)** and **p(g4T2-T)** incurring lower ones of 8 F cm^{-3} and 157 F cm^{-3}, respectively. The C^* results therefore closely reflected the aqueous CV findings, which highlighted **p(g3T2-T)** being able to pass the highest amount of charge within one electrochemical doping-dedoping cycle. **p(g4T2-T)**'s inferior C^* value, in comparison to **p(g3T2-T)**, was attributed to its lower electroactive mass percentage, therefore, diluting the fraction of conjugated polymer backbone that is responsible for electronic charge storage. On the other hand, **p(g2T2-T)**'s low C^* value was ascribed to its shortened diethylene glycol side-chains not being able to ensure sufficient ion transport and stabilisation in the polymer film.

The polymers' electronic charge carrier mobilities were estimated according to a previously published impedance matching method.[89] Here, mobilities of ~ 10^{-4} cm^2 V^{-1} s^{-1}, 0.16 cm^2 V^{-1} s^{-1}, and 0.06 cm^2 V^{-1} s^{-1} were recorded for **p(g2T2-T)**, **p(g3T2-T)**, and **p(g4T2-T)**, respectively, highlighting that the superior steady-state performance of **p(g3T2-T)** compared to the other two materials was not only due to its superior charge storage capabilities but also its greater charge carrier mobility. **p(g2T2-T)**'s low μ was postulated to be related to its low charge accumulation properties, thus meaning that only a small fraction of trap states arising from the energetic disorder in the material could be filled during electrochemical doping. On the other hand, **p(g3T2-T)**'s higher μ compared to **p(g4T2-T)** was attributed to the propensity of its crystalline domains to adopt a mixed edge-on and face-on orientation, hence improving three-dimensional charge carrier transport. Moreover, as evidenced from the MD simulations, **p(g3T2-T)** also seemed to benefit from more extended conjugated backbone conformations that not only facilitate intramolecular charge carrier transport but also lead to a higher proportion of π-π stacking thiophene rings, in turn aiding intermolecular charge carrier transport.

2.6 Conclusions and Outlook

In summary, a series of four EG functionalised polythiophenes with pendant EG side-chain lengths ranging between two and six EG repeat units was synthesised through Stille cross-coupling polymerisations and characterised for OECT applications. Electrochemical evaluation of the polymers highlighted each derivative to be able to undergo reversible electrochemical doping in aqueous media, emphasising the suitability of the polymer series as OECT channel materials. Side-chain length engineering was also found not to affect the energetics of the conjugated polymer backbone, resulting in similar onsets of oxidation and ionisation potentials of the polymers. Closer examination of the polymers' CV traces, however, revealed that EG side-chain length engineering strongly affects the amount of current passed within one electrochemical charging-discharging cycle and hence the polymers' volumetric charge storage capabilities, which are required for high-performance OECT channel materials. Specifically, **p(g3T2-T)**, the polymer employing triethylene glycol side-chains was found to pass the highest amount of charge within one CV cycle, thus also resulting in the highest C^* of 190 F cm^{-3} across the polymer series. Both EG side-chain length shortening and lengthening instead proved to be detrimental, with side-chain shortening increasing the polymers' tendency to aggregate and rendering them less permeable to charge-compensating counterions and side-chain lengthening decreasing the polymers' electroactive mass fraction.

Varying the polymers' EG side-chain length also had a significant impact on their morphological properties, with both GIWAXS measurements and MD simulations hinting towards **p(g3T2-T)** possessing the most favourable microstructure to ensure high OECT performances. Specifically, theoretical analyses revealed that the use of triethylene glycol side-chains incurs more planar and rigid conjugated polymer backbones that facilitate both intra- and intermolecular electronic charge carrier transport. Moreover, rather than adopting

a sole face-on orientation, the crystallites in **p(g3T2-T)** were found to assume a mixed edge-on/face-on orientation relative to the substrates, which should again benefit its three-dimensional electronic charge transport properties. Ultimately, the superior performance of **p(g3T2-T)** was confirmed following OECT device fabrication, with **p(g3T2-T)** incurring the highest μC^* of 135 F cm^{-1} V^{-1} s^{-1}.

The results derived from the analyses of the polymers developed within this chapter highlight how EG side-chain length modulation has a direct impact on the polymers' processability, tendency to form ordered structures in thin films, electrochemical charging capabilities, and electronic charge carrier transport abilities, which are factors that directly impact their OECT performance. The outcomes from the above analyses have hence contributed to elucidate valuable structure-property relationships for the design of high-performance OECT materials, which will also pave the way for future optimisation of OECT channel materials and spur further performance enhancements in the field. Moreover, given the requirement of mixed ionic-electronic charge carrier transport also in related organic electronic research areas, such as organic thermoelectrics, supercapacitors, batteries, actuators, and electrochromics, it is anticipated that the conclusions derived from the above study can also aid material design and development within these fields.

'I think the whole scientific community is a superhero.'
— Uğur Şahin

3

EG Side-Chain Redistribution in Polythiophenes to Maximise OECT Performance and Stability

Contents

3.1 General Information and Attributions

Gel permeation chromatography (GPC) experiments were conducted by Dr Raj Sheelamanthula (King Abdullah University of Science and Technology). Electrochemical quartz crystal microbalance with dissipation (eQCM-D) measurements were conducted by Jokubas Surgailis (King Abdullah University of Science and Technology). Grazing incidence wide-angle X-ray scattering (GIWAXS) measurements were performed by Quentin Thiburce (Stanford University) at the Stanford Synchrotron Radiation Lightsource, SLAC National Accelerator Laboratory. OECTs were fabricated by Tania Cecilia Hidalgo (King Abdullah University of Science and Technology). Polymer deposition onto OECT substrates, OECT testing, and EIS measurements were carried out in collaboration with Tania Cecilia Hidalgo during a research visit at King Abdullah University of Science and Technology. Keying Guo, Shofarul Wustoni, and Anil Koklu (all King Abdullah University of Science and Technology) conducted the OECT biosensor fabrication and measurements.

3.2 Introduction

As evidenced from **Chapter 2**, which focused on optimising the EG side-chain length in polythiophene-based OECT channel materials, grafting triethylene glycol side-chains onto the employed bithiophene monomer unit (g3T2) was found to best balance the polymers' ionic and electronic charge carrier transport and maximise the steady-state performance of the resulting OECT devices. The promising nature of the g3T2 building block to realise high-performance OECT channel materials is further highlighted when considering the performance of additional OECT channel materials, which also make use of the g3T2 moiety, see **Figure 3.1**.[151,155,172]

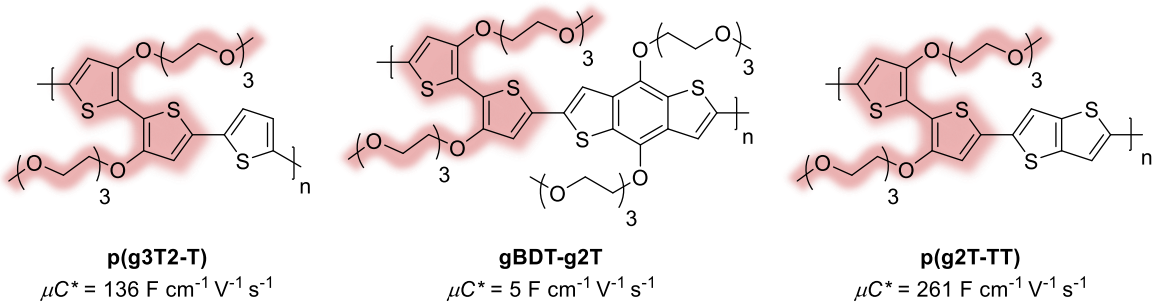

Figure 3.1. *Chemical structures of high-performance OECT channel materials employing the g3T2 unit in their conjugated polymer backbone (highlighted in red) and their respective μC* measured in devices.*

Of the OMIECs presented in **Figure 3.1**, it can be seen that the polymer **p(g2T-TT)** incurs a particularly high OECT steady-state performance (μC^* = 261 F cm^{-1} V^{-1} s^{-1}), ranking it not only as the best performing OECT channel material employing the g3T2 unit but any EG functionalised conjugated polymer.[115,155] Despite **p(g2T-TT)**'s high steady-state OECT performance, **p(g2T-TT)** still demonstrates several drawbacks, including i) a relatively low operational stability, with OECTs based on **p(g2T-TT)** retaining only 75% of their initial drain current ($I_D/I_{D,0}$) after 2 h of repeated electrochemical biasing (~ 700 doping/dedoping cycles), ii) a high dependency of its solubility and processability on its molecular weight, leading to significant batch-to-batch variability, and iii) considerable volumetric swelling during OECT operation in an aqueous 0.1 M NaCl supporting electrolyte, therefore limiting its maximum steady-state performance in devices.[118,155] With these considerations in mind, a new polymer series based on the g3T2 moiety was designed to overcome **p(g2T-TT)**'s limitations in OECTs, see **Figure 3.2**. The starting point of the polymer series was the **p(g3T2)** homopolymer, which had previously been employed for electrochemically triggered actuators and electrodes for charge storage applications.[68,74,75] The EG side-chains in **p(g3T2)** were then progressively 'redistributed' across its conjugated polymer backbone, which involved shortening the EG side-chain length by one repeat unit on one

g3T2 moiety and increasing it by one repeat unit on the successive g3T2 unit, to afford the alternating diethylene-tetraethylene glycol polymer, **p(g2T2-g4T2)**. Further EG side-chain redistribution subsequently afforded the monoethylene-pentaethylene glycol, **p(g1T2-g5T2)**, and the alternating methoxy-hexaethylene glycol, **p(g0T2-g6T2)**, polymers. An average EG side-chain length of three repeat units per thiophene ring was chosen to ensure good polymer solubility. Furthermore, the use of alkoxy substituents on each thiophene ring was also deemed to be a favourable molecular design element, as the lone pair of electrons of the oxygen atom directly conjugated to the aromatic backbone can donate electron density *via* resonance, therefore reducing the polymers' ionisation potential (*IP*) and stabilising the charged polymer species.[111,199–201] Moreover, the added steric bulk from the alkoxy substituents should help to shield the conjugated polymer backbone from interfering chemical species, further improving its stability in devices.[202]

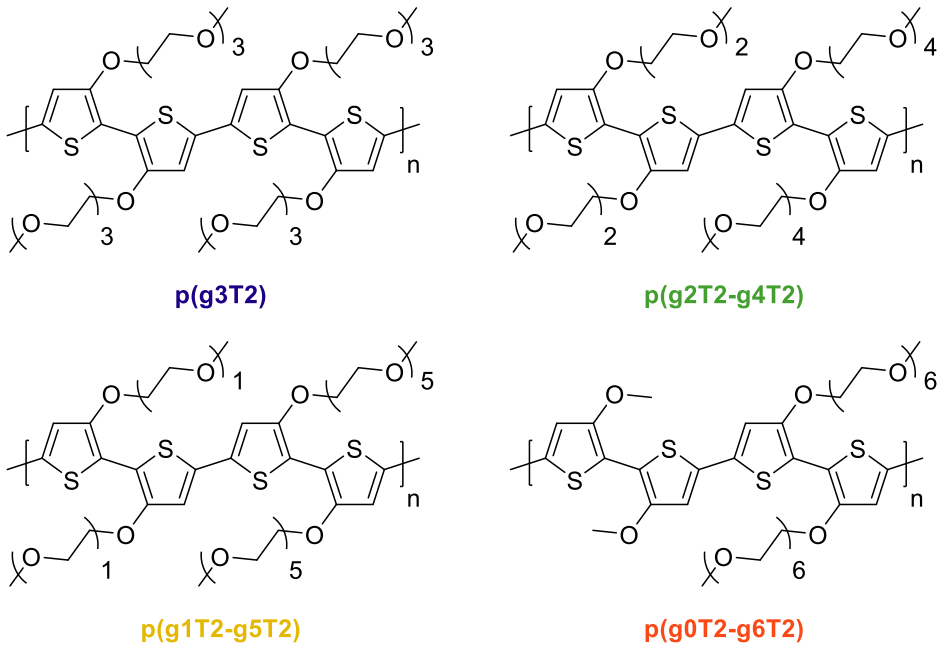

Figure 3.2. *Chemical structures of the developed polymers.*

3.3 Polymer Synthesis

The polymers' syntheses are displayed across **Schemes 3.1-3.4** and share several synthetic intermediates developed for the synthesis of the **p(g*x*T2-T)** polymer series detailed in **Chapter 2**. In short polymer synthesis involved four steps: i) grafting of the corresponding alkoxy side-chain onto the 3-position of the thiophene ring, ii) dimerisation of 3-alkoxythiophene to incur the corresponding 3,3'-bisalkoxy-2,2'-bithiophene, iii) functionalisation of the 3,3'-bisalkoxy-2,2'-bithiophene intermediate into the corresponding dibromide or distannylated monomer, and iv) Stille cross-coupling polymerisation between the various brominated and stannylated monomers.

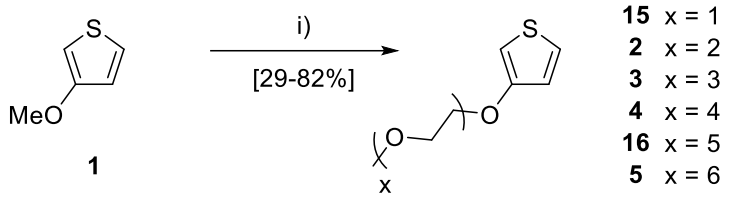

Scheme 3.1. *Acid-catalysed transetherification reaction of 3-methoxythiophene into the various 3-alkoxythiophenes. Reagents and conditions: i) Mono-, di-, tri-, tetra-, penta-, or hexaethylene glycol monomethyl ether (2.5 equiv.), PTSA (0.1 equiv.), toluene, 110 °C.*

The various EG side-chains were installed onto the 3-position of the thiophene ring by an acid catalysed transetherification reaction of 3-methoxythiophene with the respective EG monomethyl ether chains. As the pentaethylene glycol and hexaethylene glycol monomethyl ether side-chains were not commercially available, it was necessary to first synthesise these, see **Appendix Section 8.1.1** and **Section 8.1.2**. Intermediates **2-5**, **15**, and **16** were obtained in yields of 29-82%, with reaction yields decreasing almost linearly upon increasing the length of the employed EG side-chain. A potential explanation for the reduced yields of the intermediates functionalised with the longer EG side-chains might be due to each EG repeat

unit being able to bind to approximately 2.5 molecules of water, causing the longer EG monomethyl ether starting materials to bind to increasingly more water molecules per EG side-chain molecule.[178,179] The excess water molecules bound to the EG monomethyl ether starting materials may then react analogously as to the alkoxide chains with 3-methoxythiophene, thereby leading to the increased formation of undesirable side products.

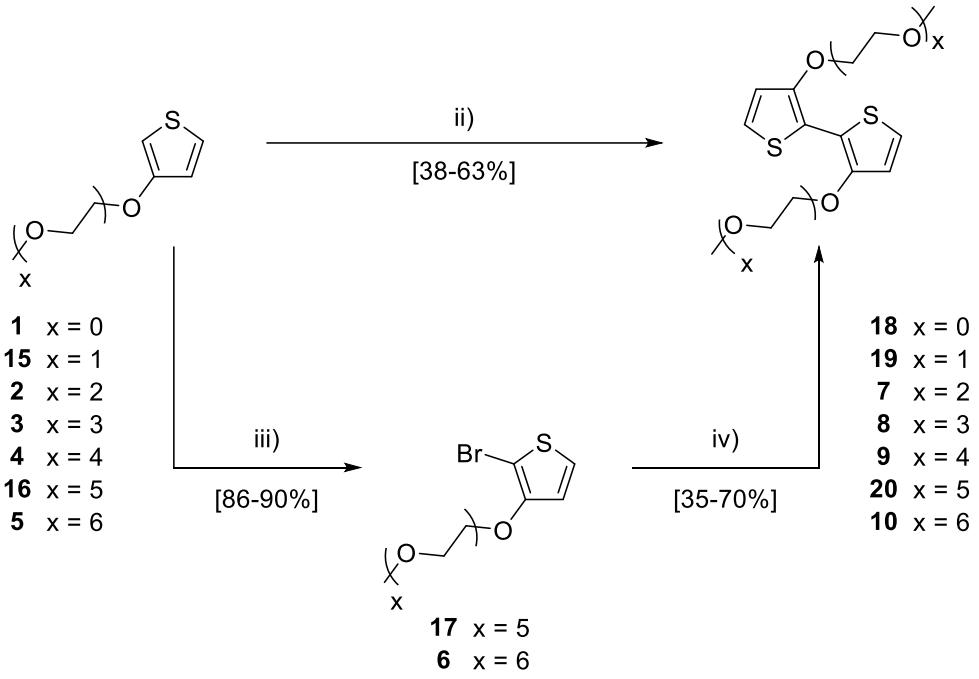

Scheme 3.2. *Synthesis of the 3,3'-bisalkoxy-2,2'-bithiophene intermediates through a) a one-step or b) two-step C–C bond forming reaction. Reagents and conditions: ii) n-BuLi (1.2 equiv.), $Fe(acac)_3$ (1.0 equiv.), THF, -20 °C then 65 °C; iii) NBS (1.0 equiv.), THF, -10 °C; iv) $Ni(COD)_2$ (1.5 equiv.), COD (1.0 equiv.), BPy (1.5 equiv.), DMF, toluene, 80 °C.*

Bithiophene intermediates **7-10** and **18-20** were obtained either through a one or two-step synthesis, see **Scheme 3.2**. The one-step procedure involved selective lithiation at the 2-position of the corresponding 3-alkoxythiophene followed by oxidative homocoupling employing iron (III) acetylacetonate. Intermediates **7-9**, **18**, and **19** could be obtained in reasonable yields between 38-63% by this transformation and are on par with those reported in the literature for related 3,3'-bisalkoxy-2,2'-bithiophene species.[174,203,204] One limitation of the employed reaction conditions was the use of stoichiometric rather than catalytic

quantities of the iron (III) species, leading to higher reagent costs and excessive iron waste generation. The use of oxidants such as di-tert-butyl peroxide (DTBP) has, however, been shown in the literature to be effective at regenerating the catalytically active iron (III) species and allowing iron (III) loadings to be reduced from 100 mol% to 5 mol% without negatively affecting reaction yields.[205] Thus, to minimise reaction costs and improve the carbon footprint of the reaction in future investigations, the use of co-oxidants should be considered.

Biaryls **10** and **20** on the other hand had to be prepared *via* a two-step route involving bromination at the 2-position of thiophenes **5** and **16** to incur compounds **6** and **17** in good yields between 86-90%. **6** and **17** were then subjected to a nickel-promoted dehalogenative dimerisation reaction, yielding biaryls **10** and **20** in reasonable yields between 35-70%, which were on par with those reported in the literature for analogous systems.[155,181]

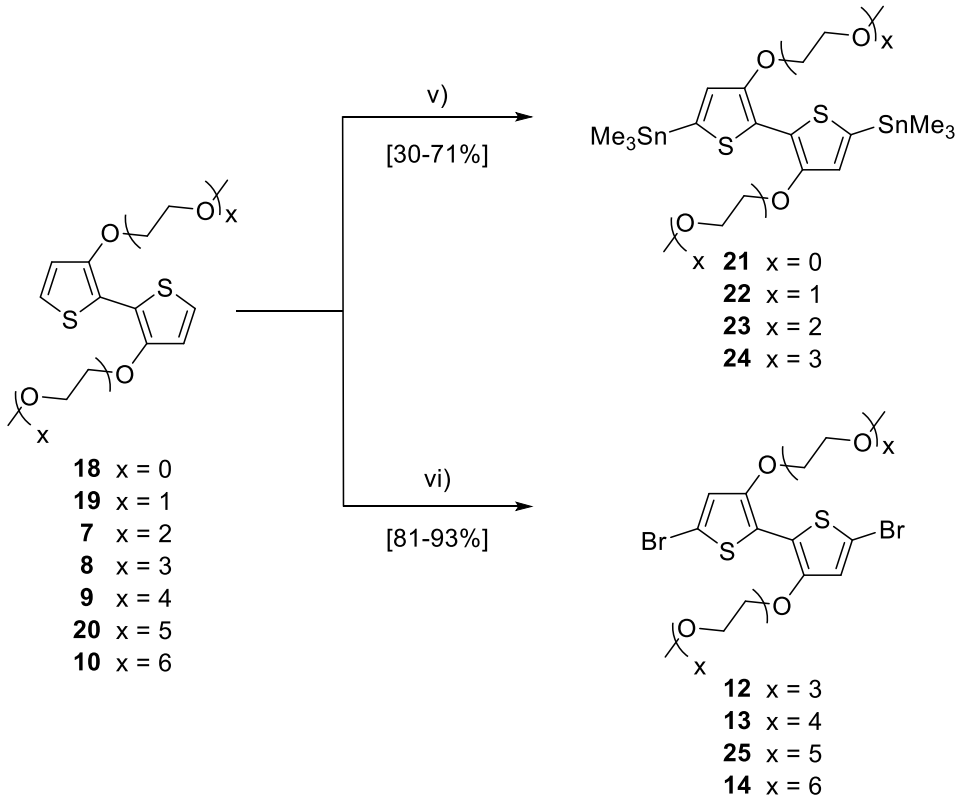

Scheme 3.3. *Synthesis of the brominated and stannylated monomers. Reagents and conditions: v) n-BuLi (4.0 equiv.), Me_3SnCl (4.4 equiv.), THF, -78 °C then RT; vi) NBS (2.1 equiv.), THF, -30 °C.*

Distannylation of bithiophene intermediates **18**, **19**, **7**, and **8** incurred the corresponding organotin monomers **21**, **22**, **23**, and **24** in yields between 30-71%. Dibromide monomers **12**, **13**, **25**, and **14** on the other hand were obtained in good yields between 81-93% by reaction of biaryls **8**, **9**, **20**, and **10** with *N*-bromosuccinimide, respectively. Finally, polymers **p(g3T2)**, **p(g2T2-g4T2)**, **p(g1T2-g5T2)**, and **p(g0T2-g6T2)** were afforded in yields between 71-89% by Stille cross-coupling polymerisation between the various brominated and stannylated monomers, see **Scheme 3.4**.

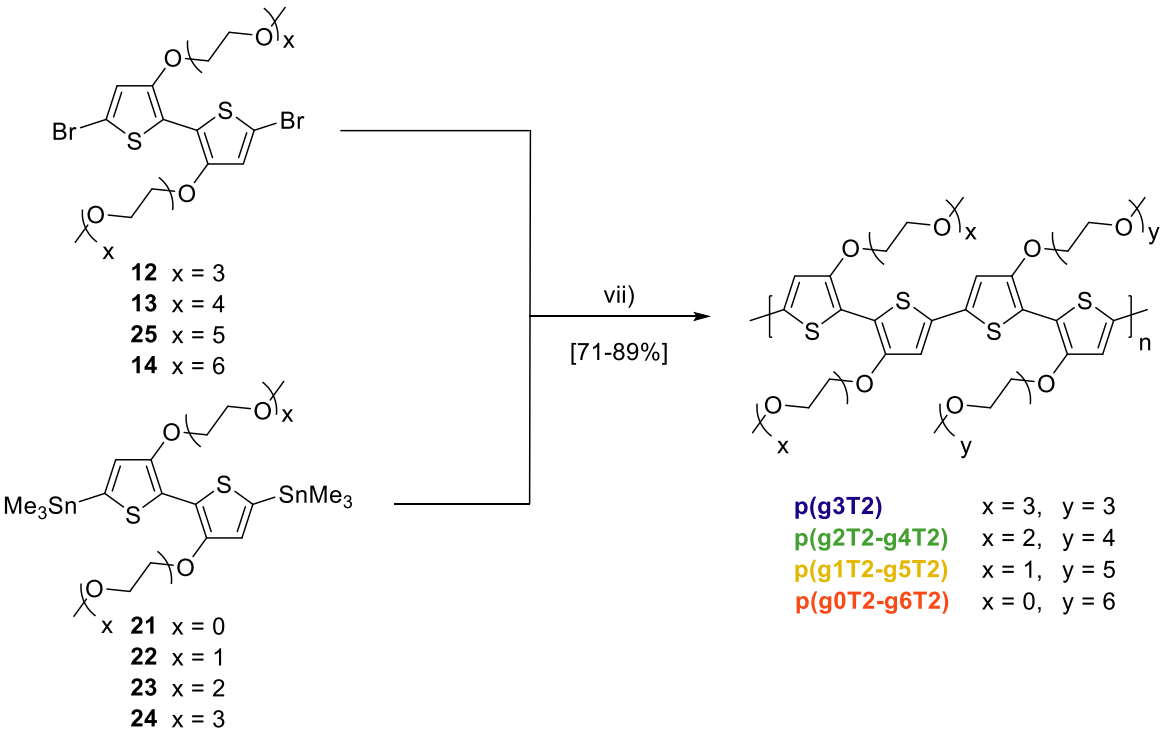

Scheme 3.4. *Synthesis of the polymers* ***p(g3T2)***, ***p(g2T2-g4T2)***, ***p(g1T2-g5T2)***, *and* ***p(g0T2-g6T2)***. *Reagents and conditions: vii)* Pd_2dba_3 *(2 mol%),* $P(o\text{-}OMePh)_3$ *(8 mol%), DMF, 110 °C.*

3.4 Polymer Characterisation

3.4.1 Electrochemical Properties

The polymers' electrochemical properties were characterised by cyclic voltammetry in both an organic (0.1 M tetrabutylammonium hexafluorophosphate in acetonitrile solution) and an aqueous (0.1 M sodium chloride in distilled water solution) supporting electrolyte, see **Figure 3.3**.

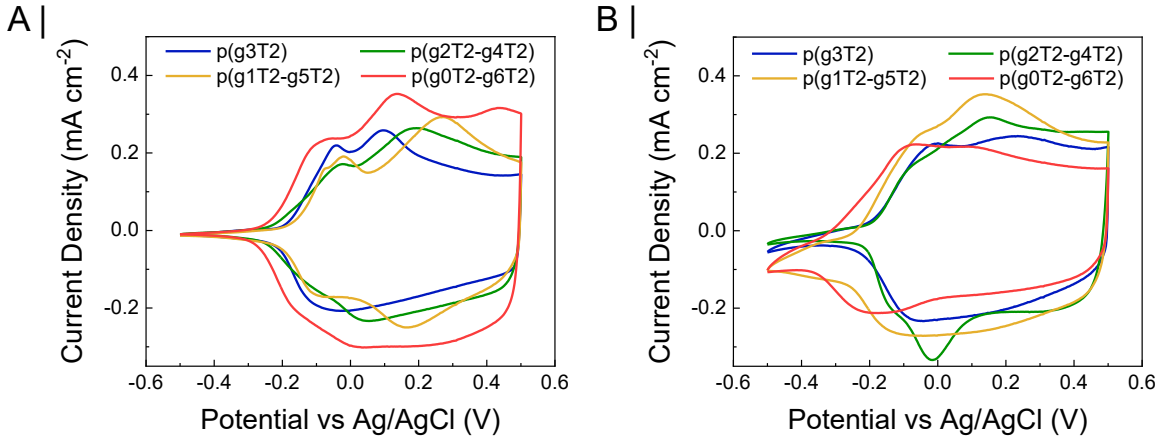

Figure 3.3. *Cyclic voltammograms recorded for* ***p(g3T2)***, ***p(g2T2-g4T2)***, ***p(g1T2-g5T2)***, *and* ***p(g0T2-g6T2)*** *employing a) a 0.1 M TBA PF_6 in acetonitrile solution and b) a 0.1 M NaCl in distilled water solution as the supporting electrolyte.*

As follows from **Figure 3.3**, all polymers featured similar onsets of oxidation in organic media ($E_{ox,org}$) between -0.22 V and -0.17 V, consequently also resulting in virtually unchanged *IP* values between 4.44-4.49 eV across the polymers series, see **Table 3.1**. The negligible impact of EG side-chain redistribution upon the energetics of the conjugated polymer backbone was confirmed by the polymers' onsets of oxidation in aqueous media ($E_{ox,aq}$), again incurring very similar values between -0.31 V and -0.18 V, see **Figure 3.3** and **Table 3.1**. In comparison to **p(g2T-TT)**, the polymers featured an approximately 0.1 eV lower *IP* and a 0.1 V smaller $E_{ox,aq}$, highlighting that the use of an alkoxy substituent at

the 3-position of each thiophene ring was a successful molecular design strategy to increase the electron density on the conjugated polymer backbone.[155]

Table 3.1. *Summary of the polymers' optoelectronic properties.*

Polymer	$E_{ox,org}$ (V vs Ag/AgCl)[a]	*IP* (eV)	$E_{ox,aq}$ (V vs Ag/AgCl)[b]	$\lambda_{max,soln}$ (nm)[c]	$\lambda_{max,film}$ (nm)[d]	$E_{g,opt}$ (eV)[d,e]
p(g3T2)	-0.19	4.47	-0.19	578	641, 698	1.63
p(g2T2-g4T2)	-0.22	4.44	-0.18	581	642, 710	1.63
p(g1T2-g5T2)	-0.17	4.49	-0.23	584	636, 698	1.63
p(g0T2-g6T2)	-0.22	4.44	-0.31	588	654, 704	1.63

[a]*Recorded employing a 0.1 M solution of TBA* PF_6 *in acetonitrile as the supporting electrolyte.* [b]*Recorded employing a 0.1 M solution of NaCl in distilled water as the supporting electrolyte.* [c]*Measured in dilute chloroform solutions.* [d]*Determined while applying a dedoping bias of -0.5 V.* [e]*Calculated from the onset of absorption in thin film.*

The cyclic voltammograms of the polymers in both organic and aqueous electrolytes also highlighted the OMIECs' ability to undergo two oxidation reactions upon application of an external doping bias, thus being in line with the findings reported for the **p(g*x*T2-T)** polymer series developed in **Chapter 2**. Moreover, the presence of cathodic peaks also highlights the reversibility of the doping process, a key attribute for ensuring the stable operation of the polymers in OECTs. These results were further supported by preliminary electrochemical stability measurements of the polymers involving repeated CV addressing, which did not show any significant degree of current degradation upon repeated electrochemical biasing, see **Figure 3.4**.

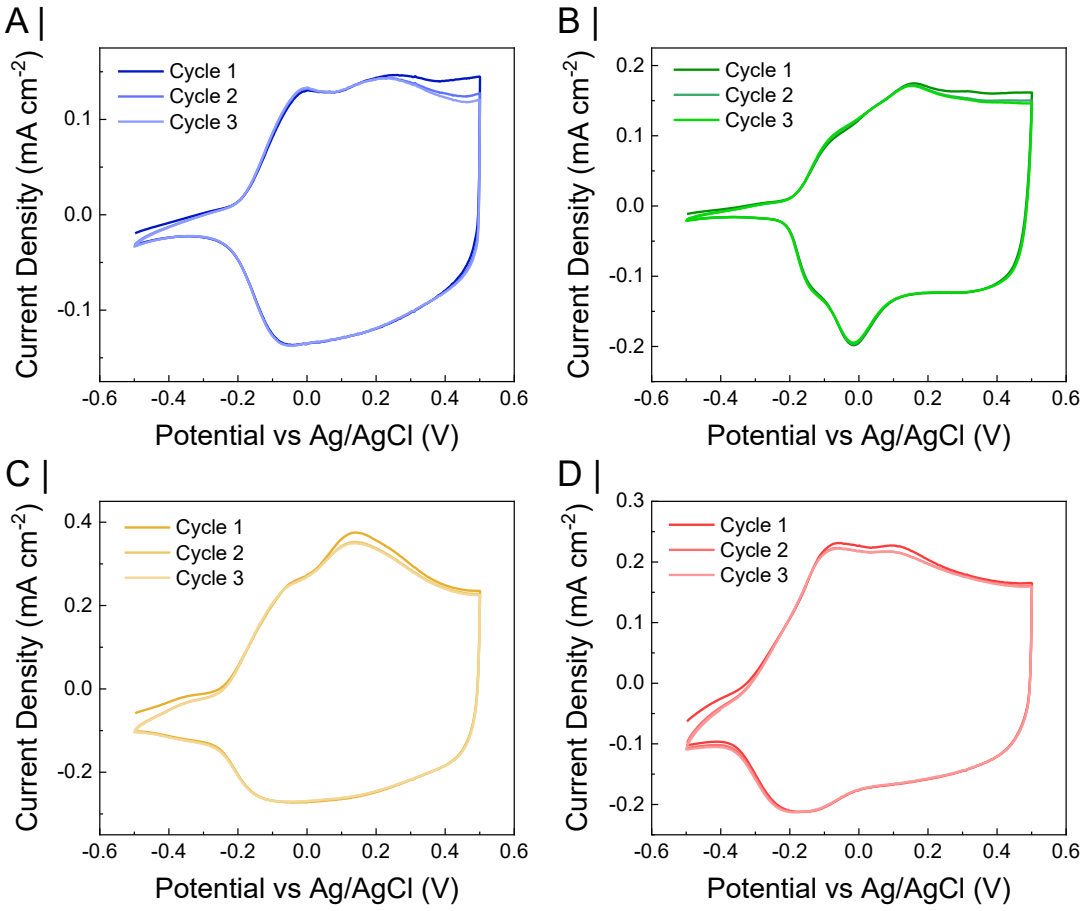

Figure 3.4. *Repeated CV addressing of the polymers in 0.1 M aqueous NaCl solutions.*

3.4.2 Optical Properties

The polymers' optical properties in solution and in the solid state were assessed by UV-Vis absorption spectroscopy, see **Figure 3.5**. As demonstrated by **Figure 3.5** and **Table 3.1**, all polymers exhibited comparable optical absorption profiles in dilute chloroform solutions, exhibiting one primary absorption band and a maximum absorption wavelength ($\lambda_{max,soln}$) at 583±5 nm, which was ascribed to a π-π* optical transition. The absence of any fine structure in the main absorption band also suggested the lack of any polymer aggregation in solution and a high degree of polymer solubility in chloroform. Upon going from the solution to the solid state, the polymers' π-π* absorption feature was significantly red-shifted by ~ 90 nm. This bathochromic shift was a result of the polymers' tendency to undergo molecular

ordering, resulting in the polymers' conjugated backbone assuming a more planar conformation and increased interchain π-π interactions. This result was further confirmed by the polymers' significantly more resolved π-π* absorption feature, giving rise to a high-energy feature ~ 640 nm and a low-energy one ~ 700 nm. These were in turn assigned to the polymers' 0-1 and 0-0 transition, respectively, whereby the similar magnitudes of the peaks suggested similar degrees of molecular ordering across the polymer series. Lastly, optical gaps ($E_{g,opt}$) of 1.63 eV were recorded across the entire polymer series, thereby confirming the findings from CV measurements, and indicating that EG side-chain redistribution does not strongly impact the polymers' energy levels.

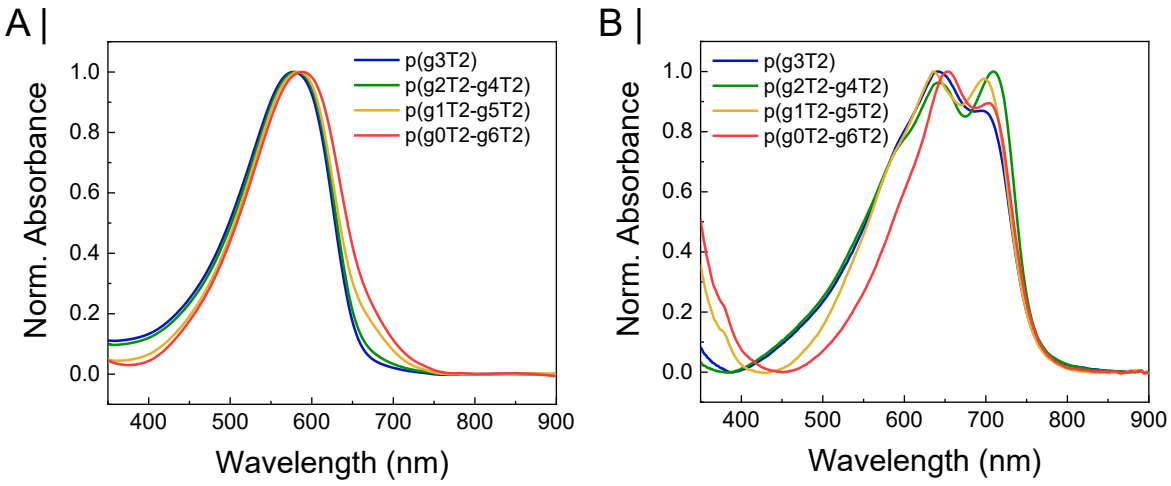

Figure 3.5. *Normalised UV-Vis absorption spectra of* ***p(g3T2)***, ***p(g2T2-g4T2)***, ***p(g1T2-g5T2)***, *and* ***p(g0T2-g6T2)*** *in a) dilute chloroform solutions and b) thin film while applying a negative dedoping bias of -0.5 V.*

The electrochromic properties and the doping mechanism of the polymers were evaluated by spectroelectrochemical measurements, employing a similar three-electrode set-up to the one used for CV measurements. Spectroelectrochemistry was performed in both aqueous and organic media, with no significant differences observed when conducting the measurements in the two different environments, see **Figure 3.6**. As shown in **Figure 3.6**,

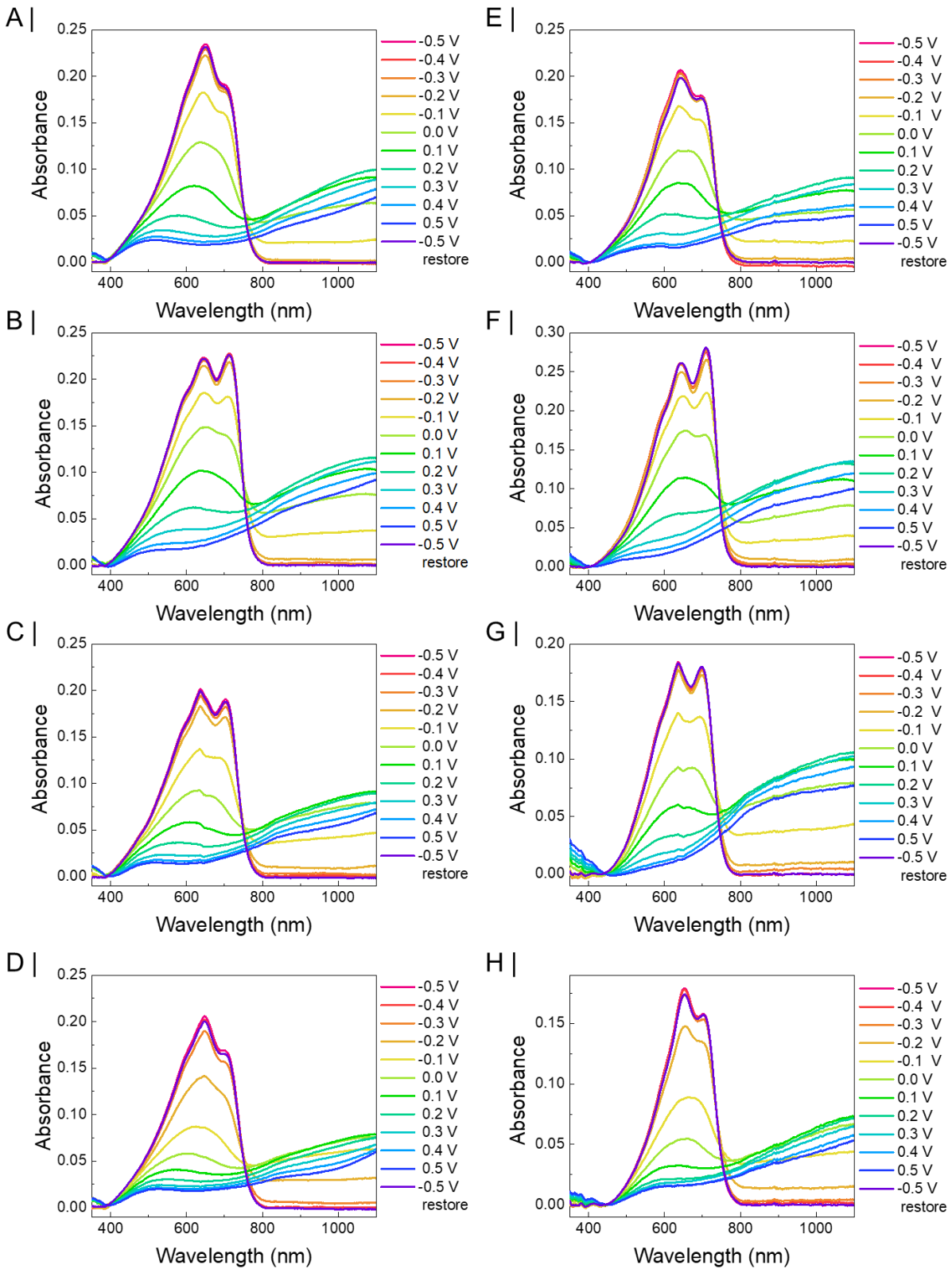

Figure 3.6. *Spectroelectrochemistry of a)* ***p(g3T2)****, b)* ***p(g2T2-g4T2)****, c)* ***p(g1T2-g5T2)****, and d)* ***p(g0T2-g6T2)*** *employing a 0.1 M TBA* PF_6 *in acetonitrile solution. Spectroelectrochemistry of e)* ***p(g3T2)****, f)* ***p(g2T2-g4T2)****, g)* ***p(g1T2-g5T2)****, and h)* ***p(g0T2-g6T2)*** *employing a 0.1 M NaCl in distilled water solution as the supporting electrolyte.*

each of the polymers was partially doped under ambient conditions, necessitating the application of a -0.5 V bias to completely dedope the films. Application of increasingly positive voltages up to +0.2 V led to a progressive depression of the π-π* absorption around 670 nm. In parallel, the emergence of a new absorption feature ~ 1100 nm occurred, which was attributed to the charged form of the polymer, specifically its polaronic form.[206] Further increments in the applied potential to +0.5 V subsequently led to a depression of this absorption feature, suggesting the formation of an even lower energy one corresponding to the polymers' bipolaronic state.[206,207] Due to the limited wavelength range of the employed photodetector, it was however not possible to confirm the formation of the doubly charged polymer species. To test the reversibility of the doping process, the applied potential was inverted from +0.5 V to -0.5 V. As shown from **Figure 3.6**, the optical signatures of all polymers in both media could be restored in their entirety, thus being indicative of no significant polymer degradation when cycling the polymers within the given voltage window and confirming the preliminary CV cycling stability measurements.

3.4.3 Swelling Properties

Following the evaluation of the polymers' electrochemical and optical properties, their swelling behaviour was investigated next. Evaluating OMIEC's swelling behaviour is of fundamental importance in order to assess their OECT performance, as the volumetric capacitance (C^*), ionic charge carrier mobility, and electronic charge mobility (μ) have all been demonstrated to be strongly dependent on the OMIECs' ability to swell.[79,80,118,185,208] Irrespective of the type of swelling measurement employed, the swelling of OMIECs typically tends to be further subdivided into their 'passive' and 'active' swelling. Passive swelling is commonly defined as the OMIEC's swelling upon electrolyte exposure in the absence of an applied electrochemical bias and is attributed to the diffusion of hydrated ions

and water molecules into polymer films. Conversely, active swelling is usually referred to as the swelling of OMIECs in the presence of an applied electrochemical bias and is ascribed to the migration of counterions and water molecules in their hydration spheres in response to the injection of electronic charge carriers into the OMIEC. Graphically the difference between the 'passive' and 'active' swelling of a p-type OMIECs is depicted in **Figure 3.7**.

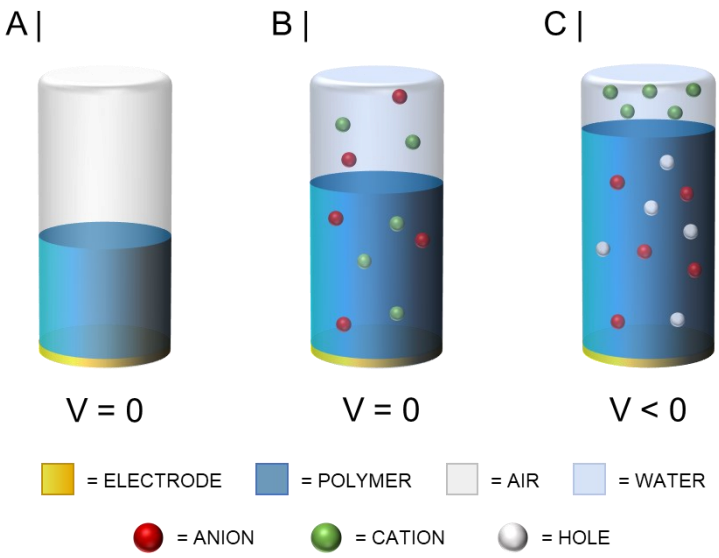

Figure 3.7. *Visual representation of the volume changes occurring for a p-type OMIEC during electrolyte exposure and electrochemical doping. a) OMIEC on a conductive substrate in air. b) Passive swelling of the OMIEC upon electrolyte exposure due to the transport of hydrated ions and water molecules into the OMIEC. c) Active swelling of the OMIEC including counterion migration into the OMIEC in response to hole injection from the conductive substrate.*

The swelling of conjugated polymers can be determined through a range of experimental techniques, including atomic force microscopy (AFM), carbon monofilament swelling experiments, and electrochemical quartz crystal microbalance with dissipation (eQCM-D).[74,75,118,185,209,210] In this case, the swelling of the OMIECs was assessed through the latter technique. In eQCM-D measurements, the polymer under evaluation is first coated onto a gold substrate, which then acts as the working electrode in a three-electrode setup. Common counter- and reference electrodes are platinum and Ag/AgCl electrodes, respectively.

Following polymer deposition, the polymer-coated gold substrate is immersed into the electrolyte, and after having reached thermodynamic equilibrium the polymer's passive swelling can be calculated. The polymer's active swelling is then evaluated by application of either a single or multiple doping/dedoping potentials. Mathematical fitting of the measured oscillation frequency (*f*) and dissipation (*D*) can then be employed to extract important parameters such as the mass uptake or swelling percentage of the polymer.

eQCM-D measurements were performed on the polymers employing a polymer-coated gold electrode as the working electrode, an Ag/AgCl couple as the reference electrode, and a platinum wire as the counter electrode. Polymer films were deposited onto the gold substrate by spin coating. An aqueous 0.1 M NaCl solution was employed as the supporting electrolyte to closely mimic the electrolyte environment encountered during device operation. The eQCM-D results obtained for **p(g3T2)**, **p(g2T2-g4T2)**, **p(g1T2-g5T2)**, and **p(g0T2-g6T2)** are summarised in **Table 3.2** and illustrated in **Figure 3.8**.

Table 3.2. *Summary of the polymers' swelling properties.*

Polymer	Dry volume (%)	Passively swollen volume (%)[a]	Actively swollen volume (%)[b]
p(g3T2)	100	162	412
p(g2T2-g4T2)	100	145	316
p(g1T2-g5T2)	100	144	154
p(g0T2-g6T2)	100	142	146

[a]*Recorded while exposing the polymer-coated gold substrate to an aqueous 0.1 M NaCl supporting electrolyte in the absence of an applied bias.* [b]*Recorded after exposing the polymer-coated gold substrate to an aqueous 0.1 M NaCl supporting electrolyte and in the presence of a +0.5 V bias.*

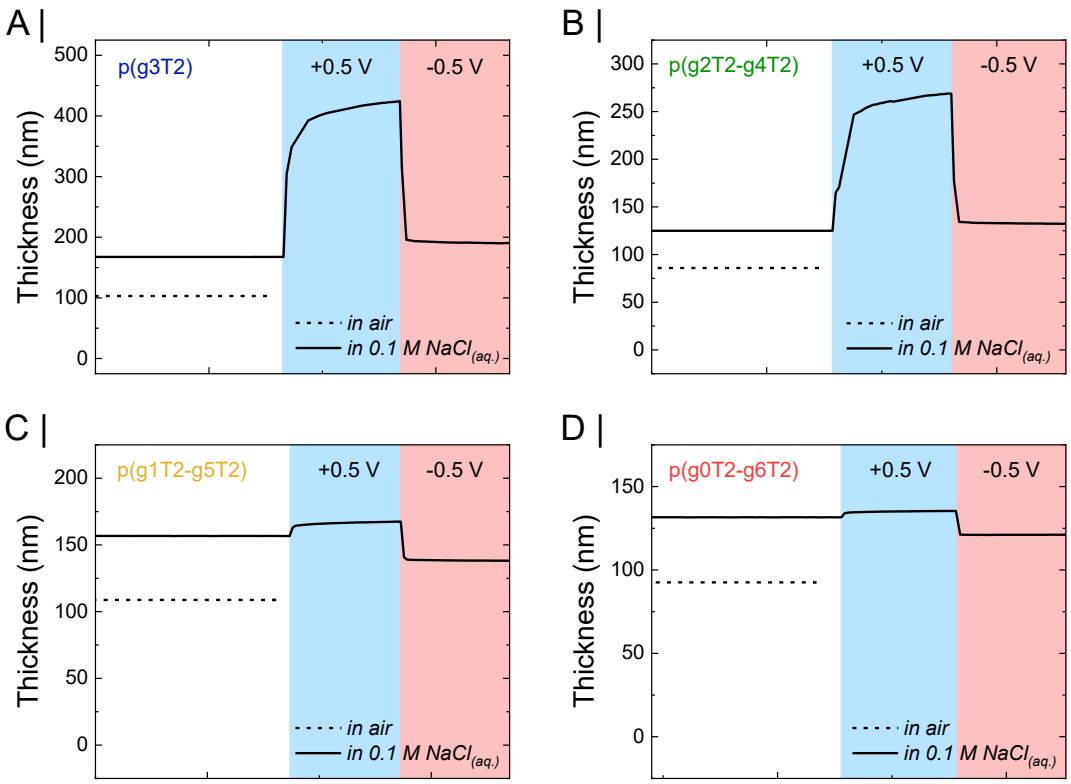

Figure 3.8. *eQCM-D results for a)* ***p(g3T2)****, b)* ***p(g2T2-g4T2)****, c)* ***p(g1T2-g5T2)****, and d)* ***p(g0T2-g6T2)****. Dashed trace corresponds to the polymer thickness on the gold substrate in air in the absence of an electrolyte and applied bias. Solid trace corresponds to the polymer thickness when immersed in an aqueous 0.1 M NaCl supporting electrolyte in the absence of an applied bias (white background), in the presence of a +0.5 V doping potential (sky blue background), and in the presence of a -0.5 V dedoping potential (amaranth background).*

As follows from **Table 3.2**, each of the polymers undergoes a similar passive swelling between 40-60% upon exposure to a 0.1 M aqueous NaCl supporting electrolyte. Compared to **p(g2T-TT)**, which typically swells passively between 10-15% upon contact with a 0.1 M aqueous NaCl supporting electrolyte, the polymers thus exhibit a larger passive swelling. This is attributed to the presence of twice as many hydrophilic EG repeat units per conjugated repeat unit in the polymers developed herein (12 EG repeat units per conjugated polymer repeat unit) compared to **p(g2T-TT)** (6 EG repeat units per conjugated polymer

repeat unit).[118] From the passively swollen data, it also follows that redistributing the EG side-chains across the conjugated polymer backbone does not have a significant impact on the polymers' passive swelling properties. Conversely, significant differences were found in the polymers' active swelling. Here, **p(g3T2)**, **p(g2T2-g4T2)**, **p(g1T2-g5T2)**, and **p(g0T2-g6T2)** were found to swell to 412%, 316%, 154%, and 146% relative to their initial dry volume, see **Table 3.2**, with the data collected for **p(g3T2)** corroborating previous literature findings.[74,75] Progressively redistributing the EG side-chains from **p(g3T2)** to **p(g0T2-g6T2)** resulted in a gradual reduction of the polymers' ability to swell. To better understand the origins of the recorded trend, the active volumetric swelling of the polymers was deconvoluted into swelling arising from the influx of hydrated counterions and water molecules, see **Figure 3.9**.

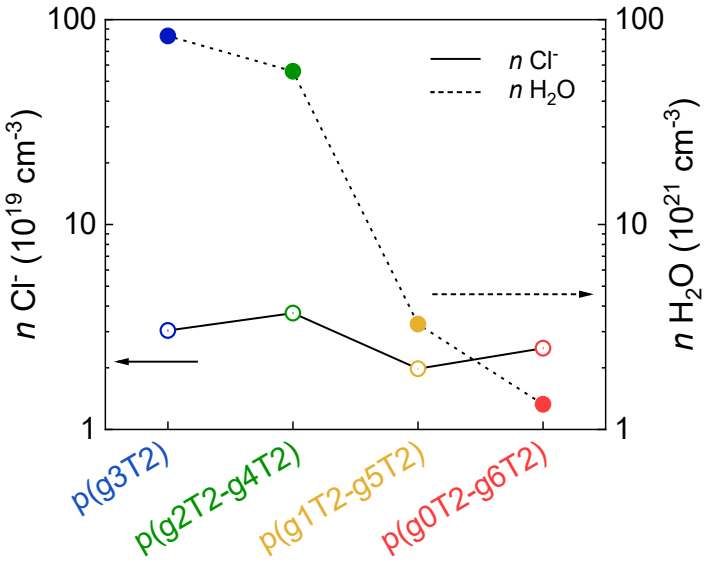

Figure 3.9. *Number of chloride ions (n Cl^-, solid line) and number of water molecules (n H_2O, dashed line) injected into the polymers upon application of a +0.5 V doping potential in an aqueous 0.1 M NaCl solution.*

As follows from **Figure 3.9**, the number of hydrated chloride ions injected into each polymer during electrochemical doping (*n* Cl^-) was of similar magnitude, while the number of water molecules taken up by each polymer (*n* H_2O) varied significantly. Consequently, side-chain redistribution does not impact the polymers' ability to take up ions, but mainly water molecules. It is currently speculated that the different ability of the polymers to take up and stabilise water molecules in their doped form arises from the different capabilities of the individual alkoxy-functionalised bithiophene units to do so. In particular, upon increasing the EG chain length on the individual bithiophene units, their hydrophilic character is increased and therefore also their ability to take up and stabilise water molecules in their doped state. The 3,3'-dimethoxy-2,2'-bithiophene (**g0T2**) moiety in **p(g0T2-g6T2)** is thus the least able to stabilise injected water molecules. Stepwise increments in the number of EG repeat units in the 3,3'-dialkoxy-2,2'-bithiophene unit from zero (**g0T2**), to one (**g1T2**), to two (**g2T2**) results in a progressively larger water molecule uptake. Importantly, however, these increments seem to be limited to the shorter members of the series, with the ability to take up additional water molecules becoming weaker for any additional EG side-chain length increase after three EG repeat units. Consequently, the **g3T2**, **g4T2**, **g5T2**, and **g6T2** units should all lead to similar degrees of water uptake, therefore resulting in the maximum water uptake in **p(g3T2)** and the least in **p(g0T2-g6T2)**. This theory is in line with the results obtained for another polymer series, where doubling the EG side-chain content in the polymers resulted in a ~ 500% increase in the polymers' active swelling with a further doubling of the EG chain length only leading to a ~ 50% increment.[185]

3.4.4 Morphological Properties

Grazing incidence wide-angle X-ray scattering measurements (GIWAXS) were conducted to evaluate the polymers' microstructure in thin films. The recorded GIWAXS scattering patterns for the polymers' dry, as-cast state are shown in **Figure 3.10**.

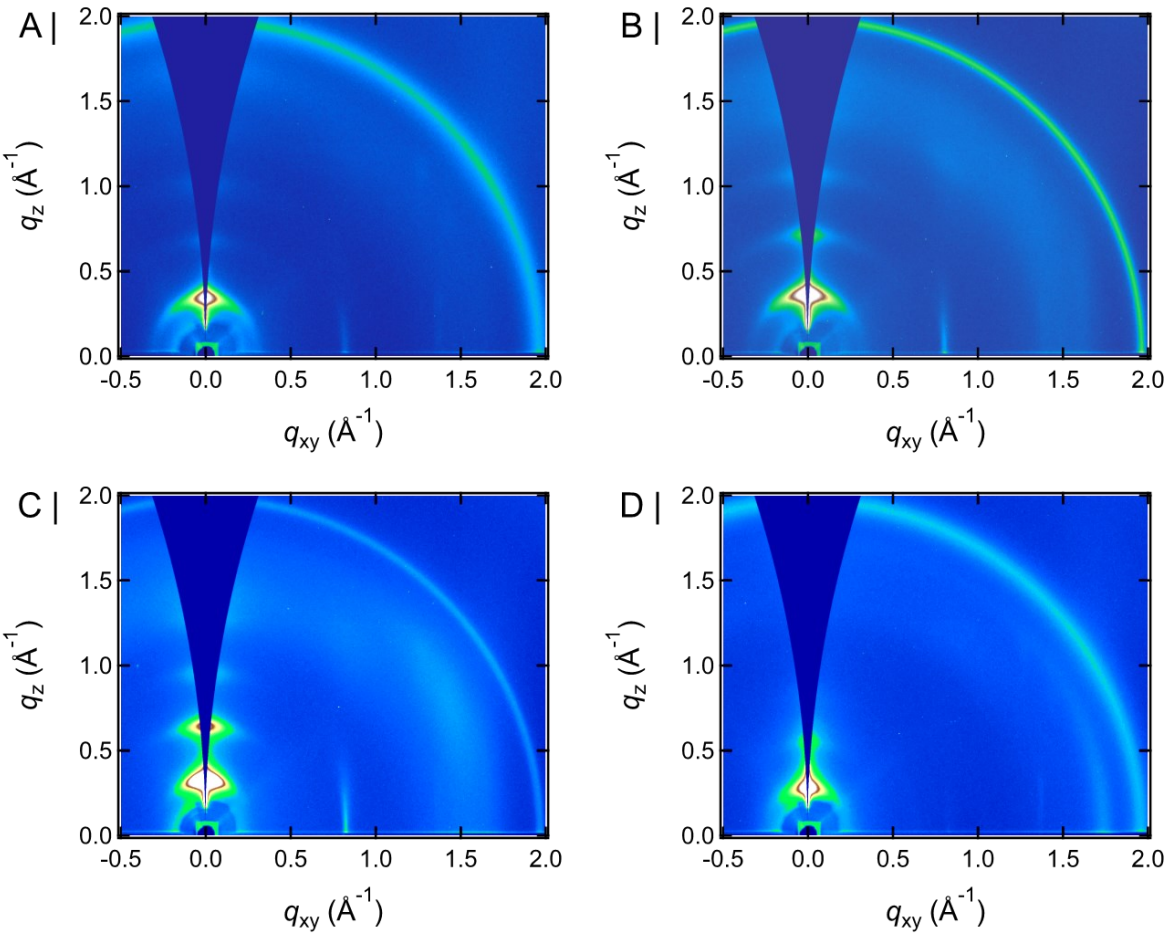

Figure 3.10. *GIWAXS scattering patterns recorded for dry, as-cast films of a)* ***p(g3T2)****, b)* ***p(g2T2-g4T2)****, c)* ***p(g1T2-g5T2)****, and d)* ***p(g0T2-g6T2)****. Note that the amorphous scattering feature occurring at 2.0 Å^{-1} is an artefact arising from the employed substrate.*

As shown in **Figure 3.10**, all the polymers adopt an edge-on orientation given the presence of intense lamellar scattering peaks in the out-of-plane (q_z) direction. Three orders of (h00) scattering were observed for all as-cast films, confirming a similar degree of order in the polymers' microstructure, as suggested by thin film UV-Vis analysis, see **Figure 3.5**.

Interestingly, no π-π stacking scattering feature could be observed for any of the polymers, thus highlighting that although the polymers exhibited a high degree of order in their lamellar domains, this was not the case for their π-π stacking domains. Care must however be taken when wanting to translate the above findings to the polymers' behaviour in OECTs, as the GIWAXS data were collected for dry, as-cast polymer films, therefore not taking into consideration the effects of passive or active polymer swelling. Passive and active polymer swelling can however have a significant impact on the GIWAXS scattering patterns recorded for EG functionalised conjugated polymers. For example, in a related EG functionalised polymer, the emergence of a new π-π scattering peak was observed upon electrochemical oxidation of the OMIEC.[211] Studies evaluating the GIWAXS features of **p(g3T2)**, **p(g4T2-g2T2)**, **p(g1T2-g5T2)**, and **p(g0T2-g6T2)** under more device relevant conditions are thus currently ongoing.

3.5 OECT Performance

Organic electrochemical transistors (OECTs) were fabricated for each polymer. Gold contacts were employed as source and drain electrodes, while an Ag/AgCl couple was employed as the gate electrode. Polymer films were deposited onto the devices by spin coating. An aqueous 0.1 M NaCl solution was employed as the supporting electrolyte for device testing. The polymers' OECT output, transfer, and transconductance curves are displayed in **Figure 3.11**. As highlighted from the polymers' transfer curves all polymers operate in a p-type accumulation mode and thus analogously to **p(g2T-TT)**, with the current passed through the device increasing upon the application of progressively smaller gate voltages. The polymers' tendency to operate in accumulation mode was deemed as favourable given that accumulation mode channel materials, typically incur higher on/off

ratios and lower power consumptions compared to their depletion mode counterparts, such as **PEDOT:PSS**.[82,151] Moreover, similar threshold voltages (V_{Th}) between +0.02 V and +0.19 V were obtained for the four polymers, hence being in line with the aqueous CV measurements, which also indicated an approximately 0.15 V variation in the polymers $E_{ox,aq}$ upon redistribution of the EG side-chains.

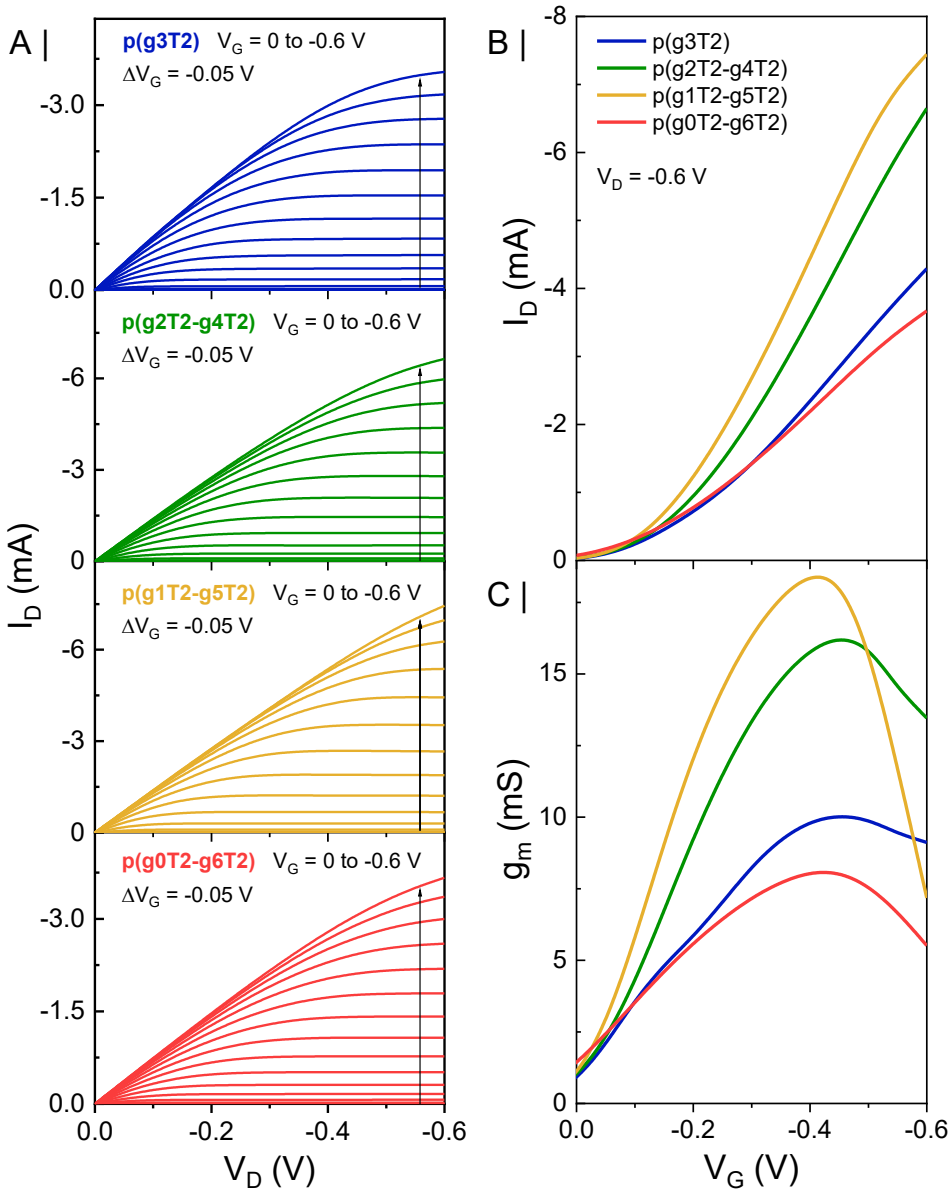

Figure 3.11. *OECT a) output, b) transfer, and c) transconductance curves recorded for* ***p(g3T2)***, ***p(g2T2-g4T2)***, ***p(g1T2-g5T2)***, *and* ***p(g0T2-g6T2)*** *employing an aqueous 0.1 M NaCl solution as the supporting electrolyte.*

The transconductance curves for the polymers are given in **Figure 3.11** and were extracted from the first derivative of the transfer curves. As demonstrated by **Figure 3.11**, **p(g2T2-g4T2)** and **p(g1T2-g5T2)** incurred the highest peak transconductances (g_m) of 18.5 mS (W = 100 µm, L = 10 µm, and d = 45 nm) and 16.3 mS (W = 100 µm, L = 10 µm, and d = 65 nm), respectively. **p(g3T2)** and **p(g0T2-g6T2)** on the other hand incurred slightly lower g_m values of 10.1 mS (W = 100 µm, L = 10 µm, and d = 75 nm) and 8.1 mS (W = 100 µm, L = 10 µm, and d = 70 nm), respectively. OECT steady-state performance comparison across the four polymers was conducted by extracting the polymers' product μC^*, with the incurred μC^* values listed in **Table 3.3**.

Table 3.3. *Summary of the polymers' OECT steady-state performance.*

Polymer	d (nm)	V_{Th} (V)	g_m (mS)	μC^* (F cm^{-1} V^{-1} s^{-1})[a]	C^* (F cm^{-3})[b]	μ (cm^2 V^{-1} s^{-1})[c]
p(g3T2)	75	+0.03	10.1	161	156	0.90
p(g2T2-g4T2)	45	+0.02	18.5	522	187	1.72
p(g1T2-g5T2)	65	+0.10	16.3	496	133	2.61
p(g0T2-g6T2)	70	+0.18	8.1	302	74	2.95

[a]Measured from the slope of g_m as a function of $(Wd/L)(V_{Th}-V_G)$. [b]Calculated from EIS curves fit to an $R_s(R_p||C)$ circuit.[89] *[c]Determined from the transistor saturation mobility using the respective C^* values.*[116,212,213]

Maximum μC^* values of 161 F cm^{-1} V^{-1} s^{-1}, 522 F cm^{-1} V^{-1} s^{-1}, 496 F cm^{-1} V^{-1} s^{-1}, and 302 F cm^{-1} V^{-1} s^{-1} were obtained for **p(g3T2)**, **p(g2T2-g4T2)**, **p(g1T2-g5T2)**, and **p(g0T2-g6T2)**, respectively. As already suggested by the transconductance data, **p(g2T2-g4T2)** and **p(g1T2-g5T2)** hence incurred the highest OECT steady-state performance, whereby the performance recorded for all polymers except for **p(g3T2)** was higher than the **p(g2T-TT)** benchmark, for which a μC^* of 261 F cm^{-1} V^{-1} s^{-1} has been reported.[115] Notably, the steady-state performance of **p(g2T2-g4T2)** and **p(g1T2-g5T2)** was also higher than the one

reported for **Crys-P** (μC^* of 490 F cm^{-1} V^{-1} s^{-1}), a highly crystalline form of **PEDOT:PSS**, which at the time of writing incurred the highest performance for any thin film-based OECT technology.[124] Besides incurring a superior OECT performance, further benefits of employing **p(g2T2-g4T2)** and **p(g1T2-g5T2)** as OECT channel materials rather than **Crys-P** stem from their accumulation mode of behaviour, thus incurring superior on/off ratios on the order of ~ 10^5 (*c.f.* ~ 10^2 for **Crys-P**) and lower power consumptions. Finally, while significant pre- and post-processing of **Crys-P** films was required to incur maximum OECT performance, no pre- or post-processing treatments were required for any of the polymers developed herein to incur the maximum reported OECT steady-state performance values.

To obtain a greater insight into the performance trend across the polymer series, electrochemical impedance spectroscopy (EIS) measurements were performed on OMIEC-coated gold electrodes. EIS experiments were performed in a 0.1 M aqueous NaCl solution and at an applied bias corresponding to the V_G incurring the maximum g_m in devices. The polymers' EIS traces were then fit to an equivalent circuit ($R_s(R_p||C)$), see **Figure 3.12**, to extract the OMIEC's capacitance to then incur the volumetric capacitance by dividing the recorded capacitance value with the polymer volume.[89] As can be seen from **Figure 3.12** a good fit between the experimental and theoretical values was obtained for each polymer, thus enabling extraction of the polymers' C^* through EIS. The C^* values incurred for the polymers are given in **Table 3.3** and were found to be 156 F cm^{-3}, 187 F cm^{-3}, 133 F cm^{-3}, and 74 F cm^{-3} for **p(g3T2)**, **p(g2T2-g4T2)**, **p(g1T2-g5T2)**, and **p(g0T2-g6T2)**, respectively, indicating that the polymer featuring an intermediate degree of volumetric swelling during OECT operation afforded the highest C^*. As evidenced in previous literature, C^* is closely related to the degree of polymer swelling and hence the number of hydrated ions and water molecules taken up by a channel material upon device operation.[185,208] Specifically, water

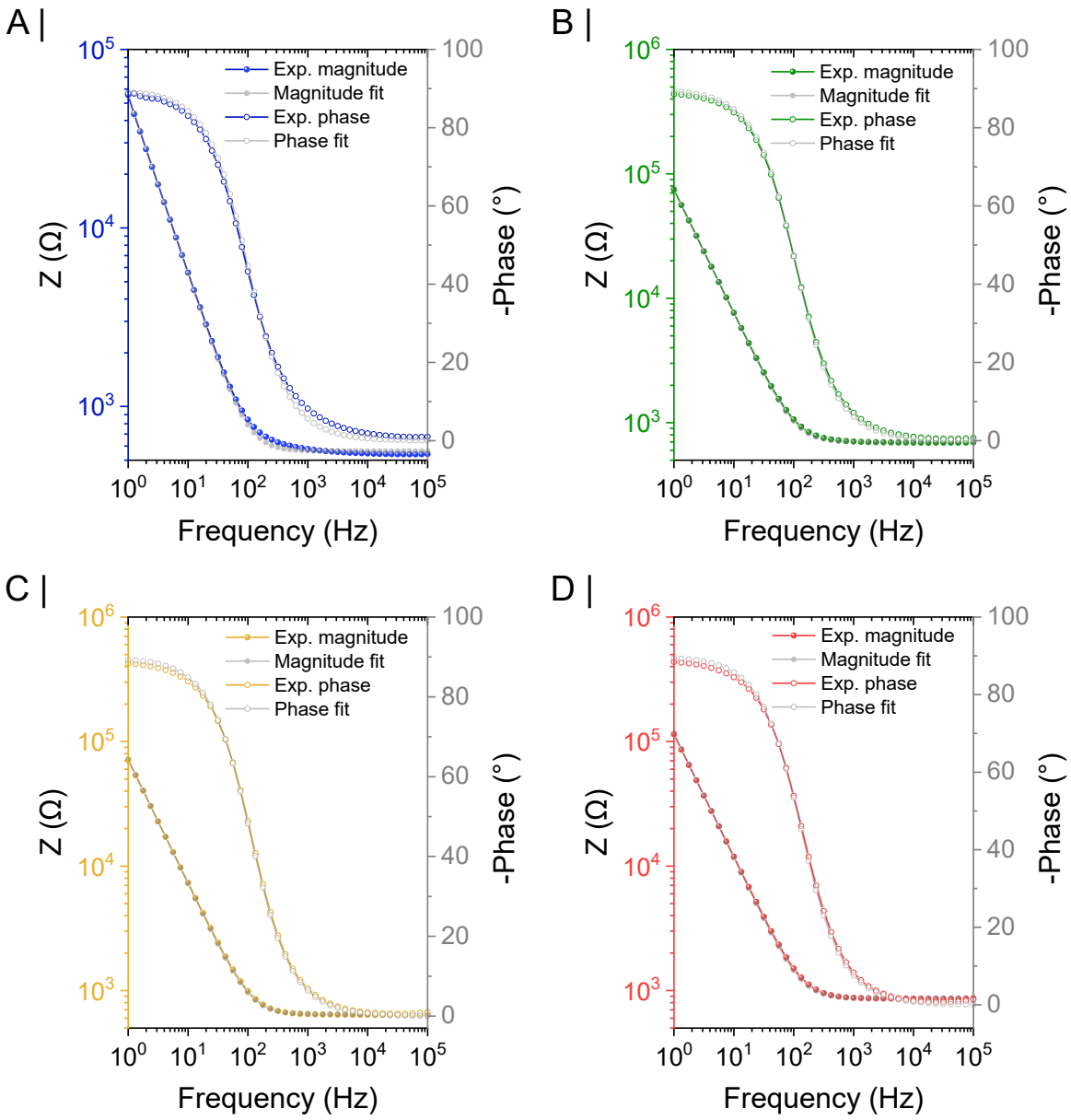

Figure 3.12. *Electrochemical impedance spectra acquired for a)* ***p(g3T2)****, b)* ***p(g2T2-g4T2)****, c)* ***p(g1T2-g5T2)****, and d)* ***p(g0T2-g6T2)*** *in a 0.1 M aqueous NaCl supporting electrolyte at the applied bias incurring the maximum transconductance in OECTs.*

uptake by the channel material has been demonstrated to be necessary to create ionic percolation pathways and enable ions to access the bulk of the channel material, thereby leading to three-dimensional volumetric doping.[155,214] Nonetheless, care must be taken when optimising the channel materials' ability to uptake water molecules, as excessive hydration has been proven to be detrimental towards C^*.[185] This is because the excess water molecules only contribute towards the volumetric expansion of the channel material, rather

than allowing for an increased ion uptake. Consequently, C^* suffers due to an increase in polymer volume without any gain in capacitance, *i.e.* from a reduced charge density. Given the above, it is therefore unsurprising that **p(g2T2-g4T2)**, the material displaying an intermediate level of swelling incurred the highest C^*, with both decreases and increases in the polymers' tendency to swell resulting in lower C^* values. Despite some degree of variation within the polymer series' C^* values, the recorded C^* values across the polymer series compare well with alternative p-type EG functionalised conjugated polymers, for which C^* values between 75-250 F cm^{-3} have been reported.[115,166,193,202]

To gain a comprehensive picture of the polymers' OECT performance, their electronic charge carrier mobility in OECTs was determined next. The μ values incurred for each polymer are shown in **Table 3.3** and were calculated according to the literature from the transistor saturation mobility using the respective C^* values.[116,212,213] In particular, μ values of 0.90 cm^2 V^{-1} s^{-1}, 1.72 cm^2 V^{-1} s^{-1}, 2.61 cm^2 V^{-1} s^{-1}, and 2.95 cm^2 V^{-1} s^{-1} were obtained for **p(g3T2)**, **p(g2T2-g4T2)**, **p(g1T2-g5T2)**, and **p(g0T2-g6T2)**, respectively. A strong inverse relationship was thus observed between the OMIECs' tendency to swell and their electronic charge carrier mobility, confirming previous findings.[80,118] Here, the presence of additional water molecules is envisaged to disrupt the packing of the conjugated polymer chains hence also disrupting the percolative networks for efficient electronic charge carrier transport.

As highlighted in **Section 1.4.2**, a high steady-state performance is critical to promote the commercial viability of OECT technologies. Another aspect of crucial importance is, however, the operational stability of OECTs. The operational stability of OECTs is commonly measured by repeated electrochemical addressing of the devices, *i.e.* cycling the devices between their 'ON' and 'OFF' states, while measuring the percentage retention of the device's initial drain current ($I_D/I_{D,0}$).[112,124,125,155,166,215] The operational stability of the

polymers developed herein over 2 h of continuous electrochemical biasing (~ 700 doping/dedoping cycles) is shown in **Figure 3.13**.

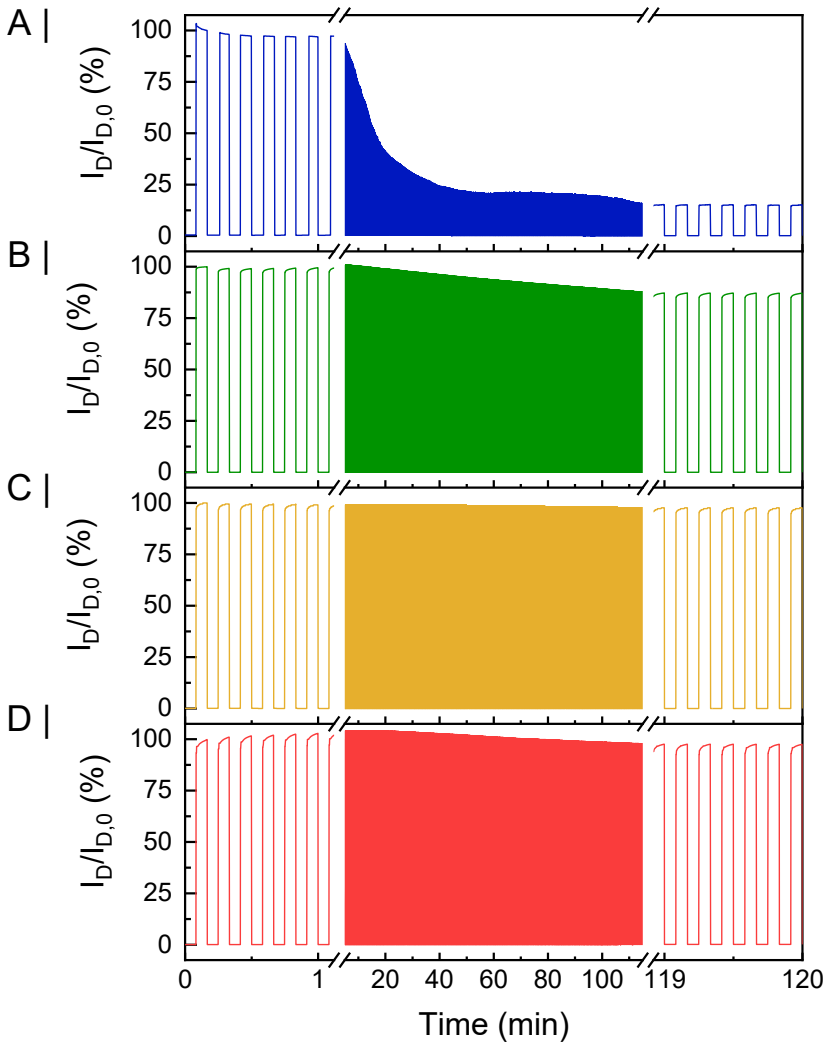

Figure 3.13. *Operational stability of a)* ***p(g3T2)****, b)* ***p(g2T2-g4T2)****, c)* ***p(g1T2-g5T2)****, and d)* ***p(g0T2-g6T2)*** *over 2 h of continuous electrochemical cycling (~ 700 doping/dedoping cycles) in a 0.1 M aqueous NaCl supporting electrolyte.*

Following 2 h of repeated electrochemical addressing, **p(g3T2)**, **p(g2T2-g4T2)**, **p(g1T2-g5T2)**, and **p(g0T2-g6T2)** yielded $I_D/I_{D,0}$ values of 15%, 87%, 98%, and 98%, respectively, see **Figure 3.13**. Note that all members of the polymer series, except for **p(g3T2)**, therefore outperformed the **p(g2T-TT)** benchmark, for which an $I_D/I_{D,0}$ of 75% following 2 h of continuous electrochemical biasing (~ 700 doping/dedoping cycles) has been reported.[155]

Given the similar *IP* values recorded across the developed polymer series, the trend in the polymers' $I_D/I_{D,0}$ could not be explained due to an energetic effect. Instead, the polymers' $I_D/I_{D,0}$ appeared to closely reflect their swelling tendency, with decreased active volumetric swelling improving the measured $I_D/I_{D,0}$. The reduced swelling of the polymers upon electrochemical addressing is likely to lead to reduced morphological changes in the channel material, therefore minimising delamination from the substrate and better retaining the charge carrier pathways for efficient electronic transport.

3.6 OECT Biosensors

The polymers' excellent OECT steady-state performances and high operational stabilities in OECTs rendered them ideal candidates as channel materials for OECT biosensors.[156,216] In this context, **PEDOT:PSS** is typically employed as the material of choice given its widespread commercial availability, good electrochemical stability, and relatively high OECT performances. Biosensors employing **PEDOT:PSS** as the channel material have previously been employed for a variety of applications, including for the recording of electrophysiological signals,[69,71,84] for the detection of neurotransmitters such as dopamine,[217,218] and for the sensing of biomolecules such as glucose, lactate, and cholesterol.[72,219,220] The detection of pathogenic organisms is another particularly exciting application area of OECTs. Here, OECTs have been used for the detection of viruses such as the human influenza A virus[221] and bacteria such as *E. coli,*[222] with limited research efforts towards the detection of alternative pathogens. In current times, a particularly relevant pathogen is the severe acute respiratory syndrome coronavirus 2 (SARS-CoV-2), which between January 2020-May 2021 has led to 3.5 million fatalities worldwide and is poised to remain a worldwide health and economic burden over the coming years.[223] Given

the facile airborne transmission of SARS-CoV-2 and a large proportion of asymptomatic carriers, molecular testing has become an essential tool to halter the spread of the virus. Nowadays, molecular testing is based on two main approaches, one based on reverse transcription polymerase chain reactions (RT-PCR) and one based on lateral flow immunoassays. RT-PCR tests benefit from high sensitivities yet require long processing times (typically on the order of several hours to days) and complex sample processing and equipment. Conversely, lateral flow immunoassays suffer from reduced sensitivities, but are compatible with unprocessed patient samples and afford fast testing results (typically on the order of 15-30 minutes). Hence, the development of sensors that combine high sensitivity with fast processing times and low complexity is of paramount importance to combat SARS-CoV-2 transmission. With the above considerations in mind, a new SARS-CoV-2 biosensor based on OECT technology employing either **PEDOT:PSS** or **p(g0T2-g6T2)** as the channel material was developed, see **Figure 3.14**.[224]

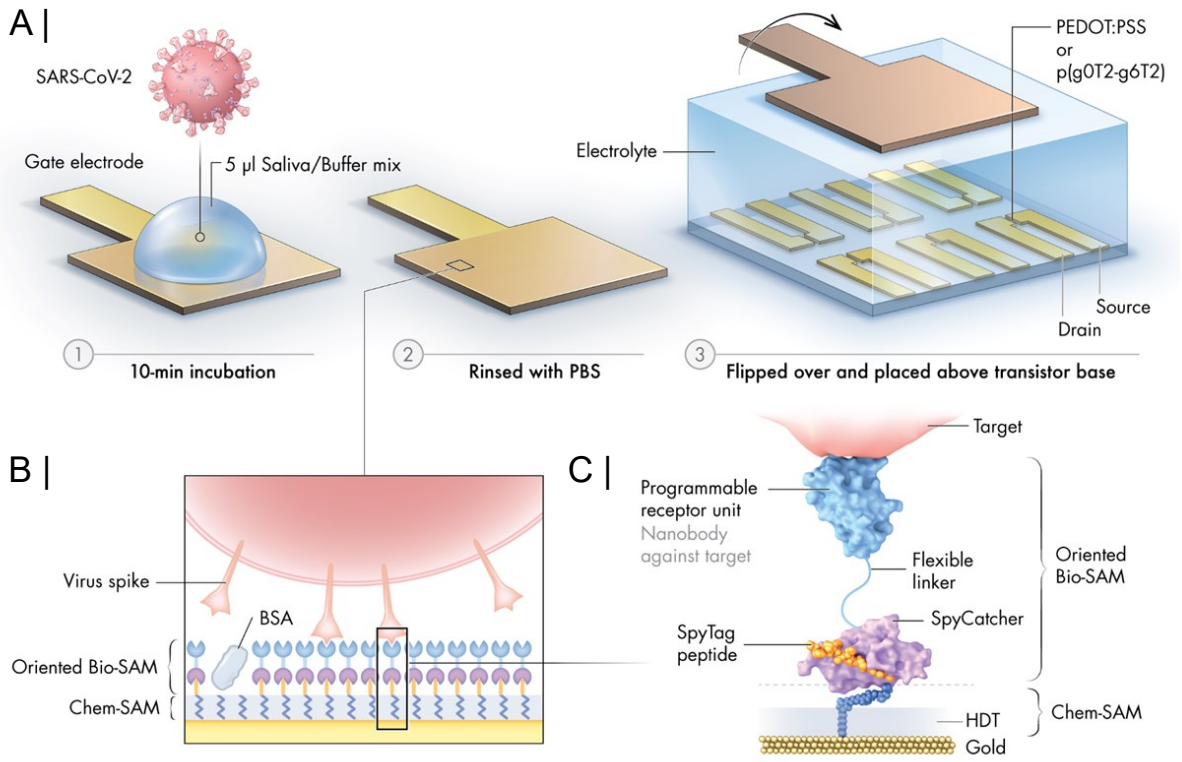

Figure 3.14. *Schematic of the SARS-CoV-2 OECT biosensor. a) Exposure of the gate electrode to the patient's sample, involving a 10 min incubation time, phosphate buffered saline (PBS) wash, and mounting of the biofunctionalised gate electrode on top of the OECT channel to allow for signal acquisition. b,c) Details of the gate biofunctionalisation. Figure taken with permission from K. Guo et al., Nat. Biomed. Eng.* ***2021****, DOI: 10.1038/s41551-021-00734-9. Copyright (2021) Springer Nature.*[224] *Springer Nature distribution licence obtained on 27.05.2021, see* ***Appendix Section 8.2****.*

While the sensing and operating mechanism of the sensor is outside of the scope of this thesis, one particularly relevant finding from a molecular design and synthetic chemistry perspective is that substitution of the **PEDOT:PSS** channel with **p(g0T2-g6T2)** resulted in significantly improved sensitivities, see **Figure 3.15**. Specifically, while the limit of detection (*LOD*) for the virus' S1 subunit in the spike protein was found to be on the order of 10^{-16} M when employing **PEDOT:PSS** as the channel material, a much lower *LOD* on the order of 10^{-20} M could be achieved when utilising **p(g0T2-g6T2)** as the channel. **p(g0T2-**

g6T2)'s superior performance was attributed to its improved on/off ratios and its higher OECT steady-state performance. Moreover, **p(g0T2-g6T2)**'s accumulation behaviour significantly reduced the biosensor's power consumption, thus rendering it compatible with a hand-held battery-driven reader. Finally, **p(g0T2-g6T2)**'s high operational stability also contributed towards the economic viability of the developed OECT biosensor, allowing for the transistor base (source electrode, drain electrode, and OECT channel) to be reused, while replacing the biofunctionalised gate electrode between test specimens.

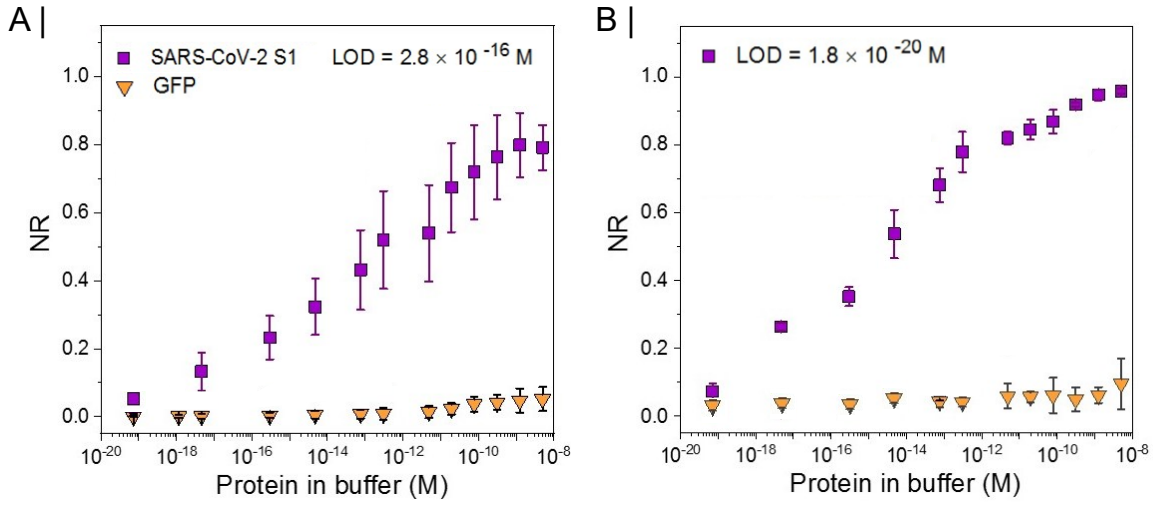

Figure 3.15. *Normalised response (NR) of the SARS-CoV-2 OECT biosensors towards the S1 subunit in the virus' spike protein (SARS-CoV-2 S1) and a green fluorescent protein (GFP) reference employing either a)* ***PEDOT:PSS*** *or b)* ***p(g0T2-g6T2)*** *as the channel material. Figure adapted with permission from K. Guo et al., Nat. Biomed. Eng.* ***2021****, DOI: 10.1038/s41551-021-00734-9. Copyright (2021) Springer Nature.*[224] *Springer Nature distribution licence obtained on 27.05.2021, see* ***Appendix Section 8.2****.*

3.7 Conclusions and Outlook

In summary, this chapter reports on the synthesis, characterisation, and OECT operation of four EG functionalised polythiophenes that differ in the relative distribution of their EG side-chains. Tuning of the EG distribution across the conjugated polymer backbone was

found not to substantially impact the optical and electrochemical properties of the materials. EG side-chain redistribution was, however, demonstrated to have a considerable impact on the swelling properties of the polymers. While all polymers incurred similar degrees of passive swelling between 40-60%, their volumetric expansion upon electrochemical addressing varied significantly, yielding volume increases between 46-312% compared to their corresponding initial dry state. Importantly, by judicious optimisation of the hydration levels within the polymer films upon electrochemical doping, unprecedented μC^* values of 496 F cm^{-1} V^{-1} s^{-1} and 522 F cm^{-1} V^{-1} s^{-1} were achieved for the two highest performing polymers in the series, namely **p(g2T2-g4T2)** and **p(g1T2-g5T2)**, respectively. The incurred μC^* hence compare favourably not only against the previously highest performing EG functionalised conjugated polymer, **p(g2T-TT)** ($\mu C^* \sim 260$ F cm^{-1} V^{-1} s^{-1}), but also against other high-performance OECT channel materials developed to date, including **PEDOT:PSS** ($\mu C^* \sim 50$ F cm^{-1} V^{-1} s^{-1}) and **Crys-P** ($\mu C^* \sim 490$ F cm^{-1} V^{-1} s^{-1}).

Control over the polymers' volumetric swelling upon electrochemical addressing was also found to be strongly correlated to their operational stability and hence their ability to retain current flowing through the device upon repeated electrochemical addressing. Specifically, progressively decreasing the polymers' active swelling during electrochemical switching was found to significantly boost OECT performance, with **p(g3T2)** incurring the lowest $I_D/I_{D,0}$ of 15% (over 2 h of repeated electrochemical cycling) and **p(g0T2-g6T2)** the joint-highest $I_D/I_{D,0}$ value of 98%. Given **p(g0T2-g6T2)**'s high steady-state performance and operational stability in OECTs, **p(g0T2-g6T2)** was also employed as OECT channel material in a newly developed SARS-CoV-2 biosensor based on OECT technology. In this sensor, the use of **p(g0T2-g6T2)** rather than **PEDOT:PSS** was found to directly improve biosensor performance, specifically by incurring a lower *LOD* and reduced power requirements, which in turn were ascribed to **p(g0T2-g6T2)**'s accumulation mode of

behaviour and its higher μC^*. The high stability of **p(g0T2-g6T2)** in devices was also found to be of fundamental importance to ensure the commercial viability of the sensor, allowing for the transistor base (source electrode, drain electrode, and OECT channel) to be reused, while replacing the biofunctionalised gate electrode between evaluated specimens.

Ultimately, the structure-property relationships established within this chapter build upon those elucidated in **Chapter 2** yet provide additional insights due to the evaluation of a different molecular design strategy and the focus on both OECT steady-state performance and operational stability. Moreover, the need to develop OECT channel materials with high OECT steady-state performances and high operational stabilities can be seen directly from the fabrication of an OECT biosensor used for the detection of viral pathogens. The OECT channel materials developed in this chapter are thus currently also being evaluated in alternative OECT-based immunosensors, including one for the detection of amyloid-β plaques, a major pathological hallmark of Alzheimer's disease.[225]

The doors of success are marked "push" and "pull."
— Yiddish proverb

4

Diketopyrrolopyrrole-based Donor-Acceptor Copolymers for p-type Accumulation Mode OECTs

Contents

4.1 General Information and Attributions

Gel permeation chromatography (GPC) experiments were conducted by Dr Hu Chen (King Abdullah University of Science and Technology). Grazing incidence wide-angle X-ray scattering (GIWAXS) measurements were performed by Dr Bryan Paulsen (Northwestern University) at the Stanford Synchrotron Radiation Lightsource, SLAC National Accelerator Laboratory. Density functional theory (DFT) calculations were carried out by Dr Karl Thorley (University of Kentucky). OECTs were fabricated by Tania Cecilia Hidalgo (King Abdullah University of Science and Technology). Polymer deposition onto OECT substrates, OECT testing, and EIS measurements were carried out in collaboration with Dr Achilleas Savva (King Abdullah University of Science and Technology) during a research visit at King Abdullah University of Science and Technology.

4.2 Introduction

Over the past thirty years, significant advances in organic electronics have been made in the design of materials with high electronic charge transport properties, with mobilities in organic field-effect transistors (OFETs) having risen beyond 10 $cm^2 V^{-1} s^{-1}$.[104,226,227] While a certain contribution to the progress in this area of organic electronics has come from advances in device architecture and material processing, the development of novel and carefully tailored organic semiconductors has been a crucial component for consistently reaching higher performances. Amongst the range of synthetic moieties employed for high-performance OFET materials, the diketopyrrolopyrrole (DPP) unit has been responsible for many high-mobility polymers, in particular as a result of its ability to form noncovalent conformational planarising interactions between its carbonyl moieties and the alpha protons of the flanking aryl groups, thereby assisting in the formation of highly ordered and strongly

π-π stacked polymer structures.[228–230] Typically, the DPP unit is functionalised at the amide positions with solubilising chains to impart processability from organic solvents, while aromatic substituents adorn the 3 and 6 positions, derived from its synthesis. Although historically the first conjugated polymers utilising the DPP unit featured flanking phenyl units, the relatively large backbone twist of ~ 27° across the DPP-phenyl bond severely limited its utility as a building block in high-mobility polymers.[228,231,232] It is therefore not surprising that currently the most eminent and well-studied DPP-based conjugated polymers feature either planarising thiophene (T) or thieno[3,2-*b*]thiophene (TT) flanking units (*e.g.* **DPPT-TT**, **PDQT, PDBT-*co*-TT**, *etc.*) giving rise to strong intermolecular π-π interactions, ultimately leading to excellent electronic charge transport properties, see **Figure 4.1**.[233–236]

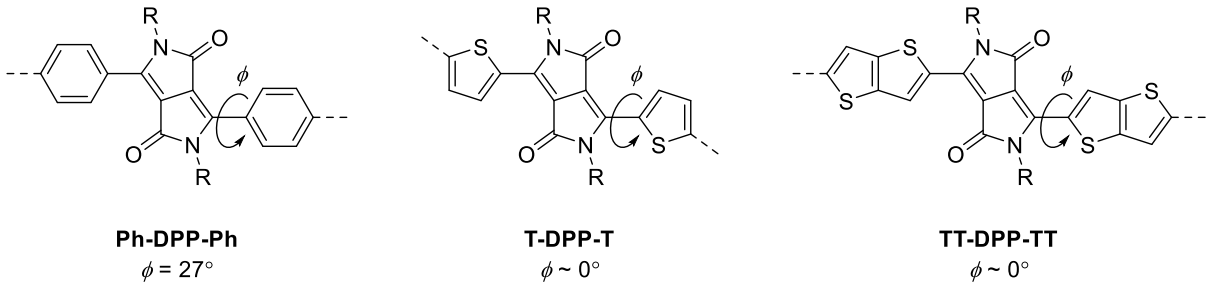

Figure 4.1. *Structure of the DPP core with various aryl flanking units at the 3 and 6 positions. Note the difference in dihedral angles upon substitution of the employed aromatic unit from ~ 27° for* ***Ph-DPP-Ph****,*[228,237] *to ~ 0° for* ***T-DPP-T*** *and* ***TT-DPP-TT****.*[238,239]

In an attempt to extend the DPP unit's favourable properties to OECT channel materials, two ethylene glycol (EG) functionalised pyridine flanked DPP-based polymers copolymerised with either 2,2'-bithiophene (T2) or 3,3'-dimethoxy-2,2'-bithiophene (MeOT2) were developed recently.[112] Of the two developed polymers, only the one employing the MeOT2 comonomer was able to incur a stable OECT performance, affording a hole mobility of 0.03 $cm^2 V^{-1} s^{-1}$ and a volumetric capacitance of 60 F cm^{-3}. Consequently, the steady-state performance recorded for this donor-acceptor (D-A) polymer is significantly

lower compared to the highest performing EG functionalised semiconductors for OECT applications, which are based on an all-donor thiophene backbone and can reach μ and C^* values > 1 $cm^2\ V^{-1}\ s^{-1}$ and > 250 F cm^{-3}, respectively, as exemplified by **p(g2T-TT)** and the polymers developed in **Chapter 3**.[126,155] The on average lower OECT steady-state performance incurred by D-A copolymers is further emphasised when considering alternative D-A polymers that have been developed as OECT channel materials, *e.g.* those employing isoindigo (IID), naphthalene tetracarboxylic diimide (NDI), or tetrafluorophenylene (TFT) moieties as the acceptor unit, for which μC^* values 0.1-10 F $cm^{-1}\ V^{-1}\ s^{-1}$ have been reported.[125,240,241] Despite D-A polymers' lower steady-state performances, this class of OECT channel materials has been demonstrated to reduce noncapacitive faradaic side reactions such as the oxygen reduction reaction (ORR) between the OECT channel material and the surrounding aqueous electrolyte in the device's 'OFF' state.[112] A direct consequence thereof is the reduced formation of hydrogen peroxide (H_2O_2), which can be detrimental towards OECT performance and safe device operation.[157–159]

With the above considerations in mind, this chapter aims to develop a series of higher performing D-A copolymers for OECT applications based on the DPP unit and minimise the current performance gap with their all-donor counterparts. The chemical structures of the investigated polymer series are shown in **Figure 4.2**, whereby each of the newly developed polymers made use of the same triethylene glycol functionalised thiophene flanked DPP unit. Thienyl flanking units were chosen to impart a high degree of planarity along the conjugated backbone, therefore ensure good intra- and intermolecular charge carrier transport. On the other hand, triethylene glycol chains were utilised as solubilising chains, as the vast majority of glycolated semiconducting p-type channel materials reported to date employs these moieties as side-chains, thereby enabling for a direct conjugated

polymer backbone performance comparison against the previously disclosed OECT channel materials.[82,83,115]

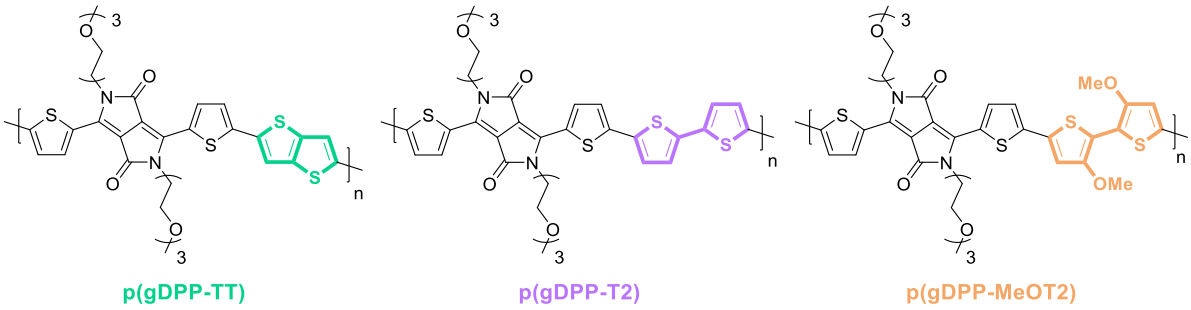

Figure 4.2. *Chemical structures of the investigated polymer series.*

4.3 Polymer Synthesis

The synthesis of the triethylene glycol functionalised thiophene flanked DPP monomer is shown in Scheme **4.1**. The first step involved a base promoted condensation of 2-thiophenecarbonitrile **26** with diethyl succinate to incur the unsubstituted thiophene flanked DPP core **28** in 53% yield. Core **28** was then functionalised at the N-termini by reaction with monomethyl ether triethylene glycol tosylate **29**, which was in turn obtained in 96% yield by reaction of triethylene glycol monomethyl ether with tosyl chloride. The alkylation of intermediate **28** with **29** to incur compound **30** proceeded in low yields of 38%, which were nonetheless on par as those reported for analogous DPP derivatives functionalised with ethylene glycol- or alkyl-based side-chains.[242–244] In previous literature, the low yielding nature of the DPP alkylation reaction has been ascribed due to both *N*- and *O*-alkylations being able to occur, thus leading to the formation of the desired *N,N*-functionalised product, as well as the unwanted *N,O*- and *O,O*-functionalised side products.[245,246] The formation of all three structural isomers, also seemed to be the case herein, given the presence of three closely eluting fractions with retention factor (R_f) values of 0.40, 0.35, and 0.30 during chromatographic purification. Nonetheless, only the structural identity of target compound

30 was confirmed, consequently preventing any firm conclusions. Finally, the dibromide functionalised monomer **31** was obtained in 73% yield by reaction of precursor **30** with *N*-bromosuccinimide.

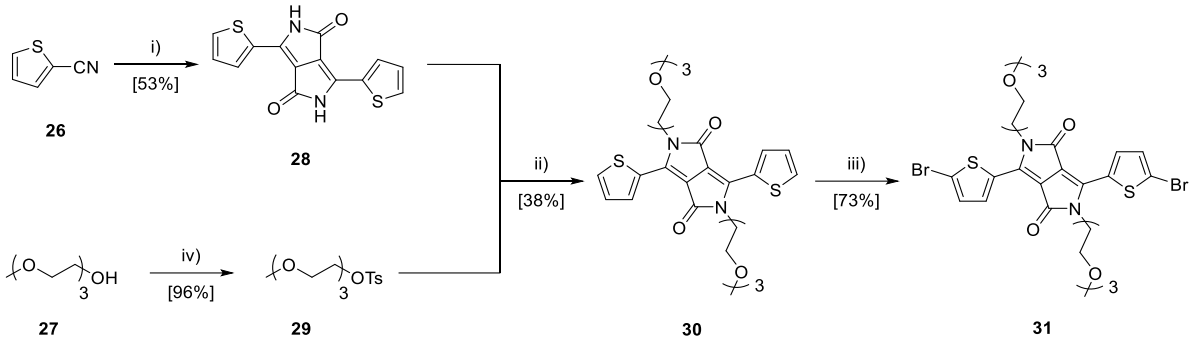

Scheme 4.1. *Synthesis of the triethylene glycol functionalised thiophene flanked DPP monomer. Reagents and conditions: i) Diethyl succinate (1.0 equiv.), Na (3.7 equiv.), iron (III) chloride (cat.), tert-amyl alcohol, 100 °C; ii) K_2CO_3 (4.0 equiv.), triethylene glycol monomethyl ether tosylate (2.5 equiv.), DMF, 120 °C; iii) NBS (2.1 equiv.), $CHCl_3$, RT; iv) TsCl (1.1 equiv.), NaOH (1.5 equiv.), THF, H_2O, 0 °C then RT.*

Having successfully synthesised compound **31**, the target polymers, **p(gDPP-TT)**, **p(gDPP-T2)**, and **p(gDPP-MeOT2)** were obtained by Stille cross-coupling polymerisation with 2,5-bis(trimethylstannyl)thieno[3,2-*b*]thiophene, 5,5'-bis(trimethylstannyl)-2,2'-bithiophene, and 3,3'-dimethoxy-5,5'-bis(trimethylstannyl)-2,2'-bithiophene, respectively, in good yields between 66-85%, see Scheme **4.2**.

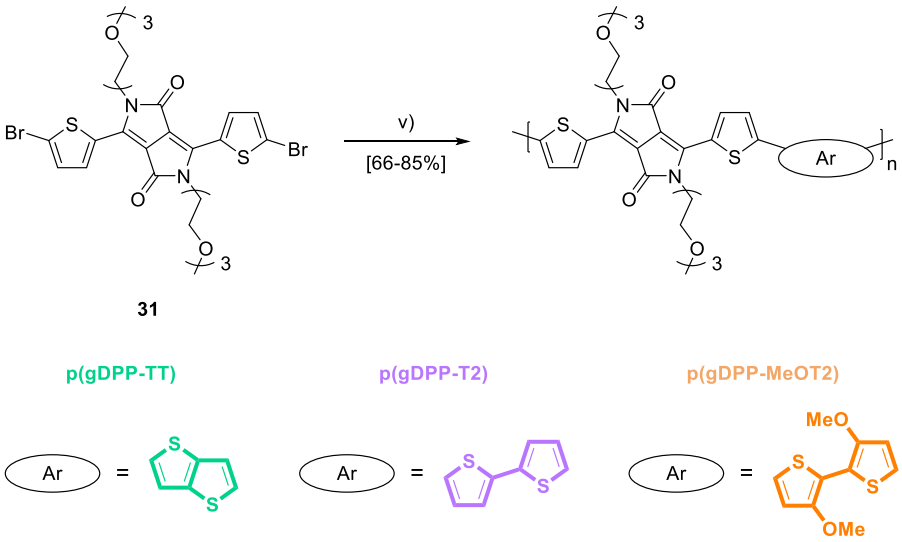

Scheme 4.2. *Synthesis of* ***p(gDPP-TT)***, ***p(gDPP-T2)***, *and* ***p(gDPP-MeOT2)***. *Reagents and conditions: v) 2,5-bis(trimethylstannyl)thieno[3,2-b]thiophene, 5,5'-bis(trimethylstannyl)-2,2'-bithiophene, and 3,3'-dimethoxy-5,5'-bis(trimethylstannyl)-2,2'-bithiophene (1.0 equiv.), Pd_2dba_3 (2 mol%), $P(o\text{-}OMePh)_3$ (8 mol%), toluene, 120 °C.*

4.4 Polymer Characterisation

p(gDPP-TT), **p(gDPP-T2)**, and **p(gDPP-MeOT2)** all exhibited good solubility in chloroform, allowing for facile solution processing. Determination of the polymers' molecular weights from conventional gel permeation chromatography (GPC) measurements, nonetheless, proved to be inconclusive, affording unrealistically high molecular weight numbers as previously reported for alternative D-A copolymers functionalised with EG side-chains.[112] The polymeric nature of the polymers could nonetheless be evidenced by the similar ^{1}H NMR and UV-Vis spectra incurred by **p(gDPP-TT)**, **p(gDPP-T2)**, and **p(gDPP-MeOT2)** compared to their alkyl counterparts.[233,234,247] In particular, as the optical gap ($E_{g,opt}$) of conjugated polymers typically only saturates upon reaching conjugated polymer backbone lengths of 10 to 15 repeat units,[248] it is, therefore, possible to deduct the polymeric nature of the developed materials.

4.4.1 Optical and Electrochemical Properties

UV-Vis absorption spectroscopy was performed on as-cast polymer films, see **Figure 4.3**. Each polymer exhibited a maximum absorption wavelength ($\lambda_{max,film}$) above 800 nm, specifically **p(gDPP-TT)**, **p(gDPP-T2)**, and **p(gDPP-MeOT2)** at 834 nm, 811 nm, and 915 nm, respectively. For each polymer, this optical transition was ascribed to intramolecular charge transfer (ICT).[249–251] **p(gDPP-TT)** and **p(gDPP-T2)** also featured relatively well-resolved vibronic features, which were ascribed to the polymers' 0-0 and 0-1 transitions, respectively. Conversely, the optical trace of **p(gDPP-MeOT2)** did not display any pronounced fine structure, suggesting a lower degree of order in its solid state compared to **p(gDPP-TT)** and **p(gDPP-T2)**. The loss in vibrational fine structure upon substituting the 2,2'-bithiophene unit in the polymer's conjugated backbone with a 3,3'-dimethoxy-2,2'-bithiophene one is consistent with previous literature.[112] Although the origin of the loss in structural order has not yet been identified, the added steric bulk around the conjugated polymer backbone might prevent efficient polymer packing in the solid state, thus resulting in reduced order. Going from the solid state to solution, the absorption profiles of the polymers remained virtually unchanged, with the polymers' maximum absorption wavelength in solution ($\lambda_{max,soln}$) lying close to their corresponding $\lambda_{max,film}$, indicative of pre-aggregation in chloroform solution. The tendency of the polymers to pre-aggregate in solution therefore also helps to explain the difficulty in accurately recording their molecular weights from the GPC measurements.

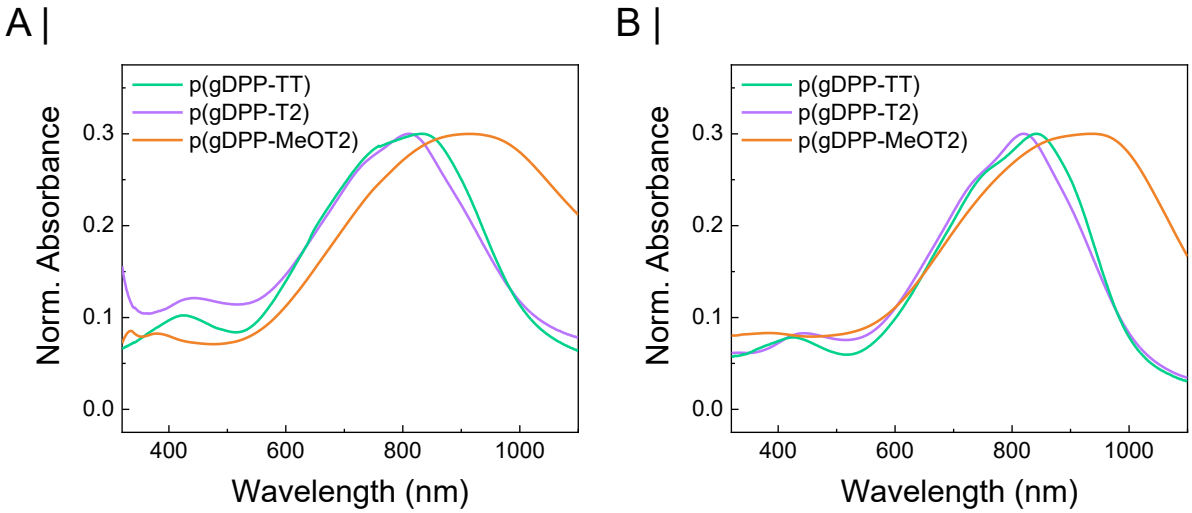

Figure 4.3. *Normalised UV-Vis absorption spectra of* ***p(gDPP-TT)***, ***p(gDPP-T2)***, *and* ***p(gDPP-MeOT2)*** *in a) as-cast thin films and b) dilute chloroform solutions.*

The optical gaps were estimated from the absorption onset of the thin film spectra, with **p(gDPP-TT)**, **p(gDPP-T2)**, and **p(gDPP-MeOT2)** all incurring relatively low values of 1.22 eV, 1.22 eV, and 0.96 eV, respectively. The origin of the polymers' low $E_{g,opt}$ can be understood from the strong push-pull character along the conjugated polymer backbone, see **Section 1.2.3**. **p(gDPP-MeOT2)**'s red-shifted $\lambda_{max,soln}$, $\lambda_{max,film}$, and $E_{g,opt}$ compared to **p(gDPP-TT)** and **p(gDPP-T2)** was ascribed to the methoxy substituents on the MeOT2 unit pushing additional electron density onto the conjugated polymer backbone, therefore leading to a shallowing of the polymers' ionisation potential (*IP*), which was later confirmed by cyclic voltammetry, *vide infra*.

Table 4.1. *Summary of the polymers' optoelectronic properties.*

Polymer	$\lambda_{max,film}$ (nm)	$\lambda_{max,soln}$ (nm)[a]	$E_{g,opt}$ (eV)[b]	$E_{ox,org}$ (V vs Ag/AgCl)[c]	*IP* (eV)	$E_{ox,aq}$ (V vs Ag/AgCl)[d]
p(gDPP-TT)	834	840	1.22	+0.10	5.09	+0.45
p(gDPP-T2)	811	821	1.22	+0.05	5.04	+0.38
p(gDPP-MeOT2)	915	925	0.96	-0.41	4.58	-0.07

[a]*In dilute chloroform solutions.* [b]*Calculated from the onset of absorption in thin film.* [c]*Recorded employing a 0.1 M solution of TBA* PF_6 *in acetonitrile as the supporting electrolyte.* [d]*Recorded employing a 0.1 M solution of NaCl in distilled water as the supporting electrolyte.*

The electrochemical processes occurring in the polymers upon the application of an external bias were evaluated by cyclic voltammetry (CV). The CV traces recorded for the polymers in an organic (0.1 M solution of TBA PF_6 in acetonitrile) and aqueous (0.1 M solution of NaCl in distilled water) supporting electrolyte are shown in **Figure 4.4**, with the polymers' onset of oxidation in organic media ($E_{ox,org}$), onset of oxidation in aqueous media ($E_{ox,aq}$), and *IP* listed in **Table 4.1**. As follows from **Figure 4.4**, it was possible to reversibly oxidise and reduce each semiconductor upon application of a positive electrical bias. Moreover, while **p(gDPP-TT)** and **p(gDPP-T2)** incurred similar onsets of oxidation, the onset of oxidation of **p(gDPP-MeOT2)** was shifted to significantly lower values, which was attributed to the presence of the electron releasing methoxy substituents on the MeOT2 unit, resulting in increased electron density on the conjugated polymer backbone and shallowing the polymer's *IP*. A similar 0.4 eV reduction in the *IP* upon substitution of the T2 and TT comonomer with MeOT2 was also reported for the polymers' alkylated analogues.[233,234,247]

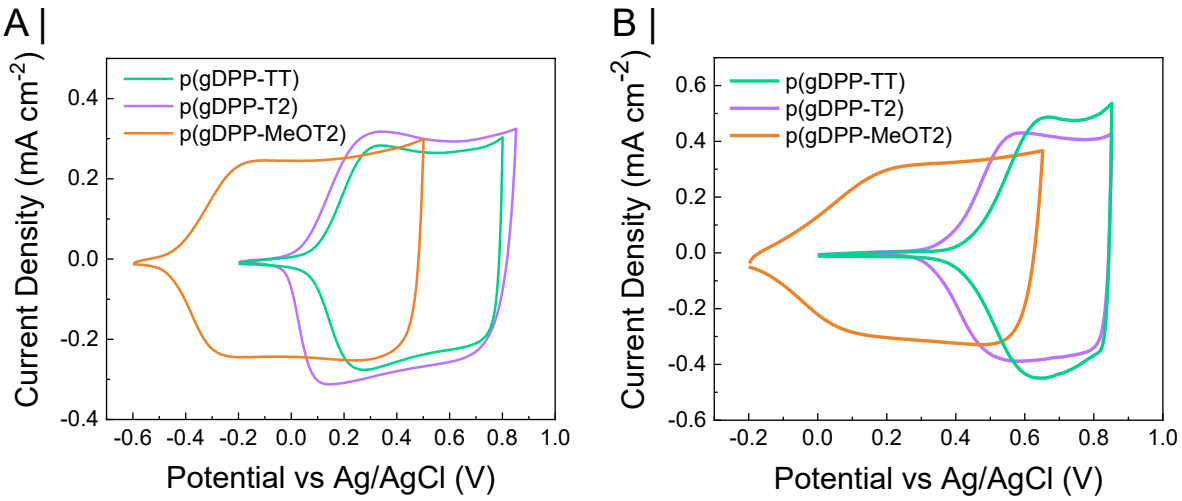

Figure 4.4. *Cyclic voltammograms recorded for* ***p(gDPP-TT)****,* ***p(gDPP-T2)****, and* ***p(gDPP-MeOT2)*** *employing a) a 0.1 M TBA PF_6 in acetonitrile and b) a 0.1 M solution of NaCl in distilled water as the supporting electrolyte.*

Insights into the kinetics of the electrochemical doping process in an aqueous medium were obtained by recording the maximum anodic current (I_{max}) as a function of the employed scan rate. The various curves recorded for the semiconductors are shown in **Figure 4.5**, whereby, potential scanning rates between 10-1250 mV s^{-1} were employed, and a negligible charge transfer resistance between the electrode and the polymer film was assumed. As evidenced from **Figure 4.5**, the I_{max} recorded for **p(gDPP-TT)** and **p(gDPP-T2)** was linearly dependent on the utilised scan rate up to a rate of 250 mV s^{-1}. Conversely, further increases in the employed scan rate resulted in a deviation from linearity of I_{max} on the scan rate with the relationship assuming a behaviour closer to I_{max} α scan rate$^{0.5}$, indicative of a diffusion limited current.[252,253] On the other hand, **p(gDPP-MeOT2)**'s I_{max} dependence on the employed scan rate remained linear across the entire probed scan rate range, highlighting that the use of the MeOT2 unit is able to overcome the kinetic limitations of the charging process faced by **p(gDPP-TT)** and **p(gDPP-T2)**. Having determined from thin film UV-Vis measurements that the MeOT2 unit in **p(gDPP-MeOT2)** results in a decreased solid state order compared to **p(gDPP-TT)** and **p(gDPP-T2)**, it appears that the reduced order in

p(gDPP-MeOT2) is responsible for the faster electrochemical charging process. This hypothesis would also be in line with previous literature, in which a higher ionic mobility was demonstrated in less ordered phases of conjugated polymers.[80,81]

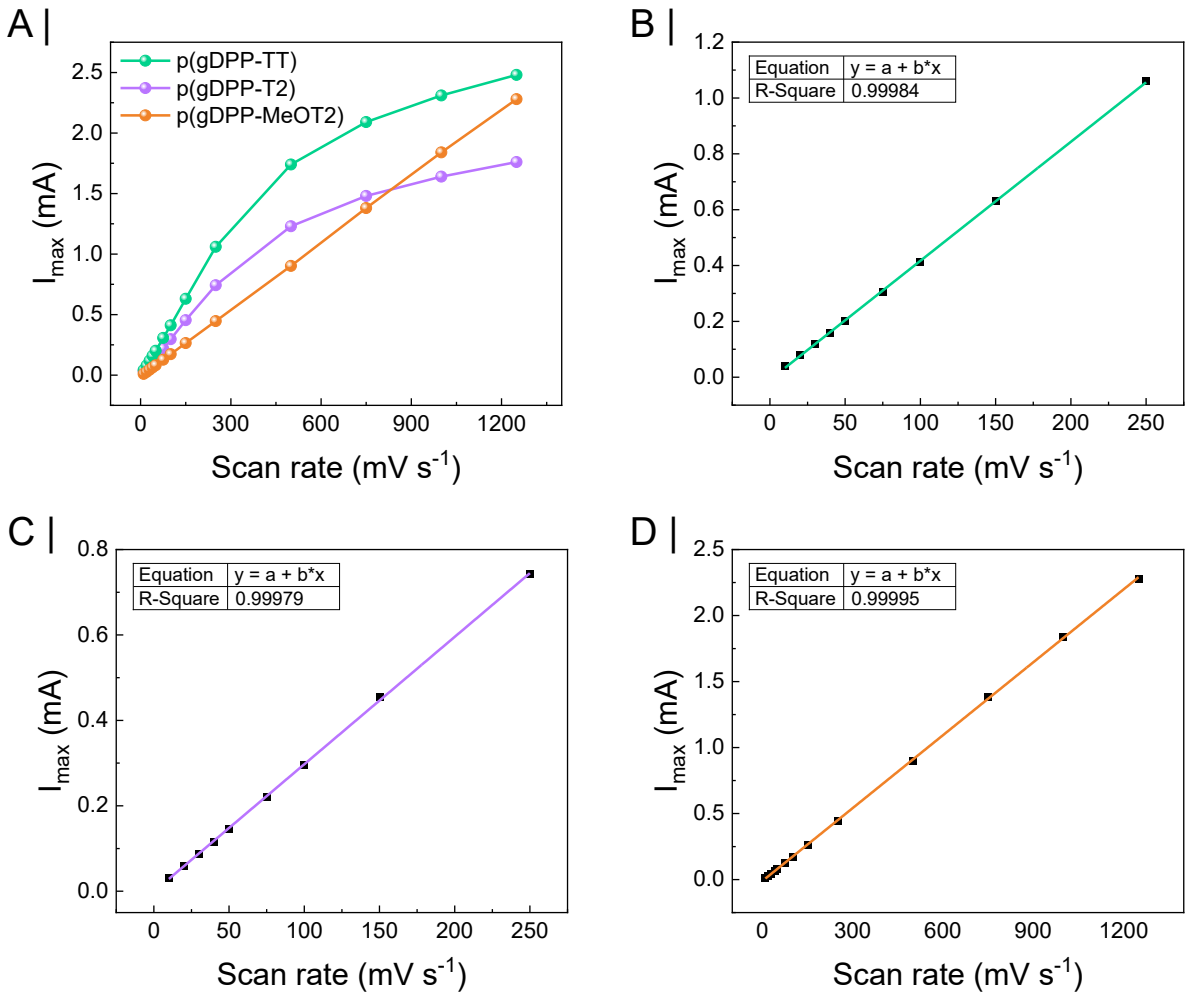

Figure 4.5. *a) Dependence of the polymers' maximum anodic current (I_{max}) on the employed scan rate in cyclic voltammetry experiments utilising an aqueous 0.1 M NaCl solution as the supporting electrolyte. Magnified plots of the I_{max} against the employed scan rate for b)* ***p(gDPP-TT)****, c)* ***p(gDPP-T2)****, and d)* ***p(gDPP-MeOT2)*** *highlighting the linearity of the relationship over the shown scan rate range.*

Spectroelectrochemical measurements were conducted to assess the electrochromic properties of the semiconductors. The spectroelectrochemical measurements were performed employing a three-electrode set-up and an aqueous 0.1 M sodium chloride solution as the supporting electrolyte. As shown in **Figure 4.6**, **p(gDPP-TT)**, **p(gDPP-T2)**,

and **p(gDPP-MeOT2)** exhibited a considerable response in their optical absorption spectra when subjecting the polymer films to an external applied bias. Specifically, a clear depression of the polymers' ICT band ~ 900 nm could be observed upon the application of a positive applied potential, thus suggesting the formation of positively charged species of the polymers. This observation was reaffirmed for **p(gDPP-TT)** and **p(gDPP-T2)** with the rise of a new longer wavelength absorption feature and appearance of an isosbestic point. Conversely, due to the limited wavelength range of the UV-Vis spectrometer's photodetector, it was not possible to detect the formation of the lower energy absorption feature. Nonetheless, given the similarity of the three polymers' CV curves and the depression of the ICT band upon the application of a positive bias, it is highly likely that **p(gDPP-MeOT2)** is also capable of forming analogous hole polarons as **p(gDPP-TT)** and **p(gDPP-T2)** in response to positive applied potentials. Finally, the reversible nature of the polymers' electrochromism further confirmed their compatibility to be cycled stably in an aqueous electrolyte and their suitability as OECT channel materials.

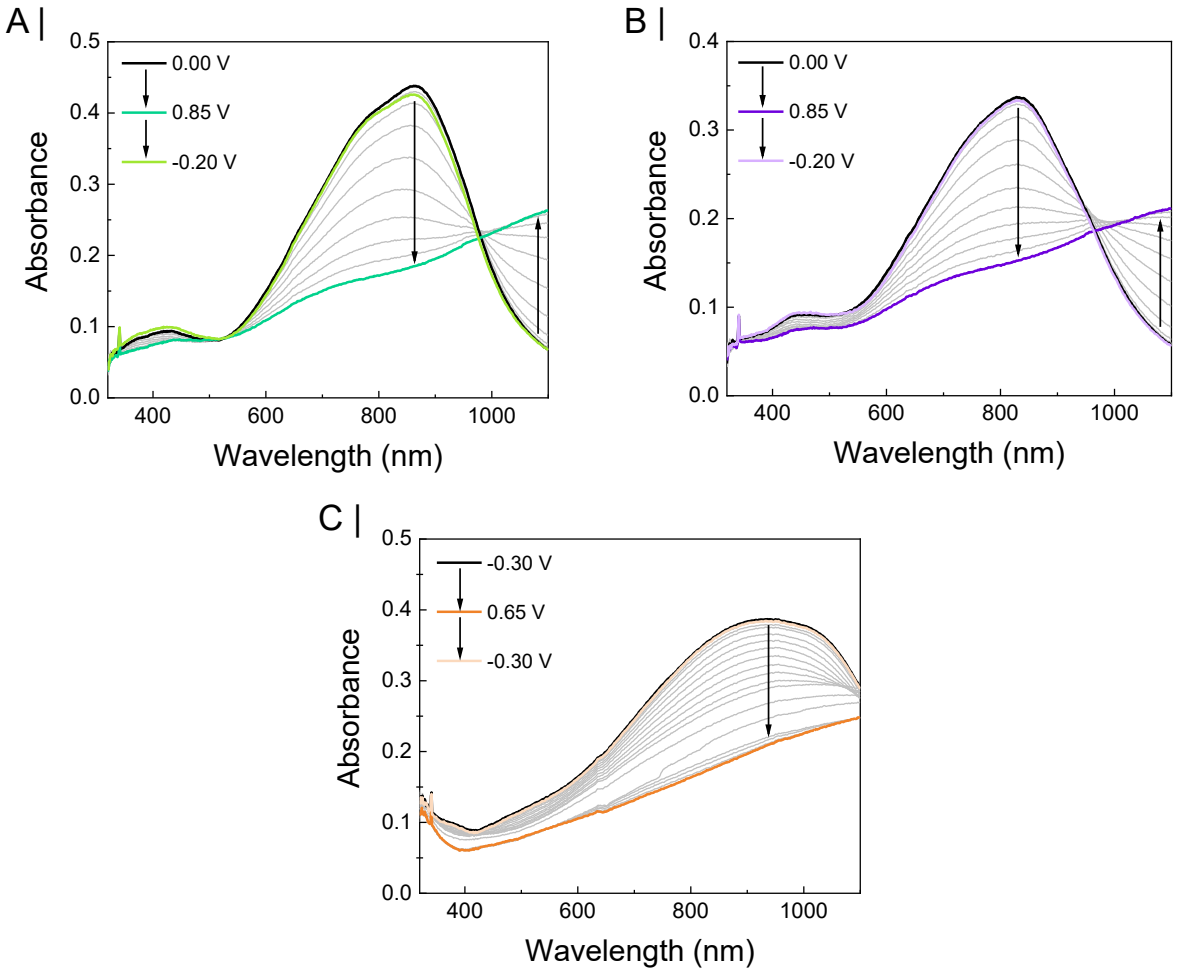

Figure 4.6. *Spectroelectrochemistry measurements of a)* ***p(gDPP-TT)****, b)* ***p(gDPP-T2)****, and c)* ***p(gDPP-MeOT2)*** *in a 0.1 M aqueous NaCl supporting electrolyte.*

4.4.2 Morphological Properties

Grazing incidence wide-angle X-ray scattering (GIWAXS) experiments were conducted to assess the structural organisation of as-cast **p(gDPP-TT)**, **p(gDPP-T2)**, and **p(gDPP-MeOT2)** films, with the two-dimensional GIWAXS patterns and linecuts recorded for the three OMIECs given in **Figure 4.7**.

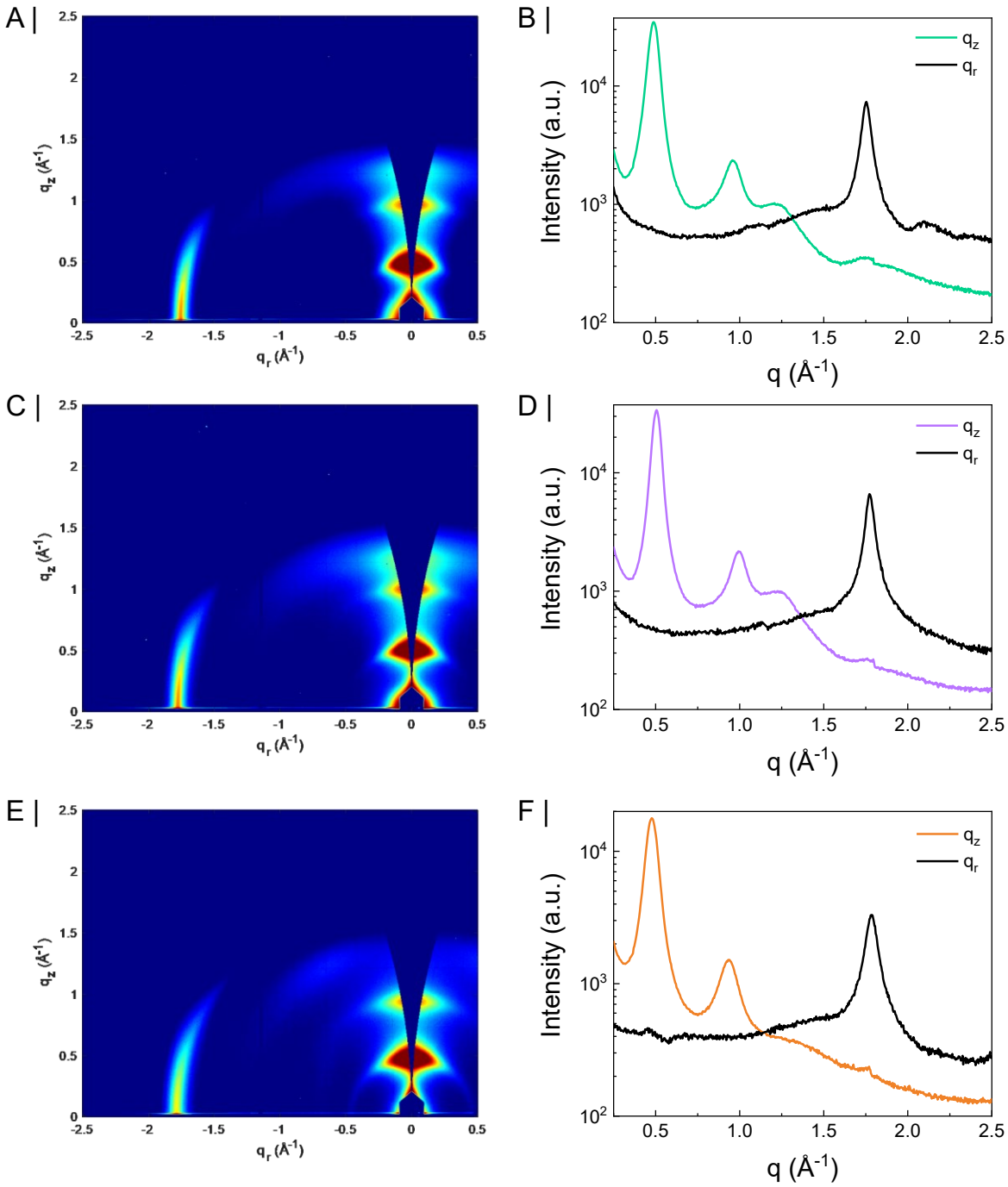

Figure 4.7. *GIWAXS scattering patterns (left panels) and in-plane (q_r) and out-of-plane (q_z) linecuts (right panels) recorded for a,b)* ***p(gDPP-TT)****, c,d)* ***p(gDPP-T2)****, and e,f)* ***p(gDPP-MeOT2)****, respectively.*

As evidenced from **Figure 4.7**, all polymers preferentially adopted an edge-on orientation with a strong in-plane (010) π-π stacking present at $q \sim 1.77$ Å^{-1}. Specifically, comparable π-π stacking distances between 3.52-3.58 Å were obtained across the polymer series and were thus ~ 0.2 Å narrower compared to each of their alkylated counterparts.[233,234,247] A

similar decrease in π-π stacking distance upon substitution of pendant alkyl side-chains with EG-based ones has been reported for alternative conjugated polymer backbones and has been attributed to the increased flexibility of the pendant EG side-chains.[254,255] This increased flexibility of EG-based side-chains, on the other hand, stems from the lower rotational barriers around C–O compared to C–C bonds, for which corresponding energy barriers of 0.08 eV and 0.11 eV have been calculated in the literature.[256]

The polymers also exhibited two clear orders of out-of-plane lamellar scattering (100) and (200), confirming the edge-on orientation of the crystallites in the polymers. Here, similar lamellar stacking distances ~ 13 Å were obtained for all three polymers, which were significantly shorter compared to those obtained for alternative triethylene glycol functionalised conjugated polymers, for which lamellar stacking distances between 15-18 Å have been reported.[126,151,155,172] Consequently, this implied either a high degree of torsion across each EG repeat unit as one might predict from the gauche effect or the interdigitation of the triethylene glycol side-chains.

To quantitatively measure the polymers' long-range packing order in the π-π stacking direction, the GIWAXS data were fit to extract the coherence length (L_c) from the (010) peak.[257] From the full width half maximum (FWHM) of the (010) peak, L_C values of 102 Å, 111 Å, and 78 Å were obtained for **p(gDPP-TT)**, **p(gDPP-T2)**, and **p(gDPP-MeOT2)**, respectively, therefore suggesting a higher degree of order within **p(gDPP-TT)** and **p(gDPP-T2)** and confirming the findings from thin film UV-Vis absorption spectroscopy. In addition to longer coherence lengths, **p(gDPP-TT)** and **p(gDPP-T2)**'s GIWAXS scattering patterns also displayed a clear peak ~ 1.2 $Å^{-1}$ in the out-of-plane direction. This peak could however not be attributed to being a multiple of either the lamellar, π-π, or backbone scatterings from the main crystallite population. Instead, the peak is speculated to

arise due to scatterings related to the triethylene glycol side-chains and thus be of similar origin as to the one observed in **p(gDPP-TT)**'s and **p(gDPP-T2)**'s alkyl counterparts.[258,259]

4.4.3 Density Functional Theory Simulations

The experimental data collected for the polymers were complemented with density functional theory (DFT) simulations. As common in the field, the conjugated polymer backbone length was reduced to four repeat units in order to minimise computational costs.[166] Furthermore, as the main outcome of the DFT simulations was to investigate the energetics of the conjugated polymer backbone rather than the interactions of the polymers' side-chains, the polymers' EG solubilising chains were replaced by short methyl caps.[112,166]

The optimised geometries of the polymers were computed using the ωB97XD functional and the 6-31G* basis set. The DFT optimised structures alongside the graphical representation of the highest occupied molecular orbital (HOMO) of the three tetramers are shown in **Figure 4.8**. From **Figure 4.8**, it follows that the DFT optimised geometries of the three polymers shared many commonalities. In fact, all polymers incurred a similar dihedral angle between 1-2° across the C–C bond linking the DPP-core with the flanking thienyl rings. Similarly, dihedral angles between 17-22° were obtained for the C–C bond connecting the thienyl rings flanking the DPP core and the TT, T2, or MeOT2 comonomers, hence highlighting the planar nature of the entire conjugated backbone. Following the optimisation of the polymers' geometries, *IP* energies were calculated as the difference in the electronic energy of the polymers' neutral state and radical cation. *IP* values of 4.97 eV, 5.00 eV, and 4.67 eV were incurred for **p(gDPP-TT)**, **p(gDPP-T2)**, and **p(gDPP-MeOT2)**, respectively, thus being in close agreement with those recorded from the experimental CV measurements, see **Section 4.4.1**.

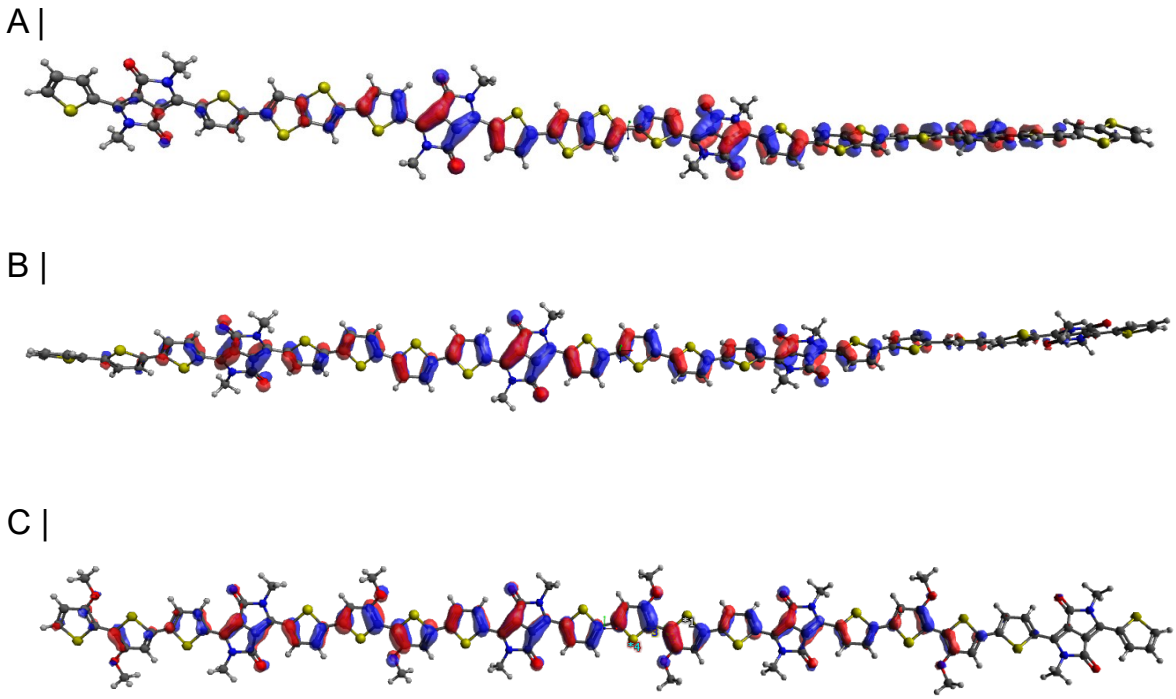

Figure 4.8. *Optimised DFT geometries and graphical representation of the HOMO of a)* ***p(gDPP-TT)****, b)* ***p(gDPP-T2)****, and c)* ***p(gDPP-MeOT2)*** *employing a ωB97XD functional, a 6-31G* basis set, and a 0.02 isovalue.*

To gain a better understanding of how the polymers' different aromatic building blocks affect the electron density on the conjugated polymer backbone, orbital population analyses of the polymers' neutral state were conducted. Such calculations have been employed in previous literature to rationalise the varying stability of EG functionalised conjugated polymers for OECT devices.[166] A fundamental requirement of the orbital population analysis approach is the requirement to divide the oligomer chains into smaller segments and determine the contribution of each segment to the orbital under study. The tetramers were therefore divided into polymer fragments as shown in **Figure 4.9**, *i.e.* analogously as to previous literature.[166]

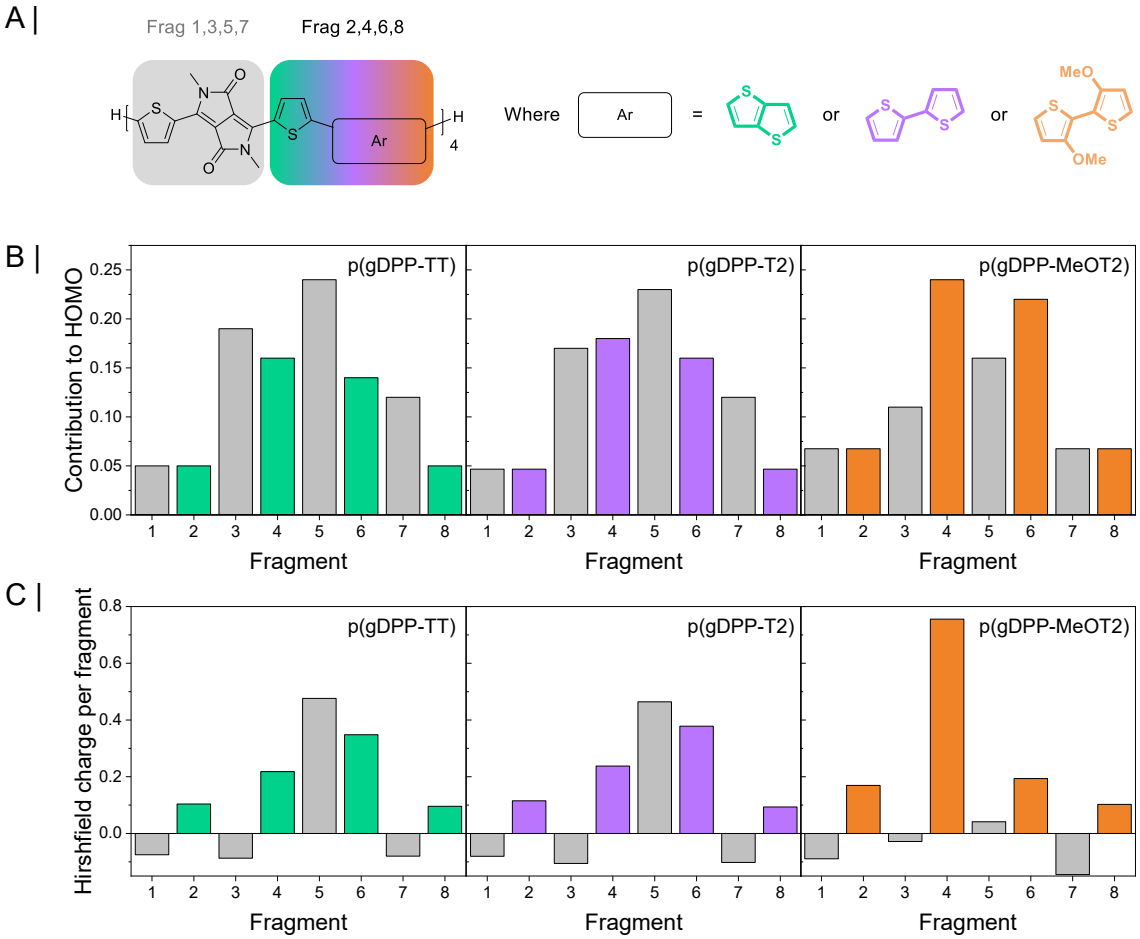

Figure 4.9. *a) Illustration highlighting the subdivision of the oligomers into shorter segments. b) DFT population analysis highlighting the contribution of the individual fragments to the oligomers' HOMO. c) DFT calculations of the charge distribution over the various polymer fragments in the polymers' polaronic form.*

From **Figure 4.9** it can be seen that **p(gDPP-TT)** and **p(gDPP-T2)** featured similar HOMO distributions with the HOMO primarily extending over fragments 3-7. Conversely, **p(gDPP-MeOT2)**'s HOMO appeared to be more localised with major contributions solely stemming from fragments 3-6. Furthermore, the HOMO in **p(gDPP-TT)** and **p(gDPP-T2)** had stronger contributions from the DPP-based (*i.e.* odd numbered) fragments compared to the one of **p(gDPP-MeOT2)**, in which the aryl comonomer-based (*i.e.* even numbered) fragments dominated the HOMO contribution. A quantitative indicator highlighting these findings is the sum of the fragment orbital distributions. Specifically, while the sum of the

DPP-based fragments in **p(gDPP-TT)** and **p(gDPP-T2)** contributed towards 60% and 57% of the oligomers' HOMO, only 40% of the HOMO was localised on the DPP-based fragments in **p(gDPP-MeOT2)**. Analogous findings were incurred for Hirshfeld charge analyses of the polymers' radical cation from (*i.e.* polaron), see **Figure 4.9**, which is of particular relevance given the polymers' electrochemical oxidation during device operation. **Figure 4.9** indicates that the positive charge is spread more evenly and over a greater number of fragments in **p(gDPP-TT)** and **p(gDPP-T2)** compared to **p(gDPP-MeOT2)**. Specifically, while in **p(gDPP-TT)** and **p(gDPP-T2)** the positive charge is spread over both aryl comonomer-based and DPP-based fragments, in **p(gDPP-MeOT2)** the charge is virtually confined to a single fragment (4). The polaron formed upon oxidation of **p(gDPP-TT)** and **p(gDPP-T2)** can therefore be considered as being more delocalised compared to the one in **p(gDPP-MeOT2)** and may thus aid electronic charge carrier mobility by two means. First, the more extended nature of the polaron should result in a lower polaron binding energy, therefore, benefiting both intra- and intermolecular charge carrier transport.[260] In addition, spreading of the charge over more atoms also incurs a larger surface area for charges to hop across neighbouring polymer chains, further benefiting intermolecular charge carrier transport. Ultimately, the more delocalised nature of the HOMO and in turn the polaron in **p(gDPP-TT)** and **p(gDPP-T2)** was attributed to the closer energy match between the DPP-based and aryl comonomer-based fragments, thereby effectively minimising the D-A character across the conjugated polymer backbone.

4.5 OECT Performance

The polymers' ability to undergo stable and reversible electrochemical doping in aqueous media rendered the materials promising candidates for OECT channel materials. OECT

devices were fabricated according to previous literature,[112,126,172] and the polymers deposited from chloroform solutions without conducting any additional pre- or post-processing treatments. OECTs were operated in a 0.1 M aqueous NaCl solution employing an Ag/AgCl couple as the gate electrode. The polymers' output, transfer, and transconductance characteristics are shown in **Figure 4.10** and their steady-state performance summarised in **Table 4.2**.

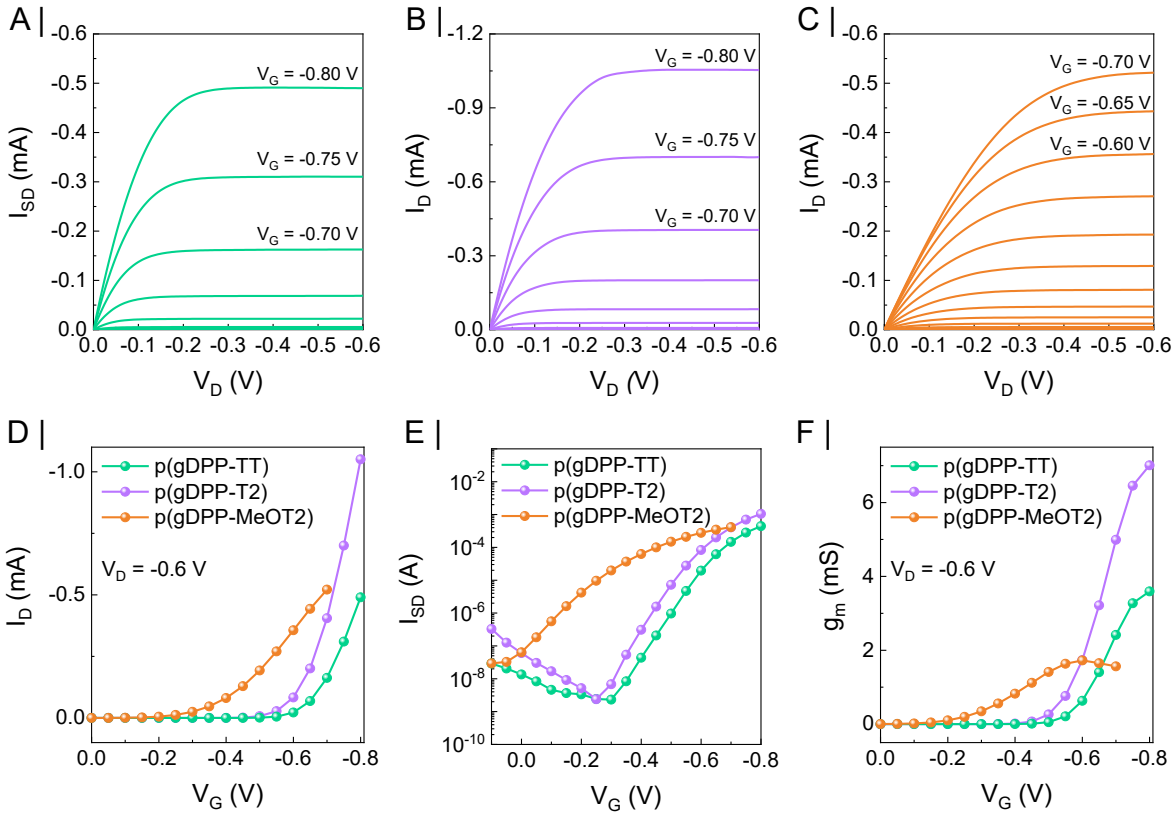

Figure 4.10. *Representative output curves recorded for a)* ***p(gDPP-TT)****, b)* ***p(gDPP-T2)****, and c)* ***p(gDPP-MeOT2)****. Corresponding transfer curves plotted on a d) linear and e) logarithmic y-axis scale. f) Corresponding transconductance curves. All devices featured a channel width (W) of 100 µm and length (L) of 10 µm and were operated in a 0.1 M aqueous NaCl solution.*

As illustrated in **Figure 4.10**, the current flowing across each device increased upon decreasing the applied gate voltage, highlighting the accumulation mode of behaviour of all three polymers. This was confirmed from the devices' threshold voltages (V_{Th}), see **Table 4.2**, which were -0.55 V for **p(gDPP-TT)**, -0.53 V for **p(gDPP-T2)**, and -0.27 V for

p(gDPP-MeOT2). Note how the trend in V_{Th} closely matches the polymers' experimental and simulated *IP* values. A direct consequence of the deeper *IP* values of **p(gDPP-TT)** and **p(gDPP-T2)** were improved on/off ratios, see **Figure 4.10**, with both polymers incurring on/off ratios on the order of 10^5, while **p(gDPP-MeOT2)** incurred a lower one around 10^4. The improved on/off ratios in **p(gDPP-TT)** and **p(gDPP-T2)** came predominantly from a decrease in their off current, which had previously been demonstrated to be linked to the tendency of OECT channel materials to undergo spontaneous oxygen reduction reactions (ORR) in their dedoped states. Specifically, polymers with *IP* values > 4.9 eV were found to be stable towards the ORR, hence explaining why **p(gDPP-TT)** and **p(gDPP-T2)** for which *IP* values ~ 5.05 eV had been obtained were less prone to ORR than **p(gDPP-MeOT2)** for which an *IP* value ~ 4.6 eV was measured.

The peak transconductances (g_m) recorded for the OECTs were 3.1 mS (W = 100 µm, L = 10 µm, and d = 123 nm) for **p(gDPP-TT)**, 6.3 mS (W = 100 µm, L = 10 µm, and d = 90 nm) for **p(gDPP-T2)**, and 1.4 mS (W = 100 µm, L = 10 µm, and d = 82 nm) for **p(gDPP-MeOT2)** and were incurred while applying a V_G of -0.8 V, -0.8 V, and -0.6 V, respectively.

Table 4.2. *Summary of the polymers' OECT steady-state performance.*

Polymer	d (nm)	V_{Th} (V)	g_m (mS)	μC^* (F cm^{-1} V^{-1} s^{-1})[a]	C^* (F cm^{-3})[b]	μ (cm^2 V^{-1} s^{-1})[c]
p(gDPP-TT)	123	-0.55	3.1	125	184	0.57
p(gDPP-T2)	90	-0.53	6.3	342	196	1.55
p(gDPP-MeOT2)	82	-0.27	1.4	57	169	0.28

[a]*Measured from the slope of g_m as a function of $(Wd/L)(V_{Th}-V_G)$.* [b]*Calculated from EIS curves fit to an $R_s(R_p||C)$ circuit.*[89] [c]*Determined from the transistor saturation mobility using the respective C* values.*[116,212,213]

To exclude any device geometry and operating condition effects from the polymers' steady-state performance, the polymers μC^* was calculated. μC^* values of 125 F cm^{-1} V^{-1} s^{-1}, 342 F cm^{-1} V^{-1} s^{-1}, and 57 F cm^{-1} V^{-1} s^{-1} were obtained for **p(gDPP-TT)**, **p(gDPP-T2)**, and **p(gDPP-MeOT2)**, respectively. **p(gDPP-T2)** therefore incurred the highest OECT steady-state performance, with **p(gDPP-TT)** incurring a slightly lower one and **p(gDPP-MeOT2)** the lowest. In comparison to previously published D-A copolymers for which μC^* products in the range of 0.1-10 F cm^{-1} V^{-1} s^{-1} have been reported,[125,240,241] the polymers developed herein therefore incurred significantly higher performances. In fact, all polymers incurred similar OECT steady-state performances compared to the best performing all-donor counterparts, for which μC^* values between 50-500 F cm^{-1} V^{-1} s^{-1} have been obtained.[115,126,151,155,172]

To gain a deeper insight into the varying OECT performance recorded across the developed polymer series, the polymers' C^* and μ were assessed individually. Electrochemical impedance spectroscopy (EIS) was conducted on polymer-coated gold electrodes to calculate their C^*. The EIS curves recorded for **p(gDPP-TT)**, **p(gDPP-T2)**, and **p(gDPP-MeOT2)** are given in **Figure 4.11**. From the EIS data, similar C^* values between 169-196 F cm^{-3} were calculated for the three polymers, indicating that variation in the polymers' aryl comonomer did not have a strong effect on their ability to be charged volumetrically. Moreover, the polymers' C^* values were also similar to those reported for alternative EG functionalised D-A copolymers developed for OECT applications.[112,240,241]

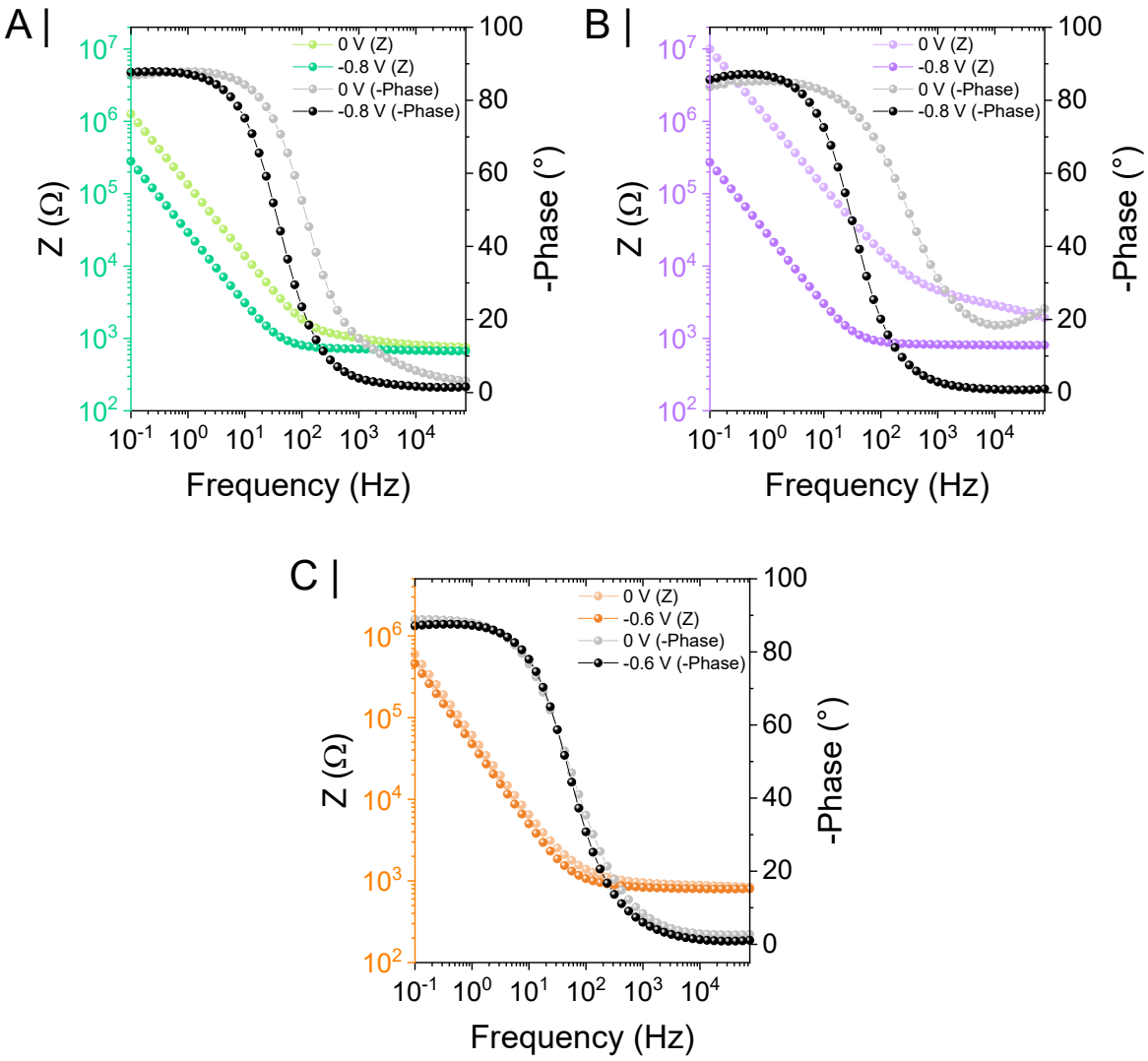

Figure 4.11. *Electrochemical impedance spectroscopy of a)* ***p(gDPP-TT)****, b)* ***p(gDPP-T2)****, and c)* ***p(gDPP-MeOT2)*** *while applying a V_G of 0 V or the one incurring the highest OECT performance.*

Considering the similar C^* values recorded for the polymers, the primary cause for their varying OECT performance was likely to be due to their different ability to conduct electronic charge carriers. In fact, the polymers' μ values reported in **Table 4.2** confirmed this theory with **p(gDPP-TT)**, **p(gDPP-T2)**, and **p(gDPP-MeOT2)** yielding a μ of 0.57 cm^2 V^{-1} s^{-1}, 1.55 cm^2 V^{-1} s^{-1}, and 0.28 cm^2 V^{-1} s^{-1}, respectively. **p(gDPP-TT)** and **p(gDPP-T2)**'s superior mobility compared to **p(gDPP-MeOT2)** was in part ascribed due to their higher degree of order in the solid state, as confirmed by thin film UV-Vis analysis and GIWAXS data. Moreover, as highlighted from the DFT simulations, the closer energy match between

the donor and acceptor components in **p(gDPP-TT)**'s and **p(gDPP-T2)**'s conjugated polymer backbone also resulted in a more delocalised polaron, further benefiting their electronic charge carrier properties. It is speculated that this is also one of the reasons why **p(gDPP-MeOT2)** was able to incur a higher μ of 0.28 $cm^2\ V^{-1}\ s^{-1}$ compared to its pyridine flanked DPP counterpart, **p(gPyDPP-MeOT2)** for which a μ of 0.03 $cm^2\ V^{-1}\ s^{-1}$ was reported.[112] This theory seems likely, given that the two polymers shared several commonalities in other properties that can impact electronic charge carrier transport, such as the lack of any vibronic fine structure in their thin film UV-Vis traces, comparable π-π stacking distances ~ 3.5 Å and similar degrees of order in their lamellar scattering. This hypothesis may thus also explain the excellent electronic charge carrier mobilities typically incurred for OMIECs based on an all-donor conjugated polymer backbone such as **PEDOT:PSS**, **p(g2T-TT)**, and the polymers developed in **Chapter 3**.[80,126,155]

Complementary to their steady-state performance, the operational stability of OECTs based on the various polymers was evaluated by repeated electrochemical addressing over 100 min (~ 600 doping/dedoping cycles) and recording the percentage retention of their initial drain current ($I_D/I_{D,0}$) as a function of switching cycles. Due to differences in the energetics of the polymers' conjugated backbones, care had to be taken to enable a fair stability comparison across the three different channel materials. Similar to previous studies, to ensure that each of the three polymers reached a similar doping level in devices, the 'ON' V_G was therefore set to -0.1 V lower than the corresponding polymers' V_{Th}.[200] The current stability traces of the polymers upon repeated electrochemical addressing are shown in **Figure 4.12**.

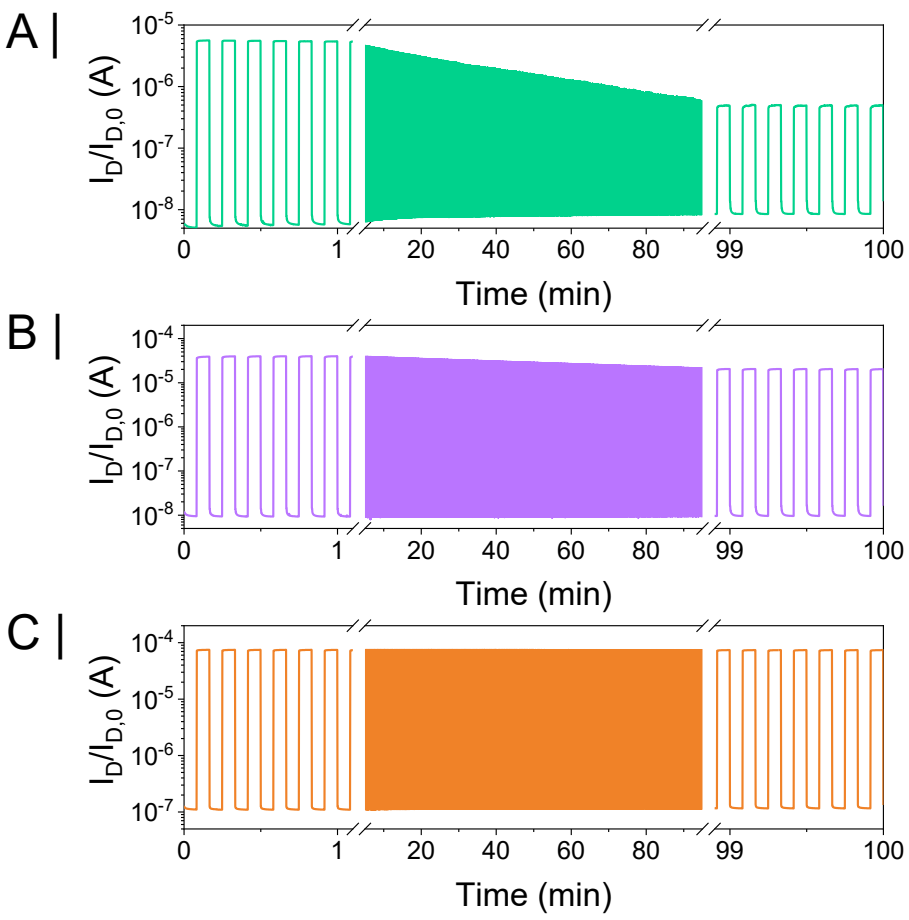

Figure 4.12. *Operational stability of a)* ***p(gDPP-TT)****, b)* ***p(gDPP-T2)****, and c)* ***p(gDPP-MeOT2)*** *upon repeated electrochemical biasing in a 0.1 M aqueous NaCl supporting electrolyte. Note that the V_G defining the 'ON' state of the polymers was set to be -0.1 V lower than the corresponding polymers' V_{Th}.*

From **Figure 4.12** it can be inferred that **p(gDPP-TT)**, **p(gDPP-T2)**, and **p(gDPP-MeOT2)** yielded $I_D/I_{D,0}$ percentage values of 9%, 53%, and 99%, respectively, with the trend in $I_D/I_{D,0}$ mirroring the polymers' recorded *IP* values. Specifically, upon lowering the polymers' *IP* a progressive increment in the operational stability could be observed due to superior stabilisation of the resulting hole polaron, as already reported in previous literature.[166,200] Note, however, that additional factors such as the polymers' degree of volumetric swelling upon repeated electrochemical addressing, see **Chapter 3**, can also have an impact on the measured $I_D/I_{D,0}$ values and may hence help to explain the relatively large difference in

$I_D/I_{D,0}$ recorded between **p(gDPP-TT)** and **p(gDPP-T2)**, despite **p(gDPP-TT)**'s *IP* only being 0.05 eV larger than the one of **p(gDPP-T2)**.

4.6 Conclusions and Outlook

In this chapter, three novel D-A polymers based on the DPP unit have been synthesised and utilised as OECT channel materials. OECT evaluation of the polymers indicated each of the three developed polymers to operate as p-type accumulation mode material, incurring μC^* values up to ~ 350 F cm^{-1} V^{-1} s^{-1}. Consequently, the steady-state OECT performance incurred by the DPP-based polymers utilised herein compares favourably with the best performing EG functionalised semiconductors reported to date and represents a considerable improvement relative to previously developed D-A polymers for which μC^* values between 0.1-10 F cm^{-1} V^{-1} s^{-1} have been achieved. Of the newly developed materials, the polymers employing either a T2 (**p(gDPP-T2)**) or TT comonomer (**p(gDPP-TT)**) were found to yield the highest performances, which was attributed in part to their higher degree of order in the solid state compared to the polymer making use of a MeOT2 comonomer (**p(gDPP-MeOT2)**). Moreover, DFT simulations of the polymers also highlighted how the use of the T2 or TT units is beneficial in terms of delocalising the polymers' hole polaron, which is formed upon electrochemical doping of the polymers, over a larger number of atoms, therefore leading to superior electronic charge carrier mobilities. Importantly, as these computational simulations can be conducted prior to the actual synthesis of the materials, they are currently being envisaged as a particularly useful screening tool in the search of even higher performing OECT channel materials, thereby further aiding material development.

'We did not come to fear the future. We came here to shape it.'

— Barack Obama

5

Outlook and Future Work

The EG functionalised conjugated polymers developed within this thesis were found to incur high steady-state performances as OECT channel materials and are currently amongst the highest performing materials reported to date. The material advances made can be seen clearly from **Figure 5.1**, which compares the electronic charge carrier mobilities and volumetric capacitances reported for the OECT channel materials reported in **Chapter 3** and **Chapter 4** against relevant literature comparisons, respectively.

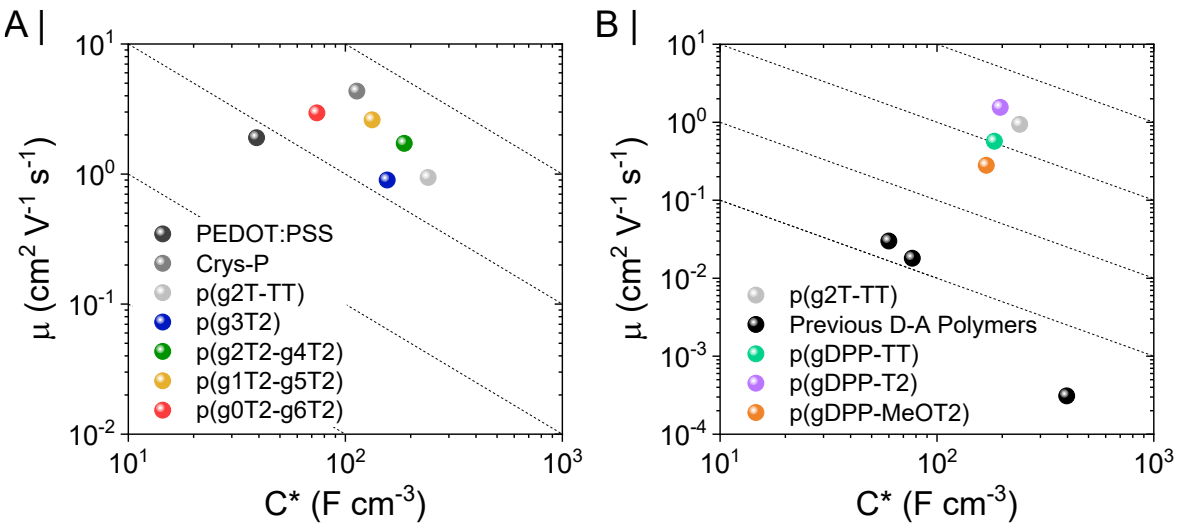

Figure 5.1. *OECT steady-state performance comparison of the polymers developed in a)* ***Chapter 3*** *and b)* ***Chapter 4*** *against relevant OECT benchmark channel materials. Data for* ***PEDOT:PSS*** *taken from reference* [115]*, for* ***Crys-P*** *from reference* [124]*, and for* ***p(g2T-TT)*** *from reference* [115]*. Previous D-A polymers include* ***p(gNDI-gT2)***, ***gBDT-gT2***, *and* ***p(gPyDPP-MeOT2)***, *whose data were obtained from reference* [115]*, reference* [115]*, and reference* [112]*, respectively.*

Although the polymers developed across **Chapters 2-4** incurred high OECT performances, one limitation across the designed polymer series was the exclusive use of ethylene glycol pendant side-chains, without consideration of alternative hydrophilic side-chains. In this context, two alternative side-chain motives that might be suitable candidates for the development of high-performance OECT channel materials are alternative polyether side-chains, such as propylene glycol (PG) or butylene glycol (BG), see **Figure 5.2**. Both PG-

based and BG-based non-conjugated polymers have been demonstrated to incur similar ion transport abilities to EG-based ones,[261,262] while simultaneously binding to significantly fewer water molecules per polyether repeat unit.[178] Consequently, this renders these more hydrophobic polyether side-chains promising candidates for the development of high-performance OECT channel materials.

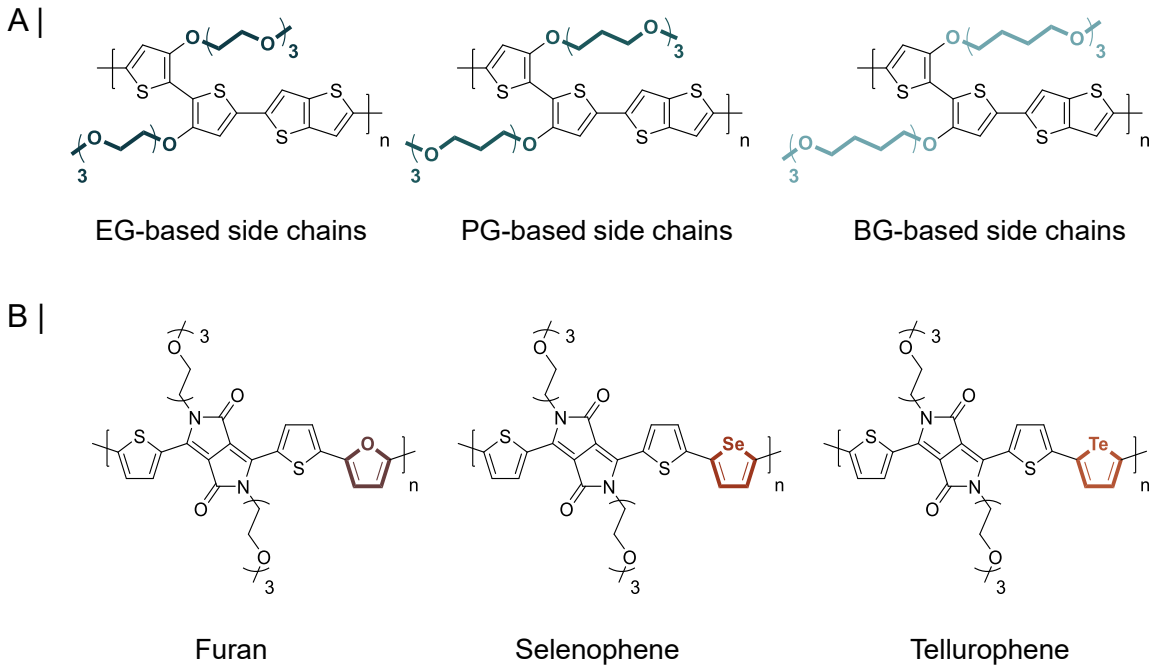

Figure 5.2. *a) Proposed polymer series making use of alternative polyether side-chains to modulate the polymers' swelling tendency. b) Proposed polymer series making use of chalcogen atom substitution to improve the polymers' electronic performance.*

In addition to the use of alternative side-chains, fine-tuning of the polymers' properties through chalcogen atom substitution may be another fruitful strategy to further maximise the polymers' OECT performance, operational stability, or biocompatibility, see **Figure 5.2**. For example, the use of selenophene and tellurophene comonomers rather than a thiophene one in DPP-based polymers has been found to double the recorded electronic charge carrier mobility in OFETs.[263] In particular, this was due to the heavier chalcogen atoms incurring

stronger intermolecular interactions across adjacent polymer chains in the solid state. The use of organoselenium and organotellurium compounds as OECT channel materials to be interfaced with biological systems may, however, come with reservations, given the on average higher toxicity of organoselenium and organotellurium compounds compared to their organosulfur analogues.[264] Nonetheless, the toxicity of organoselenium compounds is strongly dependent on the stability of the C–Se bond, with arylselenides being significantly less toxic *in vivo* compared to alkylselenides.[264] Furan introduction into conjugated polymer backbones has been shown to confer similarly high degrees of backbone planarity as to selenophene and tellurophene, with the added benefit of furan-based systems, in general, being regarded as highly biocompatible.[265,266]

In this thesis, attention has only been placed on the development of p-type OECT channel materials. The OECT steady-state performance of their n-type counterparts, however, lags far behind, with typical μC^* values reported for n-type OECT channel materials on the order of 0.1-1 F cm^{-1} V^{-1} s^{-1}.[115,240,267,268] The development of high-performance n-type OECT channel materials is, however, particularly important for the realisation of complementary circuitry and for enzymatic sensing, where reactions proceed through electron rather than hole transfer.[73,269] Therefore, future material investigations should also be directed towards minimising this performance gap and make use of the structure-property relationships elucidated within this work. Similarly, extending the structure-property relationships derived from this work to conjugated small molecules may also be of interest, in particular, due to the typically shorter synthetic routes incurred by small molecules and their reduced batch-to-batch variability compared to their polymeric counterparts. Although small molecules have recently been evaluated as p-type OECT channel materials,[270] they incurred considerably reduced performances ($\mu C^* < 1$ F cm^{-1} V^{-1} s^{-1}) and stabilities compared to

conjugated polymers, therefore, currently rendering them unsuitable for any biological interfacing.

Finally, future studies should also be directed towards the use of alternative polymerisation conditions other than Stille chemistry to incur OECT channel materials to be interfaced with biological systems. In particular, this is due to the difficulties associated with the complete removal of the highly toxic organotin by-products from the desired product.[271] In this context, the use of direct heteroarylation polymerisation (DHAP) and Aldol polycondensation as synthetic strategies should be considered, especially as these methods have already been employed for the synthesis of conjugated polymers for alternative electronic applications and incurred materials of similar electronic grade and hence performance.[63,65,66]

Lastly, given the requirement for mixed ionic-electronic charge carrier transport also in related organic electronic research areas, such as organic thermoelectrics, supercapacitors, batteries, actuators, and electrochromics, it is anticipated that the insights and conclusions derived from this thesis may also aid material design and development within these areas. The opportunities for mixed ionic-electronic polymeric conductors thus span far beyond their use in organic electrochemical transistors and may lead to advances in several other related research fields.

'The true method of knowledge is experiment.'
— William Blake

6

Experimental Procedures

Contents

6.1 General Methods

6.1.1 Material Synthesis and Purification

Reagents and solvents were purchased from commercial suppliers, specifically Sigma-Aldrich, FluoroChem, and Acros Organics, and were used without any further purification. Reactions were conducted in oven-dried flasks and under an inert nitrogen atmosphere. Thin-layer chromatography (TLC) was conducted on Merck Silicagel 60 F254 plates and developed either by irradiation with short (254 nm) or long wavelength (365 nm) UV light, by staining with potassium permanganate, or by staining with iodine. Silica flash column chromatography was carried out on Merck Geduran Silicagel 60 (40-63 μm).

6.1.2 Material Characterisation

^{1}H and $^{13}C\{^{1}H\}$ nuclear magnetic resonance (NMR) spectroscopy was performed on a Bruker AV-400 UltraShield machine (400 MHz for ^{1}H and 101 MHz for $^{13}C\{^{1}H\}$) at 298 K and using chloroform-*d* ($CDCl_3$) as the solvent unless stated otherwise. Chemical shifts (δ) are reported in parts per million (ppm) downfield from tetramethylsilane (TMS) and are referenced using residual chloroform (δ_H = 7.26 ppm and δ_C = 77.2 ppm) as internal standard. Coupling constants (*J*) are given in Hertz (Hz) and multiplicities are indicated as singlet (s), doublet (d), triplet (t), or multiplet (m).

Electrospray ionisation (ESI) mass spectrometry experiments were performed on a Micromass LCT Premier machine.

Gel permeation chromatography (GPC) was conducted using on an Agilent Technologies 1260 Infinity machine and a PLgel 10 μm Mixed-B column, either employing $CHCl_3$ at 40 °C or DMF at 80 °C as the eluent.

6.1.3 UV-Vis Absorption Spectroscopy

Ultraviolet-Visible (UV-Vis) absorption spectra were collected under ambient conditions on a UV-1800 Shimadzu Spectrophotometer machine. Solution UV-Vis absorption spectroscopy was conducted on dilute polymer solutions in chloroform employing quartz crystal cuvettes with a path length of 1 cm. Thin film UV-Vis data were collected from polymer-coated indium tin oxide (ITO) functionalised glass substrates. These were prepared by first cutting and then cleaning the substrates through sequential sonication for 10 min in soapy water, distilled water, acetone, and propan-2-ol. Polymer thin films were then deposited onto substrates by spin coating from 5 mg mL^{-1} polymer solutions in chloroform unless otherwise stated.

6.1.4 Cyclic Voltammetry

Cyclic voltammetry (CV) was carried out on an Autolab PGSTAT101 machine, which was controlled through the Metrohm Autolab NOVA software (version 2.1). A standard three-electrode configuration was employed for all measurements, with the working electrode consisting of either a polymer-coated ITO glass slide or a glassy carbon button electrode, the reference electrode a silver/silver chloride (Ag/AgCl) wire couple and the counterelectrode a platinum wire. Unless otherwise stated all CV traces were recorded using a scan rate of 100 mV s^{-1}. CV measurements were conducted either in an organic or aqueous supporting electrolyte. While the organic supporting electrolyte consisted of a 0.1 M solution of tetrabutylammonium hexafluorophosphate (TBA PF_6) in acetonitrile, the aqueous one was made up of a 0.1 M solution of sodium chloride in distilled water. Prior to conducting the CV measurements, the employed supporting electrolyte was thoroughly degassed using nitrogen. Ionisation potentials (*IP*) were determined according to **Equation 6.1**.[182]

$$IP\ (eV) = \left(5.1 + E_{ox,org} - E_{Fc/Fc^+}\right) \qquad \textbf{Equation 6.1}$$

where $E_{ox,org}$ is the semiconductor's onset of oxidation in a 0.1 M solution of TBA PF_6 in acetonitrile and E_{Fc/Fc^+} is the half-wave potential of the ferrocene/ferrocenium (Fc/Fc^+) couple in a 0.1 M solution of TBA PF_6 in acetonitrile.

6.1.5 Spectroelectrochemistry

Spectroelectrochemistry was performed on polymer-coated ITO glass slides, which were prepared analogously as described for the thin film UV-Vis measurements. The resulting polymer-coated ITO glass slides were then connected in the same three-electrode configuration that was employed for the CV experiments. The resulting electrochemical setup was then configured to reside within the UV-Vis spectrometer used for acquiring the optical properties of the polymers. Similarly to the CV experiments, spectroelectrochemical measurements were conducted either in a 0.1 M solution of TBA PF_6 in acetonitrile or a 0.1 M solution of NaCl in distilled water. Prior to recording the polymers' optical traces, each polymer was allowed to equilibrate for 15 s at the respective potentials.

6.1.6 Grazing Incidence Wide-Angle X-Ray Scattering

Two-dimensional grazing incidence wide-angle X-ray scattering (GIWAXS) patterns were acquired from polymer films cast on freshly cut and cleaned silicon wafer substrates. The silicon substrate preparation involved substrate cutting followed by sequential sonication of the substrates for 10 min in soapy water, distilled water, acetone, and propan-2-ol. Polymer thin films were then cast onto the freshly cleaned substrates by spin coating. Scattering measurements were conducted on beamlines either at the Advanced Photon Source at Argonne National Laboratory or at the Stanford Synchrotron Radiation Lightsource at

SLAC National Accelerator Laboratory. Beam energies between 10.9 keV and 12.7 keV and incident angles between 0.13° and 0.14° were employed. Data analysis was subsequently carried out using either Nika 1D SAXS29 and WAXStools in IgorPro Version 6.37 or a GIXSGUI Matlab toolbox.[272–274]

6.1.7 Electrochemical Impedance Spectroscopy

Electrochemical impedance spectroscopy (EIS) was conducted with a PG128N Metrohm Autolab machine using a three-electrode configuration. 500 µm x 500 µm polymer-coated gold electrodes were used as the working electrode, an Ag/AgCl wire as the reference electrode, and a platinum wire as the counterelectrode. EIS measurements were conducted in a 0.1 M aqueous NaCl solution and under ambient conditions. A frequency range between 100 kHz and 0.1 Hz and an AC amplitude of 10 mV over a DC voltage that achieves the maximum OECT performance for each polymer were selected. Data analysis was performed with Metrohm Autolab NOVA software (version 2.1) and using custom-built Excel codes.

6.1.8 Electrochemical Quartz Crystal Microbalance with Dissipation

Swelling measurements were done using Ti/Au-coated quartz crystals (QSensors QSX 338), the QSense Electrochemistry Module machine (QEM 401), and the QSense Analyzer machine (Biolin Scientific). First frequency (f) and dissipation (D) shifts (1^{st} – 11^{th} harmonics) of the bare sensors were recorded in both air and an aqueous 0.1 M NaCl solution. Immersion of the sensors into the liquid electrolyte causes a shift in signals, arising from the density and mass changes inside the chamber, which need to be considered for changes in the polymers upon electrolyte exposure. After signal stabilisation, the sensors were removed from the analyser, spin-coated with the polymer under evaluation, and placed

back in the module. Frequency and dissipation signals were recorded for the Ti/Au/polymer sensors until signal stabilisation, in air and in NaCl 0.1 M, as done for the bare sensors. Using the 'Stitch Data Files' function within the QSoft software obtained the shifts in *f* and *D* signals before and after the sensor was coated were obtained, for both dry and wet states. These differences were used to calculate the mass changes (Δm) on the crystal, using the Sauerbrey equation:

$$\Delta m = -C \cdot \frac{\Delta_f}{n} \qquad \textbf{Equation 6.2}$$

$$C = \frac{\nu_q \cdot \rho_q}{2f_0^2} \qquad \textbf{Equation 6.3}$$

where Δf is the frequency shift, n the overtone number, ν_q the shear wave velocity in quartz, ρ_q the density of quartz, and f_0 is the fundamental frequency.

Areal normalisation was done by dividing the mass changes over the sensor's active area, while thickness estimations were obtained by dividing areal mass over film density.

eQCM-D was performed by coupling an Autolab PGstat128N to the QSense EC machine. The employed three-electrode setup was composed of an Ag/AgCl reference electrode, a Pt counter electrode, and the polymer-coated QSX 338 as the working electrode.

Viscoelastic modelling or the Sauerbrey equation were used to calculate the mass changes during electrochemical doping/dedoping pulses, depending on the film's dissipation characteristics.[74,118] The viscoelastic model applied to fit eQCM-D data used Kelvin-Voigt elements that consist of viscous and elastic properties and for the which the complex shear modulus (G^*) can be defined as:

$$G^* = \varepsilon + i2\pi f \eta \qquad \textbf{Equation 6.4}$$

where ε is the elasticity, f the frequency, and η the viscosity.

When using such a modelling technique, 3+ frequency overtones were employed to ensure proper fitting with the software QTools.

To calculate the number of anion density penetrating/leaving the films during doping/dedoping cycles, we assumed a one injected charge to one anion coupling.[118] We then decoupled the anion mass ($5.88725 \cdot 10^{-23}$ g atom^{-1}) from the water mass by subtracting the latter from the total injected mass during electrochemical pulsing. Finally, to calculate water density, we divided the water mass by the water molecule mass ($2.99158 \cdot 10^{-23}$ g atom^{-1}). Swelling percentages were calculated using:

$$\%\, Swelling_{total} = \frac{Volume_{wet\ at\ x\ V} - Volume_{dry}}{Volume_{dry}} \cdot 100 \qquad \textbf{Equation 6.5}$$

6.1.9 Organic Electrochemical Transistor Fabrication and Characterisation

Organic electrochemical transistors (OECTs) were fabricated according to previous literature procedures involving photolithographic procedures.[275] Polymer films were deposited onto the substrates by spin coating from chloroform solutions (5 mg mL^{-1}) and subsequently dried. The sacrificial Parylene C layer was then removed using the peel-off process. Substrates were rinsed copiously with distilled water prior to testing and dried under an inert flow of nitrogen gas before testing. No pre- or post-deposition treatments were performed on the deposited polymer films prior to OECT testing. The transistors' performance was assessed in a 0.1 M aqueous NaCl electrolyte under ambient conditions. An Ag/AgCl pellet electrode with a 2 mm height and 2 mm diameter was employed as the gate electrode. The OECT's I-V characteristics were recorded using a Keithley 2602A SourceMeter machine and custom-built LabView scripts.

6.2 Synthetic Procedures

6.2.1 Synthetic Procedures for Chapter 2

3-(2-(2-Methoxyethoxy)ethoxy)thiophene (2)

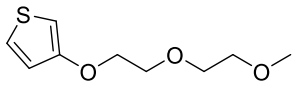

3-methoxythiophene (5.00 g, 43.8 mmol, 1.00 equiv.), diethylene glycol monomethyl ether (7.90 g, 65.8 mmol, 1.50 equiv.), and *p*-toluenesulfonic acid monohydrate (0.84 g, 4.4 mmol, 0.10 equiv.) were dissolved in 50 mL toluene and the resulting solution was heated to reflux for 6 h. Following cooling to room temperature, the reaction mixture was washed with water (100 mL) and the aqueous phase extracted with CH_2Cl_2 (3 x 150 mL). The combined organic fractions were then washed with water (2 x 150 mL) and brine (150 mL), before being dried over anhydrous sodium sulfate. Excess solvent was removed under reduced pressure and the crude product was subsequently purified using silica flash column chromatography employing a 1:2 v/v mixture of EtOAc:PE as the eluent (R_f = 0.30). The final product was obtained as a pale-yellow oil (7.22 g, 35.7 mmol, 82% yield).

^{1}H NMR (400 MHz, $CDCl_3$) δ: 7.18 (dd, J = 5.3, 3.1 Hz, 1H), 6.80 (dd, J = 5.3, 1.6 Hz, 1H), 6.28 (dd, J = 3.1, 1.6 Hz, 1H), 4.18–4.12 (m, 2H), 3.89–3.84 (m, 2H), 3.75–3.70 (m, 2H), 3.62–3.57 (m, 2H), 3.41 (s, 3H).

^{13}C{^{1}H} NMR (101 MHz, $CDCl_3$) δ: 157.6, 124.6, 119.6, 97.5, 72.0, 70.7, 69.7, 69.5, 59.1.

HRMS (ESI-TOF) *m/z*: calcd for $C_9H_{14}O_3S$ 202.0664 Da, $[M + H]^+$ found 203.0667 Da.

3-(2-(2-(2-Methoxyethoxy)ethoxy)ethoxy)thiophene (3)

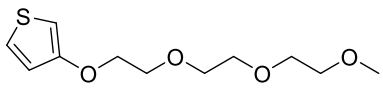

3 was synthesised analogously to **2**, using the following reagent quantities: 3-methoxythiophene (5.00 g, 43.8 mmol, 1.00 equiv.), triethylene glycol monomethyl ether (10.8 g, 65.8 mmol, 1.50 equiv.), *p*-toluenesulfonic acid monohydrate (0.84 g, 4.4 mmol, 0.10 equiv.), and 40 mL toluene. The crude product was purified using silica flash column chromatography employing a 1:2 v/v mixture of EtOAc:PE as the eluent (R_f = 0.20). The final product was obtained as a pale-yellow oil (5.46 g, 22.2 mmol, 51% yield).

^{1}H NMR (400 MHz, $CDCl_3$) δ: 7.17 (dd, J = 5.3, 3.1 Hz, 1H), 6.78 (dd, J = 5.3, 1.6 Hz, 1H), 6.27 (dd, J = 3.1, 1.6 Hz, 1H), 4.15–4.10 (m, 2H), 3.87–3.83 (m, 2H), 3.78–3.63 (m, 6H), 3.58–3.53 (m, 2H), 3.39 (s, 3H).

^{13}C{^{1}H} NMR (101 MHz, $CDCl_3$) δ: 157.6, 124.6, 119.6, 97.5, 71.9, 70.8, 70.7, 70.6, 69.7, 69.6, 59.0.

HRMS (ESI-TOF) *m/z*: calcd for $C_{11}H_{18}O_4S$ 246.0926 Da, $[M + H]^+$ found 247.0927 Da.

3-(2-(2-(2-(2-Methoxyethoxy)ethoxy)ethoxy)ethoxy)thiophene (4)

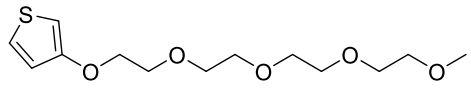

4 was synthesised analogously to **2**, using the following reagent quantities: 3-methoxythiophene (6.00 g, 52.6 mmol, 1.00 equiv.), tetraethylene glycol monomethyl ether (16.2 g, 78.9 mmol, 1.50 equiv.), *p*-toluenesulfonic acid monohydrate (1.0 g, 5.3 mmol, 0.10 equiv.), and 50 mL toluene. The crude product was purified using silica flash column chromatography employing a 1:1 v/v mixture of EtOAc:PE as the eluent (R_f = 0.30). The final product was obtained as a pale-yellow oil (5.02 g, 17.3 mmol, 33% yield).

^{1}H NMR (400 MHz, $CDCl_3$) δ: 7.15 (dd, J = 5.3, 3.1 Hz, 1H), 6.77 (dd, J = 5.3, 1.6 Hz, 1H), 6.25 (dd, J = 3.1, 1.6 Hz, 1H), 4.14–4.07 (m, 2H), 3.87–3.80 (m, 2H), 3.74–3.68 (m, 2H), 3.71–3.60 (m, 8H), 3.57–3.49 (m, 2H), 3.37 (s, 3H).

^{13}C{^{1}H} NMR (101 MHz, $CDCl_3$) δ: 157.6, 124.6, 119.6, 97.5, 71.9, 70.8, 70.6, 70.5, 69.7, 69.6, 59.0.

HRMS (ESI-TOF) *m/z*: calcd for $C_{13}H_{22}O_5S$ 290.1188 Da, $[M + H]^+$ found 291.1192 Da.

3-(2-(2-(2-(2-(2-(2-Methoxyethoxy)ethoxy)ethoxy)ethoxy)ethoxy)ethoxy)thiophene (5)

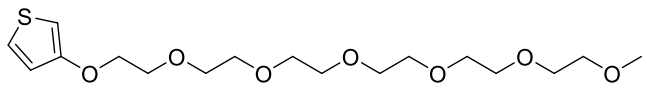

5 was synthesised analogously to **2**, using the following reagent quantities: 3-methoxythiophene (2.25 g, 19.7 mmol, 1.00 equiv.), hexaethylene glycol monomethyl ether (8.76 g, 29.6 mmol, 1.50 equiv.), *p*-toluenesulfonic acid monohydrate (0.38 g, 2.0 mmol, 0.10 equiv.), and 40 mL toluene. The crude product was purified using silica flash column chromatography employing a 9:1 v/v mixture of CH_2Cl_2:acetone as the eluent (R_f = 0.20). The final product was obtained as a pale-yellow oil (2.70 g, 7.14 mmol, 37% yield).

^{1}H NMR (400 MHz, $CDCl_3$) δ: 7.18 (dd, J = 5.2, 3.1 Hz, 1H), 6.80 (dd, J = 5.3, 1.6 Hz, 1H), 6.28 (dd, J = 3.1, 1.6 Hz, 1H), 4.16–4.12 (m, 2H), 3.88–3.84 (m, 2H), 3.77–3.62 (m, 18H), 3.58–3.55 (m, 2H), 3.40 (s, 3H).

^{13}C{^{1}H} NMR (101 MHz, $CDCl_3$) δ: 157.6, 124.6, 119.6, 97.5, 72.0, 70.8, 70.6, 70.6, 70.5, 69.7, 69.6, 59.1.

HRMS (ESI-TOF) *m/z*: calcd for $C_{17}H_{30}O_7S$ 378.1712 Da, $[M + H]^+$ found 379.1711 Da.

2-Bromo-3-(2-(2-(2-(2-(2-(2-methoxyethoxy)ethoxy)ethoxy)ethoxy)ethoxy)ethoxy)thiophene (6)

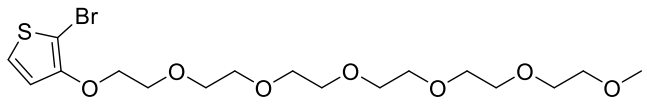

5 (2.70 g, 7.14 mmol, 1.00 equiv.) was dissolved in 100 mL anhydrous tetrahydrofuran and cooled to -10 °C. *N*-bromosuccinimide (1.33 g, 7.47 mmol, 1.05 equiv.) was added portionwise in the dark and the reaction stirred for 2 h. Upon full conversion, the reaction mixture was poured into an aqueous saturated sodium bicarbonate solution (100 mL) and the aqueous phase extracted with CH_2Cl_2 (3 x 50 mL). The combined organic layers were washed with water (2 x 100 mL) and brine (100 mL) before being dried over anhydrous sodium sulfate. Excess solvent was removed under reduced pressure. The final product was obtained by silica flash column chromatography employing a 95:5 v/v mixture of EtOAc:acetone as the eluent (R_f = 0.45). The final product was obtained as a pale-yellow oil (2.81 g, 6.16 mmol, 86% yield).

^{1}H NMR (400 MHz, $CDCl_3$) δ: 7.20 (d, J = 5.9 Hz, 1H), 6.79 (d, J = 5.9 Hz, 1H), 4.23–4.19 (m, 2H), 3.85–3.81 (m, 2H), 3.78–3.62 (m, 18H), 3.58–3.54 (m, 2H), 3.39 (s, 3H).

^{13}C{^{1}H} NMR (101 MHz, $CDCl_3$) δ: 154.4, 124.2, 118.0, 92.3, 71.9, 71.7, 71.0, 70.6, 70.5, 69.9, 59.0.

HRMS (ESI-TOF) *m/z*: calcd for $C_{17}H_{29}BrO_7S$ 456.0817 Da, $[M + H]^+$ found 457.0820 Da.

3,3'-Bis(2-(2-methoxyethoxy)ethoxy)-2,2'-bithiophene (7)

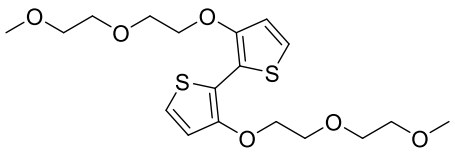

2 (7.00 g, 34.6 mmol, 1.00 equiv.) was dissolved in 70 mL anhydrous tetrahydrofuran and the resulting solution cooled to -20 °C. A *n*-BuLi solution in hexanes (1.6 M, 26.0 mL, 41.6 mmol, 1.20 equiv.) was subsequently added dropwise. The resulting solution was stirred for 1 h at -20 °C and was then transferred to a solution of iron(III) acetylacetonate (12.2 g, 34.6 mmol, 1.00 equiv.) in 160 mL anhydrous tetrahydrofuran. The reaction mixture was heated to reflux for 3 h. After cooling to room temperature, the crude reaction mixture was passed through a short silica plug using a 1:2 v/v mixture of EtOAc:PE as the eluent (R_f = 0.25). Excess solvent was removed under reduced pressure. The crude product was purified by silica flash column chromatography using a 1:2 v/v mixture of EtOAc:PE as the eluent to afford the final product as a white solid (4.36 g, 10.8 mmol, 63% yield).

^{1}H NMR (400 MHz, $CDCl_3$) δ: 7.08 (d, J = 5.6 Hz, 2H), 6.86 (d, J = 5.6 Hz, 2H), 4.29–4.23 (m, 4H), 3.93–3.89 (m, 4H), 3.77–3.73 (m, 4H), 3.61–3.54 (m, 4H), 3.39 (s, 6H).

^{13}C{^{1}H} NMR (101 MHz, $CDCl_3$) δ: 151.7, 121.9, 116.5, 114.7, 72.0, 71.4, 70.8, 70.0, 59.1.

HRMS (ESI-TOF) *m/z*: calcd for $C_{18}H_{26}O_6S_2$ 402.1171 Da, $[M + H]^+$ found 403.1174 Da.

3,3'-Bis(2-(2-(2-methoxyethoxy)ethoxy)ethoxy)-2,2'-bithiophene (8)

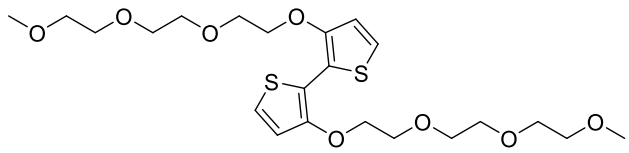

8 was synthesised analogously to **7**, using the following reagent quantities: **3** (5.40 g, 21.9 mmol, 1.00 equiv.), 50 mL anhydrous tetrahydrofuran, *n*-BuLi solution in hexanes (1.6 M, 16.4 mL, 26.2 mmol, 1.20 equiv.), iron(III) acetylacetonate (7.77 g, 22.0 mmol, 1.00 equiv.), and 100 mL anhydrous tetrahydrofuran. The crude product was purified using silica flash column chromatography employing a 3:1 v/v mixture of EtOAc:PE as the eluent (R_f = 0.40). The final product was obtained as a white solid (3.22 g, 6.57 mmol, 60% yield).

^{1}H NMR (400 MHz, $CDCl_3$) δ: 7.09 (d, J = 5.6 Hz, 2H), 6.87 (d, J = 5.6 Hz, 2H), 4.30–4.21 (m, 4H), 3.96–3.88 (m, 4H), 3.82–3.74 (m, 4H), 3.72–3.63 (m, 8H), 3.60–3.51 (m, 4H), 3.39 (s, 6H).

^{13}C{^{1}H} NMR (101 MHz, $CDCl_3$) δ: 151.7, 121.9, 116.6, 114.7, 71.9, 71.4, 70.9, 70.7, 70.6, 70.0, 59.1.

HRMS (ESI-TOF) *m/z*: calcd for $C_{22}H_{34}O_8S_2$ 490.1695 Da, $[M + H]^+$ found 491.1691 Da.

3,3'-Bis(2-(2-(2-(2-methoxyethoxy)ethoxy)ethoxy)ethoxy)-2,2'-bithiophene (9)

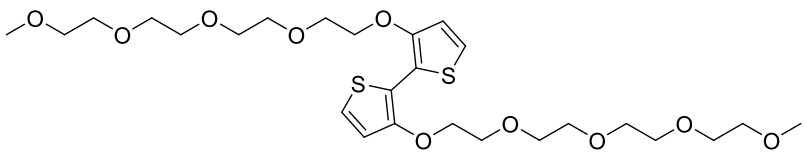

9 was synthesised analogously to **7**, using the following reagent quantities: **4** (4.50 g, 15.5 mmol, 1.00 equiv.), 40 mL anhydrous tetrahydrofuran, *n*-BuLi solution in hexanes (1.6 M, 11.7 mL, 18.7 mmol, 1.21 equiv.), iron(III) acetylacetonate (5.50 g, 15.6 mmol, 1.00 equiv.), and 80 mL anhydrous tetrahydrofuran. The crude product was purified using silica flash column chromatography employing EtOAc as the eluent (R_f = 0.35). The final product was obtained as a pale-yellow oil (1.72 g, 2.97 mmol, 38% yield).

^{1}H NMR (400 MHz, $CDCl_3$) δ: 7.07 (d, J = 5.6 Hz, 2H), 6.84 (d, J = 5.5 Hz, 2H), 4.25–4.21 (m, 4H), 3.91–3.86 (m, 4H), 3.76–3.71 (m, 4H), 3.70–3.60 (m, 16H), 3.55–3.51 (m, 4H), 3.36 (s, 6H).

^{13}C{^{1}H} NMR (101 MHz, $CDCl_3$) δ: 151.7, 121.9, 116.6, 114.7, 71.9, 71.4, 70.9, 70.6, 70.6, 70.5, 70.0, 59.0.

HRMS (ESI-TOF) *m/z*: calcd for $C_{26}H_{42}O_{10}S_2$ 578.2219 Da, $[M + H]^+$ found 579.2220 Da.

3,3'-Bis(2-(2-(2-(2-(2-(2-methoxyethoxy)ethoxy)ethoxy)ethoxy)ethoxy)ethoxy)-2,2'-bithiophene (10)

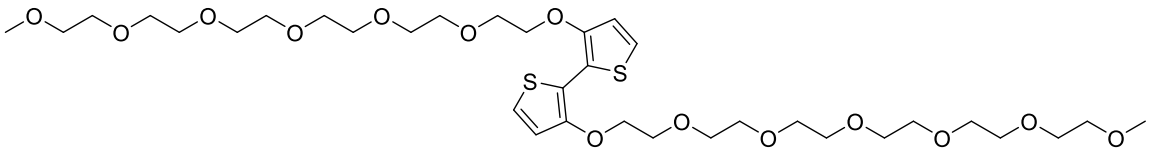

1,5-cyclooctadiene (0.66 g, 6.1 mmol, 1.0 equiv.) and 2,2'-bipyridine (1.43 g, 9.16 mmol, 1.50 equiv.) were dissolved in 30 mL anhydrous *N,N'*-dimethylformamide and stirred at room temperature. Bis(1,5-cyclooctadiene)nickel(0) (2.52 g, 9.16 mmol, 1.50 equiv.) was added and the resulting mixture heated to 80 °C for 1 h. After cooling to room temperature, a solution of **6** (2.78 g, 6.10 mmol, 1.00 equiv.) in 10 mL anhydrous toluene was added dropwise and the reaction heated to 80 °C overnight. The reaction was diluted with EtOAc (150 mL), washed with water (150 mL), and the aqueous phase extracted with EtOAc (2 x 100 mL). The combined organic layers were washed with water (2 x 150 mL) and brine (100 mL) before being dried over anhydrous sodium sulfate. Excess solvent was removed under reduced pressure. The crude product was purified by silica flash column chromatography employing a 7:3 v/v mixture of CH_2Cl_2:acetone as the eluent (R_f = 0.25). The final product was afforded as a pale-yellow oil (0.80 g, 1.1 mmol, 35% yield).

^{1}H NMR (400 MHz, $CDCl_3$) δ: 7.10 (d, J = 5.6 Hz, 2H), 6.87 (d, J = 5.6 Hz, 2H), 4.28–4.24 (m, 4H), 3.94–3.90 (m, 4H), 3.79–3.74 (m, 4H), 3.73–3.62 (m, 32H), 3.58–3.53 (m, 4H), 3.39 (s, 6H).

^{13}C{^{1}H} NMR (101 MHz, $CDCl_3$) δ: 151.7, 121.9, 116.6, 114.8, 77.4, 71.9, 71.4, 70.9, 70.7, 70.6, 70.6, 70.5, 70.0, 59.0.

HRMS (ESI-TOF) *m/z*: calcd for $C_{34}H_{58}O_{14}S_2$ 754.3268 Da, $[M + H]^+$ found 755.3271 Da.

5,5'-Dibromo-3,3'-bis(2-(2-methoxyethoxy)ethoxy)-2,2'-bithiophene (11)

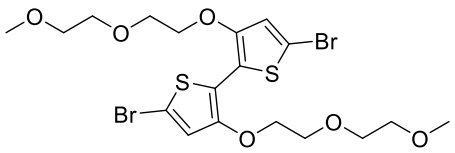

7 (1.00 g, 2.49 mmol, 1.00 equiv.) was dissolved in 60 mL anhydrous tetrahydrofuran. The resulting solution was degassed for 15 min and cooled to -20 °C. *N*-bromosuccinimide (0.93 g, 5.2 mmol, 2.1 equiv.) was then added portionwise in the dark over 10 min and the reaction allowed to proceed for an additional 10 min. The reaction mixture was then poured into a saturated aqueous sodium bicarbonate solution (100 mL). The aqueous phase was extracted with EtOAc (3 x 100 mL) and the combined organic layers were washed with water (2 x 100 mL) and brine (100 mL) prior to being dried over anhydrous sodium sulfate. Excess solvent was removed under reduced pressure. The crude product was purified by silica flash column chromatography employing a 1:2 v/v mixture of EtOAc:PE as the eluent (R_f = 0.40). The final product was afforded as a white solid (1.07 g, 1.86 mmol, 75% yield).

^{1}H NMR (400 MHz, Acetone-d_6) δ: 7.18 (s, 2H), 4.36–4.27 (m, 4H), 3.89–3.81 (m, 4H), 3.71–3.65 (m, 4H), 3.58–3.50 (m, 4H), 3.32 (s, 6H).

^{13}C{^{1}H} NMR (101 MHz, Acetone-d_6) δ: 150.6, 120.2, 115.2, 109.5, 71.8, 71.7, 70.3, 69.6, 58.0.

HRMS (ESI-TOF) *m/z*: calcd for $C_{18}H_{24}Br_2O_6S_2$ 557.9381 Da, $[M + H]^+$ found 558.9377 Da.

5,5'-Dibromo-3,3'-bis(2-(2-(2-methoxyethoxy)ethoxy)ethoxy)-2,2'-bithiophene (12)

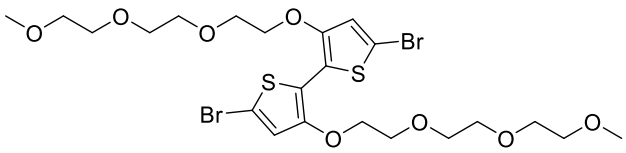

12 was synthesised analogously to **11**, using the following reagent quantities: **8** (1.70 g, 3.47 mmol, 1.00 equiv.), 100 mL anhydrous tetrahydrofuran, and *N*-bromosuccinimide (1.30 g, 7.28 mmol, 2.10 equiv.). The crude product was purified by silica flash column chromatography employing a 2:1 v/v mixture of EtOAc:PE as the eluent (R_f = 0.35). The final product was afforded as a white solid (1.92 g, 3.04 mmol, 88% yield).

^{1}H NMR (400 MHz, Acetone-d_6) δ: 7.18 (s, 2H), 4.34–4.29 (m, 4H), 3.93–3.83 (m, 4H), 3.71–3.67 (m, 4H), 3.67–3.56 (m, 8H), 3.52–3.44 (m, 4H), 3.29 (s, 6H).

^{13}C{^{1}H} NMR (101 MHz, CD_2Cl_2) δ: 150.3, 119.7, 115.6, 109.9, 71.9, 71.8, 70.8, 70.5, 70.4, 69.8, 58.6.

The ^{1}H and ^{13}C{^{1}H} NMR shifts obtained were consistent with those reported in the literature.[112]

5,5'-Dibromo-3,3'-bis(2-(2-(2-(2-methoxyethoxy)ethoxy)ethoxy)ethoxy)-2,2'-bithiophene (13)

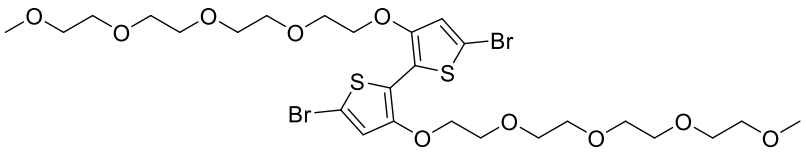

13 was synthesised analogously to **11**, using the following reagent quantities: **9** (0.50 g, 0.86 mmol, 1.0 equiv.), 30 mL anhydrous tetrahydrofuran, and *N*-bromosuccinimide (0.34 g, 1.9 mmol, 2.2 equiv.). The crude product was purified by silica flash column chromatography employing a 3:1 v/v mixture of EtOAc:PE as the eluent (R_f = 0.25). The final product was afforded as a pale-yellow oil (0.54 g, 0.75 mmol, 87% yield).

^{1}H NMR (400 MHz, Acetone-d_6) δ: 7.18 (s, 2H), 4.34–4.29 (m, 4H), 3.90–3.86 (m, 4H), 3.73–3.53 (m, 20H), 3.50–3.43 (m, 4H), 3.29 (s, 6H).

^{13}C{^{1}H} NMR (101 MHz, $CDCl_3$) δ: 151.7, 121.9, 116.6, 114.7, 71.9, 71.4, 70.9, 70.6, 70.6, 70.5, 70.0, 59.0.

HRMS (ESI-TOF) *m/z*: calcd for $C_{26}H_{40}Br_2O_{10}S_2$ 734.0430 Da, $[M + H]^+$ found 735.0428 Da.

5,5'-Dibromo-3,3'-bis(2-(2-(2-(2-(2-(2-methoxyethoxy)ethoxy)ethoxy)ethoxy)ethoxy)ethoxy)-2,2'-bithiophene (14)

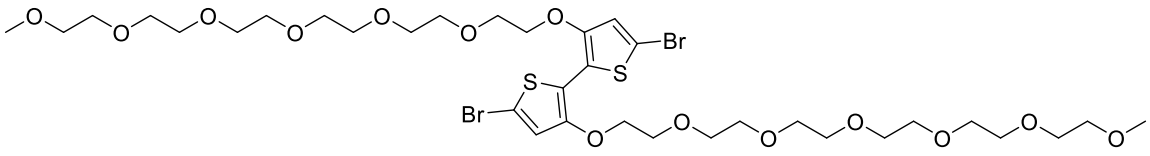

14 was synthesised analogously to **11**, using the following reagent quantities: **10** (0.80 g, 1.1 mmol, 1.0 equiv.), 65 mL anhydrous tetrahydrofuran, and *N*-bromosuccinimide (0.40 g, 2.2 mmol, 2.1 equiv.). The crude product was purified by silica flash column chromatography employing a 4:1 v/v mixture of CH_2Cl_2:acetone as the eluent (R_f = 0.20). The final product was afforded as a pale-yellow oil (0.90 g, 1.0 mmol, 93% yield).

^{1}H NMR (400 MHz, CD_2Cl_2) δ: 7.19 (s, 2H), 4.34–4.29 (m, 4H), 3.92–3.85 (m, 4H), 3.73–3.66 (m, 4H), 3.67–3.53 (m, 32H), 3.50–3.45 (m, 4H), 3.30 (s, 6H).

^{13}C{^{1}H} NMR (101 MHz, Acetone-d_6) δ: 150.6, 120.2, 115.1, 109.5, 71.8, 71.8, 70.5, 70.5, 70.4, 70.2, 69.7, 58.0.

HRMS (ESI-TOF) *m/z*: calcd for $C_{34}H_{56}Br_2O_{14}S_2$ 910.1478 Da, $[M + H]^+$ found 911.1479 Da.

p(g2T2-T)

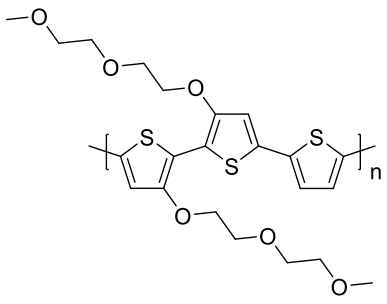

11 (143 mg, 0.248 mmol, 1.00 equiv.), 2,5-bis(trimethylstannyl)thiophene (102 mg, 0.248 mmol, 1.00 equiv.), tris(*o*-methoxyphenyl)phosphine (8.4 mg, 0.024 mmol, 0.097 equiv.), and tris(dibenzylideneacetone)dipalladium(0) (4.8 mg, 0.0052 mmol, 0.021 equiv.) were added to a 10 mL microwave vial and dissolved in 2.5 mL anhydrous toluene. The vial was sealed and the solution degassed for 10 min before being heated to reflux overnight. After cooling to room temperature, the reaction mixture was precipitated into 50 mL of a 1:1 v/v mixture of EtOAc:hexane and filtered into a Soxhlet thimble. The crude product was purified by sequential Soxhlet extractions in hexane, acetone, ethyl acetate, methanol, and chloroform. Excess solvent of the chloroform fraction was removed under reduced pressure and the product reprecipitated into EtOAc (50 mL). The final product was collected by suction filtration and was recovered as a dark blue solid (44 mg, 37% yield).

GPC ($CHCl_3$, 40 °C): M_n = 11.4 kDa, $Đ$ = 1.3.

^{1}H NMR (400 MHz, TCE-d_2) δ: 7.17 (s, 2H), 7.05 (s, 2H), 4.41 (s, 4H), 4.01 (s, 4H), 3.84 (s, 4H), 3.67 (s, 4H), 3.43 (s, 6H).

p(g3T2-T)

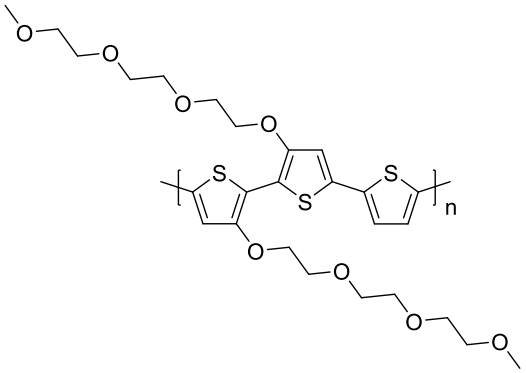

p(g3T2-T) was synthesised analogously to **p(g2T2-T)**, using the following reagent quantities: **12** (502 mg, 0.777 mmol, 1.00 equiv.), 2,5-bis(trimethylstannyl)thiophene (320 mg, 0.770 mmol, 1.00 equiv.), tris(*o*-methoxyphenyl)phosphine (23 mg, 0.065 mmol, 0.084 equiv.), tris(dibenzylideneacetone)dipalladium(0) (18 mg, 0.020 mmol, 0.025 equiv.), and 8 mL anhydrous toluene. The crude product was purified by sequential Soxhlet extractions in hexane, acetone, ethyl acetate, methanol, and chloroform. Excess solvent of the chloroform fraction was removed under reduced pressure and the product reprecipitated into EtOAc (50 mL). The final product was collected by suction filtration and was recovered as a dark blue solid (181 mg, 41% yield).

GPC ($CHCl_3$, 40 °C): M_n = 22.6 kDa, $Đ$ = 2.0.

^{1}H NMR (400 MHz, $CDCl_3$) δ: 7.10 (s, 2H), 6.99 (s, 2H), 4.36 (s, 4H), 3.99 (s, 4H), 3.83 (s, 4H), 3.77–3.71 (m, 4H), 3.71–3.65 (m, 4H), 3.58–3.52 (m, 4H), 3.37 (s, 6H).

p(g4T2-T)

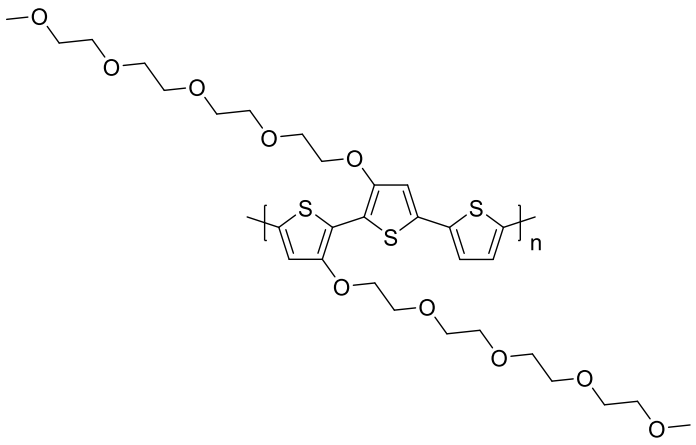

p(g4T2-T) was synthesised analogously to **p(g2T2-T)**, using the following reagent quantities: **13** (508 mg, 0.692 mmol, 1.00 equiv.), 2,5-bis(trimethylstannyl)thiophene (285 mg, 0.692 mmol, 1.00 equiv.), tris(*o*-methoxyphenyl)phosphine (22 mg, 0.063 mmol, 0.090 equiv.), tris(dibenzylideneacetone)dipalladium(0) (14 mg, 0.015 mmol, 0.022 equiv.), and 7 mL anhydrous toluene. The crude product was purified by sequential Soxhlet extractions in hexane, acetone, and ethyl acetate. It was found that both the acetone and ethyl acetate fractions contained polymer that precipitated upon cooling. These fractions were combined and reprecipitated into hexane (50 mL). The final product was collected by suction filtration and was recovered as a dark blue solid (225 mg, 49% yield).

GPC ($CHCl_3$, 40 °C): M_n = 28.0 kDa, $Đ$ = 2.5.

^{1}H NMR (400 MHz, $CDCl_3$) δ: 7.11 (s, 2H), 6.99 (s, 2H), 4.37 (s, 4H), 4.00 (s, 4H), 3.83 (s, 4H), 3.77–3.61 (m, 16H), 3.56–3.52 (m, 4H), 3.37 (s, 6H).

p(g6T2-T)

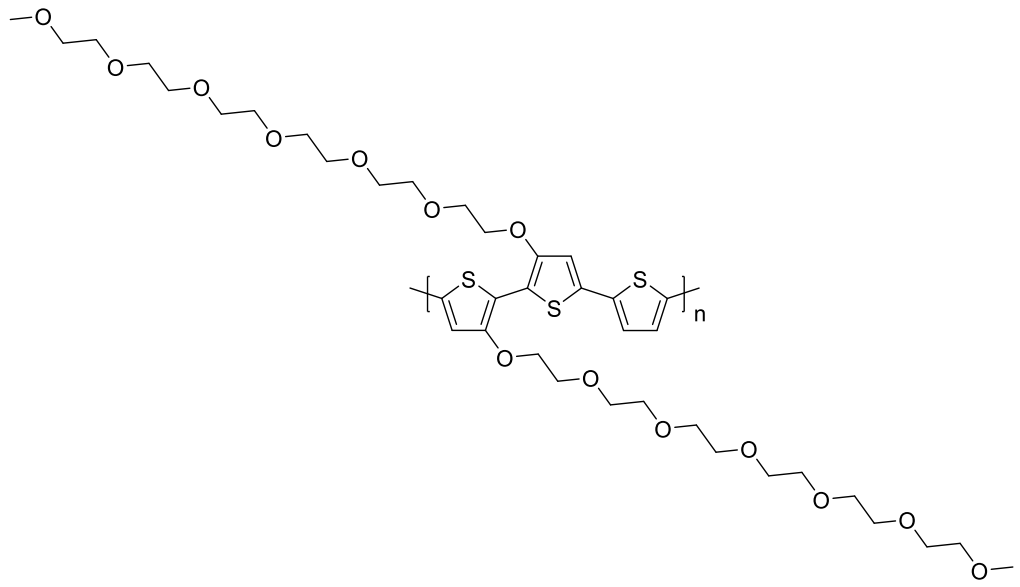

p(g6T2-T) was synthesised analogously to **p(g2T2-T)**, using the following reagent quantities: **14** (209 mg, 0.230 mmol, 1.00 equiv.), 2,5-bis(trimethylstannyl)thiophene (95 mg, 0.23 mmol, 1.0 equiv.), tris(*o*-methoxyphenyl)phosphine (7.8 mg, 0.022 mmol, 0.096 equiv.), tris(dibenzylideneacetone)dipalladium(0) (4.7 mg, 0.0051 mmol, 0.022 equiv.), and 2.5 mL anhydrous toluene. After cooling to room temperature, the reaction mixture was precipitated into *n*-hexane. The tacky crude product was purified by Soxhlet washing with hexane. The material was found to be soluble in all other commonly used solvents for Soxhlet extraction. The polymer was extracted with acetone and excess solvent was removed under reduced pressure. This highly soluble material was used without further purification and collected as a sticky dark blue solid (99 mg, 52% yield).

GPC ($CHCl_3$, 40 °C): M_n = 12.5 kDa, $Đ$ = 2.1.

^{1}H NMR (400 MHz, $CDCl_3$): 7.11 (s, 2H), 6.99 (s, 2H), 4.36 (s, 4H), 3.99 (s, 4H), 3.83 (s, 4H), 3.74 (s, 4H), 3.71–3.58 (m, 28H), 3.58–3.51 (m, 4H), 3.38 (s, 6H).

6.2.2 Synthetic Procedures for Chapter 3

3-(2-Methoxyethoxy)thiophene (15)

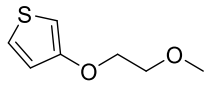

15 was synthesised analogously to **2**, using the following reagent quantities: 3-methoxythiophene (20.0 g, 175 mmol, 1.00 equiv.), 2-methoxyethanol (20.0 g, 263 mmol, 1.50 equiv.), *p*-toluenesulfonic acid monohydrate (3.30 g, 17.5 mmol, 0.100 equiv.), and 200 mL toluene. The crude product was purified using silica flash column chromatography employing a 1:8 v/v mixture of EtOAc:PE as the eluent (R_f = 0.35). The final product was obtained as a pale-yellow oil (19.6 g, 124 mmol, 71% yield).

^{1}H NMR (400 MHz, $CDCl_3$) δ: 7.20 (dd, J = 5.3, 3.1 Hz, 1H), 6.83 (dd, J = 5.3, 1.5 Hz, 1H), 6.29 (dd, J = 3.2, 1.5 Hz, 1H), 4.16–4.12 (m, 2H), 3.80–3.75 (m, 2H), 3.47 (s, 3H).

The ^{1}H NMR shifts obtained were consistent with those reported in the literature.[203]

3-(2-(2-(2-(2-(2-Methoxyethoxy)ethoxy)ethoxy)ethoxy)ethoxy)thiophene (16)

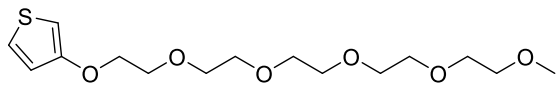

16 was synthesised analogously to **2**, using the following reagent quantities: 3-methoxythiophene (2.83 g, 24.8 mmol, 1.00 equiv.), pentaethylene glycol monomethyl ether (9.38 g, 37.2 mmol, 1.50 equiv.), *p*-toluenesulfonic acid monohydrate (0.57 g, 3.0 mmol, 0.12 equiv.), and 60 mL toluene. The crude product was purified using silica flash column chromatography employing EtOAc as the eluent (R_f = 0.30). The final product was obtained as a pale-yellow oil (2.39 g, 7.15 mmol, 29% yield).

^{1}H NMR (400 MHz, $CDCl_3$) δ: 7.18 (dd, J = 5.2, 3.2 Hz, 1H), 6.79 (dd, J = 5.3, 1.5 Hz, 1H), 6.27 (dd, J = 3.2, 1.6 Hz, 1H), 4.15–4.10 (m, 2H), 3.88–3.82 (m, 2H), 3.76–3.64 (m, 14H), 3.57–3.55 (m, 2H), 3.39 (s, 3H).

^{13}C{^{1}H} NMR (101 MHz, $CDCl_3$) δ: 157.6, 124.6, 119.6, 97.5, 71.9, 70.8, 70.6, 70.6, 70.5, 69.7, 69.6, 59.1.

HRMS (ESI-TOF) *m/z*: calcd for $C_{15}H_{26}O_6S$ 334.1450 Da, $[M + H]^+$ found 335.1449 Da.

2-Bromo-3-(2-(2-(2-(2-(2-methoxyethoxy)ethoxy)ethoxy)ethoxy)ethoxy)thiophene (17)

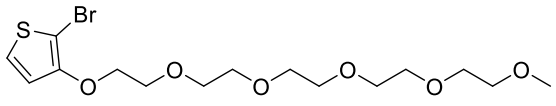

17 was synthesised analogously to **6**, using the following reagent quantities: **16** (2.53 g, 7.57 mmol, 1.00 equiv.), 100 mL anhydrous tetrahydrofuran, and *N*-bromosuccinimide (1.41 g, 7.95 mmol, 1.05 equiv.). The crude product was purified using silica flash column chromatography employing EtOAc as the eluent (R_f = 0.25). The final product was obtained as a pale-yellow oil (2.81 g, 6.82 mmol, 90% yield).

^{1}H NMR (400 MHz, $CDCl_3$) δ: 7.19 (d, J = 6.0 Hz, 1H), 6.78 (d, J = 6.0 Hz, 1H), 4.22–4.17 (m, 2H), 3.83–3.79 (m, 2H), 3.75–3.71 (m, 2H), 3.69–3.62 (m, 12H), 3.57–3.52 (m, 2H), 3.37 (s, 3H).

^{13}C{^{1}H} NMR (101 MHz, $CDCl_3$) δ: 151.7, 121.9, 116.6, 114.7, 71.9, 71.4, 70.9, 70.6, 70.6, 70.5, 70.0, 59.0.

HRMS (ESI-TOF) *m/z*: calcd for $C_{15}H_{25}BrO_6S$ 412.0555 Da, $[M + H]^+$ found 413.0552 Da.

3,3'-Dimethoxy-2,2'-bithiophene (18)

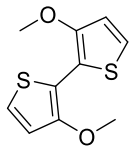

18 was synthesised analogously to **7**, using the following reagent quantities: 3-methoxythiophene (5.00 g, 43.8 mmol, 1.00 equiv.), 150 mL anhydrous tetrahydrofuran, *n*-BuLi solution in hexanes (2.5 M, 21 mL, 53 mmol, 1.2 equiv.), iron(III) acetylacetonate (18.6 g, 52.7 mmol, 1.20 equiv.), and 300 mL anhydrous tetrahydrofuran. The crude product was purified using silica flash column chromatography employing a 9:1 v/v mixture of hexane:CH_2Cl_2 as the eluent (R_f = 0.40). The final product was obtained as a white solid (3.10 g, 13.7 mmol, 63% yield).

^{1}H NMR (400 MHz, $CDCl_3$) δ: 7.11 (d, J = 5.5 Hz, 2H), 6.87 (d, J = 5.6 Hz, 2H), 3.95 (s, 6H).

The ^{1}H NMR shifts obtained were consistent with those reported in the literature.[166]

3,3'-Bis(2-methoxyethoxy)-2,2'-bithiophene (19)

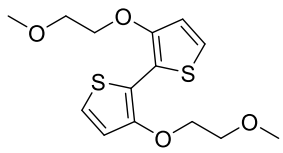

19 was synthesised analogously to **7**, using the following reagent quantities: **15** (6.00 g, 38.0 mmol, 1.00 equiv.), 100 mL anhydrous tetrahydrofuran, *n*-BuLi solution in hexanes (2.5 M, 18 mL, 45 mmol, 1.2 equiv.), iron(III) acetylacetonate (13.4 g, 38.0 mmol, 1.00 equiv.), and 170 mL anhydrous tetrahydrofuran. The crude product was purified using silica flash column chromatography employing a 1:4 v/v mixture of EtOAc:PE as the eluent (R_f = 0.30). The final product was obtained as a white solid (3.27 g, 10.4 mmol, 55% yield).

^{1}H NMR (400 MHz, $CDCl_3$) δ: 7.11 (d, J = 5.5 Hz, 2H), 6.88 (d, J = 5.5 Hz, 2H), 4.34–4.12 (m, 4H), 3.91–3.71 (m, 4H), 3.49 (s, 6H).

$^{13}C\{^1H\}$ NMR (101 MHz, $CDCl_3$) δ: 151.8, 122.0, 116.7, 115.0, 71.4, 71.3, 59.3.

HRMS (ESI-TOF) *m/z*: calcd for $C_{14}H_{18}O_4S_2$ 314.0647 Da, $[M + H]^+$ found 315.0642 Da.

3,3'-Bis(2-(2-(2-(2-(2-methoxyethoxy)ethoxy)ethoxy)ethoxy)ethoxy)-2,2'-bithiophene (20)

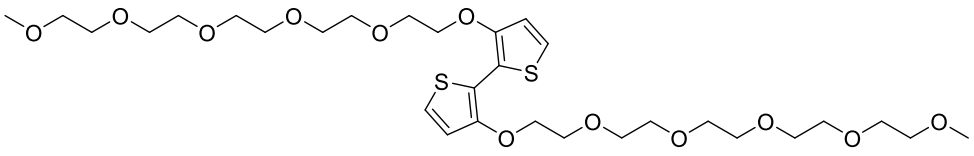

20 was synthesised analogously to **10**, using the following reagent quantities: 1,5-cyclooctadiene (0.73 g, 6.7 mmol, 1.0 equiv.), 2,2'-bipyridine (1.59 g, 10.2 mmol, 1.51 equiv.), 35 mL anhydrous *N,N'*-dimethylformamide, bis(1,5-cyclooctadiene)nickel(0) (2.80 g, 10.2 mmol, 1.51 equiv.), **17** (2.80 g, 6.79 mmol, 1.00 equiv.), and 50 mL anhydrous toluene. The crude product was purified using silica flash column chromatography employing a 1:4 v/v mixture of acetone:CH_2Cl_2 as the eluent (R_f = 0.30). The final product was obtained as a pale-yellow oil (1.57 g, 2.36 mmol, 70% yield).

^{1}H NMR (400 MHz, $CDCl_3$) δ: 7.07 (d, J = 5.6 Hz, 2H), 6.84 (d, J = 5.6 Hz, 2H), 4.25–4.21 (m, 4H), 3.91–3.87 (m, 4H), 3.76–3.71 (m, 4H), 3.69–3.58 (m, 24H), 3.54–3.50 (m, 4H), 3.36 (s, 6H).

^{13}C{^{1}H} NMR (101 MHz, $CDCl_3$) δ: 151.7, 121.9, 116.5, 114.7, 71.9, 71.4, 70.9, 70.7, 70.6, 70.6, 70.5, 70.0, 59.0.

HRMS (ESI-TOF) *m/z*: calcd for $C_{30}H_{50}O_{12}S_2$ 666.2744 Da, $[M + H]^+$ found 667.2743 Da.

(3,3'-Dimethoxy-[2,2'-bithiophene]-5,5'-diyl)bis(trimethylstannane) (21)

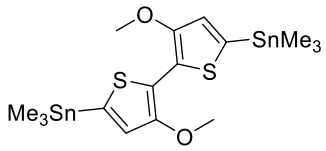

18 (0.700 g, 3.10 mmol, 1.00 equiv.) was dissolved in 150 mL anhydrous tetrahydrofuran and the resulting solution cooled to -78 °C. A *n*-BuLi solution in hexanes (2.5 M, 5.0 mL, 13 mmol, 4.0 equiv.) was subsequently added dropwise. The reaction was stirred for 30 min at -78 °C and 30 min at room temperature. The reaction was subsequently cooled back to -78 °C and trimethyltin chloride (2.59 g, 13.0 mmol, 4.20 equiv.) was added in one portion. The reaction was allowed to warm to room temperature and was stirred overnight. The reaction mixture was diluted with diethyl ether (100 mL) and washed with water (2 x 100 mL) and brine (100 mL) before being dried over anhydrous sodium sulfate. Excess solvent was removed under reduced pressure. The reaction was purified by recrystallisation from acetonitrile to yield the final product as pale-yellow crystals (1.22 g, 2.20 mmol, 71% yield). ^{1}H NMR (400 MHz, Acetone-d_6) δ: 7.09 (s, 2H), 3.94 (s, 6H), 0.36 (s, 18H).

The ^{1}H NMR shifts obtained were consistent with those reported in the literature.[166]

(3,3'-Bis(2-methoxyethoxy)-[2,2'-bithiophene]-5,5'-diyl)bis(trimethylstannane) (22)

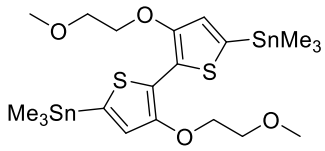

22 was synthesised analogously to **21**, using the following reagent quantities: **19** (0.600 g, 1.91 mmol, 1.00 equiv.), 130 mL anhydrous tetrahydrofuran, *n*-BuLi solution in hexanes (2.5 M, 3.1 mL, 7.8 mmol, 4.1 equiv.), and trimethyltin chloride (1.67 g, 8.40 mmol, 4.39 equiv.). The solid was suspended in hexane (50 mL) and collected by suction filtration to afford the final product as a white crystalline solid (800 mg, 1.25 mmol, 65% yield).

^{1}H NMR (400 MHz, CD_2Cl_2) δ: 6.95 (s, 2H), 4.29–4.23 (m, 4H), 3.84–3.76 (m, 4H), 3.48 (s, 6H), 0.40 (s, 18H).

The ^{1}H NMR shifts obtained were consistent with those reported in the literature.[276]

(3,3'-Bis(2-(2-methoxyethoxy)ethoxy)-[2,2'-bithiophene]-5,5'-diyl)bis(trimethylstannane) (23)

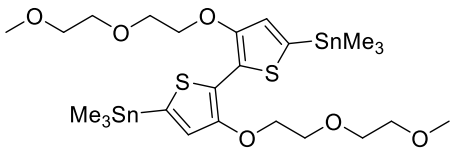

23 was synthesised analogously to **21**, using the following reagent quantities: **7** (300 mg, 0.746 mmol, 1.00 equiv.), 50 mL anhydrous tetrahydrofuran, *n*-BuLi solution in hexanes (2.5 M, 1.2 mL, 3.0 mmol, 4.0 equiv.), and trimethyltin chloride (654 mg, 3.29 mmol, 4.40 equiv.). The reaction mixture was diluted with diethyl ether (100 mL) and washed with water (2 x 100 mL) and brine (100 mL) before being dried over anhydrous sodium sulfate. Excess solvent was removed under reduced pressure. The crude product was dissolved in acetonitrile (50 mL) and washed with hexane (3 x 50 mL). Excess solvent was removed under reduced pressure. The crude product was purified by recrystallisation from diethyl ether to yield the final product as pale-yellow crystals (164 mg, 0.225 mmol, 30% yield).

^{1}H NMR (400 MHz, $CDCl_3$) δ: 6.92 (s, 2H), 4.33–4.29 (m, 4H), 3.96–3.92 (m, 4H), 3.81–3.78 (m, 4H), 3.62–3.57 (m, 4H), 3.41 (s, 6H), 0.38 (s, 18H).

$^{13}C\{^{1}H\}$ NMR (101 MHz, $CDCl_3$) δ: 153.5, 133.9, 124.2, 120.6, 72.1, 71.5, 70.9, 70.2, 59.1, -8.3.

HRMS (ESI-TOF) *m/z*: calcd for $C_{24}H_{42}O_6S_2Sn_2$ 730.0467 Da, $[M + H]^+$ found 731.0470 Da.

(3,3'-Bis(2-(2-(2-methoxyethoxy)ethoxy)ethoxy)-[2,2'-bithiophene]-5,5'-diyl)bis (trimethylstannane) (24)

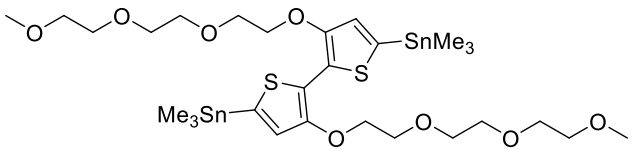

24 was synthesised analogously to **21**, using the following reagent quantities: **8** (1.00 g, 2.04 mmol, 1.00 equiv.), 130 mL anhydrous tetrahydrofuran, *n*-BuLi solution in hexanes (2.5 M, 3.3 mL, 8.3 mmol, 4.0 equiv.), and trimethyltin chloride (2.03 g, 10.2 mmol, 5.00 equiv.). The reaction mixture was diluted with diethyl ether (100 mL) and washed with water (2 x 100 mL) and brine (100 mL) before being dried over anhydrous sodium sulfate. Excess solvent was removed under reduced pressure. The crude product was dissolved in acetonitrile (50 mL) and washed with hexane (3 x 50 mL). Excess solvent was removed under reduced pressure. The crude product was purified by recrystallisation from diethyl ether to yield the final product as pale-yellow crystals (0.535 g, 0.654 mmol, 32% yield).

^{1}H NMR (400 MHz, CD_2Cl_2) δ: 6.97 (s, 2H), 4.30–4.26 (m, 4H), 3.93–3.88 (m, 4H), 3.77–3.73 (m, 4H), 3.67–3.60 (m, 8H), 3.56–3.51 (m, 4H), 3.36 (s, 6H), 0.40 (s, 18H).

^{13}C{^{1}H} NMR (101 MHz, CD_2Cl_2) δ: 153.6, 134.3, 124.2, 120.9, 71.9, 71.5, 70.9, 70.6, 70.4, 70.1, 58.6, -8.7.

The ^{1}H and ^{13}C NMR shifts obtained were consistent with those reported in the literature.[68]

5,5'-Dibromo-3,3'-bis(2-(2-(2-(2-(2-methoxyethoxy)ethoxy)ethoxy)ethoxy)ethoxy)-2,2'-bithiophene (25)

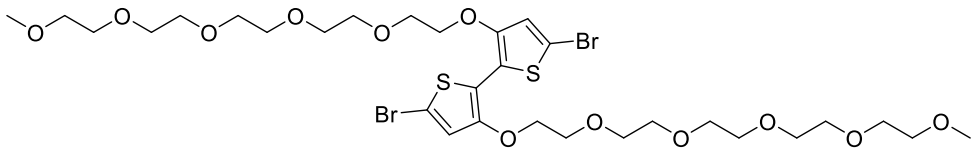

25 was synthesised analogously to **11**, using the following reagent quantities: **20** (1.10 g, 1.65 mmol, 1.00 equiv.), 100 mL anhydrous tetrahydrofuran, and *N*-bromosuccinimide (0.62 g, 3.5 mmol, 2.1 equiv.). The crude product was purified by silica flash column chromatography employing a 4:1 v/v mixture of CH_2Cl_2:acetone as the eluent (R_f = 0.25). The final product was afforded as a pale-yellow oil (1.10 g, 1.34 mmol, 81% yield).

^{1}H NMR (400 MHz, CD_2Cl_2) δ: 7.18 (s, 2H), 4.37–4.24 (m, 4H), 3.94–3.84 (m, 4H), 3.71–3.67 (m, 4H), 3.66–3.54 (m, 24H), 3.49–3.44 (m, 4H), 3.29 (s, 6H).

^{13}C{^{1}H} NMR (101 MHz, CD_2Cl_2) δ: 150.6, 120.2, 115.1, 109.5, 71.8, 71.7, 70.5, 70.5, 70.4, 70.4, 70.2, 69.7, 57.9.

HRMS (ESI-TOF) *m/z*: calcd for $C_{30}H_{48}Br_2O_{12}S_2$ 822.0954 Da, $[M + H]^+$ found 823.0955 Da.

p(g3T2)

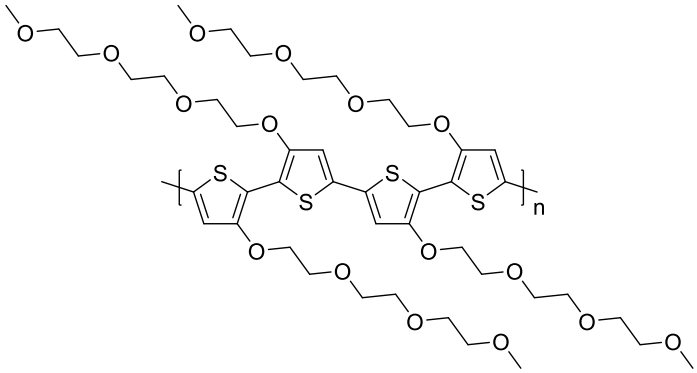

12 (124 mg, 0.192 mmol, 1.00 equiv.), **24** (157 mg, 0.192 mmol, 1.00 equiv.), tris(*o*-methoxyphenyl)phosphine (2.7 mg, 0.0076 mmol, 0.040 equiv.), and tris(dibenzylideneacetone)dipalladium(0) (1.8 mg, 0.0019 mmol, 0.010 equiv.) were added to a 10 mL microwave vial and dissolved in 6 mL anhydrous and degassed *N,N'*-dimethylformamide. The vial was sealed, and the solution degassed for 10 more min before being heated to 110 °C overnight. End capping of the polymer involved adding a 0.1 mL aliquot of a 0.1 mL 2-tributylstannylthiophene in 0.5 mL anhydrous *o*-dichlorobenzene solution, followed by heating for an additional hour. Subsequently, another 0.1 mL aliquot of a 0.1 mL 2-bromothiophene in 0.5 mL anhydrous *o*-dichlorobenzene solution was added and the mixture heated for one additional hour. After cooling to room temperature, the reaction mixture was precipitated into 50 mL of a 1:1 v/v mixture of EtOAc:hexane and filtered into a Soxhlet thimble. The crude product was purified by sequential Soxhlet extractions in hexane, acetone, ethyl acetate, methanol, and chloroform. Excess solvent of the chloroform fraction was removed under reduced pressure and the product reprecipitated into a 1:1 v/v mixture of EtOAc:hexane (50 mL). The final product was collected by suction filtration and was recovered as a dark blue solid (166 mg, 89% yield).

GPC (DMF, 80 °C): M_n = 23.9 kDa, $Đ$ = 2.4.

^{1}H NMR (400 MHz, $CDCl_3$) δ: 6.99 (s, 2H), 4.38 (s, 4H), 4.03–3.95 (m, 4H), 3.85–3.80 (m, 4H), 3.76–3.70 (m, 4H), 3.70–3.64 (m, 4H), 3.56–3.51 (m, 4H), 3.37 (s, 6H).

p(g2T2-g4T2)

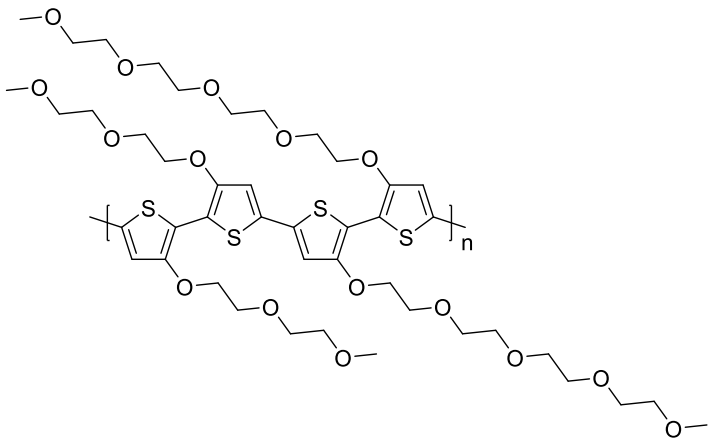

p(g2T2-g4T2) was synthesised analogously to **p(g3T2)**, using the following reagent quantities: **13** (63 mg, 0.086 mmol, 1.0 equiv.), **23** (63 mg, 0.086 mmol, 1.0 equiv.), tris(*o*-methoxyphenyl)phosphine (2.4 mg, 0.0068 mmol, 0.079 equiv.), tris(dibenzylideneacetone)dipalladium(0) (1.6 mg, 0.0017 mmol, 0.020 equiv.), and 3 mL anhydrous and degassed *N,N'*-dimethylformamide. The crude product was purified by sequential Soxhlet extractions in hexane, acetone, ethyl acetate, methanol, and chloroform. Excess solvent of the chloroform fraction was removed under reduced pressure and the product reprecipitated into a 1:1 v/v mixture of EtOAc:hexane (50 mL). The final product was collected by suction filtration and was recovered as a dark blue solid (70 mg, 83% yield). GPC (DMF, 80 °C): M_n = 19.8 kDa, $Đ$ = 2.4.

^{1}H NMR (400 MHz, $CDCl_3$) δ: 6.99 (s, 4H), 4.38 (s, 8H), 3.99 (s, 8H), 3.85–3.79 (m, 8H), 3.75–3.59 (m, 20H), 3.56–3.50 (m, 4H), 3.41 (s, 6H), 3.37 (s, 6H).

p(g1T2-g5T2)

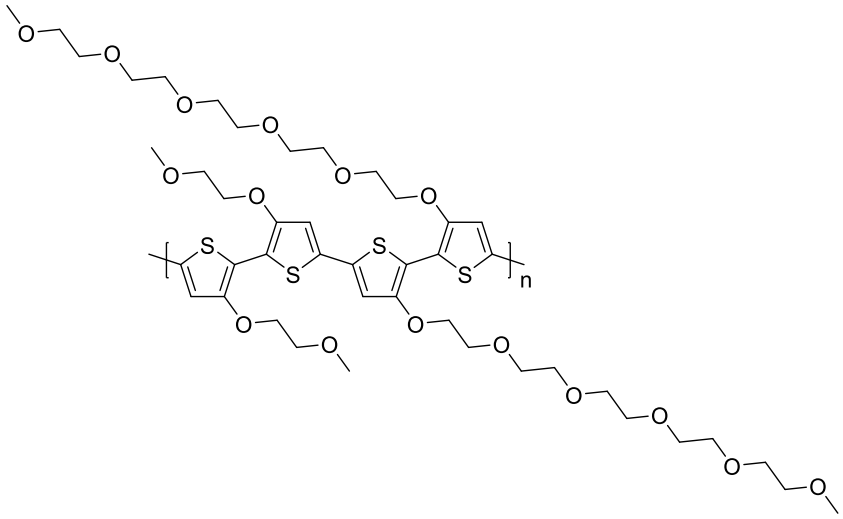

p(g1T2-g5T2) was synthesised analogously to **p(g3T2)**, using the following reagent quantities: **25** (271 mg, 0.330 mmol, 1.00 equiv.), **22** (203 mg, 0.330 mmol, 1.00 equiv.), tris(*o*-methoxyphenyl)phosphine (8.9 mg, 0.025 mmol, 0.077 equiv.), tris(dibenzylideneacetone)dipalladium(0) (5.8 mg, 0.0063 mmol, 0.019 equiv.), and 8 mL anhydrous and degassed *N,N'*-dimethylformamide. The crude product was purified by sequential Soxhlet extractions in hexane, acetone, ethyl acetate, methanol, and chloroform. Excess solvent of the chloroform fraction was removed under reduced pressure and the product reprecipitated into a 1:1 v/v mixture of EtOAc:hexane (50 mL). The final product was collected by suction filtration and was recovered as a dark blue solid (280 mg, 87% yield).

GPC (DMF, 80 °C): M_n = 14.5 kDa, $Đ$ = 2.2 kDa.

^{1}H NMR (400 MHz, $CDCl_3$) δ: 6.98 (s, 4H), 4.36 (s, 8H), 3.99 (s, 4H), 3.92–3.86 (m, 4H), 3.85–3.78 (m, 4H), 3.76–3.71 (m, 4H), 3.69–3.61 (m, 18H), 3.58–3.50 (m, 12H), 3.38 (s, 6H).

p(g0T2-g6T2)

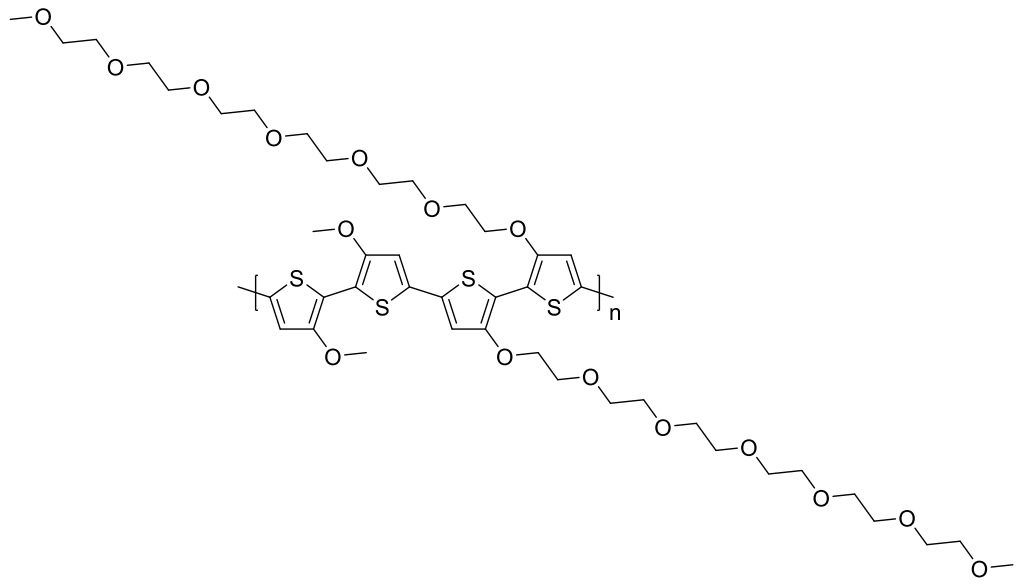

p(g0T2-g6T2) was synthesised analogously to **p(g3T2)**, using the following reagent quantities: **14** (300 mg, 0.330 mmol, 1.00 equiv.), **21** (183 mg, 0.330 mmol, 1.00 equiv.), tris(*o*-methoxyphenyl)phosphine (9.3 mg, 0.026 mmol, 0.080 equiv.), tris(dibenzylideneacetone)dipalladium(0) (6.0 mg, 0.007 mmol, 0.020 equiv.), and 8 mL anhydrous and degassed *N,N'*-dimethylformamide. The crude product was purified by sequential Soxhlet extractions in hexane, acetone, ethyl acetate, methanol, and chloroform. Excess solvent of the chloroform fraction was removed under reduced pressure and the product reprecipitated into a 1:1 v/v mixture of EtOAc:hexane (50 mL). The final product was collected by suction filtration and was recovered as a dark blue solid (230 mg, 71% yield).

GPC (DMF, 80 °C): M_n = 6.0 kDa, $Đ$ = 1.7 kDa.

^{1}H NMR (400 MHz, $CDCl_3$) δ: 7.05–6.97 (m, 4H), 4.37 (s, 4H), 4.07 (s, 4H), 3.99 (s, 4H), 3.86–3.81 (m, 4H), 3.78–3.61 (m, 34H), 3.57–3.53 (m, 4H), 3.38 (s, 6H).

6.2.3 Synthetic Procedures for Chapter 4

3,6-Di(thiophen-2-yl)-2,5-dihydropyrrolo[3,4-c]pyrrole-1,4-dione (28)

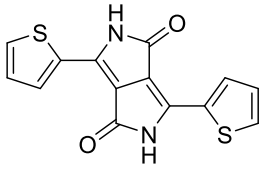

Iron (III) chloride (0.02 g, cat.) was dissolved in 100 mL anhydrous *tert*-butyl amyl alcohol. Sodium metal (4.60 g, 200 mmol, 3.62 equiv.) was added and the suspension was heated at 60 °C overnight until all of the sodium metal had dissolved. The reaction mixture was subsequently cooled to room temperature and diethyl succinate (9.62 g, 55.2 mmol, 1.00 equiv.) and 2-thiophenecarbonitrile (15.1 g, 138 mmol, 2.50 equiv.) added sequentially dropwise. The reaction was heated to reflux for 6 h. After cooling to room temperature, the reaction mixture was poured into methanol (300 mL) and the product was collected by suction filtration. The crude product was purified by washing with copious quantities of methanol (5 x 200 mL). The final product was afforded as a dark red solid (8.80 g, 29.3 mmol, 53% yield).

^{1}H NMR (400 MHz, DMSO-d_6) δ: 11.25 (s, 2H), 8.22 (dd, J = 3.8, 1.2 Hz, 2H), 7.97 (dd, J = 5.0, 1.1 Hz, 2H), 7.31 (dd, J = 5.0, 3.8 Hz, 2H).

The ^{1}H NMR shifts obtained were consistent with those reported in the literature.[277]

2-(2-(2-Methoxyethoxy)ethoxy)ethyl 4-methylbenzenesulfonate (29)

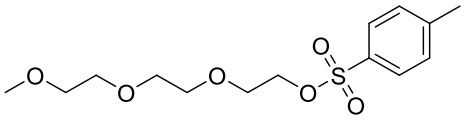

Triethylene glycol monomethyl ether (60.0 g, 366 mmol, 1.00 equiv.) was dissolved in 100 mL tetrahydrofuran and cooled to 0 °C. Sodium hydroxide (22.2 g, 555 mmol, 1.52 equiv.) was dissolved in 100 mL distilled water and added dropwise to the reaction mixture. After stirring for 30 min at 0 °C, a solution of tosyl chloride (75.0 g, 395 mmol, 1.08 equiv.) in 100 mL tetrahydrofuran was added dropwise to the reaction mixture. After overnight stirring, water (300 mL) was added to the reaction mixture and the aqueous phase extracted with diethyl ether (3 x 200 mL). The combined organic layers were washed with water (2 x 200 mL) and brine (200 mL) before being dried over anhydrous sodium sulfate. Excess solvent was removed under reduced pressure to afford the final product as a clear colourless oil (112 g, 352 mmol, 96% yield).

^{1}H NMR (400 MHz, $CDCl_3$) δ: 7.80–7.71 (m, 2H), 7.33–7.29 (m, 2H), 4.15–4.10 (m, 2H), 3.67–3.63 (m, 2H), 3.59–3.54 (m, 6H), 3.52–3.47 (m, 2H), 3.33 (s, 3H), 2.41 (s, 3H).

The ^{1}H NMR shifts obtained were consistent with those reported in the literature.[278]

2,5-Bis(2-(2-(2-methoxyethoxy)ethoxy)ethyl)-3,6-di(thiophen-2-yl)-2,5-dihydropyrrolo [3,4-c]pyrrole-1,4-dione (30)

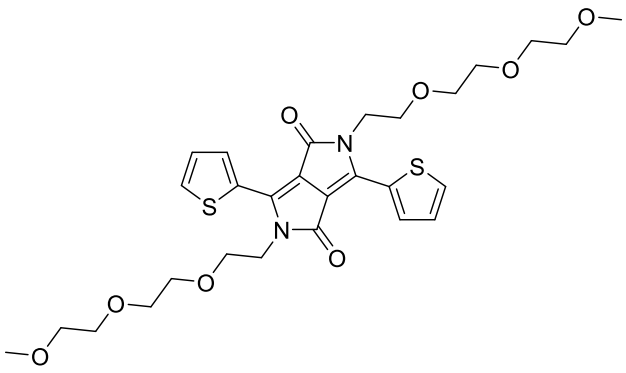

Potassium carbonate (5.0 g, 36 mmol, 4.0 equiv.) and **28** (2.7 g, 9.0 mmol, 1.0 equiv.) were dissolved in 150 mL anhydrous *N,N'*-dimethylformamide. **29** (7.2 g, 23 mmol, 2.5 equiv.) was added dropwise and the resulting mixture heated to 120 °C for 5 h. After cooling to room temperature, distilled water (200 mL) was added to the reaction mixture. The aqueous phase was extracted with ethyl acetate (3 x 200 mL) and the combined organic layers were washed with water (2 x 100 mL) and brine (100 mL) before being dried over anhydrous sodium sulfate. Excess solvent was removed under reduced pressure. The crude product was purified by silica flash column chromatography employing a 1:6 v/v acetone:CH_2Cl_2 mixture as the eluent (R_f = 0.35). The final product was afforded as a dark purple solid (2.02 g, 3.41 mmol, 38% yield).

^{1}H NMR (400 MHz, $CDCl_3$) δ: 8.77 (dd, J = 3.9, 1.2 Hz, 2H), 7.65 (dd, J = 5.0, 1.2 Hz, 2H), 7.28 (dd, J = 5.0, 3.9 Hz, 2H), 4.29 (t, J = 6.3 Hz, 4H), 3.81 (t, J = 6.3 Hz, 4H), 3.69–3.63 (m, 4H), 3.63–3.56 (m, 8H), 3.53–3.47 (m, 4H), 3.36 (s, 6H).

^{13}C{^{1}H} (101 MHz, $CDCl_3$) δ: 161.5, 140.4, 134.8, 130.8, 129.7, 128.4, 107.9, 71.9, 70.7, 70.6, 70.6, 69.0, 59.1, 41.9.

3,6-Bis(5-bromothiophen-2-yl)-2,5-bis(2-(2-(2-methoxyethoxy)ethoxy)ethyl)-2,5-dihydropyrrolo[3,4-c]pyrrole-1,4-dione (31)

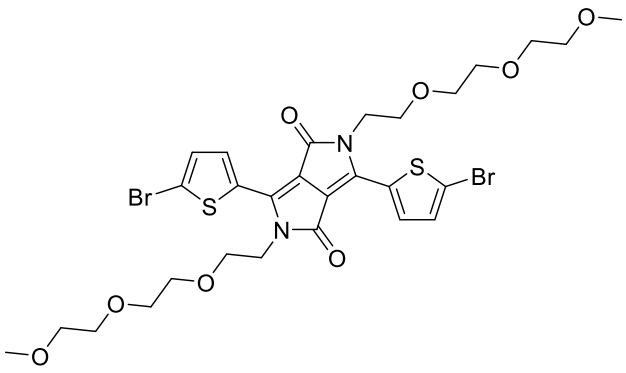

30 (500 mg, 0.844 mmol, 1.00 equiv.) was dissolved in 45 mL anhydrous $CHCl_3$ at room temperature. *N*-bromosuccinimide (320 mg, 1.80 mmol, 2.13 equiv.) was added portionwise in the dark over 10 min. The reaction mixture was allowed to stir overnight. The reaction was quenched by pouring into a saturated sodium bicarbonate solution (100 mL). The aqueous phase was extracted with CH_2Cl_2 (3 x 100 mL) and the combined organic fractions were washed with water (2 x 100 mL) and brine (100 mL) before being dried over anhydrous sodium sulfate. Excess solvent was removed under reduced pressure. The crude product was purified by silica flash column chromatography employing a 1:6 v/v acetone:CH_2Cl_2 mixture as the eluent (R_f = 0.30). The final product was afforded as a dark purple solid (461 mg, 0.616 mmol, 73% yield).

^{1}H NMR (400 MHz, $CDCl_3$) δ: 8.51 (d, J = 4.2 Hz, 2H), 7.23 (d, J = 4.2 Hz, 2H), 4.20 (t, J = 5.9 Hz, 4H), 3.80 (t, J = 5.9 Hz, 4H), 3.69–3.64 (m, 4H), 3.64–3.56 (m, 8H), 3.55–3.49 (m, 4H), 3.37 (s, 6H).

^{13}C{^{1}H} (101 MHz, $CDCl_3$) δ: 161.3, 139.5, 134.9, 131.4, 131.1, 119.3, 108.0, 71.9, 70.8, 70.6, 70.6, 69.0, 59.0, 42.3.

p(gDPP-TT)

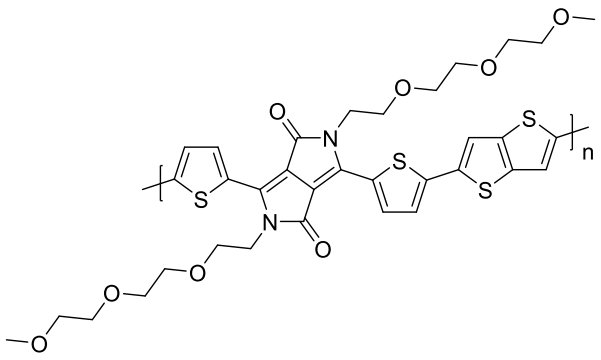

31 (94.2 mg, 0.126 mmol, 1.00 equiv.), 2,5-bis(trimethylstannyl)thieno[3,2-*b*]thiophene (58.8 mg, 0.126 mmol, 1.00 equiv.), tris(*o*-methoxyphenyl)phosphine (3.8 mg, 0.011 mmol, 0.086 equiv.), and tris(dibenzylideneacetone)dipalladium(0) (4.9 mg, 0.0054 mmol, 0.043 equiv.) were added to a 10 mL microwave vial and the reaction vessel purged for 10 min with nitrogen. 3 mL anhydrous degassed toluene was then added, and the reaction mixture heated to reflux overnight. The resulting polymer was end capped by adding a 0.1 mL aliquot of a 0.1 mL 2-(tributylstannyl)-thiophene in 0.5 mL chlorobenzene solution, followed by stirring at reflux for 1 h. Subsequently, an additional 0.1 mL aliquot of a 0.1 mL 2-bromothiophene in 0.5 mL chlorobenzene solution was added, followed by additional stirring at reflux for 1 h. After cooling to room temperature, the polymer was precipitated into methanol (30 mL) and filtered into a Soxhlet thimble. The crude product was purified by sequential Soxhlet extractions in hexane, acetone, ethyl acetate, methanol, and chloroform. Excess solvent of the chloroform fraction was removed under reduced pressure and the product reprecipitated into methanol (30 mL). The final product was collected by suction filtration and was recovered as a dark blue solid (70 mg, 69% yield).

^{1}H NMR (400 MHz, $CDCl_3$) δ: 8.92-8.72 (broad s, 6H), 4.41–4.19 (m, 4H), 4.18–3.93 (m, 4H), 3.76–3.67 (m, 4H), 3.67–3.53 (m, 8H), 3.53–3.46 (m, 4H), 3.42–3.33 (m, 6H).

GPC analysis of the polymer was not possible due to its aggregation tendency in solution and MALDI-ToF also proved to be unsuccessful.

p(gDPP-T2)

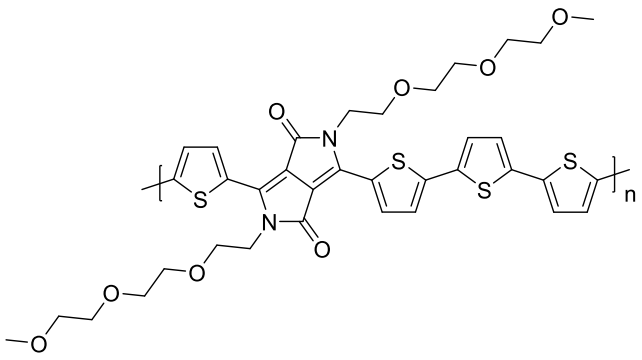

p(gDPP-T2) was synthesised analogously to **p(gDPP-TT)**, using the following reagent quantities: **31** (105 mg, 0.140 mmol, 1.00 equiv.), 5,5'-bis(trimethylstannyl)-2,2'-bithiophene (69 mg, 0.14 mmol, 1.0 equiv.), tris(*o*-methoxyphenyl)phosphine (3.8 mg, 0.011 mmol, 0.077 equiv.), tris(dibenzylideneacetone)dipalladium(0) (4.9 mg, 0.0054 mmol, 0.038 equiv.), and 3 mL anhydrous and degassed toluene. The crude product was purified by sequential Soxhlet extractions in hexane, acetone, ethyl acetate, methanol, and chloroform. Excess solvent of the chloroform fraction was removed under reduced pressure and the product reprecipitated into methanol (30 mL). The final product was collected by suction filtration and was recovered as a dark blue solid (70 mg, 66% yield). ^{1}H NMR (400 MHz, $CDCl_3$) δ: 9.07–8.86 (broad s, 8H), 4.38–4.19 (m, 4H), 3.89–3.77 (m, 4H), 3.73–3.67 (m, 4H), 3.65–3.56 (m, 8H), 3.52–3.47 (m, 4H), 3.40–3.34 (m, 6H).

GPC analysis of the polymer was not possible due to its aggregation tendency in solution and MALDI-ToF also proved to be unsuccessful.

p(gDPP-MeOT2)

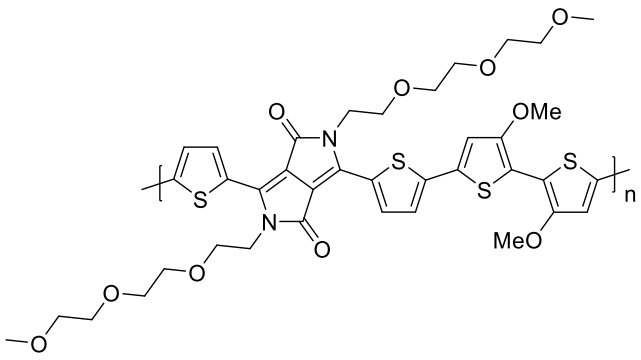

p(gDPP-MeOT2) was synthesised analogously to **p(gDPP-TT)**, using the following reagent quantities: **31** (98 mg, 0.13 mmol, 1.0 equiv.), **21** (72 mg, 0.13 mmol, 1.0 equiv.), tris(*o*-methoxyphenyl)phosphine (3.8 mg, 0.011 mmol, 0.083 equiv.), tris(dibenzylideneacetone)dipalladium(0) (4.9 mg, 0.0054 mmol, 0.042 equiv.), and 2.7 mL anhydrous and degassed toluene. The crude product was purified by sequential Soxhlet extractions in hexane, acetone, ethyl acetate, methanol, and chloroform. Excess solvent of the chloroform fraction was removed under reduced pressure and the product reprecipitated into methanol (30 mL). The final product was collected by suction filtration and was recovered as a dark blue solid (90 mg, 85% yield).

^{1}H NMR (400 MHz, $CDCl_3$): 8.90–8.75 (broad s, 6H), 4.41–4.25 (m, 4H), 4.13–4.02 (m, 4H), 3.89–3.78 (m, 4H), 3.76–3.54 (m, 12H), 3.53–3.43 (m, 6H), 3.34–3.30 (m, 6H).

GPC analysis of the polymer was not possible due to its aggregation tendency in solution and MALDI-ToF also proved to be unsuccessful.

'The pessimist sees difficulty in every opportunity. The optimist sees opportunity in every difficulty.'

— Winston Churchill

7

References

[1] V. Gold, Ed. , *The IUPAC Compendium of Chemical Terminology*, International Union Of Pure And Applied Chemistry (IUPAC), Research Triangle Park, NC, **2019**.

[2] L. H. A. Baekeland, *Method of Making Insoluble Products of Phenol and Formaldehyde*, **1907**, 942699.

[3] I. Tiseo, "Production of plastics worldwide from 1950 to 2019 (in million metric tons)," can be found under https://www.statista.com/statistics/282732/global-production-of-plastics-since-1950/, **2021**.

[4] H. Shirakawa, E. J. Louis, A. G. MacDiarmid, C. K. Chiang, A. J. Heeger, *J. Chem. Soc. Chem. Commun.* **1977**, 578.

[5] S. Allard, M. Forster, B. Souharce, H. Thiem, U. Scherf, *Angew. Chemie Int. Ed.* **2008**, *47*, 4070.

[6] H. Sirringhaus, *Adv. Mater.* **2005**, *17*, 2411.

[7] R. R. Søndergaard, M. Hösel, F. C. Krebs, *J. Polym. Sci. Part B Polym. Phys.* **2013**, *51*, 16.

[8] Y. Chen, Y. Zhao, Z. Liang, *Energy Environ. Sci.* **2015**, *8*, 401.

[9] L. Basiricò, P. Cosseddu, B. Fraboni, A. Bonfiglio, *Thin Solid Films* **2011**, *520*, 1291.

[10] M. Moser, A. Wadsworth, N. Gasparini, I. McCulloch, *Adv. Energy Mater.* **2021**, *11*, 2100056.

[11] S. Holliday, Y. Li, C. K. Luscombe, *Prog. Polym. Sci.* **2017**, *70*, 34.

[12] Apple, "iPhone," can be found under https://www.apple.com/uk/iphone/, **2021**.

[13] Audi, “Lighting Technology Pioneer Audi Fields Next-Generation OLED Technology,” can be found under https://www.audi-mediacenter.com/en/press-releases/lighting-technology-pioneer-audi-fields-next-generation-oled-technology-12988, **2021**.

[14] LG Electronics, “Rollable OLED TV R,” can be found under https://www.lg.com/global/lg-signature/rollable-oled-tv-r, **2018**.

[15] Boeing, “787 Dreamliner,” can be found under https://www.boeing.com/commercial/787/by-design/#/featured, **2020**.

[16] L. Feng, W. Tang, J. Zhao, R. Yang, W. Hu, Q. Li, R. Wang, X. Guo, *Sci. Rep.* **2016**, *6*, 20671.

[17] B. Russ, A. Glaudell, J. J. Urban, M. L. Chabinyc, R. A. Segalman, *Nat. Rev. Mater.* **2016**, *1*, 16050.

[18] T. M. Swager, *Macromolecules* **2017**, *50*, 4867.

[19] J. L. Brédas, *J. Chem. Phys.* **1985**, *82*, 3808.

[20] V. J. Eaton, D. Steele, *J. Chem. Soc. Faraday Trans. 2* **1973**, *69*, 1601.

[21] F. Grein, *J. Phys. Chem. A* **2002**, *106*, 3823.

[22] I. McCulloch, R. S. Ashraf, L. Biniek, H. Bronstein, C. Combe, J. E. Donaghey, D. I. James, C. B. Nielsen, B. C. Schroeder, W. Zhang, *Acc. Chem. Res.* **2012**, *45*, 714.

[23] M. Belletete, M. Leclerc, G. Durocher, *J. Phys. Chem.* **1994**, *98*, 9450.

[24] J. Casanovas, D. Zanuy, C. Alemán, *Polymer (Guildf).* **2005**, *46*, 9452.

[25] C. Duan, F. Huang, Y. Cao, *J. Mater. Chem.* **2012**, *22*, 10416.

[26] X. Guo, M. Baumgarten, K. Müllen, *Prog. Polym. Sci.* **2013**, *38*, 1832.

[27] K. Müllen, W. Pisula, *J. Am. Chem. Soc.* **2015**, *137*, 9503.

[28] S. Ko, E. T. Hoke, L. Pandey, S. Hong, R. Mondal, C. Risko, Y. Yi, R. Noriega, M. D. McGehee, J.-L. Brédas, A. Salleo, Z. Bao, *J. Am. Chem. Soc.* **2012**, *134*, 5222.

[29] Y. Yao, H. Dong, W. Hu, *Polym. Chem.* **2013**, *4*, 5197.

[30] A. Wadsworth, H. Chen, K. J. Thorley, C. Cendra, M. Nikolka, H. Bristow, M. Moser, A. Salleo, T. D. Anthopoulos, H. Sirringhaus, I. McCulloch, *J. Am. Chem. Soc.* **2020**, *142*, 652.

[31] M. Nikolka, K. Broch, J. Armitage, D. Hanifi, P. J. Nowack, D. Venkateshvaran, A. Sadhanala, J. Saska, M. Mascal, S.-H. Jung, J. Lee, I. McCulloch, A. Salleo, H. Sirringhaus, *Nat. Commun.* **2019**, *10*, 2122.

[32] I. McCulloch, M. Heeney, C. Bailey, K. Genevicius, I. MacDonald, M. Shkunov, D. Sparrowe, S. Tierney, R. Wagner, W. Zhang, M. L. Chabinyc, R. J. Kline, M. D. McGehee, M. F. Toney, *Nat. Mater.* **2006**, *5*, 328.

[33] R. J. Kline, D. M. DeLongchamp, D. A. Fischer, E. K. Lin, L. J. Richter, M. L. Chabinyc, M. F. Toney, M. Heeney, I. McCulloch, *Macromolecules* **2007**, *40*, 7960.

[34] M. L. Chabinyc, M. F. Toney, R. J. Kline, I. McCulloch, M. Heeney, *J. Am. Chem. Soc.* **2007**, *129*, 3226.

[35] J. L. Bredas, G. B. Street, *Acc. Chem. Res.* **1985**, *18*, 309.

[36] A. Pron, P. Rannou, *Prog. Polym. Sci.* **2002**, *27*, 135.

[37] A. Moliton, R. C. Hiorns, *Polym. Int.* **2004**, *53*, 1397.

[38] R. J. Waltman, J. Bargon, *Can. J. Chem.* **1986**, *64*, 76.

[39] J. Heinze, *Synth. Met.* **1991**, *43*, 2805.

[40] E. W. H. Jager, *Science (80-.).* **2000**, *290*, 1540.

[41] S. Tanaka, T. Iso, *J. Chem. Soc. Chem. Commun.* **1994**, 1071.

[42] S.-C. Huang, C.-Y. Lin, *Chem. Commun.* **2015**, *51*, 519.

[43] E. Poverenov, M. Li, A. Bitler, M. Bendikov, *Chem. Mater.* **2010**, *22*, 4019.

[44] Y. Xiao, J.-Y. Lin, S.-Y. Tai, S.-W. Chou, G. Yue, J. Wu, *J. Mater. Chem.* **2012**, *22*, 19919.

[45] K. Cysewska, J. Karczewski, P. Jasiński, *Electrochim. Acta* **2015**, *176*, 156.

[46] X. Du, Z. Wang, *Electrochim. Acta* **2003**, *48*, 1713.

[47] M. C. Morvant, J. R. Reynolds, *Synth. Met.* **1998**, *92*, 57.

[48] A. I. Melato, M. H. Mendonça, L. M. Abrantes, *J. Solid State Electrochem.* **2009**, *13*, 417.

[49] R. E. Myers, *J. Electron. Mater.* **1986**, *15*, 61.

[50] Y. Lu, G. Shi, C. Li, Y. Liang, *J. Appl. Polym. Sci.* **1998**, *70*, 2169.

[51] J. W. Choi, M. G. Han, S. Y. Kim, S. G. Oh, S. S. Im, *Synth. Met.* **2004**, *141*, 293.

[52] A. A. O. Sarhan, C. Bolm, *Chem. Soc. Rev.* **2009**, *38*, 2730.

[53] H. Chelawat, S. Vaddiraju, K. Gleason, *Chem. Mater.* **2010**, *22*, 2864.

[54] M. S. Cho, S. Y. Kim, J. D. Nam, Y. Lee, *Synth. Met.* **2008**, *158*, 865.

[55] R. Brooke, P. Cottis, P. Talemi, M. Fabretto, P. Murphy, D. Evans, *Prog. Mater. Sci.* **2017**, *86*, 127.

[56] R. S. Loewe, S. M. Khersonsky, R. D. McCullough, *Adv. Mater.* **1999**, *11*, 250.

[57] M. C. Stefan, M. P. Bhatt, P. Sista, H. D. Magurudeniya, *Polym. Chem.* **2012**, *3*, 1693.

[58] B. Carsten, F. He, H. J. Son, T. Xu, L. Yu, *Chem. Rev.* **2011**, *111*, 1493.

[59] J. Sakamoto, M. Rehahn, G. Wegner, A. D. Schlüter, *Macromol. Rapid Commun.* **2009**, *30*, 653.

[60] R. Tkachov, V. Senkovskyy, T. Beryozkina, K. Boyko, V. Bakulev, A. Lederer, K. Sahre, B. Voit, A. Kiriy, *Angew. Chemie Int. Ed.* **2014**, *53*, 2402.

[61] S. Xu, E. H. Kim, A. Wei, E. Negishi, *Sci. Technol. Adv. Mater.* **2014**, *15*, 044201.

[62] T. Bura, J. T. Blaskovits, M. Leclerc, *J. Am. Chem. Soc.* **2016**, *138*, 10056.

[63] J.-R. Pouliot, F. Grenier, J. T. Blaskovits, S. Beaupré, M. Leclerc, *Chem. Rev.* **2016**, *116*, 14225.

[64] G. Zhang, Y. Dai, Y. Liu, J. Liu, H. Lu, L. Qiu, K. Cho, *Polym. Chem.* **2017**, *8*, 3448.

[65] A. Onwubiko, W. Yue, C. Jellett, M. Xiao, H.-Y. Chen, M. K. Ravva, D. A. Hanifi, A.-C. Knall, B. Purushothaman, M. Nikolka, J.-C. Flores, A. Salleo, J.-L. Bredas, H. Sirringhaus, P. Hayoz, I. McCulloch, *Nat. Commun.* **2018**, *9*, 416.

[66] H. Chen, M. Moser, S. Wang, C. Jellett, K. Thorley, G. T. Harrison, X. Jiao, M. Xiao, B. Purushothaman, M. Alsufyani, H. Bristow, S. De Wolf, N. Gasparini, A. Wadsworth, C. R. McNeill, H. Sirringhaus, S. Fabiano, I. McCulloch, *J. Am. Chem. Soc.* **2021**, *143*, 260.

[67] B. D. Paulsen, K. Tybrandt, E. Stavrinidou, J. Rivnay, *Nat. Mater.* **2020**, *19*, 13.

[68] D. Moia, A. Giovannitti, A. A. Szumska, I. P. Maria, E. Rezasoltani, M. Sachs, M.

Schnurr, P. R. F. Barnes, I. McCulloch, J. Nelson, *Energy Environ. Sci.* **2019**, *12*, 1349.

[69] D. Khodagholy, T. Doublet, P. Quilichini, M. Gurfinkel, P. Leleux, A. Ghestem, E. Ismailova, T. Hervé, S. Sanaur, C. Bernard, G. G. Malliaras, *Nat. Commun.* **2013**, *4*, 1575.

[70] D. Khodagholy, J. N. Gelinas, Z. Zhao, M. Yeh, M. Long, J. D. Greenlee, W. Doyle, O. Devinsky, G. Buzsáki, *Sci. Adv.* **2016**, *2*, e1601027.

[71] G. D. Spyropoulos, J. N. Gelinas, D. Khodagholy, *Sci. Adv.* **2019**, *5*, eaau7378.

[72] A.-M. Pappa, V. F. Curto, M. Braendlein, X. Strakosas, M. J. Donahue, M. Fiocchi, G. G. Malliaras, R. M. Owens, *Adv. Healthc. Mater.* **2016**, *5*, 2295.

[73] D. Ohayon, G. Nikiforidis, A. Savva, A. Giugni, S. Wustoni, T. Palanisamy, X. Chen, I. P. Maria, E. Di Fabrizio, P. M. F. J. Costa, I. McCulloch, S. Inal, *Nat. Mater.* **2020**, *19*, 456.

[74] J. Gladisch, E. Stavrinidou, S. Ghosh, A. Giovannitti, M. Moser, I. Zozoulenko, I. McCulloch, M. Berggren, *Adv. Sci.* **2020**, *7*, 1901144.

[75] M. Moser, J. Gladisch, S. Ghosh, T. C. Hidalgo, J. F. Ponder, R. Sheelamanthula, Q. Thiburce, N. Gasparini, A. Wadsworth, A. Salleo, S. Inal, M. Berggren, I. Zozoulenko, E. Stavrinidou, I. McCulloch, *Adv. Funct. Mater.* **2021**, 2100723.

[76] Bayer, *Polythiophenes, Process for Their Preparation and Their Use*, **1989**, EP0339340A2.

[77] F. Jonas, L. Schrader, *Synth. Met.* **1991**, *41*, 831.

[78] G. Heywang, F. Jonas, *Adv. Mater.* **1992**, *4*, 116.

[79] E. Stavrinidou, P. Leleux, H. Rajaona, D. Khodagholy, J. Rivnay, M. Lindau, S. Sanaur, G. G. Malliaras, *Adv. Mater.* **2013**, *25*, 4488.

[80] J. Rivnay, S. Inal, B. A. Collins, M. Sessolo, E. Stavrinidou, X. Strakosas, C. Tassone, D. M. Delongchamp, G. G. Malliaras, *Nat. Commun.* **2016**, *7*, 11287.

[81] R. Giridharagopal, L. Q. Flagg, J. S. Harrison, M. E. Ziffer, J. Onorato, C. K. Luscombe, D. S. Ginger, *Nat. Mater.* **2017**, *16*, 737.

[82] M. Moser, J. F. Ponder, A. Wadsworth, A. Giovannitti, I. McCulloch, *Adv. Funct. Mater.* **2019**, *29*, 1807033.

[83] E. Zeglio, O. Inganäs, *Adv. Mater.* **2018**, *30*, 1800941.

[84] J. Rivnay, P. Leleux, M. Ferro, M. Sessolo, A. Williamson, D. A. Koutsouras, D. Khodagholy, M. Ramuz, X. Strakosas, R. M. Owens, C. Benar, J.-M. Badier, C. Bernard, G. G. Malliaras, *Sci. Adv.* **2015**, *1*, e1400251.

[85] D. A. Bernards, G. G. Malliaras, G. E. S. Toombes, S. M. Gruner, *Appl. Phys. Lett.* **2006**, *89*, 053505.

[86] M. Sessolo, J. Rivnay, E. Bandiello, G. G. Malliaras, H. J. Bolink, *Adv. Mater.* **2014**, *26*, 4803.

[87] A. M. Pappa, D. Ohayon, A. Giovannitti, I. P. Maria, A. Savva, I. Uguz, J. Rivnay, I. McCulloch, R. M. Owens, S. Inal, *Sci. Adv.* **2018**, *4*, 0911.

[88] L. Zhang, G. Wang, D. Wu, C. Xiong, L. Zheng, Y. Ding, H. Lu, G. Zhang, L. Qiu, *Biosens. Bioelectron.* **2018**, *100*, 235.

[89] J. Rivnay, M. Ramuz, P. Leleux, A. Hama, M. Huerta, R. M. Owens, *Appl. Phys. Lett.* **2015**, *106*, 043301.

[90] F. Hempel, J. K. Y. Law, T. C. Nguyen, R. Lanche, A. Susloparova, X. T. Vu, S. Ingebrandt, *Biosens. Bioelectron.* **2021**, *180*, 113101.

[91] G. P. Kittlesen, H. S. White, M. S. Wrighton, *J. Am. Chem. Soc.* **1984**, *106*, 7389.

[92] E. W. Paul, A. J. Ricco, M. S. Wrighton, *J. Phys. Chem.* **1985**, *89*, 1441.

[93] J. W. Thackeray, H. S. White, M. S. Wrighton, *J. Phys. Chem.* **1985**, *89*, 5133.

[94] J. E. Lilienfeld, *Method and Apparatus for Controlling Electric Currents*, **1925**, US1745175A.

[95] W. Shockley, *Semiconductor Amplifier*, **1948**, 2502488.

[96] A. Tsumura, H. Koezuka, T. Ando, *Appl. Phys. Lett.* **1986**, *49*, 1210.

[97] H. Koezuka, A. Tsumura, T. Ando, *Synth. Met.* **1987**, *18*, 699.

[98] T. B. Singh, F. Meghdadi, S. Günes, N. Marjanovic, G. Horowitz, P. Lang, S. Bauer, N. S. Sariciftci, *Adv. Mater.* **2005**, *17*, 2315.

[99] T. Yasuda, T. Goto, K. Fujita, T. Tsutsui, *Appl. Phys. Lett.* **2004**, *85*, 2098.

[100] J. Veres, S. Ogier, G. Lloyd, D. de Leeuw, *Chem. Mater.* **2004**, *16*, 4543.

[101] Y. Wang, X. Huang, T. Li, L. Li, X. Guo, P. Jiang, *Chem. Mater.* **2019**, *31*, 2212.

[102] R. K. Hallani, M. Moser, H. Bristow, M. V. C. Jenart, H. Faber, M. Neophytou, E. Yarali, A. F. Paterson, T. D. Anthopoulos, I. McCulloch, *J. Org. Chem.* **2020**, *85*, 277.

[103] C. Wang, H. Dong, W. Hu, Y. Liu, D. Zhu, *Chem. Rev.* **2012**, *112*, 2208.

[104] A. F. Paterson, S. Singh, K. J. Fallon, T. Hodsden, Y. Han, B. C. Schroeder, H. Bronstein, M. Heeney, I. McCulloch, T. D. Anthopoulos, *Adv. Mater.* **2018**, *30*,

1801079.

[105] M. Kim, S. U. Ryu, S. A. Park, K. Choi, T. Kim, D. Chung, T. Park, *Adv. Funct. Mater.* **2020**, *30*, 1904545.

[106] X. Gu, L. Shaw, K. Gu, M. F. Toney, Z. Bao, *Nat. Commun.* **2018**, *9*, 534.

[107] W. Tang, Y. Huang, L. Han, R. Liu, Y. Su, X. Guo, F. Yan, *J. Mater. Chem. C* **2019**, *7*, 790.

[108] M. J. Panzer, C. D. Frisbie, *J. Am. Chem. Soc.* **2007**, *129*, 6599.

[109] M. J. Panzer, C. D. Frisbie, *Adv. Mater.* **2008**, *20*, 3177.

[110] J. Rivnay, S. Inal, A. Salleo, R. M. Owens, M. Berggren, G. G. Malliaras, *Nat. Rev. Mater.* **2018**, *3*, 17086.

[111] D. M. de Leeuw, M. M. J. Simenon, A. R. Brown, R. E. F. Einerhand, *Synth. Met.* **1997**, *87*, 53.

[112] A. Giovannitti, R. B. Rashid, Q. Thiburce, B. D. Paulsen, C. Cendra, K. Thorley, D. Moia, J. T. Mefford, D. Hanifi, D. Weiyuan, M. Moser, A. Salleo, J. Nelson, I. McCulloch, J. Rivnay, *Adv. Mater.* **2020**, *32*, 1908047.

[113] D. Khodagholy, J. Rivnay, M. Sessolo, M. Gurfinkel, P. Leleux, L. H. Jimison, E. Stavrinidou, T. Herve, S. Sanaur, R. M. Owens, G. G. Malliaras, *Nat. Commun.* **2013**, *4*, 2133.

[114] D. A. Bernards, G. G. Malliaras, *Adv. Funct. Mater.* **2007**, *17*, 3538.

[115] S. Inal, G. G. Malliaras, J. Rivnay, *Nat. Commun.* **2017**, *8*, 1767.

[116] X. Wu, A. Surendran, J. Ko, O. Filonik, E. M. Herzig, P. Müller-Buschbaum, W. L. Leong, *Adv. Mater.* **2019**, *31*, 1805544.

[117] A. Savva, D. Ohayon, J. Surgailis, A. F. Paterson, T. C. Hidalgo, X. Chen, I. P. Maria, B. D. Paulsen, A. J. Petty, J. Rivnay, I. McCulloch, S. Inal, *Adv. Electron. Mater.* **2019**, *5*, 1900249.

[118] A. Savva, C. Cendra, A. Giugni, B. Torre, J. Surgailis, D. Ohayon, A. Giovannitti, I. McCulloch, E. Di Fabrizio, A. Salleo, J. Rivnay, S. Inal, *Chem. Mater.* **2019**, *31*, 927.

[119] C. Cendra, A. Giovannitti, A. Savva, V. Venkatraman, I. McCulloch, A. Salleo, S. Inal, J. Rivnay, *Adv. Funct. Mater.* **2019**, *29*, 1807034.

[120] L. Q. Flagg, R. Giridharagopal, J. Guo, D. S. Ginger, *Chem. Mater.* **2018**, *30*, 5380.

[121] N. Yunos, R. Bellomo, D. Story, J. Kellum, *Crit. Care* **2010**, *14*, 226.

[122] X. Niu, R. A. Bressan, P. M. Hasegawa, J. M. Pardo, *Plant Physiol.* **1995**, *109*, 735.

[123] E. Zeglio, M. Vagin, C. Musumeci, F. N. Ajjan, R. Gabrielsson, X. T. Trinh, N. T. Son, A. Maziz, N. Solin, O. Inganäs, *Chem. Mater.* **2015**, *27*, 6385.

[124] S.-M. Kim, C.-H. Kim, Y. Kim, N. Kim, W.-J. Lee, E.-H. Lee, D. Kim, S. Park, K. Lee, J. Rivnay, M.-H. Yoon, *Nat. Commun.* **2018**, *9*, 3858.

[125] Y. Wang, E. Zeglio, H. Liao, J. Xu, F. Liu, Z. Li, I. P. Maria, D. Mawad, A. Herland, I. McCulloch, W. Yue, *Chem. Mater.* **2019**, *31*, 9797.

[126] M. Moser, T. C. Hidalgo, J. Surgailis, J. Gladisch, S. Ghosh, R. Sheelamanthula, Q. Thiburce, A. Giovannitti, A. Salleo, N. Gasparini, A. Wadsworth, I. Zozoulenko, M. Berggren, E. Stavrinidou, S. Inal, I. McCulloch, *Adv. Mater.* **2020**, *32*, 2002748.

[127] M. Kemerink, S. Timpanaro, M. M. de Kok, E. A. Meulenkamp, F. J. Touwslager, *J. Phys. Chem. B* **2004**, *108*, 18820.

[128] A. M. Nardes, M. Kemerink, R. A. J. Janssen, J. A. M. Bastiaansen, N. M. M. Kiggen, B. M. W. Langeveld, A. J. J. M. van Breemen, M. M. de Kok, *Adv. Mater.* **2007**, *19*, 1196.

[129] X. Crispin, F. L. E. Jakobsson, A. Crispin, P. C. M. Grim, P. Andersson, A. Volodin, C. Van Haesendonck, M. Van Der Auweraer, W. R. Salaneck, M. Berggren, *Chem. Mater.* **2006**, *18*, 4354.

[130] S. Zhang, P. Kumar, A. S. Nouas, L. Fontaine, H. Tang, F. Cicoira, *APL Mater.* **2015**, *3*, 014911.

[131] L. Kergoat, B. Piro, D. T. Simon, M.-C. Pham, V. Noël, M. Berggren, *Adv. Mater.* **2014**, *26*, 5658.

[132] Y. Xia, K. Sun, J. Ouyang, *Adv. Mater.* **2012**, *24*, 2436.

[133] N. Kim, S. Kee, S. H. Lee, B. H. Lee, Y. H. Kahng, Y.-R. Jo, B.-J. Kim, K. Lee, *Adv. Mater.* **2014**, *26*, 2268.

[134] S. Zhang, E. Hubis, C. Girard, P. Kumar, J. DeFranco, F. Cicoira, *J. Mater. Chem. C* **2016**, *4*, 1382.

[135] S. Tekoglu, D. Wielend, M. C. Scharber, N. S. Sariciftci, C. Yumusak, *Adv. Mater. Technol.* **2020**, *5*, 1900699.

[136] J. Rivnay, P. Leleux, M. Sessolo, D. Khodagholy, T. Hervé, M. Fiocchi, G. G. Malliaras, *Adv. Mater.* **2013**, *25*, 7010.

[137] A. Håkansson, S. Han, S. Wang, J. Lu, S. Braun, M. Fahlman, M. Berggren, X. Crispin, S. Fabiano, *J. Polym. Sci. Part B Polym. Phys.* **2017**, *55*, 814.

[138] M. ElMahmoudy, S. Inal, A. Charrier, I. Uguz, G. G. Malliaras, S. Sanaur,

Macromol. Mater. Eng. **2017**, *302*, 1600497.

[139] L. H. Jimison, A. Hama, X. Strakosas, V. Armel, D. Khodagholy, E. Ismailova, G. G. Malliaras, B. Winther-Jensen, R. M. Owens, *J. Mater. Chem.* **2012**, *22*, 19498.

[140] S. Inal, J. Rivnay, A. I. Hofmann, I. Uguz, M. Mumtaz, D. Katsigiannopoulos, C. Brochon, E. Cloutet, G. Hadziioannou, G. G. Malliaras, *J. Polym. Sci. Part B Polym. Phys.* **2016**, *54*, 147.

[141] S. Carli, M. Di Lauro, M. Bianchi, M. Murgia, A. De Salvo, M. Prato, L. Fadiga, F. Biscarini, *ACS Appl. Mater. Interfaces* **2020**, acsami.0c06538.

[142] A. I. Hofmann, I. Östergren, Y. Kim, S. Fauth, M. Craighero, M.-H. Yoon, A. Lund, C. Müller, *ACS Appl. Mater. Interfaces* **2020**, *12*, 8713.

[143] R. H. Karlsson, A. Herland, M. Hamedi, J. A. Wigenius, A. Åslund, X. Liu, M. Fahlman, Olle Inganäs, P. Konradsson, *Chem. Mater.* **2009**, *21*, 1815.

[144] K. M. Persson, R. Karlsson, K. Svennersten, S. Löffler, E. W. H. Jager, A. Richter-Dahlfors, P. Konradsson, M. Berggren, *Adv. Mater.* **2011**, *23*, 4403.

[145] S. Inal, J. Rivnay, P. Leleux, M. Ferro, M. Ramuz, J. C. Brendel, M. M. Schmidt, M. Thelakkat, G. G. Malliaras, *Adv. Mater.* **2014**, *26*, 7450.

[146] A. O. Patil, Y. Ikenoue, N. Basescu, N. Colaneri, J. Chen, F. Wudl, A. J. Heeger, *Synth. Met.* **1987**, *20*, 151.

[147] M. M. Schmidt, M. ElMahmoudy, G. G. Malliaras, S. Inal, M. Thelakkat, *Macromol. Chem. Phys.* **2018**, *219*, 1700374.

[148] P. Schmode, D. Ohayon, P. M. Reichstein, A. Savva, S. Inal, M. Thelakkat, *Chem. Mater.* **2019**, *31*, 5286.

[149] H. Sun, M. Vagin, S. Wang, X. Crispin, R. Forchheimer, M. Berggren, S. Fabiano, *Adv. Mater.* **2018**, *30*, 1704916.

[150] B. V. Khau, L. R. Savagian, M. De Keersmaecker, M. A. Gonzalez, E. Reichmanis, *ACS Mater. Lett.* **2019**, *1*, 599.

[151] C. B. Nielsen, A. Giovannitti, D.-T. Sbircea, E. Bandiello, M. R. Niazi, D. A. Hanifi, M. Sessolo, A. Amassian, G. G. Malliaras, J. Rivnay, I. McCulloch, *J. Am. Chem. Soc.* **2016**, *138*, 10252.

[152] X. Guo, J. Quinn, Z. Chen, H. Usta, Y. Zheng, Y. Xia, J. W. Hennek, R. P. Ortiz, T. J. Marks, A. Facchetti, *J. Am. Chem. Soc.* **2013**, *135*, 1986.

[153] H. Pan, Y. Li, Y. Wu, P. Liu, B. S. Ong, S. Zhu, G. Xu, *J. Am. Chem. Soc.* **2007**, *129*, 4112.

[154] H. Yao, L. Ye, H. Zhang, S. Li, S. Zhang, J. Hou, *Chem. Rev.* **2016**, *116*, 7397.

[155] A. Giovannitti, D. T. Sbircea, S. Inal, C. B. Nielsen, E. Bandiello, D. A. Hanifi, M. Sessolo, G. G. Malliaras, I. McCulloch, J. Rivnay, *Proc. Natl. Acad. Sci. U. S. A.* **2016**, *113*, 12017.

[156] X. Strakosas, M. Bongo, R. M. Owens, *J. Appl. Polym. Sci.* **2015**, *132*, 41735.

[157] B. E. Watt, A. T. Proudfoot, J. A. Vale, *Toxicol. Rev.* **2004**, *23*, 51.

[158] K. Apel, H. Hirt, *Annu. Rev. Plant Biol.* **2004**, *55*, 373.

[159] R. L. Auten, J. M. Davis, *Pediatr. Res.* **2009**, *66*, 121.

[160] M. T. Dang, L. Hirsch, G. Wantz, *Adv. Mater.* **2011**, *23*, 3597.

[161] R. J. Kline, M. D. McGehee, E. N. Kadnikova, J. Liu, J. M. J. Fréchet, M. F. Toney, *Macromolecules* **2005**, *38*, 3312.

[162] A. T. Kleinschmidt, S. E. Root, D. J. Lipomi, *J. Mater. Chem. A* **2017**, *5*, 11396.

[163] J. Kim, B. Lim, K.-J. Baeg, Y.-Y. Noh, D. Khim, H.-G. Jeong, J.-M. Yun, D.-Y. Kim, *Chem. Mater.* **2011**, *23*, 4663.

[164] C. B. Nielsen, I. McCulloch, *Prog. Polym. Sci.* **2013**, *38*, 2053.

[165] D. Fichou, *Handbook of Oligo- and Polythiophenes*, Wiley, Weinheim, **1998**.

[166] A. Giovannitti, K. J. Thorley, C. B. Nielsen, J. Li, M. J. Donahue, G. G. Malliaras, J. Rivnay, I. McCulloch, *Adv. Funct. Mater.* **2018**, *28*, 1706325.

[167] J. Mei, Z. Bao, *Chem. Mater.* **2014**, *26*, 604.

[168] T. Lei, J. Y. Wang, J. Pei, *Chem. Mater.* **2014**, *26*, 594.

[169] A. Babel, S. A. Jenekhe, *Synth. Met.* **2005**, *148*, 169.

[170] B. Friedel, C. R. McNeill, N. C. Greenham, *Chem. Mater.* **2010**, *22*, 3389.

[171] R. D. McCullough, S. P. Williams, *J. Am. Chem. Soc.* **1993**, *115*, 11608.

[172] M. Moser, L. R. Savagian, A. Savva, M. Matta, J. F. Ponder, T. C. Hidalgo, D. Ohayon, R. Hallani, M. Reisjalali, A. Troisi, A. Wadsworth, J. R. Reynolds, S. Inal, I. McCulloch, *Chem. Mater.* **2020**, *32*, 6618.

[173] M. A. Keegstra, T. H. A. Peters, L. Brandsma, *Tetrahedron* **1992**, *48*, 3633.

[174] C. K. Song, B. J. Eckstein, T. L. D. Tam, L. Trahey, T. J. Marks, *ACS Appl. Mater. Interfaces* **2014**, *6*, 19347.

[175] B. Xu, S. Noh, B. C. Thompson, *Macromolecules* **2014**, *47*, 5029.

[176] X. Guo, Q. Liao, E. F. Manley, Z. Wu, Y. Wang, W. Wang, T. Yang, Y.-E. Shin, X. Cheng, Y. Liang, L. X. Chen, K.-J. Baeg, T. J. Marks, X. Guo, *Chem. Mater.* **2016**,

28, 2449.

[177] A. K. Mishra, A. Verma, S. Biswas, *J. Org. Chem.* **2017**, *82*, 3403.

[178] S. L. Hager, T. B. Macrury, *J. Appl. Polym. Sci.* **1980**, *25*, 1559.

[179] L. Huang, K. Nishinari, *J. Polym. Sci. Part B Polym. Phys.* **2001**, *39*, 496.

[180] M. Moser, K. J. Thorley, F. Moruzzi, J. F. Ponder, I. P. Maria, A. Giovannitti, S. Inal, I. McCulloch, *J. Mater. Chem. C* **2019**, *7*, 5359.

[181] X. Guo, M. D. Watson, *Org. Lett.* **2008**, *10*, 5333.

[182] C. M. Cardona, W. Li, A. E. Kaifer, D. Stockdale, G. C. Bazan, *Adv. Mater.* **2011**, *23*, 2367.

[183] M. Skompska, A. Szkurlat, *Electrochim. Acta* **2001**, *46*, 4007.

[184] S. Sweetnam, K. R. Graham, G. O. Ngongang Ndjawa, T. Heumüller, J. A. Bartelt, T. M. Burke, W. Li, W. You, A. Amassian, M. D. McGehee, *J. Am. Chem. Soc.* **2014**, *136*, 14078.

[185] A. Savva, R. Hallani, C. Cendra, J. Surgailis, T. C. Hidalgo, S. Wustoni, R. Sheelamanthula, X. Chen, M. Kirkus, A. Giovannitti, A. Salleo, I. McCulloch, S. Inal, *Adv. Funct. Mater.* **2020**, *30*, 1907657.

[186] J.-F. Chang, J. Clark, N. Zhao, H. Sirringhaus, D. W. Breiby, J. W. Andreasen, M. M. Nielsen, M. Giles, M. Heeney, I. McCulloch, *Phys. Rev. B* **2006**, *74*, 115318.

[187] J. Clark, C. Silva, R. H. Friend, F. C. Spano, *Phys. Rev. Lett.* **2007**, *98*, 206406.

[188] C. Carlberg, *Solid State Ionics* **1996**, *85*, 73.

[189] C. Enengl, S. Enengl, S. Pluczyk, M. Havlicek, M. Lapkowski, H. Neugebauer, E. Ehrenfreund, *ChemPhysChem* **2016**, *17*, 3830.

[190] D. M. DeLongchamp, B. M. Vogel, Y. Jung, M. C. Gurau, C. A. Richter, O. A. Kirillov, J. Obrzut, D. A. Fischer, S. Sambasivan, L. J. Richter, E. K. Lin, *Chem. Mater.* **2005**, *17*, 5610.

[191] L. H. Zhao, R. Q. Png, J. M. Zhuo, L. Y. Wong, J. C. Tang, Y. S. Su, L. L. Chua, *Macromolecules* **2011**, *44*, 9692.

[192] B. C. Schroeder, T. Kurosawa, T. Fu, Y.-C. Chiu, J. Mun, G.-J. N. Wang, X. Gu, L. Shaw, J. W. E. Kneller, T. Kreouzis, M. F. Toney, Z. Bao, *Adv. Funct. Mater.* **2017**, *27*, 1701973.

[193] L. Q. Flagg, C. G. Bischak, J. W. Onorato, R. B. Rashid, C. K. Luscombe, D. S. Ginger, *J. Am. Chem. Soc.* **2019**, *141*, 4345.

[194] S. Yang, P. Olishevski, M. Kertesz, *Synth. Met.* **2004**, *141*, 171.

[195] N. Vukmirović, L.-W. Wang, *J. Phys. Chem. B* **2009**, *113*, 409.

[196] Y. Lu, Z. Yu, R. Zhang, Z. Yao, H. You, L. Jiang, H. Un, B. Dong, M. Xiong, J. Wang, J. Pei, *Angew. Chemie Int. Ed.* **2019**, *58*, 11390.

[197] G. Wang, S. M. Swick, M. Matta, S. Mukherjee, J. W. Strzalka, J. L. Logsdon, S. Fabiano, W. Huang, T. J. Aldrich, T. Yang, A. Timalsina, N. Powers-Riggs, J. M. Alzola, R. M. Young, D. M. DeLongchamp, M. R. Wasielewski, K. L. Kohlstedt, G. C. Schatz, F. S. Melkonyan, A. Facchetti, T. J. Marks, *J. Am. Chem. Soc.* **2019**, *141*, 13410.

[198] M. Kong, I. Saha Dalal, G. Li, R. G. Larson, *Macromolecules* **2014**, *47*, 1494.

[199] J. L. Brédas, A. J. Heeger, *Chem. Phys. Lett.* **1994**, *217*, 507.

[200] D. Beatrup, J. Wade, L. Biniek, H. Bronstein, M. Hurhangee, J.-S. Kim, I.

McCulloch, J. R. Durrant, *Chem. Commun.* **2014**, *50*, 14425.

[201] I. Osaka, R. D. McCullough, *Acc. Chem. Res.* **2008**, *41*, 1202.

[202] L. R. Savagian, A. M. Österholm, J. F. Ponder, K. J. Barth, J. Rivnay, J. R. Reynolds, *Adv. Mater.* **2018**, *30*, 1804647.

[203] L. L. Miller, Y. Yu, *J. Org. Chem.* **1995**, *60*, 6813.

[204] J. A. Kerszulis, K. E. Johnson, M. Kuepfert, D. Khoshabo, A. L. Dyer, J. R. Reynolds, *J. Mater. Chem. C* **2015**, *3*, 3211.

[205] Z. Zhong, Z.-Y. Wang, S.-F. Ni, L. Dang, H. K. Lee, X.-S. Peng, H. N. C. Wong, *Org. Lett.* **2019**, *21*, 700.

[206] I. Zozoulenko, A. Singh, S. K. Singh, V. Gueskine, X. Crispin, M. Berggren, *ACS Appl. Polym. Mater.* **2019**, *1*, 83.

[207] S. Ghosh, V. Gueskine, M. Berggren, I. V. Zozoulenko, *J. Phys. Chem. C* **2019**, *123*, 15467.

[208] C. M. Proctor, J. Rivnay, G. G. Malliaras, *J. Polym. Sci. Part B Polym. Phys.* **2016**, *54*, 1433.

[209] E. Smela, N. Gadegaard, *Adv. Mater.* **1999**, *11*, 953.

[210] E. Smela, N. Gadegaard, *J. Phys. Chem. B* **2001**, *105*, 9395.

[211] C. G. Bischak, L. Q. Flagg, K. Yan, T. Rehman, D. W. Davies, R. J. Quezada, J. W. Onorato, C. K. Luscombe, Y. Diao, C.-Z. Li, D. S. Ginger, *J. Am. Chem. Soc.* **2020**, *142*, 7434.

[212] X. Wu, A. Surendran, M. Moser, S. Chen, B. T. Muhammad, I. P. Maria, I. Mcculloch, W. L. Leong, *ACS Appl. Mater. Interfaces* **2020**, *12*, 20757.

[213] Y. Kim, H. Noh, B. D. Paulsen, J. Kim, I. Jo, H. Ahn, J. Rivnay, M. Yoon, *Adv. Mater.* **2021**, *33*, 2007550.

[214] A. Laiho, L. Herlogsson, R. Forchheimer, X. Crispin, M. Berggren, *Proc. Natl. Acad. Sci. U. S. A.* **2011**, *108*, 15069.

[215] A. F. Paterson, A. Savva, S. Wustoni, L. Tsetseris, B. D. Paulsen, H. Faber, A. H. Emwas, X. Chen, G. Nikiforidis, T. C. Hidalgo, M. Moser, I. P. Maria, J. Rivnay, I. McCulloch, T. D. Anthopoulos, S. Inal, *Nat. Commun.* **2020**, *11*, 3004.

[216] D. T. Simon, E. O. Gabrielsson, K. Tybrandt, M. Berggren, *Chem. Rev.* **2016**, *116*, 13009.

[217] I. Gualandi, D. Tonelli, F. Mariani, E. Scavetta, M. Marzocchi, B. Fraboni, *Sci. Rep.* **2016**, *6*, 35419.

[218] H. Tang, P. Lin, H. L. W. Chan, F. Yan, *Biosens. Bioelectron.* **2011**, *26*, 4559.

[219] Z.-T. Zhu, J. T. Mabeck, C. Zhu, N. C. Cady, C. A. Batt, G. G. Malliaras, *Chem. Commun.* **2004**, 1556.

[220] M. Braendlein, A.-M. Pappa, M. Ferro, A. Lopresti, C. Acquaviva, E. Mamessier, G. G. Malliaras, R. M. Owens, *Adv. Mater.* **2017**, *29*, 1605744.

[221] W. Hai, T. Goda, H. Takeuchi, S. Yamaoka, Y. Horiguchi, A. Matsumoto, Y. Miyahara, *Sensors Actuators B Chem.* **2018**, *260*, 635.

[222] R.-X. He, M. Zhang, F. Tan, P. H. M. Leung, X.-Z. Zhao, H. L. W. Chan, M. Yang, F. Yan, *J. Mater. Chem.* **2012**, *22*, 22072.

[223] J. H. University, "COVID-19 Dashboard," can be found under https://coronavirus.jhu.edu/map.html, **2021**.

[224] K. Guo, S. Wustoni, A. Koklu, E. Díaz-Galicia, M. Moser, A. Hama, A. A. Alqahtani, A. N. Ahmad, F. S. Alhamlan, M. Shuaib, A. Pain, I. McCulloch, S. T. Arold, R. Grünberg, S. Inal, *Nat. Biomed. Eng.* **2021**, DOI 10.1038/s41551-021-00734-9.

[225] A. Koklu, S. Wustoni, V.-E. Musteata, D. Ohayon, M. Moser, I. McCulloch, S. P. Nunes, S. Inal, *ACS Nano* **2021**, *15*, 8130.

[226] H. Sirringhaus, *Adv. Mater.* **2014**, *26*, 1319.

[227] H. Luo, C. Yu, Z. Liu, G. Zhang, H. Geng, Y. Yi, K. Broch, Y. Hu, A. Sadhanala, L. Jiang, P. Qi, Z. Cai, H. Sirringhaus, D. Zhang, *Sci. Adv.* **2016**, *2*, e1600076.

[228] C. B. Nielsen, M. Turbiez, I. McCulloch, *Adv. Mater.* **2013**, *25*, 1859.

[229] S. Holliday, J. E. Donaghey, I. McCulloch, *Chem. Mater.* **2014**, *26*, 647.

[230] Q. Liu, S. E. Bottle, P. Sonar, *Adv. Mater.* **2020**, *32*, 1903882.

[231] P.-T. Wu, F. S. Kim, S. A. Jenekhe, *Chem. Mater.* **2011**, *23*, 4618.

[232] W. Li, T. Lee, S. J. Oh, C. R. Kagan, *ACS Appl. Mater. Interfaces* **2011**, *3*, 3874.

[233] Y. Li, S. P. Singh, P. Sonar, *Adv. Mater.* **2010**, *22*, 4862.

[234] Y. Li, P. Sonar, S. P. Singh, M. S. Soh, M. Van Meurs, J. Tan, *J. Am. Chem. Soc.* **2011**, *133*, 2198.

[235] Z. Chen, M. J. Lee, R. Shahid Ashraf, Y. Gu, S. Albert-Seifried, M. Meedom Nielsen, B. Schroeder, T. D. Anthopoulos, M. Heeney, I. McCulloch, H. Sirringhaus, *Adv. Mater.* **2012**, *24*, 647.

[236] H. Bronstein, Z. Chen, R. S. Ashraf, W. Zhang, J. Du, J. R. Durrant, P. Shakya Tuladhar, K. Song, S. E. Watkins, Y. Geerts, M. M. Wienk, R. A. J. Janssen, T.

Anthopoulos, H. Sirringhaus, M. Heeney, I. McCulloch, *J. Am. Chem. Soc.* **2011**, *133*, 3272.

[237] M. Grzybowski, D. T. Gryko, *Adv. Opt. Mater.* **2015**, *3*, 280.

[238] C. Kanimozhi, M. Naik, N. Yaacobi-Gross, E. K. Burnett, A. L. Briseno, T. D. Anthopoulos, S. Patil, *J. Phys. Chem. C* **2014**, *118*, 11536.

[239] C. J. Mueller, C. R. Singh, M. Fried, S. Huettner, M. Thelakkat, *Adv. Funct. Mater.* **2015**, *25*, 2725.

[240] A. Giovannitti, C. B. Nielsen, D.-T. Sbircea, S. Inal, M. Donahue, M. R. Niazi, D. A. Hanifi, A. Amassian, G. G. Malliaras, J. Rivnay, I. McCulloch, *Nat. Commun.* **2016**, *7*, 13066.

[241] Z. S. Parr, R. Halaksa, P. A. Finn, R. B. Rashid, A. Kovalenko, M. Weiter, J. Rivnay, J. Krajčovič, C. B. Nielsen, *Chempluschem* **2019**, *84*, 1384.

[242] J. Mei, K. R. Graham, R. Stalder, S. P. Tiwari, H. Cheun, J. Shim, M. Yoshio, C. Nuckolls, B. Kippelen, R. K. Castellano, J. R. Reynolds, *Chem. Mater.* **2011**, *23*, 2285.

[243] G. Krauss, F. Meichsner, A. Hochgesang, J. Mohanraj, S. Salehi, P. Schmode, M. Thelakkat, *Adv. Funct. Mater.* **2021**, *31*, 2010048.

[244] I. Meager, R. S. Ashraf, S. Mollinger, B. C. Schroeder, H. Bronstein, D. Beatrup, M. S. Vezie, T. Kirchartz, A. Salleo, J. Nelson, I. McCulloch, *J. Am. Chem. Soc.* **2013**, *135*, 11537.

[245] S. Stas, S. Sergeyev, Y. Geerts, *Tetrahedron* **2010**, *66*, 1837.

[246] Š. Frebort, Z. Eliáš, A. Lyčka, S. Luňák, J. Vyňuchal, L. Kubáč, R. Hrdina, L.

Burgert, *Tetrahedron Lett.* **2011**, *52*, 5769.

[247] S. Otep, Y.-C. Lin, H. Matsumoto, T. Mori, K.-H. Wei, T. Michinobu, *Org. Electron.* **2020**, *87*, 105986.

[248] H. Meier, U. Stalmach, H. Kolshorn, *Acta Polym.* **1997**, *48*, 379.

[249] G.-Y. Chen, C.-M. Chiang, D. Kekuda, S.-C. Lan, C.-W. Chu, K.-H. Wei, *J. Polym. Sci. Part A Polym. Chem.* **2010**, *48*, 1669.

[250] C. Kanimozhi, P. Balraju, G. D. Sharma, S. Patil, *J. Phys. Chem. B* **2010**, *114*, 3095.

[251] P. P. Khlyabich, B. Burkhart, C. F. Ng, B. C. Thompson, *Macromolecules* **2011**, *44*, 5079.

[252] T.-H. Le, Y. Kim, H. Yoon, *Polymers (Basel).* **2017**, *9*, 150.

[253] T. A. Skotheim, J. R. Reynolds, *Conjugated Polymers: Theory, Synthesis, Properties, and Characterization*, **2007**.

[254] B. Meng, H. Song, X. Chen, Z. Xie, J. Liu, L. Wang, *Macromolecules* **2015**, *48*, 4357.

[255] X. Chen, Z. Zhang, Z. Ding, J. Liu, L. Wang, *Angew. Chemie Int. Ed.* **2016**, *55*, 10376.

[256] S. Torabi, F. Jahani, I. Van Severen, C. Kanimozhi, S. Patil, R. W. A. Havenith, R. C. Chiechi, L. Lutsen, D. J. M. Vanderzande, T. J. Cleij, J. C. Hummelen, L. J. A. Koster, *Adv. Funct. Mater.* **2015**, *25*, 150.

[257] J. Rivnay, S. C. B. Mannsfeld, C. E. Miller, A. Salleo, M. F. Toney, *Chem. Rev.* **2012**, *112*, 5488.

[258] X. Zhang, L. J. Richter, D. M. Delongchamp, R. J. Kline, M. R. Hammond, I.

McCulloch, M. Heeney, R. S. Ashraf, J. N. Smith, T. D. Anthopoulos, B. Schroeder, Y. H. Geerts, D. A. Fischer, M. F. Toney, *J. Am. Chem. Soc.* **2011**, *133*, 15073.

[259] Y. Xi, C. M. Wolf, L. D. Pozzo, *Soft Matter* **2019**, *15*, 1799.

[260] R. Steyrleuthner, Y. Zhang, L. Zhang, F. Kraffert, B. P. Cherniawski, R. Bittl, A. L. Briseno, J. L. Bredas, J. Behrends, *Phys. Chem. Chem. Phys.* **2017**, *19*, 3627.

[261] M. Watanabe, S. Nagano, K. Sanui, N. Ogata, *Solid State Ionics* **1986**, *18–19*, 338.

[262] Z. Xue, D. He, X. Xie, *J. Mater. Chem. A* **2015**, *3*, 19218.

[263] R. S. Ashraf, I. Meager, M. Nikolka, M. Kirkus, M. Planells, B. C. Schroeder, S. Holliday, M. Hurhangee, C. B. Nielsen, H. Sirringhaus, I. McCulloch, *J. Am. Chem. Soc.* **2015**, *137*, 1314.

[264] C. W. Nogueira, G. Zeni, J. B. T. Rocha, *Chem. Rev.* **2004**, *104*, 6255.

[265] O. Gidron, Y. Diskin-Posner, M. Bendikov, *J. Am. Chem. Soc.* **2010**, *132*, 2148.

[266] F. Cadamuro, L. Russo, F. Nicotra, *European J. Org. Chem.* **2021**, *2021*, 374.

[267] X. Chen, A. Marks, B. D. Paulsen, R. Wu, R. B. Rashid, H. Chen, M. Alsufyani, J. Rivnay, I. McCulloch, *Angew. Chemie Int. Ed.* **2021**, *60*, 9368.

[268] I. P. Maria, B. D. Paulsen, A. Savva, D. Ohayon, R. Wu, R. Hallani, A. Basu, W. Du, T. D. Anthopoulos, S. Inal, J. Rivnay, I. McCulloch, A. Giovannitti, *Adv. Funct. Mater.* **2021**, *31*, 2008718.

[269] H. Sun, J. Gerasimov, M. Berggren, S. Fabiano, *J. Mater. Chem. C* **2018**, *6*, 11778.

[270] Z. S. Parr, R. B. Rashid, B. D. Paulsen, B. Poggi, E. Tan, M. Freeley, M. Palma, I. Abrahams, J. Rivnay, C. B. Nielsen, *Adv. Electron. Mater.* **2020**, *6*, 2000215.

[271] D. C. Harrowven, I. L. Guy, *Chem. Commun.* **2004**, 1968.

[272] J. Ilavsky, *J. Appl. Crystallogr.* **2012**, *45*, 324.

[273] S. D. Oosterhout, V. Savikhin, J. Zhang, Y. Zhang, M. A. Burgers, S. R. Marder, G. C. Bazan, M. F. Toney, *Chem. Mater.* **2017**, *29*, 3062.

[274] Z. Jiang, *J. Appl. Crystallogr.* **2015**, *48*, 917.

[275] M. Sessolo, D. Khodagholy, J. Rivnay, F. Maddalena, M. Gleyzes, E. Steidl, B. Buisson, G. G. Malliaras, *Adv. Mater.* **2013**, *25*, 2135.

[276] M. J. Marsella, R. J. Newland, P. J. Carroll, T. M. Swager, *J. Am. Chem. Soc.* **1995**, *117*, 9842.

[277] J. Qi, J. Han, X. Zhou, D. Yang, J. Zhang, W. Qiao, D. Ma, Z. Y. Wang, *Macromolecules* **2015**, *48*, 3941.

[278] S. Krakert, N. Ballav, M. Zharnikov, A. Terfort, *Phys. Chem. Chem. Phys.* **2010**, *12*, 507.

[279] R. Hooper, L. J. Lyons, M. K. Mapes, D. Schumacher, D. A. Moline, R. West, *Macromolecules* **2001**, *34*, 931.

[280] C. J. Martin, A. T. L. Lee, R. W. Adams, D. A. Leigh, *J. Am. Chem. Soc.* **2017**, *139*, 11998.

'Do it with passion or not at all.'

— Rosa Nouchette Carey

8

Appendix

Contents

8.1. Synthesis of Ethylene Glycol Monomethyl Ether Chains

8.1.1 Synthesis of Hexaethylene Glycol Monomethyl Ether

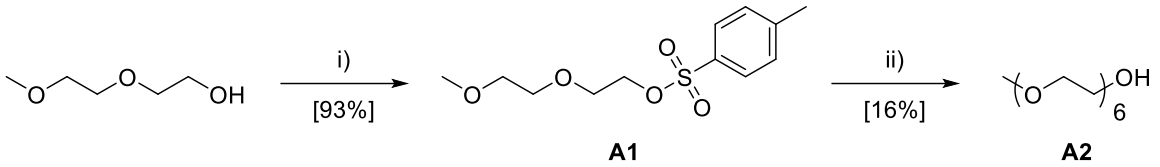

Scheme 8.1. *Synthesis of hexaethylene glycol monomethyl ether. Reagents and conditions: i) NaOH (1.5 equiv.), TsCl (1.1 equiv.), THF, H_2O, 0 °C; ii) Tetraethylene glycol (5.0 equiv.), NaH (5.0 equiv.), THF, 0 °C then 66 °C.*

2-(2-Methoxyethoxy)ethyl 4-methylbenzenesulfonate (A1)

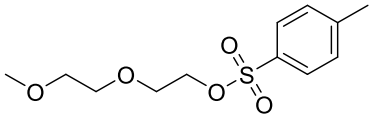

Diethylene glycol monomethyl ether (50.0 g, 416 mmol, 1.00 equiv.) was dissolved in 100 mL tetrahydrofuran and cooled to 0 °C. A solution of sodium hydroxide (25.0 g, 625 mmol, 1.50 equiv.) in 100 mL distilled water was added and the resulting mixture was left to stir for 30 min at 0 °C. Next, a solution of tosyl chloride (83.0 g, 437 mmol, 1.05 equiv.) in 100 mL tetrahydrofuran was added dropwise and the mixture stirred overnight. Distilled water (150 mL) was added, and the aqueous layer was extracted with diethyl ether (3 x 150 mL). The combined organic phases were washed with water (2 x 150 mL) and brine (150 mL), before being dried over anhydrous sodium sulfate. Excess solvent was removed under reduced pressure. No further purification was required to afford the final product as a clear colourless oil (106 g, 387 mmol, 93% yield).

^{1}H NMR (400 MHz, $CDCl_3$) δ: 7.77–7.70 (m, 2H), 7.30–7.24 (m, 2H), 4.12–4.07 (m, 2H), 3.64–3.59 (m, 2H), 3.54–3.48 (m, 2H), 3.44–3.37 (m, 2H), 3.28 (s, 3H), 2.37 (s, 3H).

The ^{1}H NMR data were consistent with the one reported in literature.[279]

Hexaethylene glycol monomethyl ether (A2)

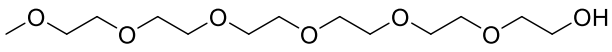

A suspension of 60% sodium hydride in mineral oil (32.0 g, 800 mmol, 5.00 equiv.) was dissolved in 800 mL anhydrous tetrahydrofuran and cooled to 0 °C. Tetraethylene glycol (166 g, 798 mmol, 4.99 equiv.) was then added dropwise. The reaction mixture was stirred for 45 min at room temperature and subsequently for 45 min at reflux. The reaction mixture was cooled to 0 °C and a solution of **A1** (44.0 g, 161 mmol, 1.00 equiv.) in 320 mL tetrahydrofuran was added dropwise. The mixture was stirred for 45 min at room temperature and then heated to reflux overnight. Water (300 mL) was added, and the aqueous phase was extracted with chloroform (3 x 200 mL). The combined organic layers were washed with water (3 x 200 mL) and brine (150 mL) before being dried over anhydrous sodium sulfate. Excess solvent was removed under reduced pressure. The final product was obtained by silica flash column chromatography employing a 95:5 v/v mixture of CH_2Cl_2:methanol as the eluent (R_f = 0.30). The final product was collected as a clear colourless oil (7.60 g, 25.6 mmol, 16% yield).

^{1}H NMR (400 MHz, $CDCl_3$) δ: 3.74–3.53 (m, 24H), 3.38 (s, 3H), 2.90 (s, 1H).

The ^{1}H NMR data were consistent with the one reported in literature.[279]

8.1.2 Synthesis of Pentaethylene Glycol Monomethyl Ether

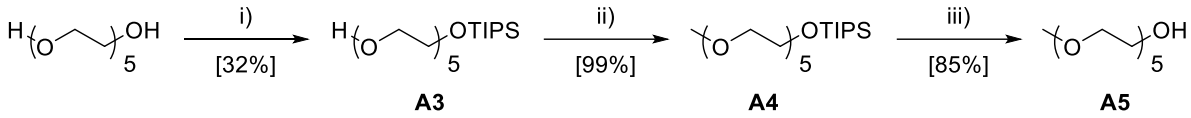

Scheme 8.2. *Synthesis of pentaethylene glycol monomethyl ether. Reagents and conditions: i) Imidazole (1.5 equiv.), TIPS-Cl (1.0 equiv.), CH_2Cl_2, RT; ii) NaH (1.2 equiv.), MeI (2.0 equiv.), THF, 0 °C then RT; iii) TBAF (1.2 equiv.), THF, RT.*

Monotriisopropylsilyl pentaethylene glycol (A3)

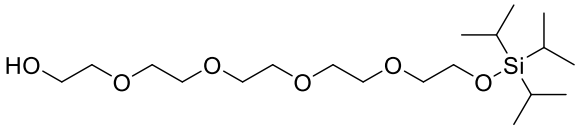

Pentaethylene glycol (25.0 g, 105 mmol, 1.00 equiv.) was dissolved in 1000 mL CH_2Cl_2 and imidazole (10.7 g, 157 mmol, 1.50 equiv.) was added portionwise. After stirring for 30 min at room temperature, triisopropylsilyl chloride (20.3 g, 105 mmol, 1.00 equiv.) was added dropwise and the reaction stirred at room temperature overnight. Water (200 mL) was added to the reaction mixture and the aqueous phase extracted with CH_2Cl_2 (3 x 200 mL). The combined organic layers were washed with water (2 x 200 mL) and brine (100 mL) before being dried over anhydrous sodium sulfate. Excess solvent was removed under reduced pressure. The crude product was purified by silica flash column chromatography employing EtOAc as the eluent (R_f = 0.30). The final product was collected as a clear colourless oil (13.9 g, 34.0 mmol, 32% yield).

^{1}H NMR (400 MHz, $CDCl_3$) δ: 3.84 (t, J = 5.6 Hz, 2H), 3.75–3.55 (m, 18H), 2.63 (s, 1H), 1.15–1.03 (m, 21H).

$^{13}C\{^1H\}$ (101 MHz, $CDCl_3$) δ: 72.7, 72.6, 70.8, 70.7, 70.6, 70.6, 70.3, 62.9, 61.7, 18.0, 12.0.

The ^{1}H and $^{13}C\{^1H\}$ NMR data were consistent with the one reported in literature.[280]

Monotriisopropylsilyl pentaethylene glycol monomethyl ether (A4)

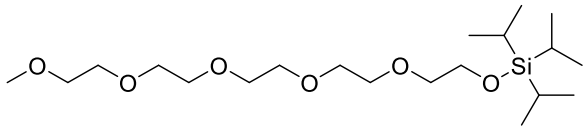

A suspension of 60% sodium hydride in mineral oil (1.70 g, 42.5 mmol, 1.21 equiv.) was dissolved in 400 mL anhydrous tetrahydrofuran and cooled to 0 °C. **A3** (13.9 g, 35.2 mmol, 1.00 equiv.) was added dropwise and the reaction stirred for 1 h at room temperature. Methyl iodide (10.0 g, 70.4 mmol, 2.00 equiv.) was then added dropwise at 0 °C. The reaction was stirred overnight and allowed to warm to room temperature. The reaction was quenched by adding distilled water (10 mL) dropwise. An additional amount of distilled water (100 mL) was added afterward. The aqueous phase was extracted with CH_2Cl_2 (3 x 150 mL) and the combined organic fractions were washed with water (2 x 100 mL) and brine (100 mL) before being dried over anhydrous sodium sulfate. Excess solvent was removed under reduced pressure. The crude product was purified by silica flash column chromatography employing EtOAc as the eluent (R_f = 0.40). The final product was collected as a clear colourless oil (14.2 g, 34.8 mmol, 99% yield).

^{1}H NMR (400 MHz, $CDCl_3$) δ: 3.85 (t, J = 5.6 Hz, 2H), 3.71–3.53 (m, 18H), 3.39 (s, 3H), 1.14–1.02 (m, 21H).

$^{13}C\{^1H\}$ (101 MHz, $CDCl_3$) δ: 72.7, 71.9, 70.8, 70.7, 70.6, 70.5, 63.0, 59.0, 18.0, 12.0.

The ^{1}H and $^{13}C\{^1H\}$ NMR data were consistent with the one reported in literature.[280]

Pentaethylene glycol monomethyl ether (A5)

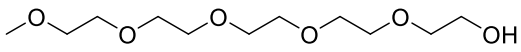

A4 (14.4 g, 35.3 mmol, 1.00 equiv.) was dissolved in 500 mL anhydrous tetrahydrofuran. A tetrabutylammonium fluoride in tetrahydrofuran solution (1.0 M, 42 mL, 42 mmol, 1.2 equiv.) was added dropwise at room temperature and the reaction was allowed to proceed overnight. The reaction was quenched by the addition of distilled water (10 mL). Additional distilled water (100 mL) was then added, and the aqueous phase was extracted with CH_2Cl_2 (3 x100 mL). The combined organic fractions were washed with water (2 x 100 mL) and brine (100 mL) before being dried over anhydrous sodium sulfate. Excess solvent was removed under reduced pressure. The crude product was purified by silica flash column chromatography employing a 95:5 v/v mixture of CH_2Cl_2:methanol as the eluent (R_f = 0.40). The final product was collected as a clear colourless oil (7.48 g, 29.7 mmol, 85% yield).

^{1}H NMR (400 MHz, $CDCl_3$) δ: 3.73–3.67 (m, 2H), 3.66–3.55 (m, 16H), 3.55–3.50 (m, 2H), 3.35 (s, 3H), 2.84 (s, 1H).

The ^{1}H NMR data were consistent with the one reported in literature.[280]

8.2. Licence Agreements

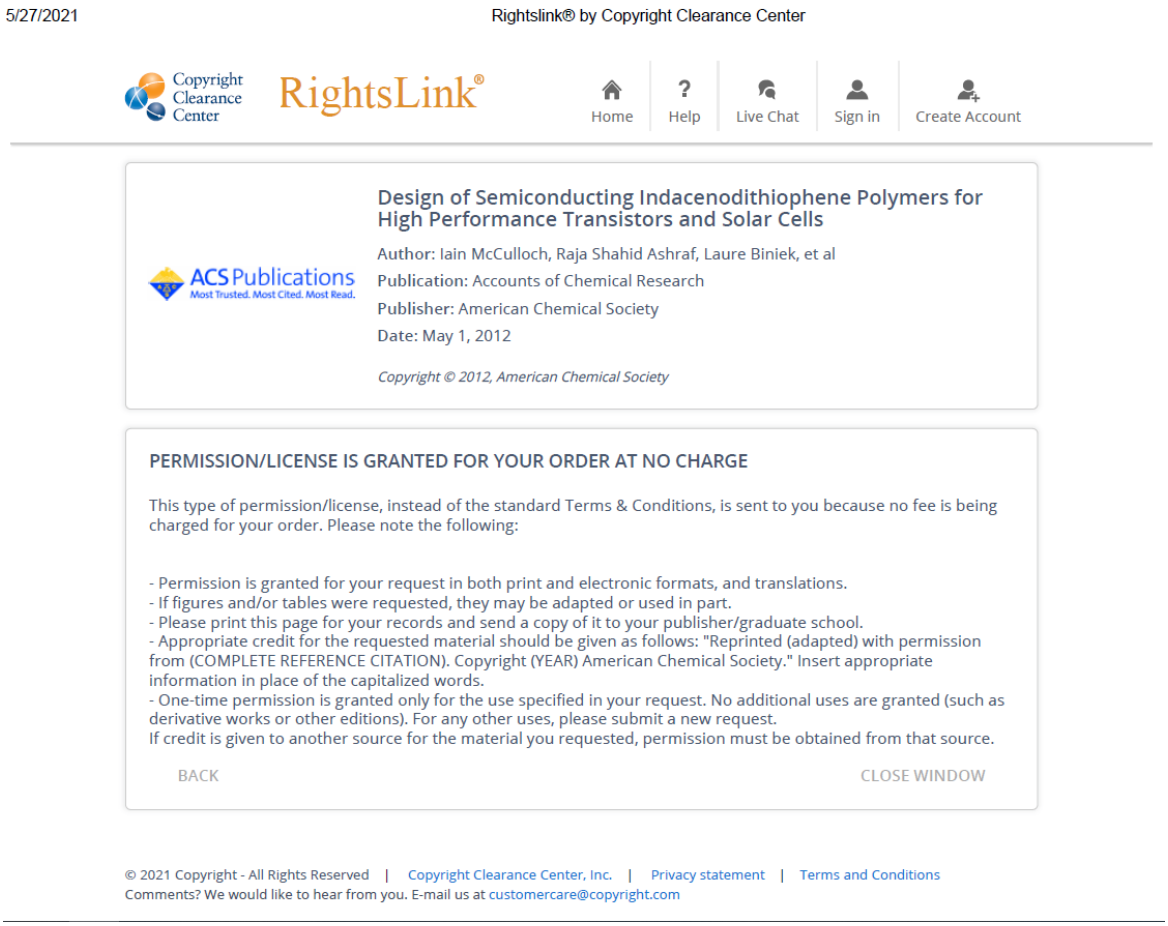

***Figure 8.1**. Licence agreement to reproduce the content reported in I. McCulloch, R. S. Ashraf, L. Biniek, H. Bronstein, C. Combe, J. E. Donaghey, D. I. James, C. B. Nielsen, B. C. Schroeder, W. Zhang, Acc. Chem. Res. **2012**, 45, 714 (Reference [22]). ACS distribution licence obtained on 27.05.2021.*

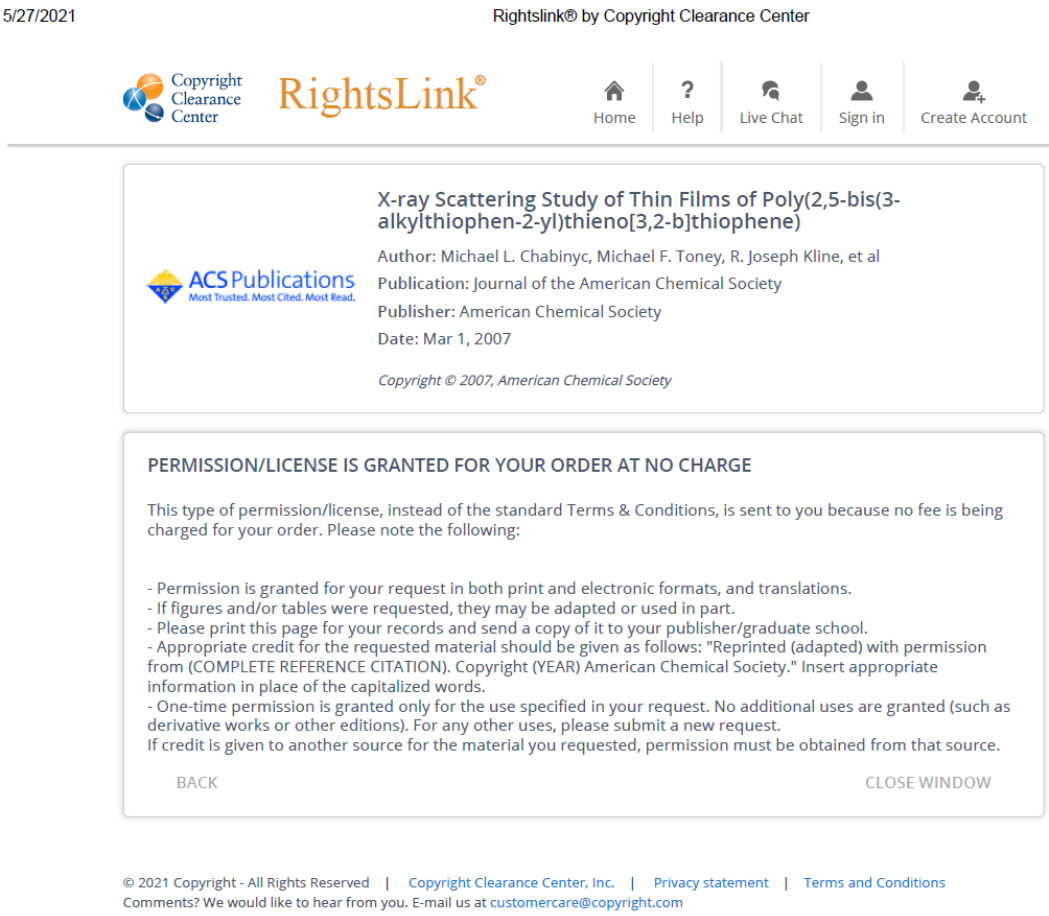

Figure 8.2. *Licence agreement to reproduce the content reported in M. L. Chabinyc, M. F. Toney, R. J. Kline, I. McCulloch, M. Heeney, J. Am. Chem. Soc.* ***2007****, 129, 3226 (Reference [34]). ACS distribution licence obtained on 27.05.2021.*

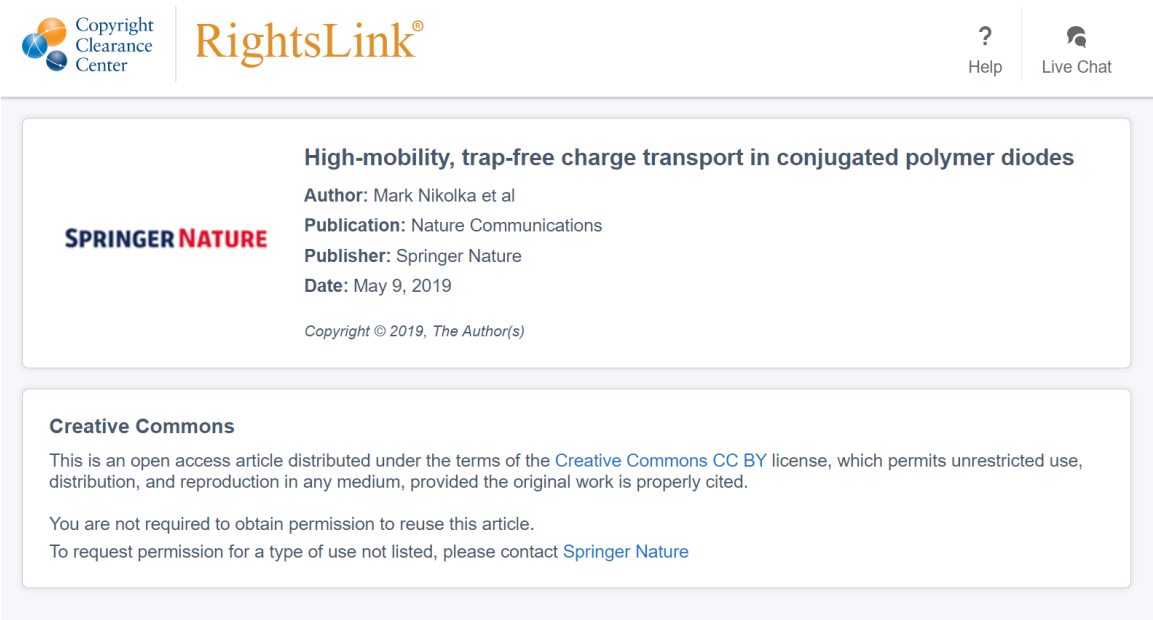

Figure 8.3. *Licence agreement to reproduce the content reported in M. Nikolka, K. Broch, J. Armitage, D. Hanifi, P. J. Nowack, D. Venkateshvaran, A. Sadhanala, J. Saska, M. Mascal, S.-H. Jung, J. Lee, I. McCulloch, A. Salleo, H. Sirringhaus, Nat. Commun.* ***2019****, 10, 2122 (Reference [31]). Springer Nature distribution licence obtained on 27.05.2021.*

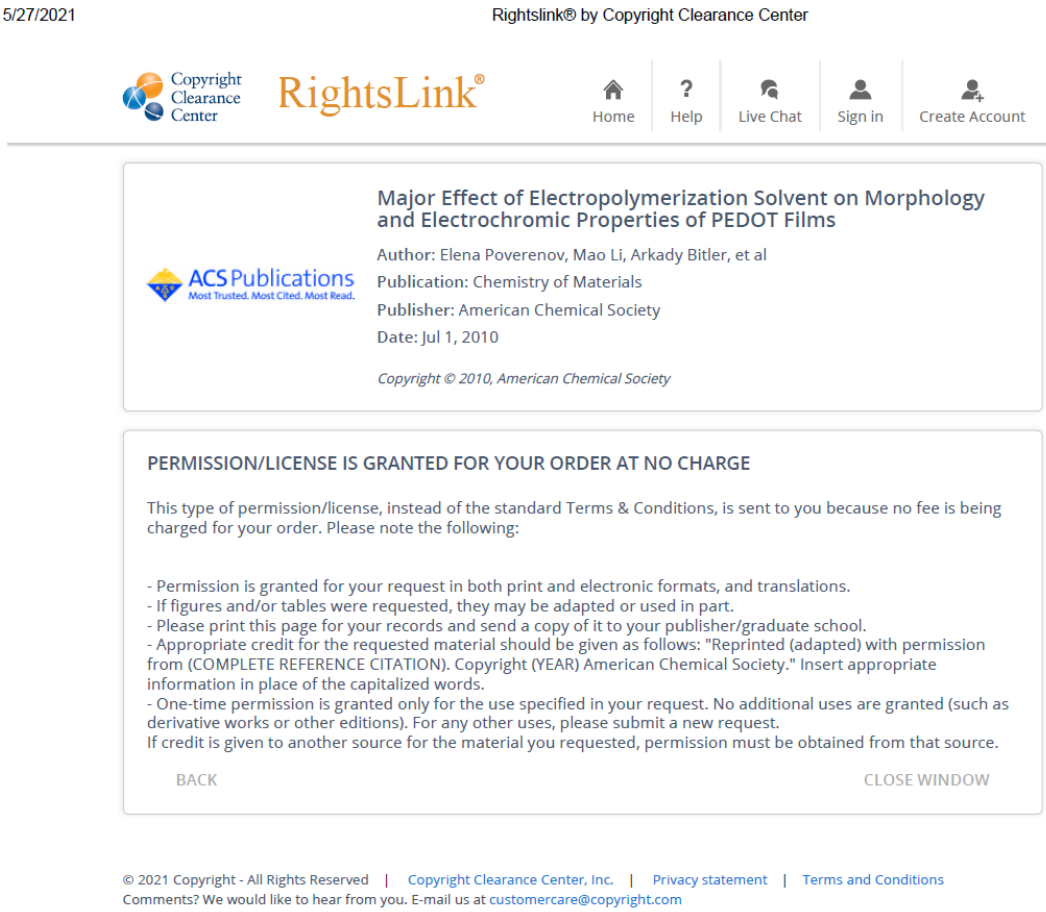

Figure 8.4. *Licence agreement to reproduce the content reported in E. Poverenov, M. Li, A. Bitler, M. Bendikov, Chem. Mater.* ***2010****, 22, 4019 (Reference [43]). ACS distribution licence obtained on 27.05.2021.*

***Figure 8.5**. Licence agreement to reproduce the content reported in J. Rivnay, S. Inal, B. A. Collins, M. Sessolo, E. Stavrinidou, X. Strakosas, C. Tassone, D. M. Delongchamp, G. G. Malliaras, Nat. Commun. **2016**, 7, 11287 (Reference [80]). Springer Nature distribution licence obtained on 27.05.2021.*

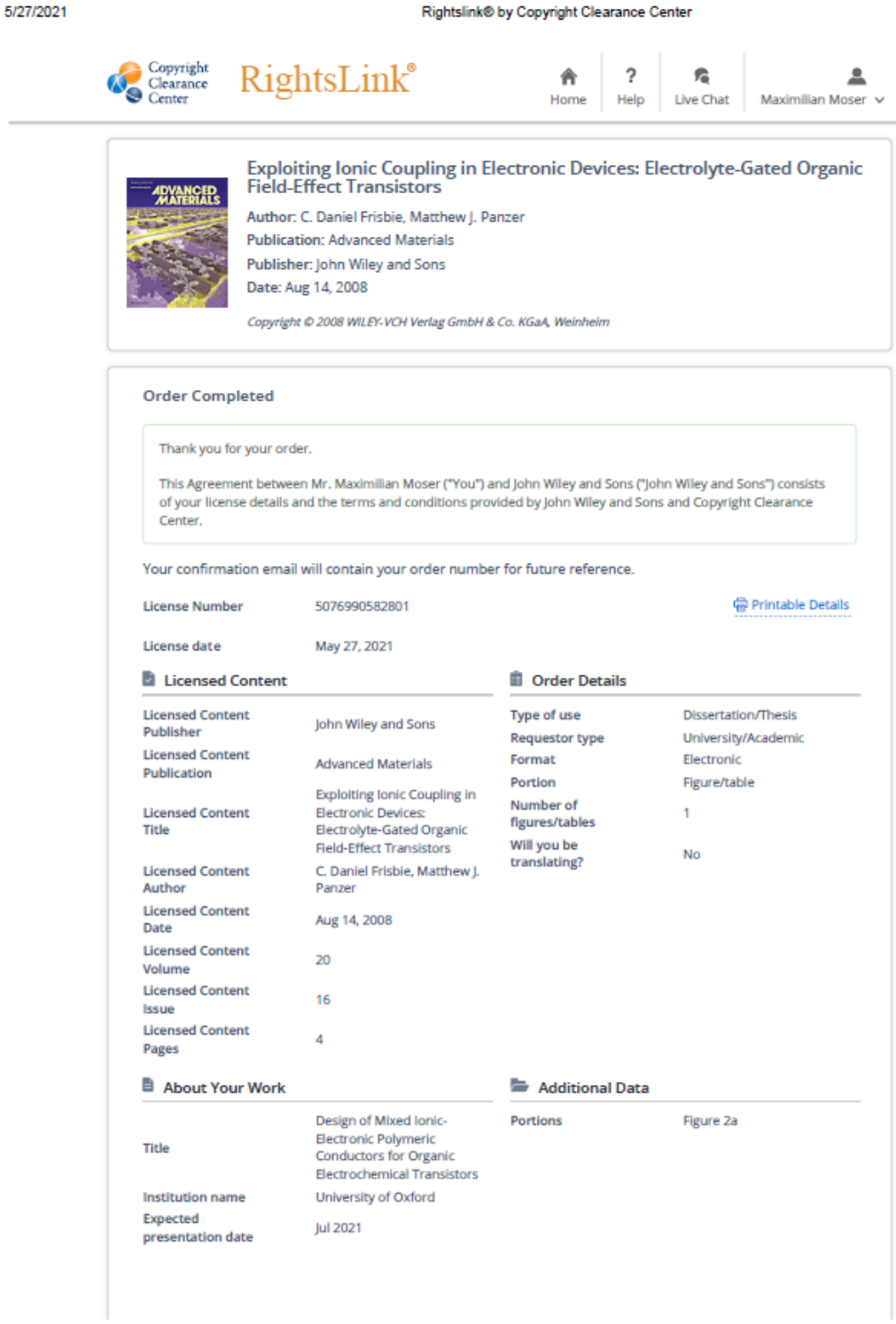

***Figure 8.6**. Licence agreement to reproduce the content reported in M. J. Panzer, C. D. Frisbie, Adv. Mater. **2008**, 20, 3177 (Reference [109]). John Wiley and Sons distribution licence obtained on 27.05.2021.*

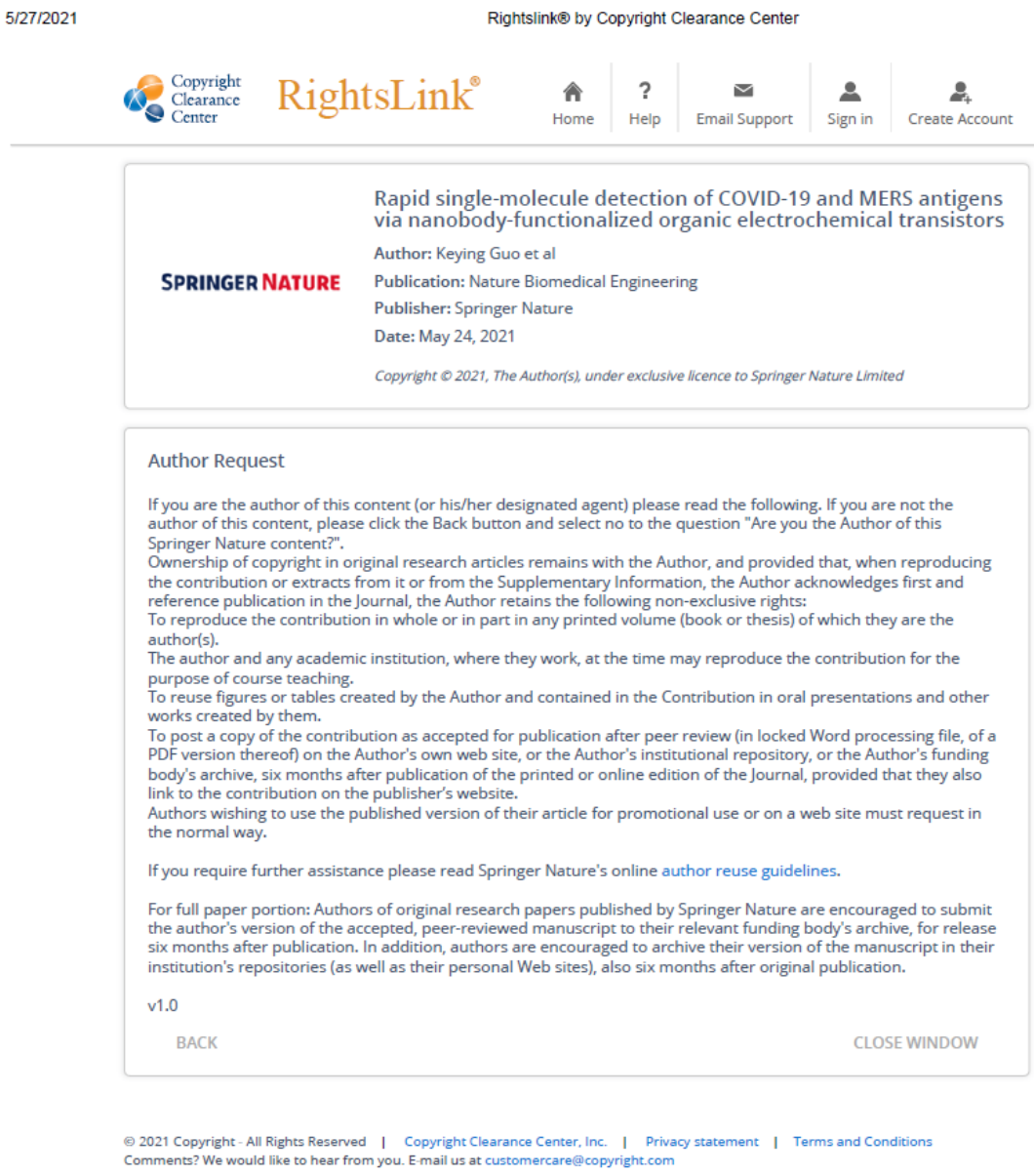

Figure 8.7*. Licence agreement to reproduce the content reported in K. Guo, S. Wustoni, A. Koklu, E. Díaz-Galicia, M. Moser, A. Hama, A. A. Alqahtani, A. N. Ahmad, F. S. Alhamlan, M. Shuaib, A. Pain, I. McCulloch, S. T. Arold, R. Grünberg, S. Inal, Nat. Biomed. Eng.* ***2021****, DOI 10.1038/s41551-021-00734-9 (Reference* [224]*). Springer Nature distribution licence obtained on 27.05.2021.*